UiT The Arctic University of Norway

Faculty of Engineering Science and Technology
Department of Electrical Engineering

CAPACITIVE POWER TRANSFER FOR MARITIME ELECTRICAL CHARGING APPLICATIONS

Hussein Mahdi Al-Sallami

A dissertation for the degree of Philosophiae Doctor, June 2023

For You is all praise, O Possessor of Bounty, Glory, and Eminence. Glory be to You – You grant to whosoever You will, and withhold.

“And above everyone possessed of knowledge is the All-Knowing One.”
–Joseph 12:76

Abstract

This study examines capacitive wireless charging for small ships and unmanned maritime vehicles. Wireless power transfer can provide the convenience of automatic charging while the ships or maritime vehicles are docking, mooring, or in a sailing maneuver. Besides, it can address the challenges that face conventional wired charging technologies, including long charging and queuing time, wear and tear of the physical contacts, handling cables and wires, and the hazards of the electric shock. Capacitive power transfer (CPT) is one of the wireless charging technologies that has received attention in on-road electric vehicle charging applications. By the main of electric fields, CPT offers an inexpensive and light charging solution with good misalignment performance. Thus, this study investigates the CPT system in which air and water are the separation medium for the electrical wireless charging of small ships and unmanned maritime vehicles.

Batteries are the main energy storage technology on ships and unmanned maritime vehicles. Charging infrastructure is essential in developing battery-powered ships and maritime vehicles. Compared to the charging infrastructure for on-road electric vehicles, electrical charging for maritime applications has attracted very little attention in the literature. Thus, this study first overviews the shore-to-ship connections by reviewing the converter topologies used in the electrification of electrical ships in the literature and on the market. Second, it examines air-gapped and underwater CPT for charging small ships and unmanned maritime vehicles.

Capacitive wireless charging, or CPT, transfers power from an electrical power source to an electrical load using alternating electric fields. The fields are confined between conductive plates separated by a dielectric medium (i.e., air or water), forming capacitors. The physical principle of the CPT is embodied in Maxwell's equations. When the frequency of alternating fields ranges from hundreds of kHz to tens of MHz, then the lumped circuit element approximations of circuit theory become valid. The network theory is an attractive methodology for analyzing CPT systems, as it bridges the gap between field analysis and circuit theory.

Unlike on-road charging applications, air or water can be utilized as charging mediums to charge small ships and unmanned maritime vehicles. Because of the low permittivity of the air, the air-gapped capacitive coupling is in the pF range. Thus, a MHz operating frequency is required to transfer power over a few hundred millimeters. This study examines an air-gapped CPT system to transfer about 135 W at a separation distance of 50 mm, a total efficiency of about 83.9%, and 1 MHz operating efficiency. The study also tests a 13.56 MHz shielded air-gapped CPT system that transfers about 100 W at a separation distance of 30 mm and a total efficiency of about 87%. The study also examines the underwater CPT system by submerging the couplers in water to increase the capacitive coupling. The system can transfer about 129 W at a separation distance of 300 mm, a total efficiency of about 81.2%, and 1.1 MHz operating efficiency. These CPT systems can upscale to provide a few kW for small ships and unmanned maritime vehicles. But they are still facing several challenges that need further investigations.

List of Included Papers

Paper	Publications
J1	**H. Mahdi**, B. Hoff and T. Østrem, "A Review of Power Converters for Ships Electrification," in *IEEE Transactions on Power Electronics*, doi: 10.1109/TPEL.2022.3227398.
J2	**H. Mahdi**, Reiji Hattori, Bjarte Hoff, Anyu Uezu, and Katsumi Akiyoshi, "Design Considerations of Capacitive Power Transfer Systems," in *IEEE Access*-submitted
J3	**H. Mahdi**, B. Hoff, P. G. Ellingsen and T. Østrem, "Conformal Transformation Analysis of Capacitive Wireless Charging," in *IEEE Access*, vol. 10, pp. 105621-105630, 2022, doi: 10.1109/ACCESS.2022.3210960.
J4	**H. Mahdi**, B. Hoff, and T. Østrem, "Optimal solutions for underwater capacitive power transfer," *Sensors*, vol. 21, no. 24, p. 8233, 2021, doi: 10.3390/s21248233.
C4	**H. Mahdi**, R. Hattori, B. Hoff, and T. Østrem, "Under seawater Capacitive Power Transfer for Maritime Charging Applications", (to be submitted).

Additional work

The author has been working with bachelor's and master's students on their graduation projects. He also lectured and supported in teaching two bachelor courses, namely MAT-1151: Matematikk 2 and ETE-2608 Elektriske anlegg 2. In addition, he has collaborated with researchers in the electromechanical research group, the Institute of Industrial Engineering at UiT, and the Global Innovation Center (GIC) at Kyushu University, Japan.

List of Additional Published Papers

Paper	Publications
J5	**H. Mahdi**, H. Arnarson, B. Solvang, and B. A. Bremdal, “Investigation of Wireless Electrification for a Reconfigurable Manufacturing Cell,” *Journal of Manufacturing Systems*, vol. 67, pp. 379-388, 2023, doi 10.1016/j.jmsy.2023.01.002.
J6	H. Arnarson, **H. Mahdi**, B. Solvang, and B. A. Bremdal, “Towards automatic configuration and programming of a manufacturing cell,” *Journal of Manufacturing Systems*, vol. 64, pp.225–235, 2022, doi 10.1016/j.jmsy.2022.06.005.
J7	**H. Mahdi**, A. M. Ammar, Y. Nour and M. A. E. Andersen, "A Class-E-Based Resonant AC-DC Converter With Inherent PFC Capability," in *IEEE Access*, vol. 9, pp. 46664-46673, 2021, doi: 10.1109/ACCESS.2021.3067800.
C1	**H. Mahdi**, B. Hoff and T. Østrem, "Evaluation of Capacitive Power Transfer for Small Vessels Charging Applications," *2020 IEEE 29th International Symposium on Industrial Electronics (ISIE)*, 2020, pp. 1605-1610, doi: 10.1109/ISIE45063.2020.9152514.
C2	**H. Mahdi**, B. Hoff and T. Østrem, "Maximum Available Power of Undersea Capacitive Coupling in a Wireless Power Transfer System," *2021 IEEE Wireless Power Transfer Conference (WPTC)*, 2021, pp. 1-4, doi: 10.1109/WPTC51349.2021.9458006.
C3	**H. Mahdi**, B. Hoff and T. Østrem, "Maximum Available Efficiency of Undersea Capacitive Coupling in a Wireless Power Transfer System," *2021 IEEE 30th International Symposium on Industrial Electronics (ISIE)*, 2021, pp. 1-5, doi: 10.1109/ISIE45552.2021.9576386.

Acknowledgements

Nearing the completion of a well-rounded academic journey, I have many to thank. First of all, I would like to thank Almighty God for granting me the determination to complete the most rewarding achievement in my life, the courage to learn, and the strength to keep going.

I want to express my gratitude to my supervisor Bjarte Hoff and co-supervisor Trond Østrem who provided excellent guidance during my research and helped me to complete the thesis. I also want to take this opportunity to thank Arild Steen, Alexander Pankratov, Ketil Hansen, Johnny Tokle, Geir Edvardsen, Hans Wiggo Johnsen, and Aleksander Pedersen for giving me support and assistance. I am also thankful to Pål Gunnar Ellingsen, Bjørn Solvang, and Bernt Arild Bremdal for their invaluable discussions and feedback. I cannot forget to thank all my colleagues at Institutt for elektroteknologi and UiT-Narvik for their support.

Words cannot express my sincere gratitude to Professor Reiji Hattori for hosting me in his laboratory, guiding my research, and helping me even after finishing my research stay. I also want to thank Anyu Uezu, Katsumi Akiyoshi, Jingang Chen, Waters-san, and all the students at Hattori-laboratory for their help and support.

Special thanks to my friends Halldor Arnarson, Mathias Sæterbø, Sujay Deshpande, Shayan Dadman, Subhashis Das, Lazar Sibul, Natalia Khan, Iveta Novakova, Aritro Banerjee, Harpal Singh, Ananya Mishra, Ashwiny Pandey, Maya Mandasari, Martin Andresen, Hafeez Omosanya, and all friends for their support and putting up with my stresses and moans.

To conclude, my most enormous thanks to my parents, my sister Farah, and my brother Hasan for the continuous support and unconditional help they have shown throughout my life, without which I would not reach this stage.

Table of Contents

List of Figures

List of Tables

List of Abbreviations

3L-NPC Three-Level Neutral-Point Clamped

AES All-Electric Ship

AIMM Industrial Mobile Manipulator

APF Active Power Filter

CPT Capacitive Power Transfer

CSC Current Source Converter

DAB Dual Active Bridge

DMS Dedicated Manufacturing System

EHF Extremely High Frequency

EMI Electromagnetic Interference

ESS Energy Storage System

EV Electrical Vehicles

FEM Finite Element Method

FMS Flexible Manufacturing System

GaN Gallium Nitride

GTO Gate turn-off thyristor

HF High Frequency

HPT Hybrid Power Transfer

IEC International Electrotechnical Commission

IEGT Injection Enhancement Insulated Gate Bipolar Transistors

IGBT Insulated Gate Bipolar Transistors

IGCT Integrated Gate Commutated Thyristors

IMO International Maritime Organization

IoT Internet-of-Thing

IPT Inductive Power Transfer

JBS Junction Barrier Schottky

LF Low Frequency

MF Medium Frequency

MIMO Multiple-Input Multiple-Output

MISO Multiple-Input Single-Output

MMC Modular Multilevel Converters

MOSFET Metal Oxide Semiconductor Field-Effect Transistors

MVDC Medium-Voltage DC

NEK Norwegian Electrotechnical Committee

PEI Power Electronics Interface

PFC power factor correction

PV Photovoltaic

PWM Pulse Width Modulation

RMS Reconfigurable Manufacturing System

SHF Super High Frequency

SiC Silicon-Carbide

SIMO Single-Input Multiple-Output

SM Submodules

THD Total Harmonic Distortion

UHF Ultra High Frequency

USV Unmanned Surface Vehicle

UUV Unmanned Underwater Vehicle

VHF Very High Frequency

VNA Vector Network Analyzer

VSC Voltage Source Converter

WBG Wide-Bandgap

WPT Wireless Power Transfer

ZCS Zero Current Switching

ZVS Zero Voltage Switching

1 Introduction

This chapter covers the motivation for proposing wireless charging for maritime vessels (ships) and unmanned vehicles. It also presents the three standard charging technologies: Battery-swapping, wired charging, and wireless charging. Focusing on wireless charging, the chapter defines different WPT technologies and briefly overviews prior research on Wireless Power Transfer (WPT) for maritime charging applications. Finally, the chapter asks the research questions and presents the organization of the thesis.

1.1 Motivation

Maritime transport is the backbone of international trade, where over 80 percent of global trading by volume is carried by ships [1]. The International Maritime Organization (IMO) expected that the emissions in 2050 could present 90 to 130 percent of 2008 emissions [2]. Electrification is one way toward the reduction of emissions. The electrification of ships has experienced a multidecade evolution starting with the earliest records dating back to the 1880s, [3, 4]. It has recently received considerable attention as it facilitates emissions reduction, improving shipping functionality, efficiency, and fuel economy.

The All-Electric Ship (AES) is a paradigm of the shift in the electrification of ships. It comprises a power generation module, an energy storage module, a power conversion module, an electric propulsion module, and ship service

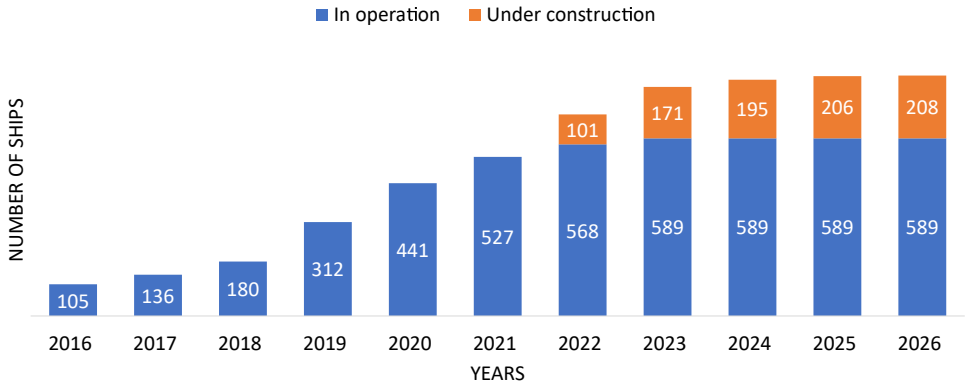

Figure 1.1: The growth of battery-powered ships [10].

loads [5]. In other words, the shipboard power system of the AES can be seen as a microgrid that integrates onboard distributed generations and integrated Energy Storage System (ESS) [6]. The shipboard ESS has mainly two merits: economic and environmental index improvements and operating flexibility improvements in long-term operation [7].

A variety of energy storage technologies are available with different operating characteristics. For instance, batteries, high-power flywheels, and supercapacitors contribute to optimal energy management by reducing fuel cost [8]. Batteries, in particular, can increase energy efficiency, improve dynamic performance, and shave peak loads [9]. Fig. 1.1 [1] shows the growth of battery-powered ships between 2016 and 2026. For long-distance sailing, hybrid battery-powered ships forms 52% of all battery-powered maritime electrified vessels [10]. However, the world's first pure battery-powered tanker "Asahi" entered service in Tokyo Bay with about 3.5 MWh lithium-ion battery in March 2022 [11].

Oceans and seas provide not only transportation routes but also other valuable ecosystem services, including food, jobs, health benefits, climate regulation, and cultural heritages [12]. For instance, aquaculture and fisheries are essential parts of the solution for the Norwegian economy as Norway moves towards a post-oil industry era [13]. Under harsh environmental conditions, unmanned maritime vehicles are expected to help in fish farming operations such as inspection, maintenance, and repair routines [14]. Thus, there is an anticipated increase in electric unmanned maritime vehicles in the near future. Table 1.1 lists some of the current commercially available unmanned maritime vehicles: Unmanned Underwater Vehicle (UUV) and Unmanned Surface Vehicle (USV) in Norway.

1. Note: The figure is adapted with permission from Alternative Fuels Insight (AFI) platform URL: `https:https://www.dnv.com/services/alternative-fuels-insight-128171`. Special thanks to Simon Adams.

Table 1.1: SOME OF THE CURRENT COMMERCIALLY AVAILABLE UUV and USV IN NORWAY.

Industry	Solutions	Specifications
Blueye Robotics [15]	UUV	485 × 257 × 354 mm, 9 kg, 5 h, 96 W h
Kongsberg [16]	UUV	49 cm diameter × 2.5 m, 70 kg, 1500 W (Cable)
Probot [17]	UUV	70 cm diameter, 20 kg, (Cable)
Maritime Robotics [18]	USV	200 × 108 × 81.5 cm, 55 kg, 20 h, 250 W

Additionally, ships and ship-borne devices record oceanographic observations, study climate change, and observe marine pollution to uncover the mysteries of oceans and seas. For the last two decades, unmanned maritime vehicles have become an essential enabling technology for operating autonomously in challenging and hazardous shallow or deep water [19]. Both USV and UUV have been extensively used in marine exploitation investigation and emergency search rescue [20, 21]. Powered by lithium-ion batteries, unmanned maritime vehicles profile up hundreds to thousands of kilometers of the ocean vertically or horizontally under remote control over months [22].

Thus far, lithium-ion batteries are a promising energy storage technology for ships and unmanned maritime vehicles. They are developing fast with significant increases in the life cycle, energy density, and current rating [23]. For ships, the maximum capacity of batteries can reach thousands of kWh depending on the ship type, sailing distance, and other owners' specifications [24]. At the same time, unmanned maritime vehicles require tens to hundreds of kWh [22]. Charging infrastructure can play a critical role in ameliorating the development of battery-powered maritime vessels and vehicles. Battery-swapping, wired charging, and wireless charging are three main charging approaches that can be adapted for maritime electric charging applications. The following section briefly discusses these technologies.

1.2 Charging technologies

Charging technologies play an essential role in the main characteristics of batteries, including their energy performance, power performance, and lifetime. The three main charging technologies are battery-swapping, wired charging,

and wireless charging. These technologies vary in power limitation, performance, way of energy supply, and charging time.

1.2.1 Battery-swapping

It is a process of exchanging depleted batteries for fully charged ones within a short time. The battery-swapping technology has several advantages: providing fast energy refueling services, integrating renewable energy resources, and improving the efficiency, flexibility, and stability of electrical grids [25, 26]. In Electrical Vehicles (EV), swapping a depleted battery with a fully charged one takes about seven times faster than the fast-charging approach [27]. China built its first on-road battery-swapping station in 2018, and since then, 14.1 million charging stations have been built across the country [28].

For maritime electrical charging applications, Wärtsilä developed and delivered two battery-swapping stations for ships in the Netherlands in 2021 [29]. In Norway, Norled, SEAM, and others have developed an autonomous battery Swap robotic station that swaps out batteries on express boats while at the quay [30]. Battery-swapping is also commonly used for UUV [22] and USV [18]. However, this charging technology faces challenges, such as the complexity of swapping structure, requiring a lot of space, high cost, station congestion, and complicated scheduling and management strategies[31, 32].

1.2.2 Wired charging

Wired charging is the conventional charging technique using charging cables that can carry high currents varying from tens to hundreds of amperes. In EV charging applications, wired charging is sub-categorized into (1) onboard, which is typically a slow charging approach, and (2) off-board, which is typically a fast charging approach. Table 1.2 [2] compares wired charging approaches in terms of power level type, charging voltage level, power level, and charging time. At high power levels, the current rating of the charging cable increases, which makes the cable bulky and increases the conduction losses. A cooling system is required to void overheating [33].

Conventional shore-to-ship connection power cables are three-phase 450 V to 600 V with up to 4800 A [34]. This approach is more convenient for large

2. Note: The data in the table is adapted in part from M. Yilmaz and P. T. Krein, "Review of Battery Charger Topologies, Charging Power Levels, and Infrastructure for Plug-In Electric and Hybrid Vehicles," in IEEE Transactions on Power Electronics, vol. 28, no. 5, pp. 2151-2169, May 2013, doi: 10.1109/TPEL.2012.2212917.

Table 1.2: A COMPARISON BETWEEN THE WIRED CHARGING APPROACHES FOR EV CHARGING APPLICATIONS.

Location	Onboard 1-Phase	Onboard 1- or 3-Phase	Off-board 3-Phase
Power level type	Slow	Primary	Fast
Voltage level (V)	230 AC	400 AC	400-800 DC
Power (kW)	1.9	19.2	100
Time (hours)	11-36	2-3	0.2 -0.5

battery-powered ships that require more power to recharge their onboard batteries. On ships, the charging system is commonly found onboard. The International Electrotechnical Commission (IEC) [35] and Norwegian Electrotechnical Committee (NEK) [36] have released some guidelines regarding plug, voltage, and current for maritime electric charging applications. The shore-to-ship connection can be achieved manually or automatically [37]. The manual approach requires carrying several heavy cables, connecting, and disconnecting plugs, usually taking several minutes. While the automatic approach can be achieved using a robotic arm to improve safety and maximize the charging time, but it adds complexity and cost to the shore infrastructure. In terms of low-power maritime charging applications, various robotic docking, and latching mechanisms are proposed for both USV [38] and UUV [39]. However, these techniques involve high-precision connection mechanisms, which increase the design complexity and overall price of the system [22].

1.2.3 Wireless charging

Wireless Power Transfer (WPT), or wireless charging, has attracted attention due to its capability to transfer electric power without mechanical contact. International Telecommunication Union [40] defines WPT as "*the transmission of power from a power source to an electrical load using the electromagnetic field.*" The three main groups of these technologies are near-field, mid-range, and far-field [41]. Near-field wireless charging is more suitable for charging applications than mid-range and far-field WPT. It can potentially address the challenges in the wired charging approach, including long charging time, long queuing time at the charging stations, and hazard of the electric shock [42]. In addition, it provides the convenience of automatic charging through three different modes: static, quasi-dynamic, and dynamic charging modes.

The research focuses on proposing WPT to charge roadway EV [42–49]. Many

Table 1.3: SOME OF THE MANUFACTURES OF WIRELESS CHARGING SYSTEMS.

Provider	**Country**	**Power (kW)**	**Ref.**
Plugless Power	U.S.	3.3 & 7.2	[61]
WiTricity	U.S.	3.6 & 11	[62]
Momentum Dynamics	U.S.	450	[63]
Mojo Mobility	U.S	20	[64]
Hevo	U.S.	8	[65]
TGood	Hong Kong	60	[66]
Toshiba	Japan	7	[67]
INTIS	Germany	50 & 100	[68]

Table 1.4: A COMPARISON BETWEEN THE MAIN CHARGING TECHNOLOGIES.

Features	**Battery-swapping**	**Wired**	**Wireless**
Power level	High	High	Low
Charging time	Very fast	Fast	Low to fast
Complexity	Very high	Low-moderate	low
Cost	Very high	Low-high	low-high
Maintenance	High	Low-moderate	Low
Autonomous	Extrinsic	Extrinsic	Inherent

manufacturers have proposed wireless charging solutions for EV charging applications. Table 1.3 lists some manufacturers that have recently started to provide wireless charging stations. For maritime electrical charging applications, WPT were proposed for charging ships [50–53], and unmanned martime vehicles [54–60]. More detail about wireless charging applications for ships and unmanned maritime vehicles will be discussed in section 1.4.

Thus far, the three charging approaches can be utilized for maritime electrical charging applications. Each approach has its own merits and drawbacks. Table 1.4 summarizes the main characteristics of the three charging technologies. Wireless charging provides flexibility, mobility, convenience, safety, and maintenance-free solution for maritime vessels and vehicles. Thus, it has recently received more attention in the literature. There are various wireless charging technologies, and the following section briefly discusses them.

Table 1.5: A COMPARISON BETWEEN THE MAIN GROUPS OF WPT.

	Near-field	**Mid-range**	**Far-field**
Wave	Electric/Magnetic	Magnetic	Electromagnetic
Rang	Very short (cm)	Short (m)	Moderate-long (km)
Frequency	Low-high	High	Very high-extremely high
Power	Low-Moderate	Moderate	Ultra low
Architecture	Simple/Moderate	Complex	Complex

1.3 Wireless power transfer technologies

Wireless charging technologies use electromagnetic waves to transfer energy. The classification depends on the size of the transmitter and receiver and the transfer distance between them. Table 1.5 summarizes a comparison between the three main groups in terms of the type of wave, distance range, operating frequency range [3], power level, and system architecture.

1.3.1 Far-field

It is a radiative WPT technique that utilizes Very High Frequency (VHF) (30 MHz to 300 MHz) to Extremely High Frequency (EHF) (30 GHz to 300 GHz) electromagnetic waves over kilometers separation distance between transmitters and receivers. Chen et al. [69] tried to transfer 3.5 kW over a distance of 48.8 m at 2.46 GHz, but the receiving power was only 2.87 W which varies with the separate working conditions. Yang et al. [26] also attempted to transfer 1.87 kW over a distance of 5 m at 5.8 GHz, the receiving power was 142 W.

These systems require a high-precision and high-stability source, complex design of the antennas, and sophisticated tracking mechanisms. Besides, far-field WPT is unsafe for higher power levels. Thus, it is deployed for ultra-low power (i.e., µW ranges) commercial research applications [70]. Optical WPT is another type of radiative WPT which operates in THz frequency ranges. It can transfer tens of watts over a few kilometers of distance [71]. However, this type of radiative WPT suffers from low efficiency (i.e., around 10 to 20%), safety challenges, and interference or blockages by obstacles.

3. Frequency ranges are according to the International Telecommunication Union definitions.

1.3.2 Medium-field

Krus et al. [72] define the mid-range WPT as when the transmitter and receiver sizes are two to three times smaller than the distance between them. In 2007 at the Massachusetts Institute of Technology, they experimentally demonstrated transferring 60 W over distances excess of 2 m with about 40% efficiency using four self-resonant coils with the radius of 20 cm. Mid-range WPT requires self-resonance as a stringent condition to achieve high efficiency.

Medium-field WPT needs an impedance matching system and frequency tuning techniques to adapt to the distance variation and the interferences caused by conductive objects in the vicinity [73]. Impedance matching accompanies complex engineering structures under practical situations [74]. The frequency tuning operates under the frequency splitting phenomenon. It requires a controller which incorporates a directional coupler [4] in the driver loop [76]. Transferring high power at MHz self-resonance faces significant challenges in practice.

1.3.3 Near-field

Near-field WPT, also referred to "non-beam" WPT, is a non-radioactive propagation WPT technique in which the sizes of the transmitter and the receiver are much smaller than the wavelength of the electromagnetic waves [41]. Imura T. [77] categorized near-field WPT based on the coupling type into magnetic and electric field coupling.

Inductive Power Transfer (IPT) [5] transfers power by means of alternating magnetic fields. The transmitter coil generates time-varying magnetic fields that transverse the receiver coil, resulting in an induced voltage in the receiver side circuitry. Capacitive Power Transfer (CPT) [6] transfers power wirelessly using alternating electric fields confined between conductive plates. Combining the merits of IPT and CPT, Hybrid Power Transfer (HPT) have better power scalability, Electromagnetic Interference (EMI) tolerance, and power transfer density [78]. Table 1.6 lists a comparison between IPT, CPT, and HPT in terms of frequency, power levels, misalignment sensitivity, power transfer density, voltage stress, architecture complexity, and cost.

Although Nikola Tesla introduced both IPT and CPT in 1891, it took about a century until IPT was commercialized in the mid-1990s [79]. Since then, IPT

4. W.W. Mumford [75] defined the directional coupler as "*a device which samples separately the direct and the reflected waves in a transmission line*."
5. It is also called "magnetic induction", "magnetic coupling", "inductive coupling", or "inductive charging."
6. It is also called "electric coupling", "capacitive coupling", or "capacitive charging."

Table 1.6: A COMPARISON BETWEEN THE NEAR-FIELD WPT.

WPT	IPT	CPT	HPT
Frequency	Medium	High	High
Power level	upto MW	upto kW	upto MW
Misalignment sensitivity	High	Low	Moderate
Power density	Low	High	Moderate
Voltage stress	Low	High	Moderate
Architecture	Moderate	Simple	Complex
Cost	High	Low	Moderate

has received considerable attention in industrial automation, public transportation, and EV. In contrast, CPT started to be investigated and researched for EV charging applications in 2008 [80]. In the literature, many papers investigated and compared between IPT and CPT in terms of converter topologies, compensation circuits, power pads, and coupler structures [42, 48, 78, 79, 81–84]. The main focus is the roadway EV, as they have experienced remarkable growth in research and on the market. The next section, however, focuses on the WPT technologies for maritime charging applications.

1.4 Prior work in maritime wireless charging

This section focuses on the previous research about WPT for maritime electric charging applications. Compared to the on-road EV charging, the maritime WPT charging can utilize air or water as a medium to transfer the required power with mechanical contact. Fig. 1.2 illustrates some of the prior works of underwater WPT for maritime applications, which shows the research institutes, WPT technology, the compensation circuits, separation distance, efficiency, the operating frequency, and power transferred.

1.4.1 Inductive charging

Researchers proposed IPT for charging ships from shore-side [50–52], or offshore connections from tugboat [53]. Guidi et al. [50] transferred 580 W over air-gapped separation distance ranged from 20 mm to 56 mm at operating frequency of 104 kHz to 137 kHz. Upscaling the transfer power to 1 MW to 2 MW, Guidi et al. [51] discussed the design challenges of high-power inductive charg-

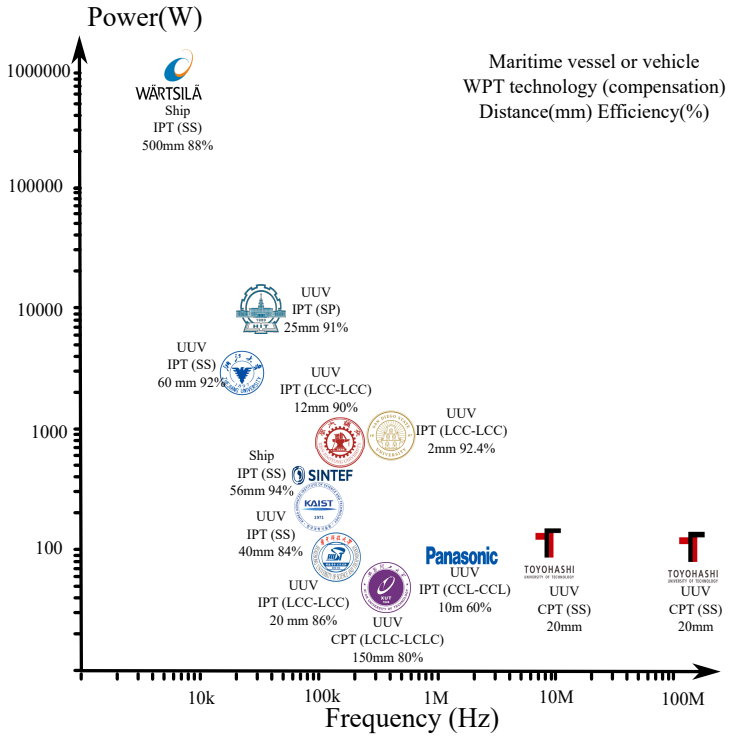

Figure 1.2: Some of the prior works of underwater WPT for maritime applications.

ing systems in maritime applications. Kumar et al. [53] investigated the feasibility of IPT in tugboat operation to improve fuel efficiency. On the market, there are some commercially IPT-based charging stations for ship charging applications. The IPT technology offers a 100 kW wireless charging option for electric and hybrid ferries, yachts, fishing vessels, tugboats, and research vessels [85]. Wärtsilä Norway offers an IPT system that can transfer more than 2 MW with a distance up to 50 cm using the series-series compensation [86].

The first underwater IPT system was developed and tested in 1998 for communications and power transfer between UUV and a dock [54, 55]. The system could transfer 200 W with an efficiency of 83% and operating frequencies varied from 65 kHz to 80 kHz. Since then, the focus has continued using underwater IPT for charging UUV. Kojiya et al. [56] confirmed the possibility of transmitting about 1 kW of electric power at about 90% efficiency and over a 11 mm separation distance using underwater IPT. Li et al. [57] transferred up to 400 W electrical power with a 2 mm distance in saltwater at 40 MPa representing 4000 m deep sea. Cheng et. al [58] succeeded to transfer 10 kW at 21 kHz in fresh- and seawater over 25 mm distance. Orekan et al. [59] tried to increase the separation distance to 40 mm at which they managed to transfer 34 W with operating frequency 178 kHz and efficiency of 58%. Yan et al. [60] further in-

crease the separation distance between the transmitter and receiver to 66 mm to transfer up to 10 W with operating frequency 504.5 kHz and efficiency about 85%.

Teeneti et al. [22] reviewed the state-of-the-art IPT solutions for underwater applications and discussed the engineering challenges of the design of the system. The IPT suffers from eddy current losses, possibly resulting in a fire hazard. It also comprises expensive, fragile, bulky parts, including ferrite iron plates and Litz wires. Besides, the misalignment between the transmitter and receiver power pads has a negative impact on the system performance [87]. In contrast, CPT is less expensive and lighter, with negligible eddy current and misalignment losses compared to IPT [46].

1.4.2 Capacitive charging

Capacitive coupling can provide an attractive alternative for shore-to-ship connection [88–90]. For instance, Yang et al. [88] proposed a bidirectional CPT system for charging USVs under seawater. They transferred 100 W power over 140 mm distance at 625 kHz and about 80.15% efficiency. However, they put seawater bags between the couplers. In this way, the stray coupling between the plates and the fringing fields are neglected, which explains the high efficiency. Other researchers [91, 92] also proposed underwater CPT systems for charging USVs. Tamura et al. [91] transferred 400 W power under freshwater over 20 mm distance at 10.77 MHz and ac-ac efficiency exceeding 90%. While in [92], they designed under seawater CPT system that can transfer data and 100 W power under freshwater over 20 mm distance at 6.78 MHz and ac-ac efficiency exceeding 90%.

Thus far, IPT systems have received more attention for maritime electric charging applications. Alternatively, CPT can tackle IPT challenges, making it a candidate for charging small ships or unmanned maritime vehicles. Adapting CPT raises a number of questions. The next section asks the main research questions.

1.5 Research questions

Although the first commercially available shipboard electrical systems date back to the 1880s, the world's first fully-electric battery-powered ferry was set into operation in 2015 in Norway [90]. Since then, the trend toward battery-powered ships and maritime vehicles appears likely to continue [4]. Providing convenient, reliable, and flexible charging infrastructure can accelerate the

development of battery-powered ships and maritime vehicles. This raises the following research questions:

Q1: *What are the current and future trends and potential challenges facing the electrification of ships?*

Q2: *What are the current shore-to-ship power solutions in the literature and on the market?*

Q3: *What are the design considerations of CPT system for charging applications?*

Q4: *What are the effects of the separation distance and the operating frequency on the capacitive coupling, the power transferability, and the overall efficiency of the CPT?*

The questions above were answered in several published manuscripts: 9 were published, and two will be submitted for publication. Five manuscripts are selected to form the main chapters. The next section shows the structure of the dissertation-selected manuscripts.

1.6 Dissertation organization

This thesis comprises seven chapters. They are divided as follows:

Chapter 1 presented the motivation behind the research, defined different charging technologies, reviewed the current literature on maritime wireless charging technologies, and asked the main research questions.

Chapter 2 investigates the shore-to-ship connections by reviewing the converters proposed in the literature and available on the market. It also overviews the shipboard converters that connect loads, ESS, and renewable energy technologies. The chapter examines the current shore-to-ship and shipboard technologies, anticipates the future trends and potential challenges facing these technologies, and stimulates the research to accelerate more efficient and reliable electric ships.

Chapter 3 provides a theoretical framework and explains the methodology used for conducting the research. Network theory is a common useful tool in the study of microwave engineering. It bridges the gap between circuit theory and electromagnetic theory. For the reader's convenience to better understand the published work, this chapter gives fundamental principles and selected

theorems that help in the analysis of CPT. It aims to present the main design considerations, limitations and challenges of CPT systems.

Chapter 4 studies the capacitive coupling when air, freshwater, and seawater are the mediums separating the couplers. Using the conformal transformation, the chapter proposes a mathematical model to calculate the capacitive coupling. Besides, it shows that submerging the couplers under seawater can enhance the coupling, and changes in the gap distance and the operating frequency does not significantly affect the underwater coupling.

Chapter 5 proposes three possible solutions to achieve maximum efficiency, maximum power, or conjugate matching. Mathematical analysis shows that all the solutions are a function of the coupling admittances. The chapter investigates the efficiency and power transferability of underwater CPT at medium-range operating frequencies.

Chapter 6 expands the work in chapter 5 by considering the losses in the source to calculate the maximum efficiency of a CPT system. It shows that the input resistance of CPT system seen watching from the source should be high enough to achieve good efficiency. Thus, an impedance matching or more complex compensation on the transmitter side should be adopted to achieve high efficiency.

Chapter 7 summarizes the main findings of the research, discusses the relationship between the results of this study and the results of similar studies in the published literature, and indicates the research limitations. It also concludes and suggests future works.

2

A Review of Power Converters for Ships Electrification

Hussein Mahdi, Bjarte Hoff, Trond Østrem

DOI: 10.1109/TPEL.2022.3227398

Paper's Contribution

This paper presents the current situation and future trends in the electrification of ships. Although power converters play a key role in electrification, they have received much less attention in the research. Thus, The main contributions of the paper are: (1) It focuses on the reviews of the shore-to-ship and shipboard converters found in the literature and on the market, (2) it also gives instructions for designing, analyzing, and selecting suitable ship converters, and (3) it tries to anticipate future trends and potential challenges.

3

Design Considerations of Capacitive Power Transfer Systems

Hussein Mahdi, Reiji Hattori, Bjarte Hoff, Anyu Uezu, and Katsumi Akiyoshi

DOI: Submitted

Hussein Mahdi, Reiji Hattori, Bjarte Hoff, Anyu Uezu, and Katsumi Akiyoshi, "Design Considerations of Capacitive Power Transfer Systems," in *IEEE Access*

Paper's Contribution

This paper discusses the theoretical and practical considerations, challenges, and limitations of designing CPT systems. The main contributions of the paper are: (1) It provides a theoretical framework by explaining the methodology used for conducting the research, (2) it proposes one- and two-port measuring approaches using vector network analyzers to determine the coupling parameters and validate the measurements by simulated values using COMSOL Multiphysics, and (3) it uses the two-port measurements to design and test a 13.56 MHz CPT system.

IEEE Access
Multidisciplinary ⋮ Rapid Review ⋮ Open Access Journal

Date of publication xxxx 00, 0000, date of current version xxxx 00, 0000.

Digital Object Identifier 10.1109/ACCESS.2023.DOI

Design Considerations of Capacitive Power Transfer Systems

HUSSEIN MAHDI[1], (Graduate Member, IEEE), REIJI HATTORI[2],BJARTE HOFF.[1], (Senor Member, IEEE), ANYU UEZU[2], and KATSUMI AKIYOSHI[2]

[1]Department of Electrical Engineering, UiT The Arctic University of Norway, Narvik 8514, Norway (e-mail: hussein.al-sallami@uit.no; bjarte.hoff@uit.no)
[2]Interdisciplinary Graduate School of Engineering Sciences, Kyushu University, Fukuoka 816-8580, Japan (e-mail: hattori@gic.kyushu-u.ac.jp, uezu.anyu.340@s.kyushu-u.ac.jp, akiyoshi.katsumi.178@s.kyushu-u.ac.jp)

Corresponding author: Hussein Mahdi (e-mail: hussein.al-sallami@uit.no).

The publication charges for this article have been funded by a grant from the publication fund of UiT The Arctic University of Norway

ABSTRACT Capacitive power transfer (CPT) is a near-field wireless power transfer (WPT) technology that has attracted attention in different charging applications. Using electric fields, CPT gives charging systems advantages in terms of cost, weight, flexibility, and mobility. This paper discusses theoretical and practical design considerations of a CPT system to understand and improve the technology and its applications. The paper proposes one- and two-port measuring approaches using vector network analyzers to determine the coupling parameters and validate the measurements by simulated values using COMSOL Multiphysics©. The two-port approach gives more accurate results than the one-port approach. The paper designs and tests a 13.56 MHz CPT system using the two-port measurement results. The system transfers 100 W at 87.4% efficiency and 30 mm separation distance. The paper also discusses the design limitations and challenges of the CPT systems aiming to highlight the design challenges that can advance the CPT systems for wireless charging applications.

INDEX TERMS Wireless power transmission, Capacitive power transfer, Couplings, VNA, Two-port

I. INTRODUCTION

WIRELESS power transfer (WPT) has received considerable attention in various electric charging applications. The International Telecommunication Union [1] defines WPT as "*the transmission of power from a power source to an electrical load using the electromagnetic field.*" Near-field WPT, or "non-beam" WPT, is a non-radioactive propagation WPT technique in which the sizes of the transmitter and the receiver are much smaller than the wavelength of the electromagnetic waves [2]. It can transfer low to medium levels of electric power over a range of hundreds of millimeters without mechanical contact and using simple to moderate system architecture. It provides an autonomous, safe, flexible, and reliable charging approach for high-power charging applications.

Based on the type of coupling, near-field WPT comprises magnetic field coupling and electric field coupling. Magnetic coupling, or Inductive Power Transfer (IPT), transfers power between a power source and an electrical load by means of magnetic fields. Capacitive coupling, or Capacitive Power Transfer (CPT), transfers power wirelessly using alternating electric fields confined between conductors. Unlike magnetic field coupling based WPT technologies, CPT has some merits, including lightweight, low-cost, low eddy-losses in nearby metals, and good misalignment tolerance [3], [4].

Capacitive charging provides solutions in many applications such as safety fields, consumer electronics, transport, electric machines, biomedical, and miscellaneous applications [5]. For transport charging applications, CPT was proposed to charge on-road vehicles [6], maritime vessels [7]–[9], and unmanned maritime vehicles [10], [11]. In the literature, many papers have reviewed different perspectives on CPT investigating converter topologies, compensation circuits, and structures [12]–[17].

However, this paper discusses the theoretical and practical considerations, challenges, and limitations of designing a CPT system. It also proposes measurement techniques using Vector Network Analyzer (VNA) to determine the capacitive coupling parameters. Based on the measurement results, a 13.56 MHz CPT system is designed as a case study. The paper aims to highlight aspects of designing a CPT system.

II. ELEMENTARY CONSIDERATIONS

This section discusses the fundamental principle of capacitive coupling, the main design factors, and the general structure of CPT system.

A. FUNDAMENTAL OPERATION PRINCIPLE

As previously defined in the introduction, CPT transfers power from an electrical power source to an electrical load using alternating electric fields. The fields induce displacement current between the transmitter and the receiver electric circuits. The physical principle of the CPT is embodied in Maxwell's equations which can be presented by

$$\vec{\bigtriangledown} \times \left(\vec{\bigtriangledown} \times \vec{E} \right) = -\frac{\partial}{\partial t} \left(\bigtriangledown \times \vec{B} \right), \tag{1}$$

where E is the electric field $(\mathrm{V/m})$, B is the magnetic field (T). Isolating electric and magnetic fields in (1) gives

$$\vec{\bigtriangledown} \left(\vec{\bigtriangledown} \cdot \vec{E} \right) - \bigtriangledown^2 \vec{E} = -\frac{\partial}{\partial t} \left(\mu\sigma\vec{E} + \mu\varepsilon \frac{\partial \vec{E}}{\partial t} \right), \tag{2}$$

where μ permeability $(\mathrm{H/m})$, σ is the conductivity of the medium Ω/m, and ε is the absolute permittivity of the medium (F/m). The right terms in (2) are the displacement currents corresponding to the time-varying electric displacement fields.

If two conductive plates are charged with opposite charges uniformly distributed over their surface, uniform electric fields are confined between them. When the separation distance between the plates is comparable to the dimensions of the plates, the uniform electric field assumption is no longer valid, and the fringing effect cannot be neglected. The fringing is the nonuniform distribution and the bending of electric fields near the edges. Several analytical and numerical models tried to calculate the capacitance considering the fringing effects [18]. The fringing fields can couple the plates with the ground or any charged object in the proximity of the plates, forming stray and parasitic capacitors. The stray and other parasitic coupling capacitances have an essential effect on the design and performance of CPT system. Besides capacitance, some factors are important in the design of CPT systems.

B. DESIGN FACTORS

The power transferred using a CPT system is a function of the capacitive coupling, the frequency of the alternating electrical fields, the voltage across the coupling plates, and the phase angle between the voltages and the currents in the systems. Thus, the design metrics or factors that can affect the overall system performance of a CPT system and play an essential role in enhancing power transfer for charging applications are [9]:

1) The capacitive coupling

The capacitance depends on the geometries of the plates, the distance between the couplers, and the medium characteristics between them. The plate thickness can negligible affect the coupling [19]. But it should be considered for accurate design depending on the side-by-side distance between the plates and the separation distance. Various geometric configurations were adopted for CPT coupling structures, namely, conventional rectangular shape, cylindrical [20], disk [20], and matrix platform [21]. The coupling factors of these structures widely vary, where the rectangular factor is higher than 0.95, whereas the disk shape is less than 0.5 [20]. The matrix structure gives freedom of movement, but it suffers from low efficiency and may require complex control techniques.

A large surface area of the plates causes an increase in the capacitance, a reduction in the electric field, and a reduction in the fringing effect. However, vast areas can be a challenge to realize in practice. The separation distance between the couplers is another factor that affects the value of the coupling capacitance. If the transmitter and the receiver couplers are farther apart, the effective coupling drastically decreases, and the system is said to be "loosely coupled."

The electric properties of the separation medium between the transmitters and receivers play a critical role in capacitive coupling. The air is the common medium between the plates for on-road EV charging applications. As the permittivity of the air is about 1.0006 times the permittivity of the vacuum (i.e., $\varepsilon_0 \approx 8.85 \times 10^{-12}$ F/m), the air-gapped coupling capacitance is in the pF range. Inserting a material layer with a high dielectric between the couplers instead of air enhances the coupler's capacitance.

Researchers proposed the vehicle's wheels [22], windows [23], or bumper [12] to minimize the air gap and confine the field during charging. Water or air can be a separation medium for maritime charging applications between the CPT couplers. Unlike air, the permittivity of water is about 80 times higher than that of air. The permittivity of water depends on the characteristics of water, such as salinity and temperature. The salinity of seawater can increase the coupling capacitance. But it also causes a dielectric loss that degrades the overall efficiency of the system [10], [11], [18].

2) The operating frequency

Operating at a higher operating frequency can result in improving the overall energy density of the system and the capability of increasing the distance of power transfer between the couplers. Operating frequency ranges from Medium Frequency (MF) to High Frequency (HF) were proposed in the literature. In the MF ranges, $200\,\mathrm{kHz}$ [24], [25] and $848\,\mathrm{kHz}$ [26] were used but over air-gapped separation distance of less than $1\,\mathrm{mm}$. Higher frequencies in the MF ranges were also proposed such as $1\,\mathrm{MHz}$ [27], $1.5\,\mathrm{MHz}$ [28], and $2\,\mathrm{MHz}$ [29]. In the HF ranges, $3.4\,\mathrm{MHz}$ [30], $6.78\,\mathrm{MHz}$ [31], $13.56\,\mathrm{MHz}$ [32] and $27.12\,\mathrm{MHz}$ [33]. But, high operation frequency can cause high losses and complicate the design and controlling processes.

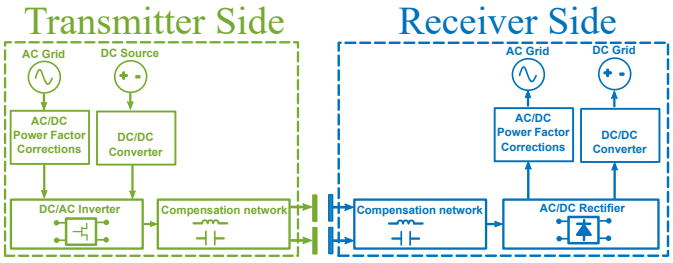

FIGURE 1. Block diagram of a CPT system.

3) The voltage across couplers

The power transfer is proportional to the voltage squared, and it also depends on the phase shift between the voltage across the couplers and the induced current flows through the circuit nodes. Thus, if a high voltage is applied across the couplers, electric fields increase, and more energy can be transferred. A wide variation of compensation networks helps achieve high voltage levels and compensates the phase shift between the voltage and current to achieve high power transfer. The compensation networks can be categorized based on the resonation principle, where each category has pros and cons [3]. Isolating transformers can also isolate, compensate and boost the voltages [34].

If the separation medium between the couplers is the air, the coupling capacitance is in pF range, and the voltage across the couplers can reach hundreds or thousands of volts. Applying a very high voltage across the couplers may result in arcing or even a breakdown voltage fault. It also requires expensive components for the compensation circuits that can withstand high voltage ranges. Besides, increasing the voltage increases the electric field between the plates and the fringing field intensity field, which may exceed the safety requirements of the human body.

C. GENERAL SYSTEM STRUCTURE

A block diagram of a CPT for charging applications is shown in Fig. 1. The power source can be an ac grid, a dc grid, a battery unit, or a hybrid combination of ac and dc sources. The connection to an ac grid can face harmonics and power factor challenges due to the nonlinear behavior of the power electronics interface. Thus, the connection should comply with the international standard, IEC 61000-3-2, which prescribes the maximum amplitude of the line frequency harmonics [35].

Passive filters or front-end ac-dc converters are needed to correct the power factor and minimize the current harmonics. Whereas the passive filters comprise bulky components and cannot regulate the power flow and output voltage levels, front-end converters suppress the harmonic contents and control the power flow actively. Various bridgeless converters are proposed for power factor correction applications [36], [37] that can be an attractive option for a CPT charging system. In contrast, connecting to a dc grid or batteries requires dc-dc converters to step up or down the source voltage to the required input voltage for the CPT system.

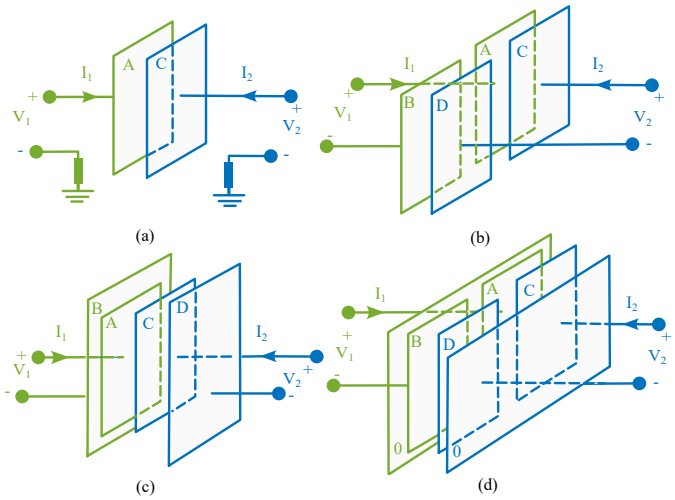

FIGURE 2. Capacitive couplers structure: (a) A Two-plate structure [38]. (b) A four-plate horizontal structure [39]. (c) A four-plate vertical structure [40]. (d)A six-plate structure [19], [31], [41].

Capacitive coupling is the essential part that transfers between electrical networks by means of electric fields. Various arrangements of plates to form capacitive couplers were proposed, as illustrated in Fig. 2. The two-plate arrangement is a quasi-CPT, proposed to simplify the capacitive coupling structure, where the ground forms the common return path [38]. In this structure, the stray capacitance between the chassis of Electrical Vehicles (EV) and the ground provides a return path that can result in dangerous high voltage variation on the vehicle chassis and Electromagnetic Interference (EMI) problems.

The four-plate horizontal structure is the most commonly used and tested in the literature [39]. Compared to the four-plate horizontal structure, the four-plate vertical structure was proposed as a more compact arrangement to save space [40]. But the size of plates B and D should be larger than that of plates A and B. Finally, the six-plate recently received more attention, a four-plate horizontal structure with two extra plates shielding the electric field and expanding the safety area [19], [31], [41].

Compensation circuits are required to achieve zero reactive power and Zero Phase Angle (ZPA) reducing the reactive power and increasing the active power transferability. Double-sided symmetrical compensation typologies, including L, LC, LCL, LCLC, CLLC compensations, were commonly used [5]. Other researchers proposed a single-sided primary compensation [27], [31], [41]. Although the compensation for a capacitive coupling can be applied on the transmitter side only, an impedance-matching network is required at the secondary side to achieve high efficiency over a wide load variation.

The configuration of compensation circuits depends on the type of input and output of the resonant circuits. For instance, a T-circuit configuration is required to have a constant-voltage output. In contrast, a π-circuit configuration is re-

quired to achieve a constant-current output for a constant-voltage input of the compensation circuits [14]. Increasing the resonant components in the compensation circuits will increase the overall cost of an CPT system and the difficulties of the design and realization in practice.

The compensation or impedance-matching network on the receiver side is followed by an ac-dc rectifier which converts the received alternating power to constant power. Following the rectifier, a dc-dc converter is required to keep the effective output load of the rectifier close to the optimal load. The dc-dc converter is needed to connect to the onboard dc grid or batteries, whereas a dc-ac converter might be required to connect the CPT system to the ac grid. The dc-dc or dc-ac converters adjust the output voltage to the required voltage level and can also be operated as active impedance matching.

III. THEORETICAL CONSIDERATIONS

Operating in MF to HF, the corresponding electromagnetic wavelength will range from tens to hundreds of meters, making the lumped circuit element approximations of circuit theory valid. The network theory would help bridge the gap between field analysis and circuit theory. Thus, this section presents some of the elements of the network theory that are useful in the study of CPT systems.

The section discusses the main concepts, the fundamental principles, and the basic elementary network theorems based on the details in [42], [43]. Then, it presents the admittance matrix, its corresponding impedance matrix, and their representation as π-network and T-network models. Finally, it introduces the s-parameters and how they can be used to analyze CPT.

The physical principles of the network theory are embodied in Maxwell's equations, as expressed in (2). Thus, the network theory follows some physical principles.

The first principle is the linearity principle, which is based on the linearity of Maxwell's equations. A CPT system can be modeled as a linear two- or multi-port network, characterized by using a number of linear impedance elements, which are passive elements with two terminals. Capacitance and inductance are impedance element values that describe the lossless operation of a network and represent the flow of energy in the form of electric and magnetic fields. The resistance and conductance are the impedance element values that represent the losses in the network.

The second principle is the duality principle, resulting from Maxwell's equations' symmetries. The duality gives great convenience in analyzing WPT systems. Based on this principle, the inductive coupling or Inductive Power Transfer (IPT) systems can be considered dual for CPT systems. For instance, a IPT system can be modeled as a black box that contains a network of impedances. In contrast, a CPT system can generally be modeled as a black box with a network of admittances.

Four network theorems are helpful for WPT analysis: superposition, reciprocity, Thevenin/Norton, and bisection theorems. The superposition theorem follows directly from the linearity of Maxwell's equations. It states that if more than one source is present in a linear bilateral network, the response across any element in the network is the sum of the responses obtained from each source separately. The reciprocity theorem, which follows the symmetry of Maxwell's equations, states that the admittance and impedance matrices are symmetrical. However, this theorem fails if the network contains active devices or nonreciprocal mediums (e.g., Ferrites).

Norton's (Thevenin's) theorem states that any network having two accessible terminals can be simplified to an equivalent circuit consisting of a single current source (a single voltage source) and parallel admittance (series impedance) that is connected to a load. Finally, the bisection theorem states that if equal voltages are applied to the terminals of a symmetrical network, no current will flow across the symmetrical components.

A capacitive coupler is an electrical network with one or more impedance elements connected at nodes forming electric meshes. If the impedance elements are known, then the current flows into, and the voltages applied on a network can be found using the law of conservation of energy and the law of conservation of charge (i.e., Kirchhoff's voltage law and Kirchhoff's current law, respectively). Using these two laws, the mesh currents can be expressed as a function of the applied voltages in a mesh.

Various electrical network configurations were proposed to model the capacitive coupling between plate structures. Theoretically, capacitive couplers can be modeled considering the medium losses using coupling admittance, as illustrated in Fig. 3 (a). In practice, however, three types of coupling can exist (1) effective-coupling (Y_{AC} and Y_{BD}), (2) cross-coupling (Y_{AD} and Y_{BC}), and (3) self-coupling (Y_{AB} and Y_{CD}), as shown in Fig. 3 (b).

An ideal voltage or current transformation can be used to model these coupling admittances, which are equivalent to a transformer model, as in Fig 3 (c) and (d), respectively. In these models, the admittance Y_{12} or the impedance Z_{12} are equivalent to the mutual coupling in an electromagnetic network, while the admittances Y_{11} and Y_{22} or the impedances Z_{11} and Z_{22} are equivalent to the leakage or the stray coupling to the ground.

Using the concept of the electrical network, the voltages, and currents in the network can be considered unknown variables, which can be obtained using a simple set of equations. Fig 3 (e) shows the circuit equivalent π-network model, which is the most common model used to model CPT systems in the literature. The circuit equivalent T-network model is mainly used in modeling IPT. Still, it can be used to model CPT systems using the duality principle, as illustrated in Fig 3 (f).

Behavior source models are other approaches to represent WPT system. 3 (g) shows the behavior current-source model, which is the most commonly used in CPT [19], [38]. The behavior current-source model has recently attracted more attention in CPT analysis [25], [44], as shown in 3 (h).

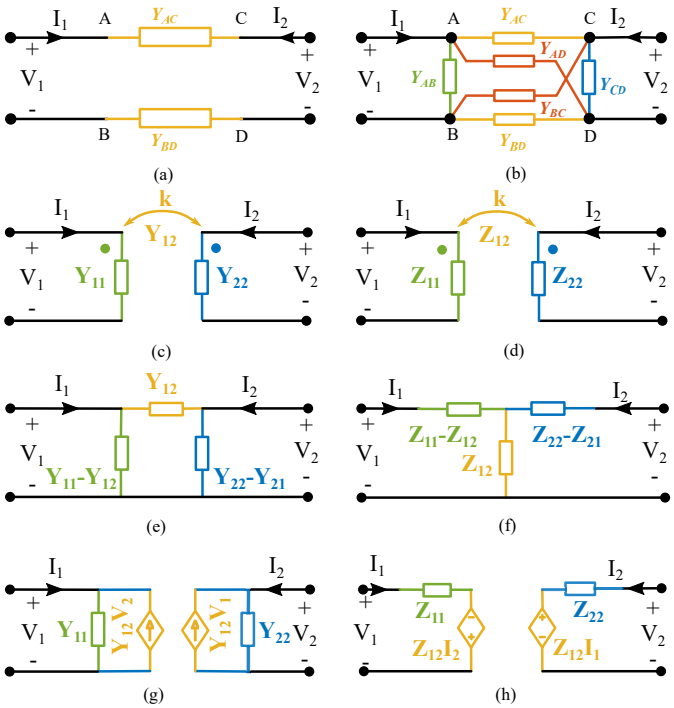

FIGURE 3. Capacitive couplers: (a) Theoretical coupling admittances. (b) Mutual-, self-, and cross-coupling admittances. (c) Circuit current type model. (d) Circuit voltage type. (e) Circuit equivalent π- network model. (f) Circuit equivalent T-network model. (g) Behavior current-source model. (h) Behavior voltage-source model.

All the models presented in Fig. 3 are 2-port models. The models shown in Fig. 3 (d), (f), and (h) are proposed to compare magnetic field coupling to electric field coupling. However, the models in Fig. 3 (c), (e), and (g) are closer to the actual capacitive coupling system. The calculated or measured values of the coupling admittance can be implemented directly into these models.

Mathematically, the π-network model can be expressed as

$$Y_{11} - Y_{12} = Y_{\mathrm{AB}} + \frac{(Y_{\mathrm{AC}} + Y_{\mathrm{AD}}) \cdot (Y_{\mathrm{BC}} + Y_{\mathrm{BD}})}{Y_{\mathrm{AC}} + Y_{\mathrm{AD}} + Y_{\mathrm{BC}} + Y_{\mathrm{BD}}} \tag{3}$$

$$Y_{22} - Y_{12} = Y_{\mathrm{CD}} + \frac{(Y_{\mathrm{AC}} + Y_{\mathrm{BC}}) \cdot (Y_{\mathrm{AD}} + Y_{\mathrm{BD}})}{Y_{\mathrm{AC}} + Y_{\mathrm{AD}} + Y_{\mathrm{BC}} + Y_{\mathrm{BD}}} \tag{4}$$

$$Y_{12} = \frac{Y_{\mathrm{AC}} \cdot Y_{\mathrm{BD}} - Y_{\mathrm{AD}} \cdot Y_{\mathrm{BC}}}{Y_{\mathrm{AC}} + Y_{\mathrm{AD}} + Y_{\mathrm{BC}} + Y_{\mathrm{BD}}} \tag{5}$$

Using the duality principle, the connections between the π- and T-network models can be linked by the following equations

$$Z_{11} - Z_{12} = \frac{Y_1 \cdot Y_{12} + Y_{12} \cdot Y_2 + Y_2 \cdot Y_1}{Y_2} \tag{6}$$

$$Z_{22} - Z_{21} = \frac{Y_1 \cdot Y_{12} + Y_{12} \cdot Y_2 + Y_2 \cdot Y_1}{Y_1} \tag{7}$$

$$Z_{12} = \frac{Y_1 \cdot Y_{12} + Y_{12} \cdot Y_2 + Y_2 \cdot Y_1}{Y_{12}} \tag{8}$$

If the impedance elements are known, the current flows into, and the voltages applied on a network can be found using Kirchhoff's voltage and current laws. The mesh currents can be expressed as a function of the applied voltages in a mesh as follows.

$$\begin{bmatrix} I_1 \\ I_2 \end{bmatrix} = \begin{bmatrix} Y_{11} & Y_{12} \\ Y_{21} & Y_{22} \end{bmatrix} \begin{bmatrix} V_1 \\ V_2 \end{bmatrix}, \tag{9}$$

The diagonal elements are the self-admittance Y_{11}, which is the input admittance seen in port 1 when port two is short-circuited. Similarly, the self-admittance Y_{22} is the input admittance seen in port 2 when port two is short-circuited. The off-diagonal element Y_{21} is the mutual admittance and is driving port 1 with the voltage V_1, short-circuiting port 2 and measuring the short-circuit current at port 2 (i.e., $Y_{21} = \frac{I_2}{V_2}|_{V_1=0}$).

Likewise, an impedance matrix can express the T-network model as

$$\begin{bmatrix} V_1 \\ V_2 \end{bmatrix} = \begin{bmatrix} Z_{11} & Z_{12} \\ Z_{21} & Z_{22} \end{bmatrix} \begin{bmatrix} I_1 \\ I_2 \end{bmatrix} \tag{10}$$

The element Z_{ii} is the input admittance seen looking into ports i when all other ports are open-circuited. The element Y_{ij} can be determined by driving port j with the current I_{j}, open-circuiting all other ports and measuring the open-circuit voltage at port i (i.e., $Z_{\mathrm{ij}} = \frac{V_{\mathrm{i}}}{I_{\mathrm{j}}}|_{I_k=0}$). The admittance or impedance matrix size is 2×2 symmetrical matrix for an arbitrary 2-port network. The impedance elements do not change with changing current or voltage in any direction in the network, as they are only functions of the geometry of the couplers. An electrical network is called "a bilateral" if its behavior remains the same regardless of the direction of currents flow through its various components.

From the duality principle, the elements in the admittance matrix can be expressed as a function of the elements in the impedance matrix.

$$Y_{11} = \frac{Z_{22}}{\Delta} \tag{11}$$

$$Y_{12} = -\frac{Z_{12}}{\Delta} \tag{12}$$

$$Y_{22} = \frac{Z_{11}}{\Delta} \tag{13}$$

$$\Delta = Z_{11}Z_{22} - Z_{12}^2, \tag{14}$$

where Δ is the determinant of the impedance matrix, the negative sign in 12 is due to the direction of the currents in the circuit equivalent T-network model.

If a 2-port network is connected to a current source (I_{s} and Y_{s}) and an arbitrary load Y_{L}, as shown in Fig. 4 (a). Then, the input admittance Y_{in}, as seen watching from the source side is expressed as

$$Y_{\mathrm{in}} = Y_{11} - \frac{Y_{12}^2}{Y_{22} + Y_{\mathrm{L}}} \tag{15}$$

The source circuit can be replaced by its Norton equivalent, as illustrated in Fig. 4 (b), and expressed as

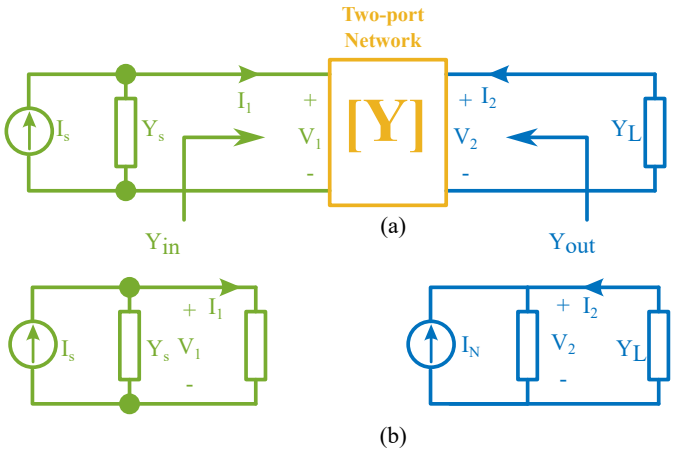

FIGURE 4. A general representation of CPT system connected to a source and a load: (a) Two-port network connected to a source and an arbitrary load. (b) The equivalent circuits use Norton's theorem.

$$Y_{\text{out}} = Y_{\text{N}} = Y_{22} - \frac{Y_{12}^2}{Y_{11} + Y_{\text{S}}}, \tag{16}$$

$$I_{\text{N}} = \frac{-Y_{12}}{Y_{11} + Y_{\text{S}}} I_{\text{s}}. \tag{17}$$

The degree of coupling between the transmitter and the receiver side is the coefficient of coupling and can be expressed as

$$k = \frac{Z_{12}}{\sqrt{Z_{22} \cdot Z_{22}}} = \frac{Y_{12}}{\sqrt{Y_{22} \cdot Y_{22}}} \tag{18}$$

This parameter ranges from negative unity to unity, where the negative represents the phase inversions.

Equations (9) can be rewritten to express the relationship between the input current and voltage to the output current and voltage as

$$\begin{bmatrix} V_1 \\ I_1 \end{bmatrix} = \begin{bmatrix} A & B \\ C & D \end{bmatrix} \begin{bmatrix} V_2 \\ I_2 \end{bmatrix} \tag{19}$$

$$= \begin{bmatrix} \frac{Y_{22}-Y_{21}}{Y_{12}} & \frac{1}{Y_{12}} \\ \frac{(Y_{11}-Y_{12})(Y_{22}-Y_{21})-Y_{12}^2}{Y_{21}} & \frac{Y_{11}-Y_{12}}{Y_{21}} \end{bmatrix} \begin{bmatrix} V_2 \\ I_2 \end{bmatrix} \tag{20}$$

The determinant of the matrix is unity, and for a lossless CPT system, A and D are purely real, and B and C are pure imaginary values if the CPT system is symmetric (i.e., $Y_{12} = Y_{21}$), then $A = D$. This representation is more convenient when the capacitive two-port network is cascaded with other networks, such as the compensation circuits. Corresponding to impedance or admittance matrices is the scattering matrix which comprises the scattering parameters, also known as "s-parameters". Researchers also used the s-parameters to analyze CPT systems [10], [45], [46]. The admittance Y and impedance Z matrices are related to the scattering matrix S by

$$Y = 50 \cdot (E + S)^{-1} \cdot (E - S) \tag{21}$$

$$Z = 50 \cdot (E - S)^{-1} \cdot (E + S), \tag{22}$$

where E is the identity matrix, $50\,\Omega$ is the reference resistance, and $S = \left[\begin{smallmatrix} S_{11} & S_{12} \\ S_{21} & S_{22} \end{smallmatrix}\right]$ is the scattering matrix.

Accurate determination of coupling parameters is essential in designing a CPT system. Some researchers use Finite Element Method (FEM)-based software [19], [38], [40] to calculate the coupling between the plates, or they measure the parameters using impedance analyzer [18], [31], [32], [41]. Other researchers [10], [11], [46], [47] use VNA to utilize the s-parameters directly. Calculating or measuring the coupling parameters requires accurate modeling. The next section will introduce some practical considerations for finding these parameters.

IV. PRACTICAL CONSIDERATIONS

Selecting the required compensation and optimizing the efficiency of the system depends on accurately measured or calculated capacitive coupling parameters. Usually, FEM-based software calculates the coupling capacitance between the plates. Calculating the capacitances between several plates is achieved by calculating the charge of any plate and the electrostatic potentials on all other plates. The relations between the charge of the i^{th} plate to the voltages of all plates in the system are described by the Maxwell capacitance matrix [48]. The diagonal elements of his matrix C_{ii} are determined by calculating the charge on the i^{th} plate when only the voltage is applied to this plate and other plates are grounded. Thus, the diagonal elements are the addition of the self-capacitance (i.e., the stray or parasitic capacitance between the plate to infinity.) and the mutual capacitances (i.e., the capacitances due to the potential differences between the plates.)

The Maxwell capacitance matrix is calculated numerically by solving the electrostatic potential, which depends on the boundary condition. In Ansys Maxwell©, the boundary condition is floating at infinity in which a matrix reduction operation is applied within a margin of error [49]. In this condition, the boundary is disconnected from the ground at infinity and assumed as it is a perfectly conducting surface over which the potential is constant. The condition implies that the electric fields are perpendicular to the boundary. Another approach is the zero charge boundary condition which assumes that the electric field lines are tangential to the boundary. In this condition, the boundary is assumed to be a perfectly insulating surface through which the charge cannot redistribute itself. COMSOL Multiphysics© can apply both conditions and take the average of the two is sufficient for practical application [50].

The coupling parameters can be measured using either an impedance analyzer or VNA. An impedance analyzer is a four-terminal device that uses the I-V method (i.e., a current source and sensitive voltmeter) to measure the impedance

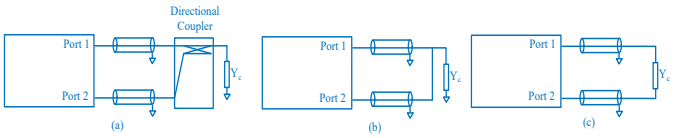

FIGURE 5. Types of measurement techniques: (a) Reflection, (b) Shunt-through. (c) Series-through.

over a wide frequency range accurately. It has excellent measurement stability after calibration, but test fixture stray impedance and admittance need to be accurately eliminated [51]. In contrast, VNA is a device that has one or two ports that use s-parameters to measure the impedance over a frequency range from a few hundreds of hertz to GHz. It requires calibration each time the instrument is turned on or the frequency setting is changed [51]. Both devices should give results that agree with each other within the uncertainty in a frequency range from 30 kHz to 100 MHz [52].

Several measurement techniques can measure the coupling parameters using VNA: reflection, shunt-through, series-through, π-network, and the I-V method [51]. Fig. 5 illustrates the reflection, shunt-through, and series-through techniques.

The reflection technique requires one port only to achieve the measurements, as it uses the reflection coefficient by measuring the ratio of the incident signal and reflected signal (i.e., $\Gamma = {}^{V_r}/_{V_i}$). The admittance can be calculated from the reflection coefficient as

$$Y_c = \frac{1}{50} \cdot \frac{1-\Gamma}{(1+\Gamma)} \tag{23}$$

The directional coupler measures the reflected signal at a null balance point. Thus, this technique gives accurate results if the measured impedance is close to or equal to the device reference impedance (50 Ω).

The shunt-through technique requires two ports. The couplers are connected parallel to the two ports, and the measurements can be calculated using the following expression.

$$Y_c = \frac{2}{50} \cdot \frac{1-S_{21}}{S_{21}} \tag{24}$$

This technique is more suitable for high admittance measurements since it depends on the transmission coefficient.

The series-through technique requires two ports. The couplers are connected in series to the two ports, and the measurements can be calculated using the following expression.

$$Y_c = 2 \cdot 50 \cdot \frac{S_{11}}{1-S_{11}} \tag{25}$$

This technique is more suitable for low-admittance measurements as it depends on the reflection coefficient but is still sensitive to calibration uncertainty.

The series-through can measure the coupling capacitance between using a one-port of VNA. Measurements can be modeled using the π-network model for capacitive coupling. For instance, the effective-coupling admittance between plates A and C is modeled as $\mathrm{Y_{AC}}$, as illustrated in Fig.

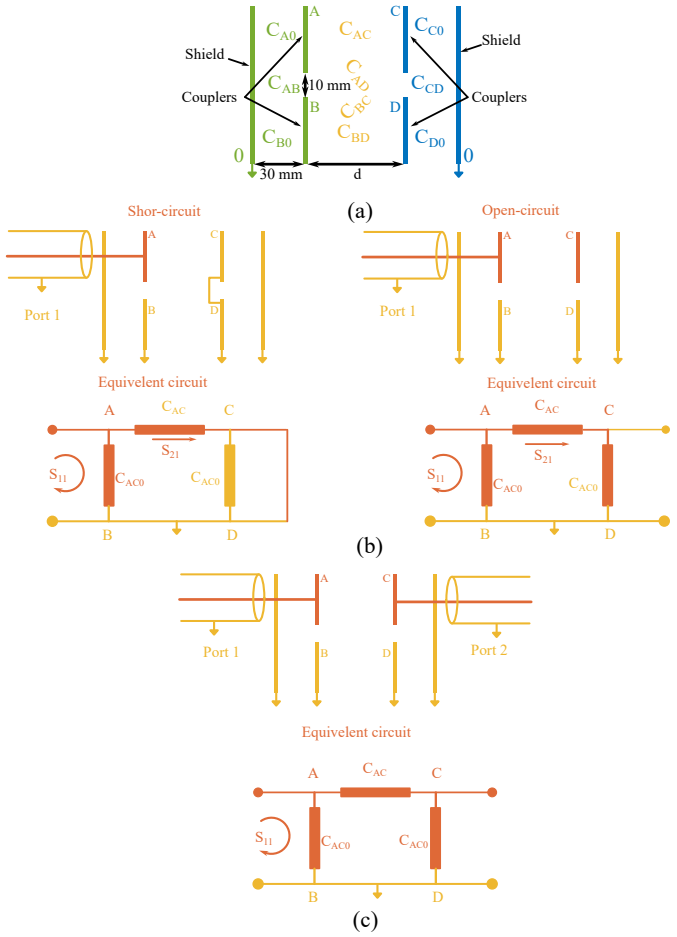

FIGURE 6. Shielded CPT: (a) physical dimensions. (b) One-port measurement approach. (c) Two-port measurement approach.

6. The stray admittance $\mathrm{Y_{AC0}}$ models the leakage admittances to the ground and the parasitic coupling with other plates.

The short-circuit and open-circuit approaches can be used to measure the effective-coupling admittance as

$$Y_{\mathrm{sc}} = Y_{\mathrm{AC0}} = Y_{\mathrm{AC0}} \tag{26}$$

$$Y_{\mathrm{oc}} = Y_{\mathrm{AC0}} - \frac{Y_{\mathrm{AC}}^2}{Y_{\mathrm{AC0}}}, \tag{27}$$

where $Y_{\mathrm{AC0}} = g_{\mathrm{AC0}} + j\omega C_{\mathrm{AC0}}$ models all the stray and parasitic addmitances. In the air-gapped shielded CPT system, the conductivity (i.e., the real part of the admittance) is negligible. Then the capacitances can be calculated directly from the imaginary part of the admittances.

The two-port of VNA can also measure the capacitive coupling. Fig 6(c) shows the measurement can be achieved using the two-port of the VNA. The two-port approach can achieve the measurement in one step compared with the one-port approach, which requires two measurement steps. The

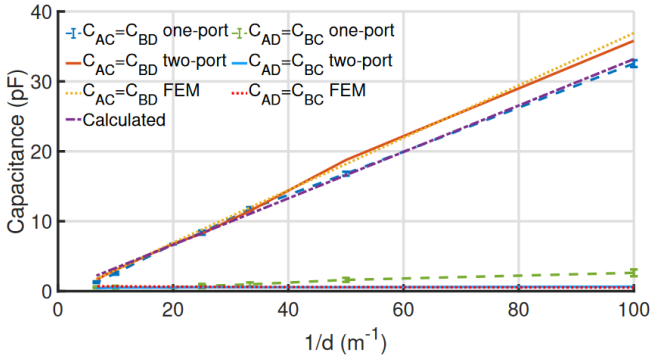

FIGURE 7. Calculated and measured values of effective and cross-coupling coupling capacitance.

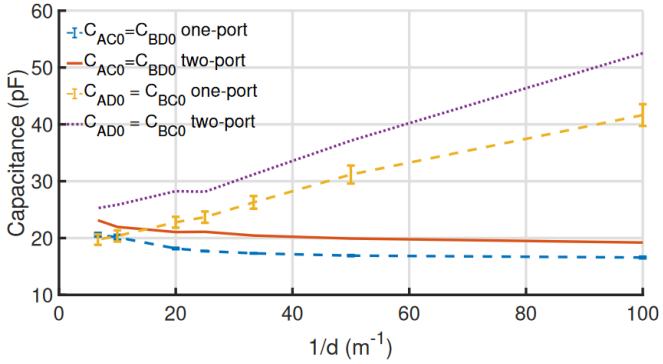

FIGURE 8. Measured values of stray capacitance.

admittances can be measured using the two-port as follows

$$Y = \frac{1}{Z_0}(E - S)(E + S)^{-1} \tag{28}$$

$$= \begin{bmatrix} Y_{\mathrm{AC}} + Y_{\mathrm{AC0}} & -Y_{\mathrm{AC}} \\ -Y_{\mathrm{AC}} & Y_{\mathrm{AC}} + Y_{\mathrm{AC0}} \end{bmatrix}, \tag{29}$$

where $Z_0 = 50\Omega$ is the reference impedance, E is the identity matris, and S is the s-parameter matrix that achieved from the measurements.

V. CASE STUDY: DESIGN A 13.56 MHZ CPT SYSTEM

This section discusses the design of a 13.56 MHz shielded CPT system. The system composes four 150 × 250 mm plates which form the couplers (A, B, C, and D), and two 250 × 300 mm shield plates. The distance between the adjacent plates (i.e., AB or CD) is 10 mm, and the distance between the plates and shields is 30 mm, as shown in Fig. 6(a).

The coupling parameters can be measured using the one- and two-port approaches discussed in section IV. Using the one-port approach, the effective-coupling capacitance can be calculated using the short-circuit and open-circuit techniques, as illustrated in Fig. 6 (b). In contrast, the parameters of the π-network model are directly achieved from (29) using the connection shown in Fig. 6(C). Similarly, the cross-coupling between plates A and D or B and C can be measured using the aforementioned approaches.

Fig. 7 shows the measured and simulated changes in the effective- and cross-coupling capacitances with the changing of separation distance. The calculated values are achieved using $C = {}^{\varepsilon A}/_{d}$, the simulated values are given by COMSOL Multiphysics©, and the measured values are achieved using both one- and two-port approaches.

The two-port measurement approach gives close values to the simulated ones. In contrast, the one-port measurements give close values to calculated ones. The difference between the one-port and the two-port measurements is attributed to the high stray capacitance values at short separation distances resulting in calculation error using (26) and (27), making the two-port approach more accurate than the one-port approach.

Fig. 8 shows the stray capacitances for both the effective and cross-coupling cases. The stay capacitances have higher values than effective and cross-coupling ones. It results in an inaccurate calculation of the effective coupling capacitance using (27). The stray capacitance of the effective coupling (Y_{AC0} or Y_{BD0}) mainly composes the self-coupling capacitance and the parasitic capacitance between the plates and shields. Thus, it merely changes when the separation distance between the plates is increased. In contrast, The stray capacitance of the cross-coupling (Y_{AD0} or Y_{BC0}) mainly composes of the stray capacitance between A and C. Thus, it decreases when the separation distance is increased.

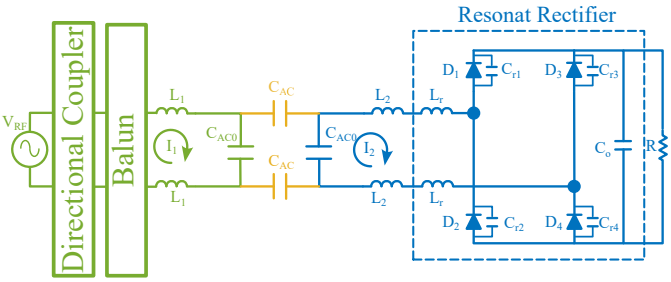

FIGURE 9. A schematic of the 13.56 MHz CPT system.

The effective coupling capacitances and the stray capacitance are the main design factors. While the distances between the plates and the shields and between the adjutant plates affect the stray capacitance, the separation distance between the transmitter and receiver couplers affects the effective coupling. In practice, the plate D is not connected to the ground, resulting in a π-network model similar to the one shown in Fig. 9.

Fig. 9 illustrates the schematic of the proposed CPT system. An RF generator (Advanced Energy RFX600A) generates a 13.56 MHz ac power. A Ruthroff balun is connected to the shield plate to achieve a stable ground level. The series compensation enhances the overall efficiency, reduces the reflected power, and achieves ZPA operation condition. The compensation inductance should compensate for both the stray and coupling capacitance. The compensation inductances can be calculated as

$$L_1 = L_2 = \frac{1}{2\omega_0} \frac{C_{AC0}}{C_{AC0}^2 - \left(\frac{C_{AC}}{2}\right)^2}, \tag{30}$$

TABLE 1. Design parameters

Symbol	Quantity	Value
f	Operating frequency	13.56 MHz
d	Separation distance	30 mm
C_{AC}	Effective coupling capacitance	11.5 pF
C_{AC0}	Stray capacitance	20.6 pF
L_1 & L_2	Compensation inductance	3.6 µH
C_r	Resonant capacitance	63.1 pF
L_r	Resonant inductance	1 µH
R	Load resistance	400 Ω
D_1, D_2, D_3 & D_4	Diode of the rectifier	GD30MPS12H

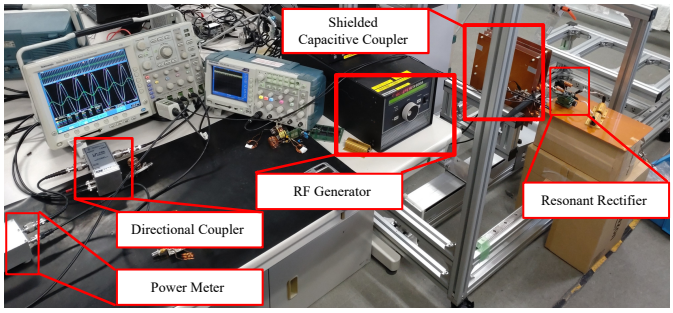

FIGURE 10. The CPT system undertest.

where ω_0 is the angular resonant frequency. Symmetrical compensations on each side are used to achieve stabilized ground voltage.

Resonant rectifier achieves dc output at power factor operation and minimizes the reflected power. The components of the resonant rectifiers are optimized using LTspice© to achieve minimum reflected power [53]. Reflected power is an important factor to achieve an efficient CPT. Minimizing the reflected power maximizes the forward transferred power and the overall system efficiency.

At a 30 mm separation distance, the design parameters are listed in Table 1. Fig. 10 depicts the proposed CPT system under test. The proposed system transfer 100 W input power at an 87.4% efficiency at 187 V output voltage. Fig. 11 shows the testing results. The input voltage is in phase with the input current resulting in minimum reflected voltage. Table 2 lists a comparison of this work with other underwater CPT systems in the literature in terms of the number of plates, transfer power, system efficiency, operating frequency, transfer distance, and coupler size. Compared to other underwater CPT systems, this work proposes a shield CPT system is shielded to reduce the EMI problem and increase the safety around the couplers. Although the system transferred 100 W at an efficiency of over 87.4% at 30 mm separation distance, it can operate at higher power than 100 W.

VI. DESIGN LIMITATIONS AND CHALLENGES

This section discusses design challenges, including operating frequency, voltage stress, stray capacitance and ground stability, and overall system efficiency.

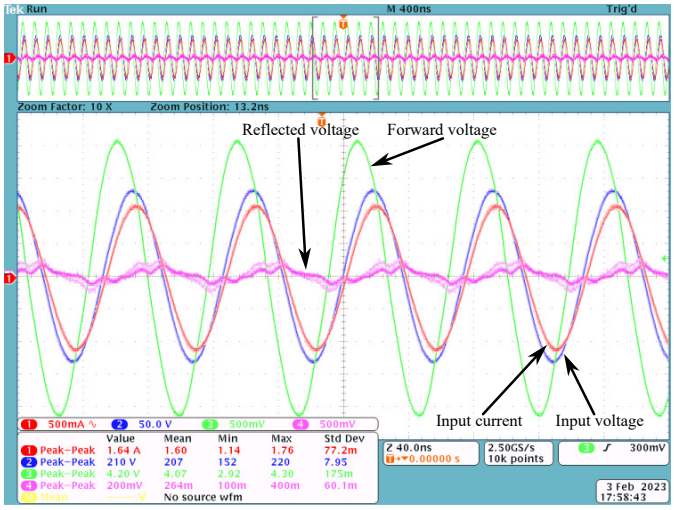

FIGURE 11. The waveform results.

A. OPERATING FREQUENCY

Unlike IPT, the operating frequency of CPT systems has not been standardized, as these systems are still under testing in laboratories. Medium to the high-frequency range is adapted to transfer from hundreds of watts to a few kW. Operating at high frequency adds an extra challenge to designing and tuning circuits in practice. Besides, if the intensity of the fields exceeds the limits, they can induce electric fields in the exposed bodies that cause tissue heating or nerve stimulation. Although the electric fields in this frequency range are non-ionizing, they are only safe within a prescribed limit. The International Commission on Non-Ionizing Radiation Protection (ICNIRP) [57] specifies the basic restriction for the electric field exposure from 100 kHz to 10 MHz for any region of the human body by the following

$$E_{\text{ind}} = 2.7 \times 10^{-4} f, \text{ Occupational} \quad (31)$$

$$E_{\text{ind}} = 1.35 \times 10^{-4} f, \text{ General public} \quad (32)$$

where E_{ind} the induced electric fields (V/m) and f is the operating frequency (Hz). The induced electric field is a function of voltage stress across the couplers; increasing the voltage stress increases the safety clearness around the coupling plates.

B. VOLTAGE STRESS

The voltage across the plates in a CPT system can reach several kV to transfer power effectively over a few hundreds of mm. As the breakdown voltage of the air is 3 kV/mm, this limits the distances between the plates to avoid arcing or breakdown faults. For a non-shielded CPT system, operating with high voltage stress not only increase the safety clearness around the system but also induces voltage through the stray capacitors on the metallic body of the vehicle or nearby objects, which increases the risk of electric shocks in case of any contact with these objects.

For a shielded CPT, the shields can decrease the range of the safety clearance from the plates. However, it still has lim-

TABLE 2. Comparison between the proposed CPT System and other systems in the literature.

Ref.	Plates No.	Power (W)	Efficiency (%)	Frequency (MHz)	Distance (mm)	Size (mm)
[54]	4	590	88.4	6.78	120	122.5 × 122.5
[55]	4	100	83.5	6.78	12	100 × 100
[56]	4	122.9	73.6	16.5	1	100 × 100
This work	6	100	87.4	13.56	30	250 × 150 and 250 × 300

itations concerning the compactness of the system due to the high voltage stress. Operating frequency at 13.56 MHz and a separation distance of 180 mm, the shielded-CPT coupling structure requires about 30 mm gap between the shields and the coupling plates [58]. Several voltage stress optimization methods were proposed to reduce the voltage stress across the couplers in [25], [59]–[61].

C. STRAY CAPACITANCES AND GROUND STABILITY

The electric fields are divergent, terminating between any two electrodes with potential differences. Because of the potential difference between the coupling plates and the ground resulting in stray capacitances, which can be a source of EMI. Besides, the leakage fields around the plates can couple with any low electric potential objects, which raises safety issues. The shielded CPT [19], [31], [41], using a six-plate structure shown in Fig.2 (d), results in a small field leaking out to the surroundings, and it decreases the safety range to about 100 mm away from this plates. However, the coupling between the shielding plates and the ground through the stray capacitances results in an unbalanced ground of the CPT. The Ruthroff transmission line transformer balun can tackle the unbalanced ground of the shielded CPT and enhance the stability of ground level at the shield plate [62].

D. EFFICIENCY

The efficiency of the coupling capacitance is a function of the coupling parameters. Any change in these parameters might result in a degradation of the overall efficiency. For instance, by increasing the separation distance, any interference of objects between the couplers can directly degrade the overall system efficiency [63]. Operating in the high-frequency range is another challenge for the CPT systems. Soft-switching in both the inverter and rectifier is required to achieve low losses. Impedance matching circuits are also required to enhance the overall system efficiency and power transferability, but they also contribute to some of the overall losses in the system.

VII. CONCLUSIONS

This paper overviews and discusses the theoretical and practical considerations in designing a CPT system. It presents the fundamental operation principle and some theoretical and practical considerations for measuring the coupling parameters. The coupling parameters are determined in the literature using numerical calculations using the FEM approach or measuring the s-parameters using VNA. This paper proposes the measurement of the coupling admittances using one- or two-port VNA. The two-port approach gives more accurate measurements than the one-port one. Based on the two-port measurement results, a 13.56 MHz CPT system is designed. The system transfers 100 W at 87.4% efficiency and 30 mm separation distance. Finally, the paper highlights some of the design limitation and challenges of CPT systems. Voltage stress and breakdown issues, EMI and ground stability, and overall system efficiency are the main challenges that need further study.

.

REFERENCES

[1] ITU-R Recommendation ITU-R SM.2110, "Frequency ranges for operation of non-beam wireless power transmission systems," Available at https://www.itu.int/rec/R-REC-SM.2110-0-201709-S (2021/11/09).
[2] T.-C. Alicia, G.-G. José, M, and A. José, A, *Wireless Power Transfer for Electric Vehicles: Foundations and Design Approach*. Springer International Publishing, 2020.
[3] F. Lu, H. Zhang, and C. Mi, "A Review on the Recent Development of Capacitive Wireless Power Transfer Technology," *Energies*, vol. 10, no. 11, p. 1752, nov 2017.
[4] Y. Wang, H. Zhang, and F. Lu, "Review, analysis, and design of four basic cpt topologies and the application of high-order compensation networks," *IEEE Transactions on Power Electronics*, vol. 37, no. 5, pp. 6181–6193, 2022.
[5] M. Z. Erel, K. C. Bayindir, M. T. Aydemir, S. K. Chaudhary, and J. M. Guerrero, "A comprehensive review on wireless capacitive power transfer technology: Fundamentals and applications," *IEEE Access*, vol. 10, pp. 3116–3143, 2022.
[6] A. Ahmad, M. S. Alam, and R. Chabaan, "A comprehensive review of wireless charging technologies for electric vehicles," *IEEE Transactions on Transportation Electrification*, vol. 4, no. 1, pp. 38–63, 2018.
[7] L. Yang, M. Ju, and B. Zhang, "Bidirectional undersea capacitive wireless power transfer system," *IEEE Access*, vol. 7, pp. 121 046–121 054, 2019.
[8] H. Zhang and F. Lu, "Feasibility study of the high-power underwater capacitive wireless power transfer for the electric ship charging application," *2019 IEEE Electric Ship Technologies Symposium (ESTS), Washington, DC, USA*, pp. 231–235, 2019.
[9] H. Mahdi, B. Hoff, and T. Østrem, "Evaluation of capacitive power transfer for small vessels charging applications," in *2020 IEEE 29th International Symposium on Industrial Electronics (ISIE)*, 2020, pp. 1605–1610.
[10] M. Tamura, Y. Naka, K. Murai, and T. Nakata, "Design of a capacitive wireless power transfer system for operation in fresh water," *IEEE Transactions on Microwave Theory and Techniques*, vol. 66, no. 12, pp. 5873–5884, 2018.
[11] M. Tamura, K. Murai, and M. Matsumoto, "Design of conductive coupler for underwater wireless power and data transfer," *IEEE Transactions on Microwave Theory and Techniques*, vol. 69, no. 1, pp. 1161–1175, 2021.
[12] J. Dai and D. C. Ludois, "A survey of wireless power transfer and a critical comparison of inductive and capacitive coupling for small gap applications," *IEEE Transactions on Power Electronics*, vol. 30, no. 11, pp. 6017–6029, 2015.
[13] X. Lu, P. Wang, D. Niyato, D. I. Kim, and Z. Han, "Wireless charging technologies: Fundamentals, standards, and network applications," *IEEE Communications Surveys & Tutorials*, vol. 18, no. 2, pp. 1413–1452, 2016.

[14] W. Zhang and C. C. Mi, "Compensation topologies of high-power wireless power transfer systems," *IEEE Transactions on Vehicular Technology*, vol. 65, no. 6, pp. 4768–4778, 2016.

[15] H. T. Nguyen, J. Y. Alsawalhi, K. A. Hosani, A. S. Al-Sumaiti, K. A. A. Jaafari, Y.-J. Byon, and M. S. E. Moursi, "Review map of comparative designs for wireless high-power transfer systems in ev applications: Maximum efficiency, zpa, and cc/cv modes at fixed resonance frequency independent from coupling coefficient," *IEEE Transactions on Power Electronics*, vol. 37, no. 4, pp. 4857–4876, 2022.

[16] D. Vincent, P. S. Huynh, N. A. Azeez, L. Patnaik, and S. S. Williamson, "Evolution of hybrid inductive and capacitive ac links for wireless ev charging—a comparative overview," *IEEE Transactions on Transportation Electrification*, vol. 5, no. 4, pp. 1060–1077, 2019.

[17] B. Minnaert, F. Mastri, N. Stevens, A. Costanzo, and M. Mongiardo, "Coupling-Independent Capacitive Wireless Power Transfer Using Frequency Bifurcation," *Energies*, vol. 11, no. 7, p. 1012, 2018.

[18] H. Mahdi, B. Hoff, P. G. Ellingsen, and T. Østrem, "Conformal transformation analysis of capacitive wireless charging," *IEEE Access*, vol. 10, pp. 105 621–105 630, 2022.

[19] H. Zhang, F. Lu, H. F. Hofmann, W. Liu, and C. C. Mi, "Six-plate capacitive coupler to reduce electric field emission in large air-gap capacitive power transfer," *IEEE Transactions on Power Electronics*, vol. 33, pp. 665–675, 2018.

[20] C. Liu, A. P. Hu, and M. Budhia, "A generalized coupling model for capacitive power transfer systems," in *IECON 2010 - 36th Annual Conference on IEEE Industrial Electronics Society*, 2010, pp. 274–279.

[21] C. Liu, A. P. Hu, B. Wang, and N.-K. C. Nair, "A capacitively coupled contactless matrix charging platform with soft switched transformer control," *IEEE Transactions on Industrial Electronics*, vol. 60, no. 1, pp. 249–260, 2013.

[22] N. Sakai, D. Itokazu, Y. Suzuki, S. Sakihara, and T. Ohira, "One-kilowatt capacitive power transfer via wheels of a compact electric vehicle," in *2016 IEEE Wireless Power Transfer Conference (WPTC)*, 2016, pp. 1–3.

[23] K. Hyun Yi, "Capacitive coupling wireless power transfer with quasi-llc resonant converter using electric vehicles'windows," *Electron.*, vol. 9, no. 4, 2020.

[24] J. Dai and D. C. Ludois, "Single active switch power electronics for kilowatt scale capacitive power transfer," *IEEE Journal of Emerging and Selected Topics in Power Electronics*, vol. 3, no. 1, pp. 315–323, 2015.

[25] J. Lian and X. Qu, "Design of a Double-Sided LC Compensated Capacitive Power Transfer System with Capacitor Voltage Stress Optimization," *IEEE Transactions on Circuits and Systems II: Express Briefs*, vol. 67, no. 4, pp. 715–719, 2020.

[26] D. C. Ludois, M. J. Erickson, and J. K. Reed, "Aerodynamic fluid bearings for translational and rotating capacitors in noncontact capacitive power transfer systems," *IEEE Transactions on Industry Applications*, vol. 50, no. 2, pp. 1025–1033, 2014.

[27] T. M. Mostafa, A. Muharam, A. P. Hu, and R. Hattori, "Improved cpt system with less voltage stress and sensitivity using a step-down transformer on receiving side," *IET Power Electronics*, 2019.

[28] F. Lu, H. Zhang, H. Hofmann, and C. C. Mi, "A double-sided lc-compensation circuit for loosely coupled capacitive power transfer," *IEEE Transactions on Power Electronics*, vol. 33, no. 2, pp. 1633–1643, 2018.

[29] S. Zang and S. K. Nguang, "Capactive power transfer design for multiple receivers on conveyors," in *IECON 2019 - 45th Annual Conference of the IEEE Industrial Electronics Society*, vol. 1, 2019, pp. 4183–4188.

[30] J. Dai, S. S. Hagen, and D. C. Ludois, "High-efficiency multiphase capacitive power transfer in sliding carriages with closed-loop burst-mode current control," *IEEE Journal of Emerging and Selected Topics in Power Electronics*, vol. 7, no. 2, pp. 1388–1398, 2019.

[31] S. Ahmad, A. Muharam, R. Hattori, A. yu Uezu, and T. M. Mostafa, "Shielded capacitive power transfer (s-cpt) without secondary side inductors," *Energies*, 2021.

[32] A. Muharam, S. Ahmad, R. Hattori, and A. Hapid, "13.56 mhz scalable shielded-capacitive power transfer for electric vehicle wireless charging," in *2020 IEEE PELS Workshop on Emerging Technologies: Wireless Power Transfer (WoW)*, 2020, pp. 298–303.

[33] C. D. Rouse, S. R. Cove, Y. Salami, P. Arsenault, and A. Bartlett, "Three-phase resonant capacitive power transfer for rotary applications," *IEEE Journal of Emerging and Selected Topics in Power Electronics*, vol. 10, no. 1, pp. 160–169, 2022.

[34] S. Li, Z. Liu, H. Zhao, L. Zhu, C. Shuai, and Z. Chen, "Wireless power transfer by electric field resonance and its application in dynamic charging," *IEEE Transactions on Industrial Electronics*, vol. 63, no. 10, pp. 6602–6612, 2016.

[35] International Electrotechnical Commission, "Electromagnetic compatibility (EMC) - Part 6-1: Generic standards - Immunity standard for residential, commercial and light-industrial environments," Tech. Rep., 2016.

[36] Z. Chen, P. Davari, and H. Wang, "Single-phase bridgeless pfc topology derivation and performance benchmarking," *IEEE Transactions on Power Electronics*, vol. 35, no. 9, pp. 9238–9250, 2020.

[37] Z. Chen, B. Liu, Y. Yang, P. Davari, and H. Wang, "Bridgeless pfc topology simplification and design for performance benchmarking," *IEEE Transactions on Power Electronics*, vol. 36, no. 5, pp. 5398–5414, 2021.

[38] F. Lu, H. Zhang, and C. Mi, "A two-plate capacitive wireless power transfer system for electric vehicle charging applications," *IEEE Transactions on Power Electronics*, vol. 33, no. 2, pp. 964–969, 2018.

[39] F. Lu, H. Zhang, H. Hofmann, and C. Mi, "A double-sided lclc-compensated capacitive power transfer system for electric vehicle charging," *IEEE Transactions on Power Electronics*, vol. 30, no. 11, pp. 6011–6014, 2015.

[40] H. Zhang, F. Lu, H. F. Hofmann, W. Liu, and C. C. Mi, "A four-plate compact capacitive coupler design and lcl-compensated topology for capacitive power transfer in electric vehicle charging application," *IEEE Transactions on Power Electronics*, vol. 31, pp. 8541–8551, 2016.

[41] S. Ahmad, R. Hattori, and A. Muharam, "Generalized circuit model of shielded capacitive power transfer," *Energies*, vol. 14, p. 2826, 2021.

[42] C. G. Montgomery, R. H. Dicke, and E. M. Purcell, *Principles of Microwave Circuits (Electromagnetic Waves)*. IET, 1987.

[43] D. M. Pozar, *Microwave Engineering*, 4th ed. Hoboken, NJ :Wiley, 2011.

[44] L. Pamungkas, S. H. Wu, and H. J. Chiu, "Equivalent circuit approach for output characteristic design of capacitive power transfer," *IEEE Transactions on Circuits and Systems II: Express Briefs*, vol. 68, no. 7, pp. 2513–2517, 2021.

[45] T. Ohira, "Extended k-q product formulas for capacitive- and inductive-coupling wireless power transfer schemes," *IEICE Transactions on Electronics*, vol. 11, no. 9, pp. 1–7, 2014.

[46] M. Tamura, Y. Naka, and K. Murai, "Design of capacitive coupler in underwater wireless power transfer focusing on kq product," *IEICE Transactions on Electronics*, no. 10, pp. 759–766, 2018.

[47] H. Mahdi, B. Hoff, and T. Østrem, "Optimal solutions for underwater capacitive power transfer," *Sensors*, vol. 21, no. 24, p. 8233, 2021.

[48] S. Friedel, "How to calculate a capacitance matrix in comsol multiphysics," Available at https://www.comsol.com/blogs/how-to-calculate-a-capacitance-matrix-in-comsol-multiphysics/ (2023/2/10).

[49] E. Bracken and G. Pitner, "Module 4: Q3d capacitance matrix reduction," Available at https://courses.ansys.com/wp-content/uploads/2021/07 (2023/2/10).

[50] Comsol, "Computing the effect of fringing fields on capacitance," Available at https://www.comsol.jp/model/computing-the-effect-of-fringing-fields-on-capacitance-12605 (2023/2/10).

[51] Agilent, "Advanced impedance measurement capability of the rf i-v method compared to the network analysis method- application note 1369-2," Agilent Technologies, Tech. Rep., 2001.

[52] M. Horibe, "Performance comparisons between impedance analyzers and vector network analyzers for impedance measurement below 100 mhz frequency," in *2017 89th ARFTG Microwave Measurement Conference (ARFTG)*, 2017, pp. 1–4.

[53] K. Akiyoshi, R. Hattori, and A.-y. Uezu, "High frequency shielded-capacitive power transfer system with resonance rectifier," in *2022 Asian Wireless Power Transfer Workshop*, 2022, pp. 1–4.

[54] S. Sinha, A. Kumar, B. Regensburger, and K. K. Afridi, "A new design approach to mitigating the effect of parasitics in capacitive wireless power transfer systems for electric vehicle charging," *IEEE Transactions on Transportation Electrification*, vol. 5, no. 4, pp. 1040–1059, 2019.

[55] ——, "Design of high-efficiency matching networks for capacitive wireless power transfer systems," *IEEE Journal of Emerging and Selected Topics in Power Electronics*, vol. 10, no. 1, pp. 104–127, 2022.

[56] A. Amler, N. Weitz, and M. März, "Improved capacitive power transfer with non-resonant power transfer link using radio frequency push-pull inverter," *IEEE Journal of Emerging and Selected Topics in Power Electronics*, vol. 10, no. 6, pp. 7808–7823, 2022.

[57] ICNIRP, "Guidelines for limiting exposure to electromagnetic fields (100 khz to 300 ghz)," Health Phys, Tech. Rep., 2020.

[58] A. Muharam, S. Ahmad, and R. Hattori, "Scaling-factor and design guidelines for shielded-capacitive power transfer," *Energies*, vol. 13, no. 16, 2020.

[59] B. Luo, R. Mai, Y. Chen, Y. Zhang, and Z. He, "A voltage stress optimization method of capacitive power transfer charging system," in *2017 IEEE Applied Power Electronics Conference and Exposition (APEC)*, 2017, pp. 1456–1461.
[60] R. Mai, B. Luo, Y. Chen, and Z. He, "Double-sided cl compensation topology based component voltage stress optimisation method for capacitive power transfer charging system," *IET Power Electronics*, vol. 11, no. 7, pp. 1153–1160, 2018.
[61] S. Yang, Y. Zhang, Y. Zhang, Y. Wang, Z. Wang, B. Luo, and R. Mai, "Analysis and design of a dual-frequency capacitive power transfer system to reduce coupler voltage stress," *Electronics*, vol. 12, no. 6, 2023.
[62] A. Muharam, S. Ahmad, R. Hattori, D. Obara, M. Masuda, K. Ismail, and A. Hapid, "An improved ground stability in shielded capacitive wireless power transfer," in *2019 International Conference on Sustainable Energy Engineering and Application (ICSEEA)*, 2019, pp. 1–5.
[63] B. Regensburger, A. Kumar, S. Sinha, and K. K. Afridi, "Impact of foreign objects on the performance of capacitive wireless charging systems for electric vehicles," in *2018 IEEE Transportation Electrification Conference and Expo (ITEC)*, 2018, pp. 892–897.

HUSSEIN MAHDI (Graduate Student Member, IEEE) received the M.Sc. degree in electrical engineering from The Arctic University of Norway (UiT) in 2019, where he is currently pursuing a Ph.D. degree. He also works as a Graduate Research with the UiT-The Arctic University of Norway. His research interests include resonant converters, soft switching, wireless power transfer, and power factor correction.

REIJI HATTORI (Member, IEEE) received the B.S. and M.S. degrees in electrical engineering and the Ph.D. degree from Osaka University, Japan, in 1986, 1988, and 1992, respectively. He became a Research Associate at the Department of Electrical Engineering, Osaka University, in 1989. In 1997, he moved to Kyushu University, Fukuoka, Japan, as an Associate Professor, where he was promoted to Professor in 2009. He is currently working on display and related technologies, including OLED, touch panels, and wireless power transfer systems. He is a member of SID, IEICE, and JSAP.

BJARTE HOFF (SM'22) received the B.S. degree in maritime electroautomation from Vestfold University College, Borre, Norway, in 2008, the M.Sc. degree in electrical engineering from Narvik University College, Narvik, Norway, in 2010, and the Ph.D. degree in Electrical Power Engineering from the Norwegian University of Science and Technology (NTNU), in 2016. Dr. Hoff was certified as an Electrician in 2004.

His research interests power electronics with application within future energy system and electric transport, two inspiring areas that are important for the transition to a sustainable future. The use of power conversion technology through power electronics and associated control algorithms is essential for renewable energy, electric transport and energy storage. Charging of electric vehicles, maritime vessels and aircrafts is combining all those research areas on both component and system level, representing an important element for the electric future.

ANYU UEZU received the M.Sc. degree in engineering from The Interdisciplinary Graduate School of Engineering Sciences, Kyushu University, Japan 2023. His research interests include wireless power transfer and electric vehicles.

KATSUMI AKIYOSHI received the B.Sc. degree in engineering from Ryukyu University, Japan, in 2022. He is currently pursuing a M.Sc. degree in engineering. His research interests include wireless power transfer, electric vehicles, and robot arms. He is a member of IEICE, SID.

4

Conformal Transformation Analysis of Capacitive Wireless Charging

Hussein Mahdi, Bjarte Hoff, Pål Gunnar, Ellingsen and Trond Østrem

DOI: 10.1109/ACCESS.2022.3210960

Paper's Contribution

This paper studies the capacitive coupling when the mediums separating the couplers are air, freshwater, and seawater. The main contributions of the paper are: (1) It uses the conformal transformation to calculate the coupling capacitance and model the capacitive coupling, (2) it verifies the negative impact of the parasitic capacitance on the efficiency and power transferability of the CPT system, and (3) it shows that submerging the couplers under seawater can enhance the coupling and changes in the gap distance and the operating frequency do not significantly affect the underwater coupling.

IEEE Access
Multidisciplinary ⋮ Rapid Review ⋮ Open Access Journal

Received 15 August 2022, accepted 22 September 2022, date of publication 30 September 2022,
date of current version 10 October 2022.

Digital Object Identifier 10.1109/ACCESS.2022.3210960

RESEARCH ARTICLE

Conformal Transformation Analysis of Capacitive Wireless Charging

HUSSEIN MAHDI, (Graduate Student Member, IEEE), BJARTE HOFF, (Senior Member, IEEE), PÅL GUNNAR ELLINGSEN, AND TROND ØSTREM, (Member, IEEE)

Department of Electrical Engineering, UiT–The Arctic University of Norway, 8514 Narvik, Norway

Corresponding author: Hussein Mahdi (hussein.al-sallami@uit.no)

This work was supported by the Grant from the Publication Fund of UiT–The Arctic University of Norway.

ABSTRACT This paper studies the capacitive coupling in a capacitive power transfer (CPT) system designed for charging applications. It proposes mathematical models using the conformal transformation for calculating air-gapped and underwater capacitance and verifies the proposed models using COMSOL multiphysics and measurements. The measured results show that we can achieve nano-farad capacitance ranges if we submerge the capacitor in seawater. The seawater's capacitance slightly changes when we increase the gap distance or the operating frequency. As the under seawater CPT system can be an attractive option for loosely-coupled charging applications, we further examine the system by focusing on the cross-coupling effects. The results show that the cross-coupling between the plate degrades the system's power transfer capability and efficiency. With negligible cross-coupling effects, the system gives 129 W output power at an efficiency of 81.2%.

INDEX TERMS Wireless power transmission, capacitive power transfer, couplings, energy efficiency, conformal mapping, network theory.

I. INTRODUCTION

Wireless power transfer (WPT) utilizes electromagnetic fields to transfer power between a transmitter and a receiver (couplers) without mechanical contact. It has emerged in high-power charging applications providing safe and convenient solutions. In such applications, the standard practice is to use near-field WPT in which the distance between the couplers is much shorter than the wavelength of the electromagnetic fields. Near-field WPT comprises two main groups: inductive and capacitive power transfer.

Inductive power transfer (IPT) carries the power between the inductive couplers using magnetic fields. IPT is the most commonly used technique in high-power charging [1], as it provides the convenience of automatic charging through three modes: static, quasi-dynamic, and dynamic [2]. Thus, it has begun to receive attention for electric cars, buses, and trains charging applications [3].

The associate editor coordinating the review of this manuscript and approving it for publication was Kaigui Bian.

IPT suffers from eddy-current losses in the nearby metal, causing temperature rise problems [4]. Additionally, it contains expensive and heavy parts. As an alternative, capacitive power transfer (CPT) provides a cheaper and lighter solution than IPT using alternating electric fields. In the literature, many papers have proposed CPT charging on-road electric vehicles [5], [6], electric ships [7], [8], [9], and autonomous underwater vehicles [10], [11], [12].

Three performance metrics affect the overall system performance: the operating frequency of the system, the voltage across the capacitive couplers, and the coupling capacitance [7]. Decreasing the transfer distance, increasing the operating frequency, or increasing the voltage across the capacitors can enhance the power transfer of the system [12]. While safety regulations limit the operating frequency and voltage, we can improve the capacitance between the couplers.

The air-gapped capacitance is in the pico-farad (pF) range which limits the power transfer capability of the CPT system [5], [6]. One way to improve the coupling capacitance is

by decreasing the separation distance between the couplers or increasing the couplers' dimensions, but in both ways, we limit the applications of the CPT systems. Another way is by increasing the electrical permittivity of the medium between the couplers.

In electrical vehicle charging applications, researchers have tried inserting a layer of material with a high dielectric between the couplers instead of air to enhance the coupler's capacitance. For instance, Sakai *et al.* [13] proposed a CPT system through the road surface and the vehicle wheels utilizing steel belts in tires to overcome the short field-reachable range. Another approach by Yi [14] used the vehicle's windows to trap the electric fields for the coupling. In contrast, Dai and Ludois [15] transferred power through a flexible and compressive bumper that molds and contours itself to the vehicle to minimize the air gap and confine the field during charging.

Submerging the couplers in fresh- or seawater enhances the coupling and makes the CPT system more attractive for charging ships and underwater vehicles. In [9], the study analyzed the underwater CPT system using the finite element method (FEM) at a high frequency (HF) range. Similarly, other studies investigated the capacitive coupling at a short separation distance (up to 20 mm) in freshwater [10] and seawater [11], [12] at a MHz frequency range. The capacitor's behavior at the frequency range below the MHz range has received less attention.

This paper investigates the admittance of an air-gapped capacitor and capacitors submerged in fresh- and seawater. The investigation is carried out over 100 kHz to 1 MHz frequency range and 10 mm to 500 mm separation distances. We analyze the capacitance using a conformal transformation approach to consider the fringing effect. We propose mathematical models to calculate the capacitance of the air-gapped and underwater couplers. Moreover, we explain how we can consider the two-port π model as a conformal transformation in the complex domain. Finally, we investigate the effect of cross-coupling on the power transferability and efficiency under seawater CPT systems.

We arrange the rest of the paper as follows: Section II investigates the fringing effect on the capacitance of the coupling plates in air and underwater. It also proposes analytical models based on the conformal transformation analysis. Section III presents the two-port model and explains how we can consider this model as a conformal transformation in the complex domain. In section IV, we verify the proposed analytical models using numerical analysis and experimental results. Then, we examine in detail the effect of the cross-coupling admittance on the under seawater CPT system's power transferability and efficiency in section V. Finally, we conclude in section VI.

II. FRINGING EFFECT

Using a simplified electrostatic approximation model, we can approximate capacitance of the plates (coupling plates) as

$$C_0 = \frac{\kappa \epsilon_0 A}{d}, \tag{1}$$

TABLE 1. Capacitance models considering fringing effects.

Model	Formula	Shape
Simplified	$C_0 = \frac{\kappa A}{d}$	General
Ignatius's 1932 [18]	$C = C_0[1 + \frac{2d}{\pi R} \ln(\frac{32R}{ed})]$	Disc
Palmer 1937 [17]	$C = C_0[1 + \frac{d}{\pi L} \ln(\frac{2\pi L}{d})]^2$	Square
Cooke 1958 [18]	$C = C_0[1 + \frac{2d}{\pi R} \ln(\frac{\pi eR}{d})]$	Disc
Huston 1963 [18]	$C = C_0[1 + \frac{2d}{\pi R} \ln(\frac{8\pi R}{ed})]$	Disc
Nishiyama 1994 [19]	$C = C_0(1 + 2.343b^{0.992})$	Square

where κ is the dielectric constant, ϵ_0 (C/V · m) is the permittivity of the free space, A (m^2) is the area of the plates, and d (m) is the distance between the plates.

In this model, assumptions are a uniform charge density distribution on the plates and negligible fringing fields at the edges. However, these assumptions are only valid when the aspect ratio (b), given by

$$b = \frac{\text{electrode distance}}{\text{electrode width}}, \tag{2}$$

is very close to zero [16]. The assumptions fail when the charge density at the edges of the plates is more extensive than at the center. The electric fields near the edges of the plates are weaker than between them due to the fringing effect, which is the bending of electric field lines near the edges. Thus, the total capacitance of the plates increases because of the non-uniform distribution of fields near the edges.

A. THE FRINGING EFFECT IN AIR

Although we might know the total charge on the plates, it is not easy to calculate the total charge density because of the non-uniform distribution of charges. We can attribute the non-uniformity to the induced charge densities on nearby conductors or polarization of dielectric material. Conformal transformation and the finite element method (FEM) are two approaches that can deal with the boundary problem. While the FEM approach might require expensive software to calculate the capacitance numerically, the conformal transformation can be a cheaper alternative.

Palmer [17] derived an analytical model using the conformal transformation approach for square-shaped plates. Sloggett *et al.* [18] also used the conformal transformation approach to study the fringing capacitance for a disc-shaped capacitor. In contrast, Nishiyama and Nakamura [19] proposed a numerical model using the boundary element method to derive the capacitance of square and rectangular plates. Table 1 lists some of the proposed models for both square- and disc-shaped plates.

We can apply the disc plates' models for square ones by assuming that the area of the disc electrode equals the area of the squared one.

$$A = L^2 = \pi R^2, \tag{3}$$

where L is the length of the edges of the square electrode and R is the radius of the disc.

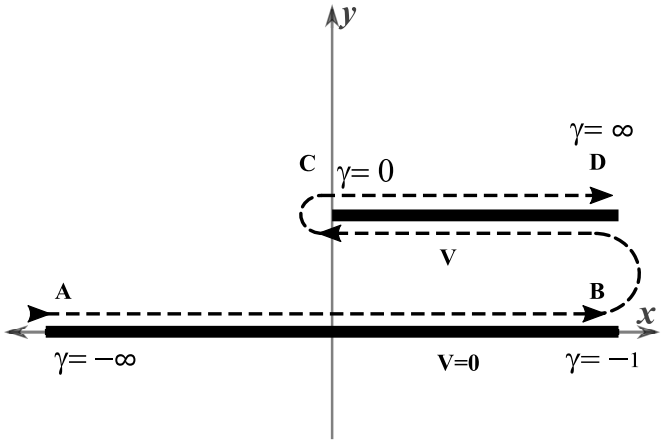

FIGURE 1. Illustration of the Schwartz-Christoffel transformation for the plates.

The conformal transformation approach uses complex conjugate functions to solve two-dimensional problems. According to [20], the theorem of Schwartz-Christoffel is a conformal mapping technique that transforms any polygon bounded by straight lines in the z-plane, where $z = x+jy$, into the real axis α of a new γ-plane, where $\gamma = \alpha + j\beta$. We can express the Schwartz-Christoffel transformation as [20]

$$\frac{dz}{d\gamma} = k\prod_{i=1}^{n}(\gamma - \gamma_i)^{a_i/\pi - 1}, \tag{4}$$

where a_i are the internal angles of the polygon in the z-plane, k is a constant and γ_i are points on the real axis in γ-plane that correspond to the angular points of the polygon in the z-plane. The $a_1, a_2, \ldots, a_n$ in (4) are given values, while we can arbitrarily assume the constants $\gamma_1, \gamma_2, \ldots, \gamma_n$.

The value of $dz/d\gamma$ ($|dz/d\gamma|$) in (4) is either infinite or zero at the angles of the polygon. In contrast, $|dz/d\gamma|$ cannot vanish or become infinite for the area bounded by the real axis (α-axis) and infinite semi-circle in the γ-plane. This area corresponds to the area bounded by the polygon in the z-plane. If the boundaries of the plates are considered the side of the polygon, then (4) transfer these lines into the real axis in the γ-plane.

Let ϕ be the potential function and ψ be the electric field function, where $\omega = \phi + j\psi$, are conjugate functions that each solve Laplace's equation ($\nabla^2\phi = 0$). A point in the boundary of the plate in z-plane corresponds to a point on the real axis in the γ-plane, and a line constant potential in the ω-plane.

Fig. 1 illustrates the successive Schwartz-Christoffel transformation of the plates in three planes: z-plane, γ-plane, and ω-plane. The upper electrode (CD) is assumed to be a semi-infinite plane with a potential function ($\phi = V$) in parallel to the electrode (AB) in an infinite plane with a potential function ($\phi = 0$). The sides of the plates describe the polygon (ABCD) as a dashed line in the direction of the arrows. The surfaces of the plates are straight lines stretching from $x = -\infty$ on the AB electrode to $x = \infty$ on the CD electrode in the z-plane.

In the z-plane, if a point travels over a straight line parallel to the y-axis, then the point moves around a semi-circle in the γ-plane, as (4) implies. Thus, the polygon consists of the two arc lines at the plates' edges. In the γ-plane, we arbitrarily select the values of γ to be $\gamma = -1$ corresponding to the corner at B and $\gamma = 0$ corresponding to the corner at C. The internal angles of the polygon are zero at B and 2π at C. By substituting the values of γ and the corresponding angles in (4), it gives

$$\frac{dz}{d\gamma} = k_1\frac{\gamma}{\gamma + 1}, \tag{5}$$

where k_1 is a constant. When the polygon passes through $\gamma = -1$, then the value of y increases $k_1\pi$ and hence $y = d = k_1\pi$, where d is the separation distance.

The ω-plane only consists two lines, V and zero, as shown in Fig. 1. The internal angle at $\gamma = -1$ is zero. Thus, the transformation of ω-plane to a real axis in the γ-plane can be expressed as

$$\frac{d\omega}{d\gamma} = k_2\frac{1}{\gamma + 1}, \tag{6}$$

where k_2 is a constant.

When the polygon passes through $\gamma = -1$, then the value of y decreases $k_2\pi$, that is, $y = V = -k_2\pi$. Solving (5) and (6) give

$$z = \frac{d}{\pi}[1 + \gamma - \ln(1 + \gamma) + j\pi] \tag{7a}$$

$$w = -\frac{V}{\pi}[\ln(1 + \gamma) - j\pi] \tag{7b}$$

From (7a), the real part of the z-plane can be written as

$$x = \frac{d}{\pi}[1 + \gamma - \ln(1 + \gamma)] \tag{8}$$

The surface charge density σ can be expressed as

$$\sigma = \pm\frac{1}{4\pi}\frac{d\psi}{dy} = \pm\frac{1}{4\pi}\frac{d\phi}{dx} \tag{9}$$

Now, we can calculate the surface charge density for the upper surface and the lower surface of the CD plate. Starting with the lower surface, as the values of γ ranges from -1 to zero, then we can simplify γ from (8) as

$$\gamma = \frac{\pi x}{d} \tag{10}$$

From (7b), (9), and (10), we can express the charge density of the lower surface from zero to γ, in the γ-plane, as

$$\begin{aligned}\int \sigma\, da &= \frac{1}{4\pi}[\phi(\gamma) - \phi(0)] = -\frac{V}{4\pi^2}[\ln(1 + \gamma)] \\ &\approx \frac{V}{4\pi^2}(1 + \gamma) = \frac{V}{4\pi d}\left(x + \frac{d}{\pi}\right),\end{aligned} \tag{11}$$

where da is an element of the section of the conductor.

The charge density on the lower part of the electrode equals the uniform charge distribution on an infinite electrode that its width increases by a factor (d/π).

For the upper surface, as the values of γ ranges from zero to infinity, then we can simplify γ from (8) as

$$\gamma = \left[\frac{\pi x}{d} + \ln(1 + \frac{\pi x}{d})\right] \tag{12}$$

Similarly from (7b), (9), and(12), the surface charge density of the upper surface of the electrode is

$$\begin{aligned}\int \sigma da &= \frac{1}{4\pi}\left[\phi(0) - \phi(\gamma)\right] = -\frac{V}{4\pi^2}\left[\ln(1+\gamma)\right] \\ &\approx \frac{V}{4\pi^2}\left\{\ln\left[1 + \frac{\pi x}{d} + \ln\left(1 + \frac{\pi x}{d}\right)\right]\right\}\end{aligned} \tag{13}$$

The total charge surface density is the algebraic summation of the charge density on the upper and the lower surfaces. If the width of the plate is not semi-infinite, that is $x = L$, then the capacitance because of the fringing can be expressed as

$$C_f = \frac{\epsilon_0}{4\pi}\left\{1 + \frac{\pi L}{d} + \ln\left[1 + \frac{\pi L}{d} + \frac{1}{\pi}\ln\left(1 + \frac{\pi L}{d}\right)\right]\right\} \tag{14}$$

We can physically interpret the fringing capacitance as a capacitor that is connected in parallel with the capacitor of a uniform charge distribution on the plates, which is given in (1). Thus, we express the total capacitive of the air-gapped coupler as:

$$\begin{aligned}C = C_0 + C_f &= \frac{\epsilon_0 L^2}{d} \\ &+ \frac{\epsilon_0}{4\pi}\left\{1 + \frac{\pi L}{d} + \ln\left[1 + \frac{\pi L}{d} + \frac{1}{\pi}\ln\left(1 + \frac{\pi L}{d}\right)\right]\right\}\end{aligned} \tag{15}$$

B. THE FRINGING EFFECT IN WATER

Taking the electrical properties of water into consideration, we can write (6) as

$$\frac{d\omega}{d\gamma} = k_2 \frac{1}{\gamma + a}, \tag{16}$$

where the factor a represents the conductivity effect of water and we can assume it to be $a = \pi^2/x$. From Fig. 1, if we neglect the surface charge density of the upper surface of the plates, due to the higher concentration of charges between the coupling plates in comparison with upper surfaces. Then we can express the charge density of the plates equals the charge on the lower surface as

$$\int \sigma da \approx \frac{V}{4\pi d}\left(x + \frac{\pi d}{x}\right) \tag{17}$$

The charge density equals the uniform charge distribution on an infinite plate whose width increases by a factor $(\pi d/L)$. Similar to (15), we can approximate the total capacitance in water as:

$$C \approx \frac{\kappa\epsilon_0 L^2}{d} + \frac{\kappa\epsilon_0}{4\pi d}\left(L + \frac{\pi d}{L}\right) \tag{18}$$

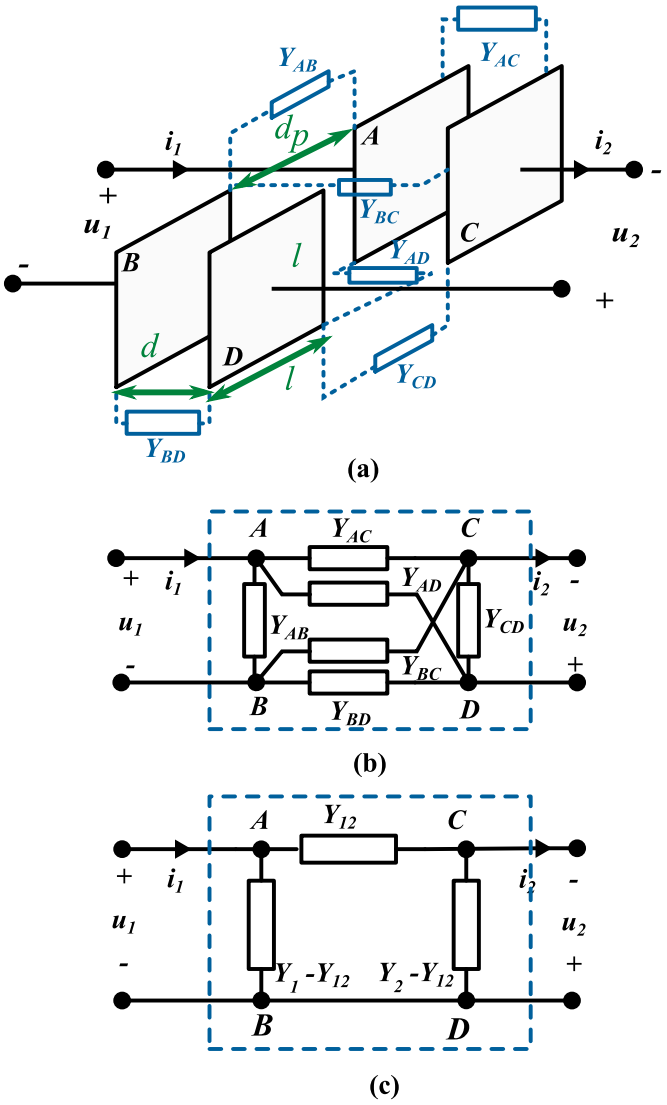

FIGURE 2. Model of the plate coupling: (a) The coupling between the four plates structures. (b) The circuit model of coupling admittance between the plates. (c) The π model.

III. TWO-PORT MODEL

The coupling between plates depends on the dimension of the plates and the medium's characteristics between the plates, as shown in (15) and (18). In the case of the air-gapped CPT system, we can neglect the air's conductivity and use the capacitors as circuit elements to represent the coupling between the plates. While in the case of an underwater CPT system, we cannot neglect the water's conductivity due to the presence of the dissolved ions in the water; hence, we represent the conductivity of the water by the conductance. As a general case, we can principally use the admittance to model the coupling between the plates in a CPT as

$$Y = G + jB, \tag{19}$$

where G is the conductance of the medium and B is the susceptance between the plates.

Fig. 2(a) shows four plates (A, B, C, and D) which are a simple CPT structure where the plates (B and D) generate

a return path for the resonant current. The admittance Y_{AC} and Y_{BD} are the mutual coupling between the plates. While the admittance Y_{AD} and Y_{BC} are the cross-coupling between the plates. Finally, the admittance Y_{AB} and Y_{CD} are the self-coupling between the plates, as illustrated in Fig. 2(b).

The mutual and cross coupling form a general lattice network which is unstable due to the inevitable interaction between the elements of the network. We can simplify in to a π-network whose elements are [21]

$$Y_{ab} = \frac{(Y_{AC} + Y_{AD}) \cdot (Y_{BC} + Y_{BD})}{(Y_{AC} + Y_{AD}) + (Y_{BC} + Y_{BD})} \tag{20}$$

$$Y_{cd} = \frac{(Y_{AC} + Y_{BC}) \cdot (Y_{AD} + Y_{BC})}{(Y_{AC} + Y_{BC}) + (Y_{AD} + Y_{BC})} \tag{21}$$

$$Y_{12} = \frac{Y_{AB} \cdot Y_{CD} - Y_{AD} \cdot Y_{BC}}{Y_{AC} + Y_{AD} + Y_{BC} + Y_{BD}} \tag{22}$$

As Y_{ab} and Y_{cd} are in parallel with Y_{AB} and Y_{CD}, we can express them in

$$Y_1 = Y_{AB} + Y_{ab} \tag{23}$$

$$Y_2 = Y_{CD} + Y_{cd} \tag{24}$$

Using (20) to (24), we can illustrate the π-network model, as in Fig. 2(c). Based on [21], we can consider the two-port π-network model as a conformal transformation in the complex domain. In other words, if we consider the load admittance as a point on the complex domain Y_L-plane, the input admittance is a point on the complex domain Y_{in}-plane, then the two-port model maps the output plane onto the input plane or vice versa without changing the angles.

Fig. 3 illustrates the connection of the two-port network to a source and a load and the mapping between the input and the output complex planes. The input admittance (Y_{in}) is a conformal transformation of the load admittance to the input complex plane. In contrast, the two-port model maps the source admittance (Y_s) and the current source (I_s) to the output complex plane, as the output admittance (Y_{out}) and the output current source (I_{out}).

Thus, we can express the mapping as

$$Y_{in} = Y_1 - \frac{Y_{12}^2}{Y_2 + Y_L}, \tag{25}$$

$$Y_N = Y_{out} = Y_2 - \frac{Y_{12}^2}{Y_1 + Y_s} \tag{26}$$

$$i_N = \frac{Y_{12}}{Y_1 + Y_s} i_s \tag{27}$$

$$Y_{in} = Y_1 - \frac{Y_{12}^2}{Y_2 + Y_L}, \tag{28}$$

IV. EXPERIMENTAL VERIFICATION

In the first step, we made a capacitor for verifying the fringing effect using two 150 × 150 mm aluminum plates insulated by covering them with a plastic lamination pouch. Using an Agilent 4285A LCR meter in the four-terminal pair measurement configuration, we measured the air-gapped admittance at a distance ranging from 10 mm to 500 mm. In the second step,

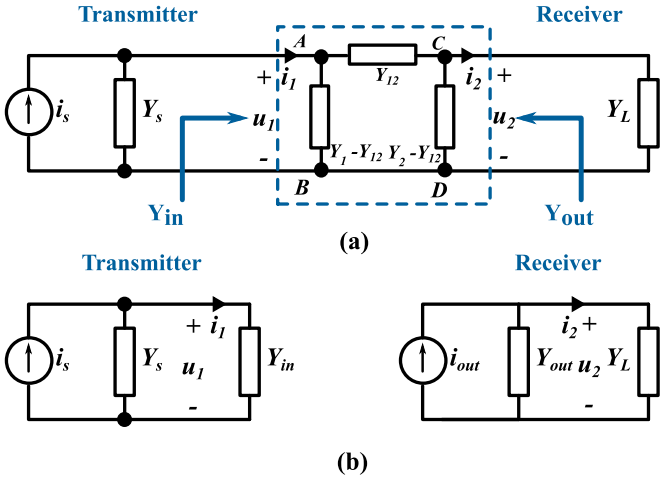

FIGURE 3. Model of source and a load connected to the *pi*-network: (a) *pi*-network connected to source and load. (b) The conformal transformation of admittance between transmitter and receiver sides [8].

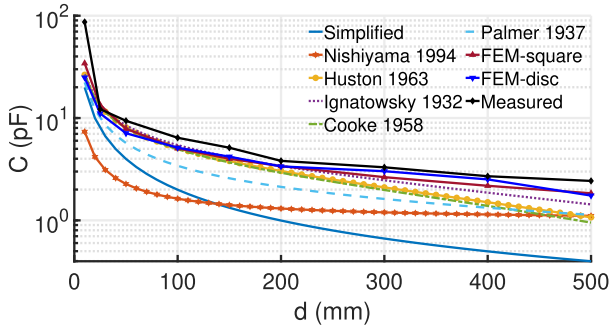

FIGURE 4. Comparison between the models listed in Table 1 and the measured capacitance as a function of separation distance in air.

we compared the measurements with the proposed analytical model, the models in Table 1, and the numerical model based on FEM using COMSOL Multiphysics. We used tap water as freshwater and collected seawater from the local harbor. In the last step, we tested a series compensated CPT system in seawater to examine the cross-coupling effect on the system's power transferability and efficiency.

A. AIR-GAPPED CAPACITANCE

Fig. 4 shows a comparison between the models in Table 1, the FEM model, and the measured air-gapped capacitance at 100 kHz. The results, with an experimentally determined error that does not exceed 2 pF, show that the simplified model fails to predict the measurements. Fig. 5 explains the reason for the difference between the measured values and the ones based on the simplified model. It shows the electric field norm contours where the electric field is about 10 V/m at the edges of the plates. The fringing effect cannot be neglected for the air-gapped or submerged capacitor even when the aspect ratio (b) is small.

The FEM models for squared- and disc electrodes give approximately the same results, which shows that the approximation in (3) is valid. The maximum difference between the FEM-square and FEM-disc is 10 pF at 10 mm separation

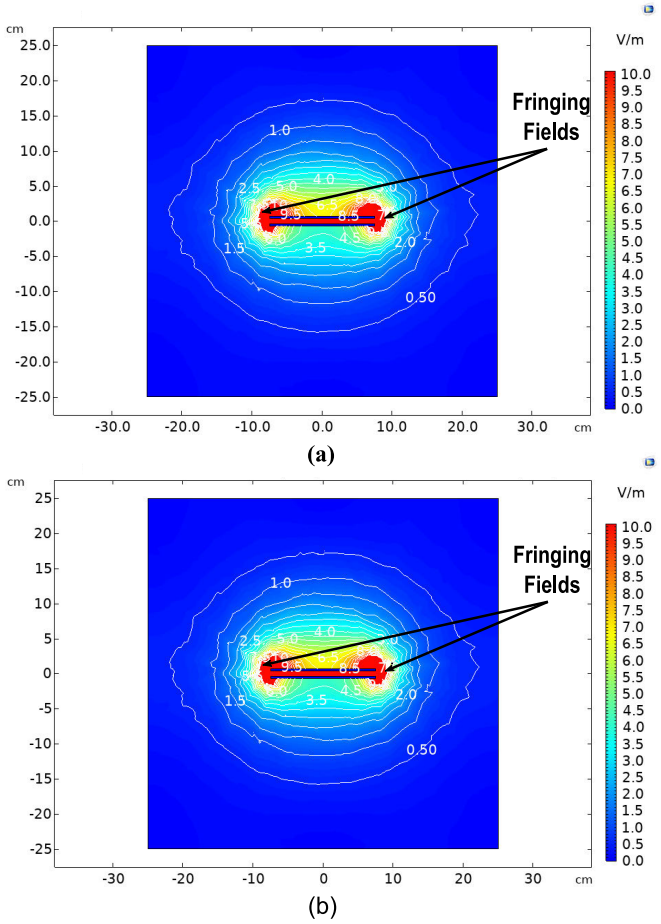

FIGURE 5. Fringing effect with aspect ratio b = 0.067: (a) Air-gapped capacitor. (b) Underwater capacitor.

distance, which we can attribute to the fields irregularities near the edges of the squared plate. The FEM models predict the measured values more accurately than the other models over the distance range. In contrast, the other models such as Palmer 1927, Ignatowsky 1932, Cooke 1958, and Huston 1963 can predict the measured values when the gap is in the range of 50 mm to 200 mm. These models can predict the measured capacitance more accurately when the aspect ratio b is tiny.

Fig. 6 illustrates the proposed analytical approach (conformal transformation model), the numerical approach (FEM), and the measured capacitance for the air-gapped capacitor. Using (15) the conformal transformation model predicts the measured capacitance better than the FEM analysis. The highest achieved capacitance is 37.9 pF at 10 mm distance, and it reduces exponentially with the increase of the gap to reach 3.4 pF at 500 mm. The percent error of the conformal transformation model is lower than that for FEM, as shown in Fig 7. The error for both models increases as the aspect ratio b approaches zero. The analytical approach must consider electrode thickness to reduce errors for small aspect ratios.

B. WATER CAPACITANCE

Like the air-gapped capacitor, we investigated the proposed analytical model, the numerical model, and the measured

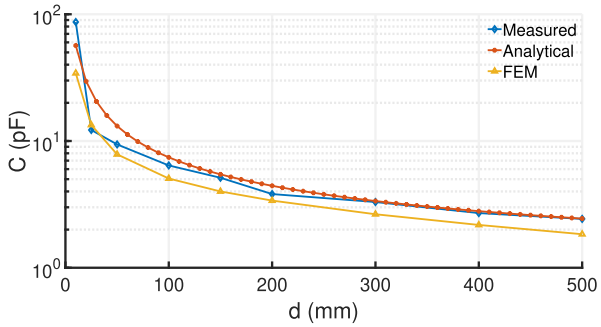

FIGURE 6. Comparison between the analytical approach, the numerical approach, and the measured capacitance of separation distance in air.

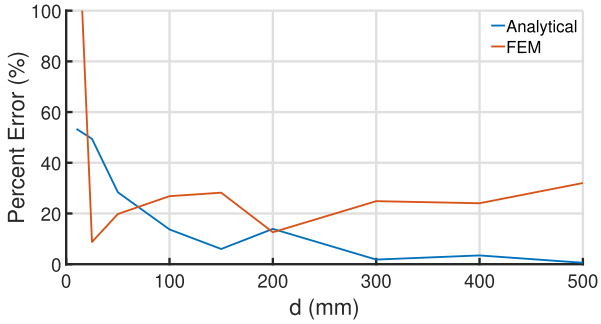

FIGURE 7. Percent error of the analytical and numerical approaches for the air-gapped capacitor.

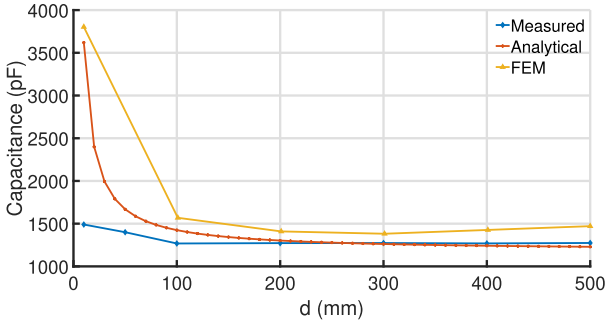

FIGURE 8. Comparison between the analytical approach, the numerical approach, and the measured capacitance of separation distance in water with $\kappa = 82$.

capacitance for the seawater capacitor. Fig 8 shows that using (18) the conformal transformation has a better prediction of the measured capacitance than the FEM analysis. However, both models fail to predict the measured values when the separation distance is 100 mm or lower. We can attribute this difference between the models and measured values at a short separation distance to the air bubbles that got trapped in the plastic lamination pouch.

The percent error of the conformal transformation model is lower than FEM for the submerged capacitor in seawater with 82 dielectric constant, as shown in Fig. 9. The plots show that the analytical approach predicts the capacitance in seawater more accurately than the FEM approach. The differences between the measured, the analytical, and the numerical values could be explained by different water characteristics, such

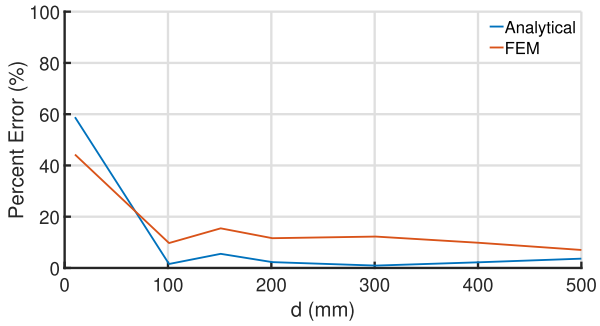

FIGURE 9. Percent error of the analytical and numerical approaches for the submerged capacitor.

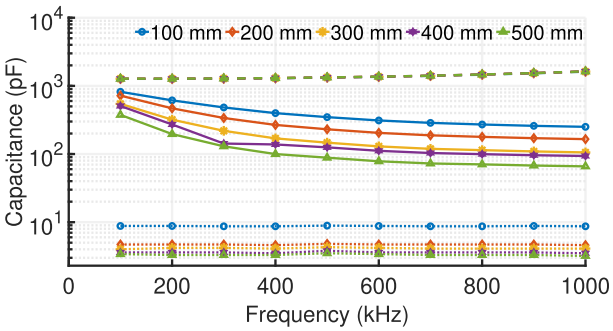

FIGURE 10. Measured capacitance of air-gapped electrodes (dotted line), in freshwater electrodes (solid line), and in seawater electrodes (dashed line).

as temperature and salinity. Both the analytical and numerical approaches can give a good approximation to the design of a CPT system.

V. UNDERWATER CAPACITIVE CHARGING

The air-gapped capacitance range is much lower than those of the submerged in water, as shown in Fig.10. At 100 mm, the air-gapped capacitance decreases by only 0.1 pF when the frequency increases from 100 kHz to 1 MHz. The increase in the transfer distance has more effect on the capacitance. In contrast, the underwater capacitance can reach the nF range, which is about a thousand times higher than that of an air-gapped one. This high difference attributes to the presence of the water dipoles and the ions.

At 100 mm, the freshwater capacitance is about 819 pF at 100 kHz and decreases to 250 pF at 1 MHz. At the same separation distance, the under seawater capacitance is 1.3 nF at 1 MHz and increase to 1.6 nF at 1 MHz. The capacitance in freshwater is monotonically decreasing when the gap distance and frequency increase. In contrast, the capacitance in seawater slightly increases with increasing the frequency, and it does not significantly change with changing the transfer distance. We can attribute these differences between fresh- and seawater capacitance to the higher percentage of dissolved ions in the seawater than in freshwater.

The conductance of the air-gapped coupling is almost negligible compared to underwater coupling, as shown in Fig. 11. It is in the μS range and does not change with frequency

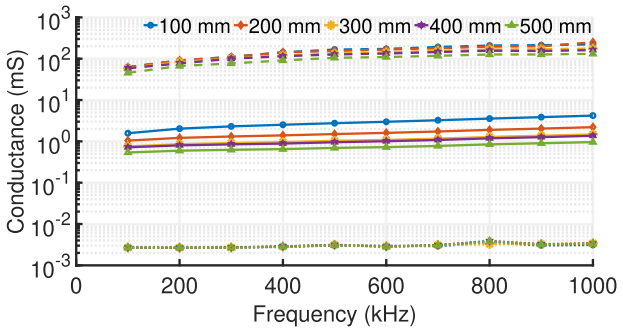

FIGURE 11. Measured conductance of air-gapped electrodes (dotted line), in freshwater (solid line), and in seawater electrodes (dashed line).

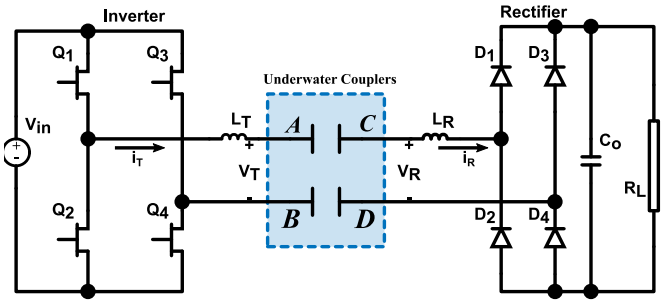

FIGURE 12. Converter topology.

or distance, which we can attribute to the insulation characteristic of the air. Fig. 11 also shows that the conductance of the freshwater is about a hundred times lower than the one under seawater. Both the conductivity of the fresh- and seawater decrease with the separation distance and rise with the increase of the frequency.

From the above results, we continue testing the power transfer capability of the CPT system in seawater. Fig. 12 illustrates the converter topology we used to test underwater CPT. We used a four-plates structure by submerging four aluminum plates in the seawater. In addition, we utilized a GaN bridge inverter (Infineon EVAL1EDFG1HBGAN) and four Schottky diodes (C6D04065A) to build the rectifier bridge. The series L-compensation was chosen as a simple design that can provide electromagnetic interference (EMI) suppression. We set the switching frequency slightly higher than the resonant frequency to operate in the inductive mode and achieve soft-switching.

Using a single inductor in series at both transmitter and receiver sides, we can operate the CPT system in constant-current (CC) or constant-voltage (CV) modes through frequency splitting. It was chosen to operated the system in CC mode to achieve a zero-phase angle, aiming to cancel transferring reactive power, which is hard to achieve in CV mode. Table 2 lists the design parameters used in the experiment.

In a previous work [8], we showed that both the power transfer capability and the system's efficiency are a function of the admittance Y_{12}. Increasing the mutual capacitive coupling can enhance the power transfer capability and the system's efficiency. However, we notice from (20) that the

TABLE 2. Design parameters.

Parameters	Values
Input voltage [V]	250
Operating frequency [MHz]	1.1
L_T[μH]	29.3
L_R[μH]	30.9
Plates' dimensions [mm×mm]	150 × 150
d [mm]	300
d_p [mm]	100
Water's depth [mm]	280

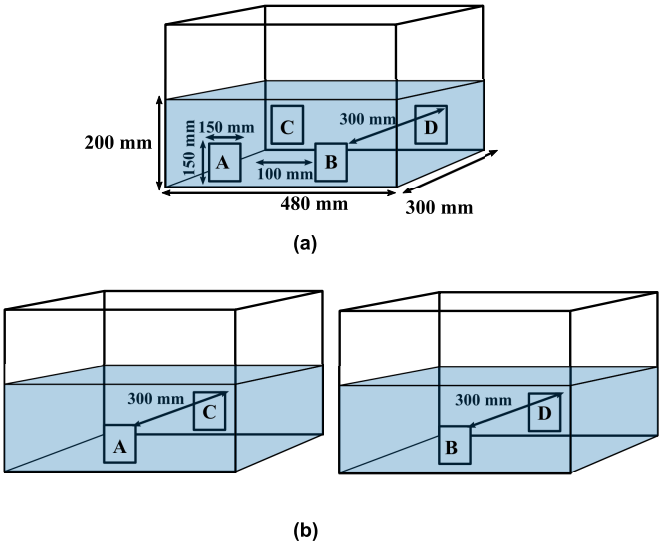

FIGURE 13. Experimental setups: (a) With the cross coupling effect. (b) Without the cross coupling.

cross-coupling, Y_{AD} and Y_{BC}, has a negative impact on the admittance Y_{12} and hence the system's power transfer capability and the efficiency. To examine the influence of the cross-coupling, we submerged the four plates in a common container, as shown in Fig. 13(a). While neglecting the effect of the cross-coupling, we submerged the plates (A and C) and (B and D) in two different containers, as depicted in Fig. 13(b). In practice, we can increase the distance between plates A and B and C and D to eliminate the cross-coupling effect.

Firstly, when we submerged the plates in the same container, we achieved 14.7 W the output power with 41.9 % efficiency. Fig. 14 shows the currents on both the transmitter and the receiver sides and the voltage across the couplers A and C. The phase shifts between the currents and voltage indicate a high reactive power circulating in the system, which explains the system's low power and efficiency. The figure also shows that the switches Q_1 and Q_4 switched on when the transmitter side's current is negative, thus achieving a zero voltage switching (ZVS) condition. In addition, the results show that the current on the receiver side suffers from high harmonic contents, as shown in impure sinusoidal sine wave, which may result in EMI problems.

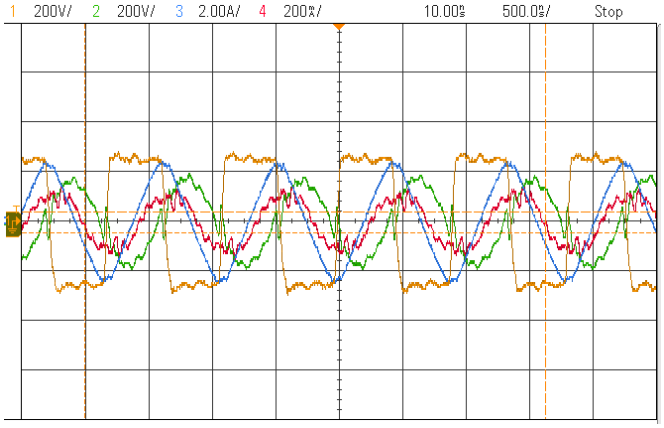

FIGURE 14. With the cross coupling effect: the output voltage of the inverter (yellow), the current on the transmitter side i_T (blue) the current on the receiver side i_R (red), and the voltage across the couplers A and C (green).

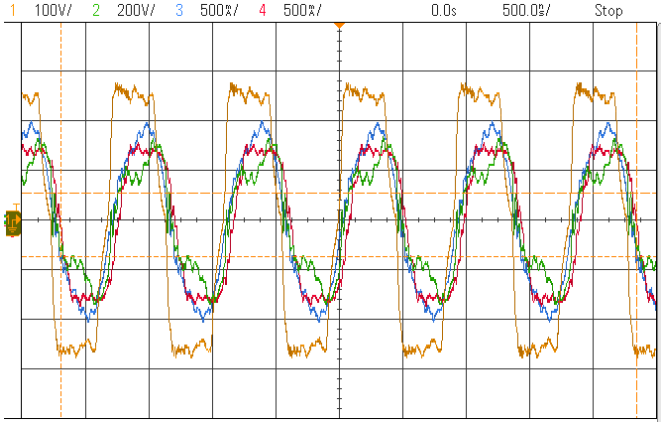

FIGURE 15. Without the cross coupling effect: the output voltage of the inverter (yellow), the current on the transmitter side i_T (blue) the current on the receiver side i_R (red), and the voltage across the couplers A and C (green).

Secondly, we separated plates A and C from plates B and D to neglect the cross-coupling effect. Under the same design parameters, we achieved an output power of 129.2 W with about 81.2 % efficiency. Fig. 15 shows the currents and the voltages with a neglected cross-coupling case study. The phase shift between the current and voltage is small, which explains the system's high output power and good efficiency. Moreover, the result shows that the inverter achieved zero current switchings (ZCS), as the switching frequency is close to the CC mode frequency. As with the fringing, the harmonics problem increases in the current on the receiver side.

Fig. 16 shows the breakdown losses of the system with and without the effect of the cross-coupling. More than 90% of the losses are in the underwater capacitive coupling for both cases. We can attribute the losses to the water conductivity. The cross-coupling also increases the losses underwater resulting in low efficiency and less transfer power. Table 3 lists a comparison of this work with other underwater CPT systems in the literature in terms of compensation circuit, transfer power, system efficiency, operating frequency,

TABLE 3. Comparison between underwater CPT systems.

Ref.	Compensation	Power (W)	Efficiency (%)	Frequency (MHz)	distance (mm)	size (mm)
[9]	LC	226.9	60.2	1	500	200 × 200 × 1
[11]	LC	400	90	107.7	20	150 × 205 × 1.6
[12]	LCLC	100	80.2	0.625	150	500 × 500 × 3
This work	L	129	81.2	1.1	300	150 × 150 × 3

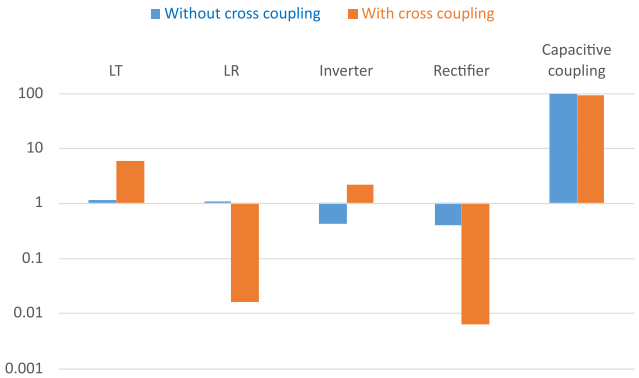

FIGURE 16. Power loss breakdown: without the cross coupling effect and with the cross coupling effect.

transfer distance, and coupler size. In this work, the underwater CPT system is smaller in size and simpler in compensation than the others and can achieve an efficiency of over 80% at 300 mm separation distance if we solve the problem of cross-coupling.

VI. CONCLUSION

This paper investigated the fringing effect on the capacitance of both an air-gapped CPT system and an underwater CPT system. It proposes mathematical models to calculate the air-gapped and underwater capacitance using the conformal transformation and verified the models using FEM models in COMSOL and experimentally measured values. The proposed models showed improvements over previously proposed FEM and other analytical approaches. The paper also modeled the capacitive coupling using the two-port model and analyzed it as a conformal mapping transformation in the complex domain. The experimental measurements demonstrated that we can improve the coupling by submerging the coupling plates in seawater. The results also showed that changes in the gap distance and the operating frequency do not significantly affect the underwater coupling. Thus, the paper further examined the effect of cross-coupling on the underwater system's power transferability and efficiency and found that it can degrade the system's power transfer capability and efficiency. A system without cross-coupling effects can achieve an output power of 129 W with an efficiency of 81.2%.

REFERENCES

[1] M. Z. Erel, K. C. Bayindir, M. T. Aydemir, S. K. Chaudhary, and J. M. Guerrero, "A comprehensive review on wireless capacitive power transfer technology: Fundamentals and applications," *IEEE Access*, vol. 10, pp. 3116–3143, 2022.

[2] A. Ahmad, M. S. Alam, and R. Chabaan, "A comprehensive review of wireless charging technologies for electric vehicles," *IEEE Trans. Transport. Electrific.*, vol. 4, no. 1, pp. 38–63, Mar. 2018. [Online]. Available: https://ieeexplore.ieee.org/document/8101562/

[3] G. A. Covic and J. T. Boys, "Modern trends in inductive power transfer for transportation applications," *IEEE J. Emerg. Sel. Topics Power Electron.*, vol. 1, no. 1, pp. 28–41, Mar. 2013.

[4] F. Lu, H. Zhang, and C. Mi, "A review on the recent development of capacitive wireless power transfer technology," *Energies*, vol. 10, no. 11, p. 1752, Nov. 2017.

[5] H. Zhang, F. Lu, H. Hofmann, W. Liu, and C. C. Mi, "A four-plate compact capacitive coupler design and LCL-compensated topology for capacitive power transfer in electric vehicle charging application," *IEEE Trans. Power Electron.*, vol. 31, no. 12, pp. 8541–8551, Dec. 2016.

[6] F. Lu, H. Zhang, and C. Mi, "A two-plate capacitive wireless power transfer system for electric vehicle charging applications," *IEEE Trans. Power Electron.*, vol. 33, no. 2, pp. 964–969, Feb. 2018.

[7] H. Mahdi, B. Hoff, and T. Ostrem, "Evaluation of capacitive power transfer for small vessels charging applications," in *Proc. IEEE 29th Int. Symp. Ind. Electron. (ISIE)*, Jun. 2020, pp. 1605–1610.

[8] H. Mahdi, B. Hoff, and T. Østrem, "Optimal solutions for underwater capacitive power transfer," *Sensors*, vol. 21, no. 24, p. 8233, Dec. 2021.

[9] H. Zhang and F. Lu, "Feasibility study of the high-power underwater capacitive wireless power transfer for the electric ship charging application," in *Proc. IEEE Electric Ship Technol. Symp. (ESTS)*, Aug. 2019, pp. 231–235.

[10] M. Tamura, Y. Naka, K. Murai, and T. Nakata, "Design of a capacitive wireless power transfer system for operation in fresh water," *IEEE Trans. Microw. Theory Techn.*, vol. 66, no. 12, pp. 5873–5884, Dec. 2018.

[11] M. Tamura, K. Murai, and M. Matsumoto, "Design of conductive coupler for underwater wireless power and data transfer," *IEEE Trans. Microw. Theory Techn.*, vol. 69, no. 1, pp. 1161–1175, Jan. 2021.

[12] L. Yang, M. Ju, and B. Zhang, "Bidirectional undersea capacitive wireless power transfer system," *IEEE Access*, vol. 7, pp. 121046–121054, 2019.

[13] N. Sakai, D. Itokazu, Y. Suzuki, S. Sakihara, and T. Ohira, "One-kilowatt capacitive power transfer via wheels of a compact electric vehicle," in *Proc. IEEE Wireless Power Transf. Conf. (WPTC)*, May 2016, pp. 16–18.

[14] K. Yi, "Capacitive coupling wireless power transfer with quasi-LLC resonant converter using electric vehicles' Windows," *Electronics*, vol. 9, no. 4, p. 676, Apr. 2020.

[15] J. Dai and D. C. Ludois, "Capacitive power transfer through a conformal bumper for electric vehicle charging," *IEEE J. Emerg. Sel. Topics Power Electron.*, vol. 4, no. 3, pp. 1015–1025, Sep. 2016.

[16] H. Zhang, F. Lu, H. Hofmann, W. Liu, and C. C. Mi, "Six-plate capacitive coupler to reduce electric field emission in large air-gap capacitive power transfer," *IEEE Trans. Power Electron.*, vol. 33, no. 1, pp. 665–675, Jan. 2018.

[17] H. B. Palmer, "The capacitance of a parallel-plate capacitor by the Schwartz-Christoffel transformation," *Trans. Amer. Inst. Elect. Eng.*, vol. 56, no. 3, pp. 363–366, Mar. 1937. [Online]. Available: http://ieeexplore.ieee.org/document/5057547/

[18] G. J. Sloggett, N. G. Barton, and S. J. Spencer, "Fringing fields in disc capacitors," *J. Phys. A, Math. Gen.*, vol. 19, no. 14, pp. 2725–2736, Oct. 1986.

[19] H. Nishiyama and M. Nakamura, "Form and capacitance of parallel-plate capacitors," *IEEE Trans. Compon., Packag., Manuf. Technol. A*, vol. 17, no. 3, pp. 477–484, Sep. 1994. [Online]. Available: http://ieeexplore.ieee.org/document/311759/

[20] T. A. Driscoll and L. N. Trefethen, *Schwarz-Christoffel Mapping*. Cambridge, U.K.: Cambridge Univ. Press, 2009.

[21] C. G. Montgomery, R. H. Dicke, and E. M. Purcell, *Principles of Microwave Circuits*. New York, NY, USA: McGraw-Hill, 1987.

HUSSEIN MAHDI (Graduate Student Member, IEEE) received the M.Sc. degree in electrical engineering from The Arctic University of Norway (UiT), in 2019, where he is currently pursuing the Ph.D. degree. He also works as a Graduate Research with the UiT. His research interests include resonant converters, soft switching, wireless power transfer, and power factor correction.

BJARTE HOFF (Senior Member, IEEE) received the B.S. degree in maritime electroautomation from Vestfold University College, Borre, Norway, in 2008, the M.Sc. degree in electrical engineering from Narvik University College, Narvik, Norway, in 2010, and the Ph.D. degree in electrical power engineering from the Norwegian University of Science and Technology (NTNU), in 2016.

He was certified as an electrician, in 2004. His research interests include power electronics with application within future energy systems and electric transport, two inspiring areas that are important for the transition to a sustainable future. The use of power conversion technology through power electronics and associated control algorithms is essential for renewable energy, electric transport, and energy storage. Charging of electric vehicles, maritime vessels, and aircrafts is combining all those research areas on both component and system level, representing an important element for the electric future.

PÅL GUNNAR ELLINGSEN received the M.S. degree in applied physics from the Norwegian University of Science and Technology (NTNU), in 2010, and the Ph.D. degree in physics (optics) from NTNU.

He is currently an Associate Professor at UiT–The Arctic University of Norway. He is also a part of several research projects related to remote sensing, satellite construction, marine sciences, and optical communication. His research interests include optics, polarimetry, spectroscopy, remote sensing, satellite technology, data management, and education.

TROND ØSTREM (Member, IEEE) was born in Kjollefjord, Norway, in August 1956. He received the M.S. degree in electrical engineering and the Ph.D. degree from Narvik University College, Narvik, in 2002 and 2007, respectively.

He is currently an Associate Professor at UiT–The Arctic University of Norway. His research interests include distributed generation, power electronics, power system stability, and electric transportation.

5

Optimal Solutions for Underwater Capacitive Power Transfer

Hussein Mahdi, Bjarte Hoff, and Trond Østrem

DOI: 10.3390/s21248233

Paper's Contribution

Submerging the capacitive couplers under seawater results in the strong conductive coupling, which can highly affect the overall system efficiency and power transferability. The main contributions of the paper are: (1) It proposes three possible solutions to achieve maximum efficiency, maximum power, or conjugate matching considering the dielectric losses of the medium, and (2) it investigates the underwater coupling efficiency and power transferability at low operating frequencies.

sensors

MDPI

Article

Optimal Solutions for Underwater Capacitive Power Transfer

Hussein Mahdi *,† **, Bjarte Hoff** † **and Trond Østrem**

Department of Electrical Engineering, UiT—The Arctic University of Norway, 8514 Narvik, Norway; bjarte.hoff@uit.no (B.H.); trond.ostrem@uit.no (T.Ø.)

* Correspondence: hussein.al-sallami@uit.no; Tel.: +47-48-665-250

† These authors contributed equally to this work.

Abstract: Capacitive power transfer (CPT) has attracted attention for on-road electric vehicles, autonomous underwater vehicles, and electric ships charging applications. High power transfer capability and high efficiency are the main requirements of a CPT system. This paper proposes three possible solutions to achieve maximum efficiency, maximum power, or conjugate-matching. Each solution expresses the available load power and the efficiency of the CPT system as functions of capacitive coupling parameters and derives the required admittance of the load and the source. The experimental results demonstrated that the available power and the efficiency decrease by the increasing of the frequency from 300 kHz to 1 MHz and the separation distance change from 100 to 300 mm. The maximum efficiency solution gives 83% at 300 kHz and a distance of 100 mm, while the maximum power solution gives the maximum normalized power of 0.994 at the same frequency and distance. The CPT system can provide a good solution to charge electric ships and underwater vehicles over a wide separation distance and low-frequency ranges.

Keywords: wireless power transfer; wireless energy transfer; capacitive coupling; network theory; underwater losses; conjugate matching; maximum efficiency; maximum power

Citation: Mahdi, H.; Hoff, B.; Østrem, T. Optimal Solutions for Underwater Capacitive Power Transfer. *Sensors* **2021**, *21*, 8233. https://doi.org/10.3390/s21248233

Academic Editors: J.-C. Chiao and Jenshan Lin

Received: 2 November 2021
Accepted: 3 December 2021
Published: 9 December 2021

1. Introduction

Wireless power transfer (WPT) is a promising alternative to conductive (wired) power transfer for on-road electric vehicles, underwater vehicles, and ship charging applications. It has the potential to provide the convenience of automatic charging through three different modes, namely, static, quasi-dynamic, and dynamic [1]. Near-field WPT technologies are the most commonly used for high-energy charging applications. In the near-field WPT, the transmitter and the receiver sizes are much smaller, and the distance between them is much shorter than the wavelength.

The main near-field WPT approaches are inductive power transfer (IPT) and capacitive power transfer (CPT). IPT has begun to receive attention for charging electric cars, buses, and trains [2]. Many manufacturers have recently started to provide wireless charging stations with power transfer capability ranges from 3.3 up to 450 kW. However, the challenges associated with IPT are electromagnetic interference (EMI) with communication systems and human safety issues, eddy current losses, bulky size, and high cost [3,4].

CPT uses the alternating electric fields confined between the coupling plates (capacitive coupler) to transfer energy between a source and a load without physical connections. It provides a cheaper and lighter alternative to IPT with a better misalignment performance. It also addresses the IPT's interaction problem with nearby metals and results in avoiding the eddy current losses and fire hazard potential. Consequently, it has been proposed for on-road electric vehicles [5–7], underwater vehicles [8–11], and ship charging applications [12–14].

In the electric vehicle charging applications, papers use an equivalent π-model to analyze and design air-gapped capacitive couplers [5–7,15]. Using this model, Orihara provides a simple formula to calculate the maximum efficiency of a CPT system using the

coupling coefficient (k), the quality factor (Q), and parameters of their extended product (kQ) [16]. Dionigi et al. [17] extend Orihara's analysis to include three possible solutions, namely, the one that maximizes the efficiency, one that maximizes the transferred power, and one that realizes power matching.

For underwater vehicles, Tamura et al. examine the efficiency of submerged CPT systems in freshwater [9,10] and seawater [11] using the same parameters that Orihara proposed. However, they do not consider the medium losses between the coupler. Moreover, they investigate the seawater at the MHz frequency range and separation distance between the couplers up to 180 mm. In contrast, Mahdi et al. study the CPT system's maximum available efficiency and power using a conjugate matching approach and consider the dissipative losses of the seawater [14]. The main contributions of this paper are:

1. It extends the analysis proposed in [14] to include three possible solutions, namely, the one that maximizes the efficiency, the one that maximizes the transferred power, and the one that realizes power matching.
2. It considers the dielectric losses of seawater, unlike the previous analysis for lossless medium in [17].
3. It investigates the under seawater CPT system behavior at the 0.3 to 1 MHz frequency range and separation distance up to 300 mm.

The analysis shows under which conditions each solution is achieved and demonstrates the reciprocal relationship between power and efficiency.

2. System Analysis

As proposed in [14], the reciprocal two-port network representation provides a general formulation for the CPT scheme. In this representation, the capacitive couplers are a black box from which only the voltages (u_1, u_2) and the currents (i_1, i_2) can be measured. The two-port model presents the admittance representations of the π-model in a matrix form, as illustrated in Figure 1. The system is assumed to be passive, linear, and reciprocal.

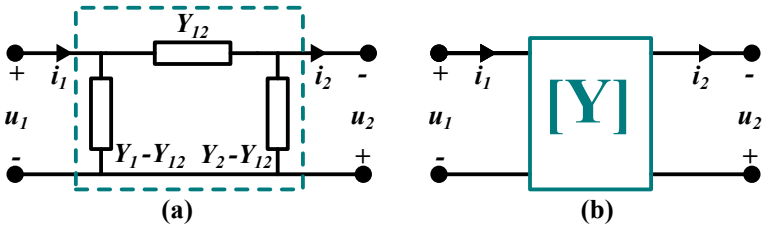

Figure 1. Network representation of CPT: (**a**) A π model. (**b**) A linear two-port network.

2.1. Passive Linear Reciprocal System

The black box model of the system contains passive components, which means there are no energy sources. Thus, the power on the receiver is less or equal to the power on the transmitter side. In addition, the system is linear as the admittance is assumed to be independent of the voltages and currents. Moreover, it is reciprocal, meaning that the transmission of the signals at any side does not depend on the direction of the propagation. The reciprocal characteristics are a result of the fundamental symmetries of Maxwell's equations. Based on these assumptions, the admittance matrix expresses the voltage-to-current relationship as:

$$\begin{bmatrix} i_1 \\ i_2 \end{bmatrix} = \begin{bmatrix} Y_1 & Y_{12} \\ Y_{12} & Y_2 \end{bmatrix} \begin{bmatrix} u_1 \\ u_2 \end{bmatrix}, \tag{1}$$

where $Y_i = g_i + jb_i$, $i = 1$, 2, or 12 is the admittance. The direction of u_2 has been reversed to achieve a positive definite matrix as noticed in Equation (1).

Figure 2a illustrates when the two-port network is connected to a source and a load. The current flows through the load is ($i_2 = -Y_L u_2$); where the negative sign is attributed to the reversed direction of the receiver voltage (u_2). By substituting this current in the

second row of the matrix, the input admittance (Y_{in}) as it is seen by the transmitter side, can be expressed as:

$$Y_{\text{in}} = Y_1 - \frac{Y_{12}^2}{Y_2 + Y_{\text{L}}}, \tag{2}$$

where Y_{L} is the load admittance at the receiver side. The input admittance replaces the two-port network and the load. The voltage gain across the coupler can be expressed:

$$G_u = -\frac{u_2}{u_1} = -\frac{Y_{12}}{Y_2 + Y_{\text{L}}} \tag{3}$$

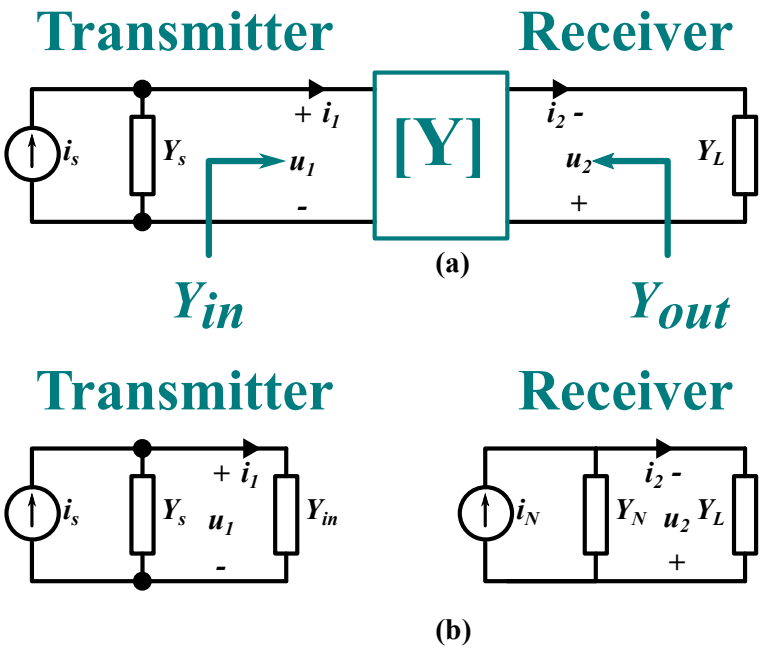

Figure 2. A general representation of CPT system: (**a**) two-port network connected to source and load. (**b**) The transmitter and receiver are equivalent circuits.

By substituting the source current ($i_{\text{s}} = Y_{\text{s}} u_1 + i_1$) in the matrix the two port model, Equation (1), can be replaced by:

$$\begin{bmatrix} i_{\text{s}} \\ i_2 \end{bmatrix} = \begin{bmatrix} Y_1 + Y_{\text{s}} & Y_{12} \\ Y_{12} & Y_2 + Y_{\text{L}} \end{bmatrix} \begin{bmatrix} u_1 \\ u_2 \end{bmatrix} \tag{4}$$

This matrix is an extended form of the matrix in the Equation (1) when the two-port network is connected to the source and the load. By applying an open circuit condition ($i_2 = 0$) in the second row and substituting the results in the first row, then the transmitter voltage can be expressed as a function of the source current:

$$u_1 = \frac{Y_2 + Y_{\text{L}}}{\Delta} i_{\text{s}}, \tag{5}$$

where $\Delta = (Y_1 + Y_{\text{s}})(Y_2 + Y_{\text{L}}) - Y_{12}^2$ is the determinant of the matrix in Equation (4). While Equation (3) shows that the voltage gain depends on the load, Equation (5) indicates that the current gain is independent of the load.

Similarly, the source and the two-port network can be replaced using the Norton equivalent circuit connected to the receiver side. The corresponding Norton equivalent at the receiver side, as illustrated in Figure 2b, can be expressed as:

$$Y_{\text{N}} = Y_{out} = Y_2 - \frac{Y_{12}^2}{Y_1 + Y_{\text{s}}} \tag{6}$$

$$i_N = \frac{Y_{12}}{Y_1 + Y_s} i_s \tag{7}$$

From Equations (3) to (7), the source power is expressed as:

$$P_s = \frac{1}{2}\mathrm{Re}(Y_s)|u_1|^2 = \frac{1}{2} g_s \left| \frac{Y_2 + Y_L}{\Delta} \right|^2 |i_s|^2 \tag{8}$$

The input power can also be expressed as:

$$P_{in} = \frac{1}{2}\mathrm{Re}(Y_{in})|u_1|^2 = \frac{1}{2} g_{in} \left| \frac{Y_2 + Y_L}{\Delta} \right|^2 |i_s|^2 \tag{9}$$

Likewise, the power transfer to the load can be defined as:

$$P_L = \frac{1}{2}\mathrm{Re}(Y_L)|u_2|^2 = \frac{1}{2} g_L \left| \frac{Y_{12}}{\Delta} \right|^2 |i_s|^2 \tag{10}$$

Then, the efficiency of the system can be expressed as:

$$\eta = \frac{P_L}{P_s + P_{in}} = \frac{\mathrm{Re}(Y_L)}{\mathrm{Re}(Y_s + Y_{in})} \left| \frac{Y_{12}}{Y_2 + Y_L} \right|^2 \tag{11}$$

Based on the previous analysis, there are three possible solutions to design the system:

(a) Maximum efficiency: determine the value of the source and the load admittance that achieve maximum efficiency.
(b) Maximum power: determine the value of the source and the load admittance that achieve maximum power transfer to the load.
(c) Conjugate-image: determine the values of the admittance that realize the principle of power matching.

2.2. Maximum Efficiency Solution

For mathematical convenience, the source is considered lossless ($g_2 = 0$), and the following expressions are defined:

$$\begin{cases} \alpha = g_1 \\ \beta = 2\,g_1\,g_2 - g_{12}^2 + b_{12}^2 \\ \gamma = 2\,g_1\,b_2 - 2\,g_{12}\,b_{12} \\ \lambda = g_1(\,g_2^2 + b_2^2\,) - g_2(\,g_{12}^2 + b_{12}^2\,) - 2\,b_2(\,g_{12}\,b_{12}\,) \\ \zeta = g_{12}^2 + b_{12}^2 \end{cases} \tag{12}$$

The Equation (11) can be rewritten as:

$$\eta = \frac{\zeta\, g_L}{\alpha(\,g_L^2 + b_L^2\,) + \beta\, g_L + \gamma\, b_L + \lambda} \tag{13}$$

In addition, defining the following two parameters for the convenience of mathematical symbols in [14]:

$$\psi^2 = \frac{g_{12}^2}{g_1\, g_2} \tag{14a}$$

$$\chi^2 = \frac{b_{12}^2}{g_1\, g_2}, \tag{14b}$$

where ψ represents the ratio between the coupling conductance and the self-conductance and χ is an equivalent to the quality factor. Another two expressions θ_G and θ_B are used, which were defined in [18] as intermediate variables, but their physical meanings are not given. The source and load admittance can be rewritten as:

$$\theta_G = \sqrt{(1-\psi^2)(1+\chi^2)} \tag{15a}$$

$$\theta_B = \psi\chi \tag{15b}$$

The maximum efficiency is achieved when $\partial\eta/\partial g_L = 0$ and $\partial\eta/\partial b_L = 0$. By solving $\partial\eta/\partial b_L = 0$, the $b_L^{(a)}$ can be calculated. This paper denotes the following: superscript (a) the parameters of the maximum efficiency solution, superscript (b) those relative to the maximum power solution, and superscript (c) those related to the conjugate-image solution. Substituting the calculated value $b_L^{(a)}$ in Equation (13), the $g_L^{(a)}$ can be calculated:

$$g_L^{(a)} = g_2\,\theta_G \tag{16a}$$

$$b_L^{(a)} = g_2\,\theta_B - b_2 \tag{16b}$$

The source admittance is expressed as:

$$Y_s^{(a)} = jb_s^{(a)} = -jb_1 \tag{17}$$

The expression for the maximum efficiency is obtained by substituting Equation (16) into (13), giving:

$$\eta^{(a)} = \frac{\psi^2+\chi^2}{(1+\theta_G)^2+\theta_B^2} \tag{18}$$

Evaluation of $|\Delta|^2$ for a given values in Equation (16) gives:

$$|\Delta|^2 = (g_1 g_2)^2\left\{\left[\theta_G(1+\theta_G)+\theta_B^2\right]^2-\theta_B^2\right\} \tag{19}$$

The maximum power available from the source can be calculated from Equation (9) as:

$$P_{s,max} = \frac{1}{8}\frac{|i_s|^2}{g_{in}} \tag{20}$$

The available power transfer to the load at the maximum efficiency can be calculated from Equation (16) and (19) into (10) as:

$$P_L^{(a)} = 4P_{s,max}\frac{(\psi^2+\chi^2)\,\theta_G}{\left[\theta_G(1+\theta_G)+\theta_B^2\right]^2+\theta_B^2} \tag{21}$$

If the loses of the seawater is neglected, then the conductance, the ψ parameter, the θ_G parameter are zeros. Then Equations (18) and (21) can be rewritten as:

$$\eta^{(a)} = \frac{\chi^2}{\left(1+\sqrt{1+\chi}\right)^2} \tag{22a}$$

$$P_L^{(a)} = 4P_{s,max}\frac{\chi^2}{\sqrt{1+\chi^2}\left(1+\sqrt{1+\chi^2}\right)^2} \tag{22b}$$

Equations (22) are the same for the lossless medium analysis reported in [17].

2.3. Maximum Power Solution

The load admittance (Y_L) that realizes maximum power transfer can be achieved in a simpler way than the procedures in Section 2.2. By using the equivalent circuit at the receiver side, which is illustrated in Figure 2b, the load admittance can be calculated using the maximum power transfer theorem. This theorem states that maximum power transfer is achieved when the Y_L is the conjugate of the output admittance expressed in Equation (6) (i.e., when the following condition is achieved $g_L = g_N$ and $b_L = -b_N$). Thus, the value $b_L^{(b)}$ and the $g_L^{(b)}$ can be calculated:

$$g_L^{(b)} = g_2 \left(\theta_G^2 + \theta_B^2 \right) \tag{23a}$$

$$b_L^{(b)} = 2\, g_2\, \theta_B - b_2 \tag{23b}$$

The source admittance can be expressed as:

$$Y_s^{(b)} = j b_s^{(b)} = -j b_1 \tag{24}$$

The expression for the maximum efficiency is obtained by substituting Equation (23) into (13), giving:

$$\eta^{(b)} = \frac{\psi^2 + \chi^2}{2\left(1 + \theta_G^2 + \theta_B^2\right)} \tag{25}$$

Evaluation of $|\,\Delta\,|^2$ for a given values in Equation (23) gives:

$$|\,\Delta\,|^2 = (\,2\, g_1\, g_2\,)^2 \left[\theta_G^2 + \theta_B^2 \right]^2 \tag{26}$$

Similarly, the available power transfer to the load at the maximum efficiency can be calculated from Equation (23) and (26) into (10) as:

$$P_L^{(b)} = P_{s,max} \frac{\psi^2 + \chi^2}{\theta_G^2 + \theta_B^2} \tag{27}$$

If the loses of the seawater is neglected, then the conductance, the ψ parameter, the θ_G parameter are zeros. Then the Equations (25) and (27) can be rewritten as:

$$\eta^{(b)} = \frac{1}{2} \frac{\chi^2}{(\,2 + \chi^2\,)} \tag{28a}$$

$$P_L^{(b)} = P_{s,max} \frac{\chi^2}{1 + \chi^2} \tag{28b}$$

Similarly, the two equations (28) are the same for the lossless medium analysis reported [17].

2.4. Conjugate-Image Solution

In this solution, the conjugate-image theorem [18] considers the input admittance as the conjugate of the source admittance ($Y_{in} = Y_s^*$), and the output admittance as the conjugate of the load admittance ($Y_N = Y_L^*$). Equations (4) and (5) are identical, if the dielectric losses of the water is neglected. In contrast, if the dielectric losses is considered, then these two Equations (4) and (5) can be solved for Y_s and Y_L. Thus, the source and load admittance can be rewritten as [14]:

$$Y_s^{(c)} = g_1\, \theta_G + \mathrm{j}(\, g_1\, \theta_B - b_1\,) \tag{29a}$$

$$Y_L^{(c)} = g_2\, \theta_G + \mathrm{j}(\, g_2\, \theta_B - b_2\,) \tag{29b}$$

If the real part of the Equation (29a) is assumed to be zero, then the expression for the maximum efficiency is obtained, which is exactly the same results of the maximum efficiency solution in the Section 2.2. Likewise, the maximum available power derived from the load is expressed in [14] is the same solution achieved in the Section 2.3.

In contrast to [14], if the real part of Equation (29a) is not neglected, which is the case (i.e., $g_s = g_1$ and $\theta_G \neq 0$), a more precise solution can be achieved. The expression for the maximum efficiency is obtained by substituting Equation (23) into (11), giving:

$$\eta^{(c)} = \frac{1}{2}\frac{\psi^2 + \chi^2}{(1+\theta_G)^2 + \theta_B^2} \tag{30}$$

Evaluation of $|\Delta|^2$ for a given value in Equation (29) gives:

$$|\Delta|^2 = (2\,g_1\,g_2)^2\left[\theta_G^2(1+\theta_G)^2 + \theta_G^2\theta_B^2\right] \tag{31}$$

The maximum available power to the load when $g_s = g_1\,\theta_G \neq 0$ becomes:

$$P_L^{(c)} = P_{s,max}\frac{\psi^2 + \chi^2}{\theta_G\left[(1+\theta_G)^2 + \theta_B^2\right]} \tag{32}$$

Again, if the losses of the seawater are neglected, then the conductance, the ψ parameter, and the θ_G parameter are zeros. Then Equations (30) and (32) can be rewritten as:

$$\eta^{(c)} = \frac{1}{2}\frac{\chi^2}{\left(1+\sqrt{1+\chi}\right)^2} \tag{33a}$$

$$P_L^{(c)} = P_{s,max}\frac{\chi^2}{\sqrt{1+\chi^2}\left(1+\sqrt{1+\chi^2}\right)^2} \tag{33b}$$

Similarly, the two equations (33) are the same for the lossless medium analysis reported [17]. Table 1 lists a summary of the three solutions.

Table 1. A summary of the three solutions.

	Maximum Efficiency	**Maximum Power**	**Conjugate-Image**
g_s	0	0	$g_1\theta_G$
b_s	$-b_1$	$-b_1$	$g_1\theta_B$
g_L	$g_2\theta_G$	$g_2(\theta_G^2+\theta_B^2)$	$g_2\theta_G$
b_L	$g_2\theta_B - b_2$	$2g_2\theta_B - b_2$	$g_2\theta_B - b_2$
		Lossy System	
P_L	$4P_{s,max}\frac{(\psi^2+\chi^2)\,\theta_G}{\left[\theta_G(1+\theta_G)+\theta_B^2\right]^2+\theta_B^2}$	$P_{s,max}\frac{\psi^2+\chi^2}{\theta_G^2+\theta_B^2}$	$P_{s,max}\frac{\psi^2+\chi^2}{\theta_G\left[(1+\theta_G)^2+\theta_B^2\right]}$
η	$\frac{\psi^2+\chi^2}{(1+\theta_G)^2+\theta_B^2}$	$\frac{1}{2}\frac{\psi^2+\chi^2}{(1+\theta_G^2+\theta_B^2)}$	$\frac{1}{2}\frac{\psi^2+\chi^2}{(1+\theta_G)^2+\theta_B^2}$
		Lossless System	
P_L	$4P_{s,max}\frac{\chi^2}{\sqrt{1+\chi^2}\left(1+\sqrt{1+\chi^2}\right)^2}$	$P_{s,max}\frac{\chi^2}{1+\chi^2}$	$P_{s,max}\frac{\chi^2}{\sqrt{1+\chi^2}\left(1+\sqrt{1+\chi^2}\right)^2}$
η	$\frac{\chi^2}{\left(1+\sqrt{1+\chi}\right)^2}$	$\frac{1}{2}\frac{\chi^2}{(2+\chi^2)}$	$\frac{1}{2}\frac{\chi^2}{\left(1+\sqrt{1+\chi}\right)^2}$

3. Calculated and Measured Results

This section provides the calculated and the measured results of the three solutions mentioned in the previous section.

3.1. Calculated Results

The normalized load power to the maximum available power from the source ($P_L / P_{s,max}$) and the efficiency of the three solutions are shown in Figure 3 as a function of ψ and χ. The results show that, for the three solutions to increase the efficiency, the χ coefficient should be increased. In particular, the mutual capacitance should be increased and the resistances should be decreased. The maximum efficiency solution gives 100% efficiency as ψ asymptotically approaches 1.

It is also clear that the power transfer capability might reduce if the system is designed to achieve maximum efficiency. This result demonstrates the reciprocal relationship between the power and the efficiency of the system. The maximum power solution can achieve 50% efficiency, but with a high power transfer range. On the other hand, the conjugate-image solution shows that if the source inductance is not zero, both the efficiency and the power transfer capability of the system decrease. However, the three solutions fail if the value of the ψ is asymptotically approaching 1.

3.2. Measurement Results

Figure 4 shows the experimental setup in which two pairs of square-shaped aluminum plates covered with a plastic lamination pouch for isolation were used. The coupling parameters were measured using a PicoVNA Vector Network Analyzer. The measurement was carried out over a distance (d) from 100 to 300 mm and a frequency range from 300 kHz to 1 MHz in seawater collected from the local harbor. Equation (14) is used to calculate the two coefficients ψ and χ from the measured parameters.

Figure 5 shows the two parameters ψ and χ with the change of the separation distance between the plates and the change of the frequency. Both parameters reduce with the increase in the separation distance, as the susceptance (b_{12}) decreases. Figure 5a shows that the ψ cannot be neglected over the frequency or the distance ranges. Thus, if the analysis for a lossless system is considered, then imprecise results are achieved.

In Figure 5b, the parameter χ decreases with the increase in the distance and the frequency ranges. As χ decreases, it is expected from Figure 3 that the efficiency will also decrease. Figure 6a depicts the change of the efficiency of the three solutions with the change of the distance and frequency. The efficiency of the system decreases with both the increase in the distance and the frequency. The maximum efficiency solution gives the highest efficiency of about 83% at 300 kHz and 100 mm. Both the maximum power and conjugate-image solutions give about half of the maximum efficiency solutions.

Figure 6 also shows the normalized power of the three solutions versus frequency and distance. The maximum power solutions have higher normalized power transfer capability as expected. The maximum normalized power at 100 mm distance and at 300 kHz is 0.994 and decreases to 0.976 at 1 MHz. The maximum efficiency solution gives a higher normalized power solution than the conjugate-image one, as shown in Figure 3. The increase in the normalized power of the later two solutions with the increase of the frequency is caused by the increase of the ψ parameter, as shown in Figure 5a.

Dionigi et al. [17] previously studied the three solutions for non-dissipative CPT systems where the dielectric of the medium is neglected. The analysis in that study works for air-gapped CPT systems but not for underwater ones. Due to the dissolved ions in the seawater, the conductivity of the water causes the losses, as shown in Figure 5b. Figure 7 depicts the relationship between the efficiency and normalized power of the underwater CPT for both dissipative (lossy) analysis and non-dissipative (lossless) analysis. It is clear that, regardless that the difference between them is small, the medium losses should be considered in the design of the system to obtain more accurate results.

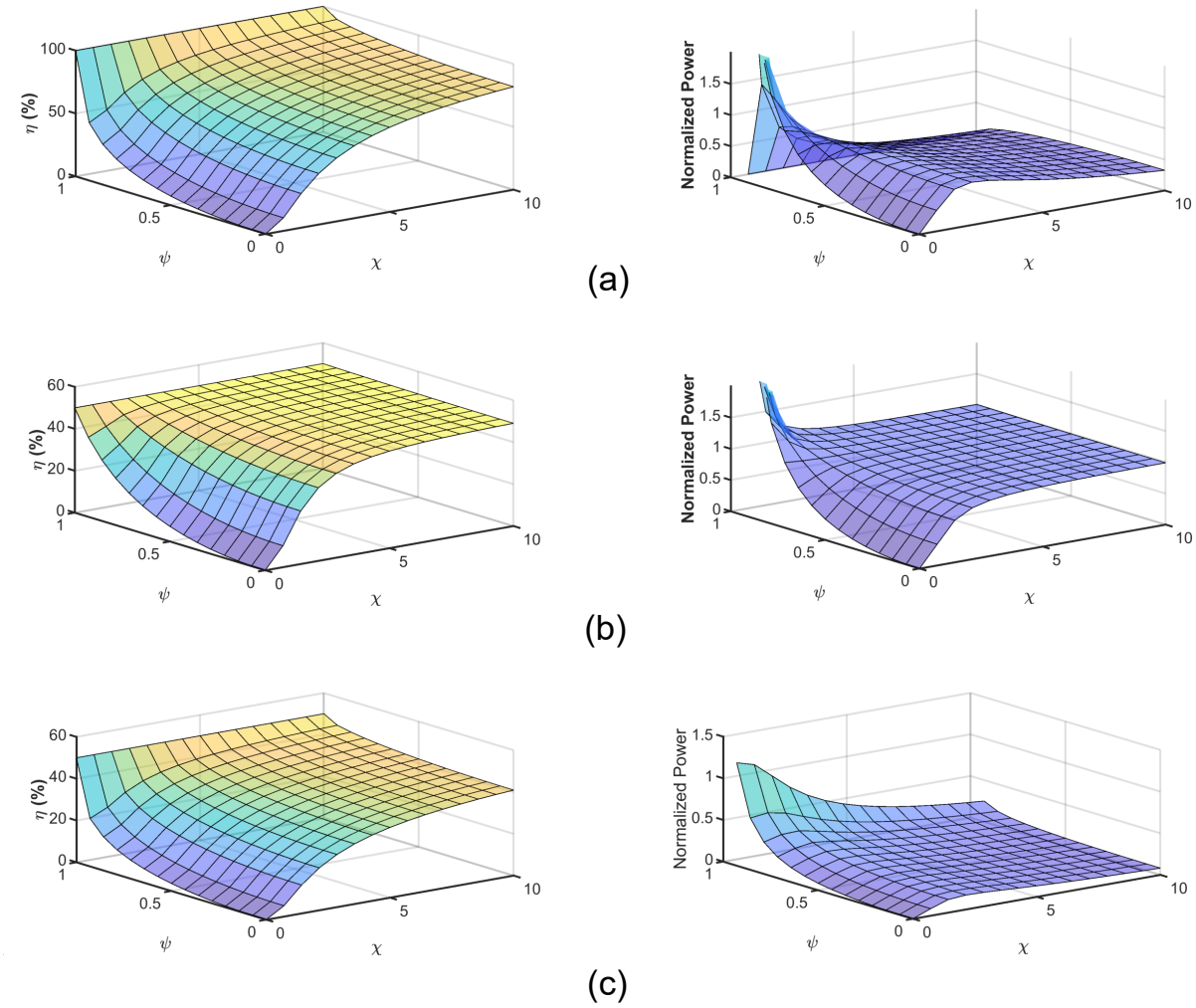

Figure 3. The efficiency of CPT system: (**a**) Maximum efficiency solution. (**b**) Maximum power solution. (**c**) Conjugate-image solution.

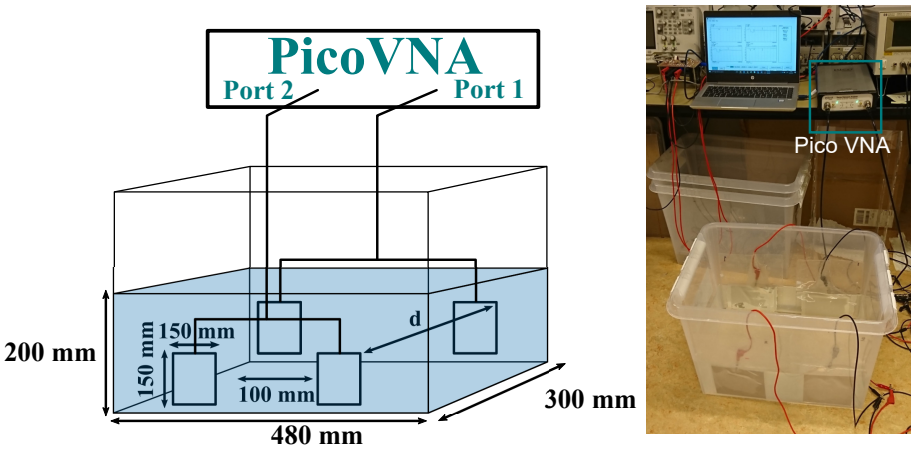

Figure 4. The measurement setup [14].

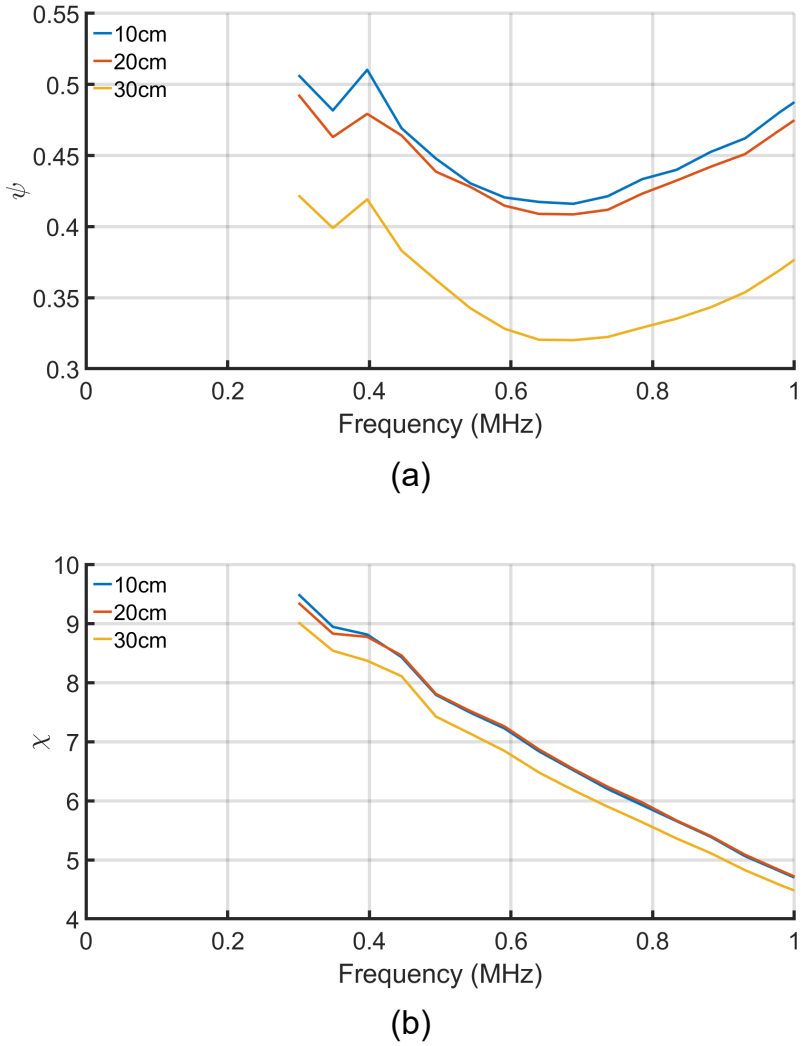

Figure 5. The measured ψ and χ versus the separation distance and the frequency: (**a**) The ψ coefficient. (**b**) The χ coefficient.

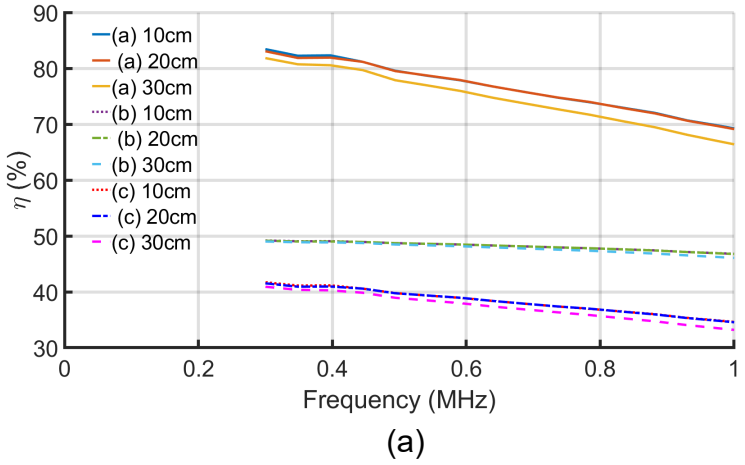

Figure 6. *Cont.*

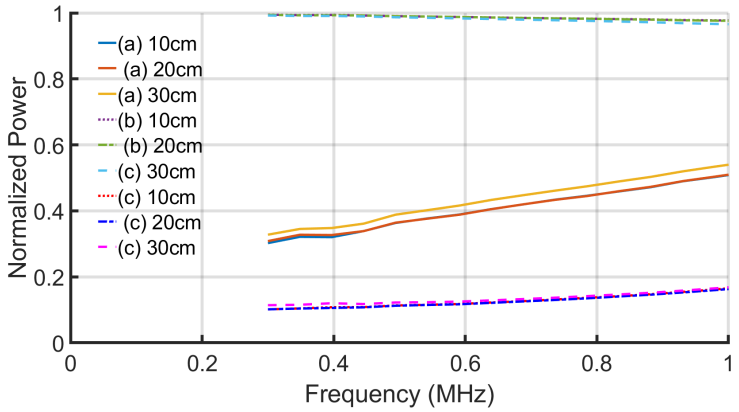

(b)

Figure 6. The efficiency and normalized power versus the separation distance and the frequency: (a) Maximum efficiency solution. (b) Maximum power solution. (c) Conjugate-image solution.

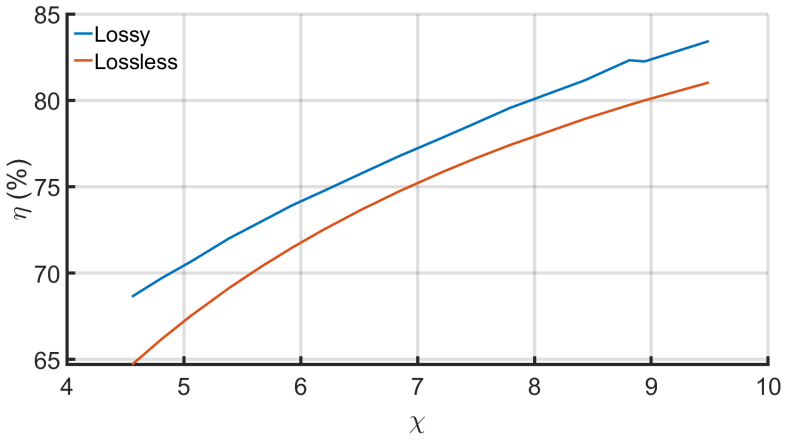

(a)

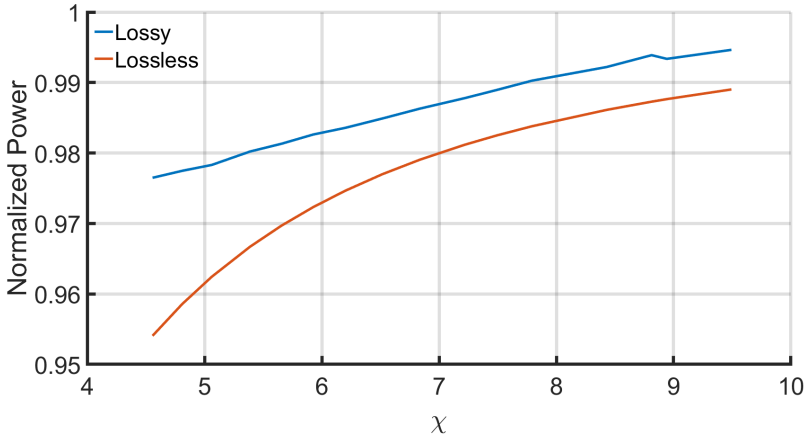

(b)

Figure 7. The efficiency and normalized power versus χ for lossy and lossless solutions: (**a**) Maximum efficiency solution. (**b**) Maximum power solution.

4. Discussion

This section discusses the results of the three proposed solutions: maximum efficiency, maximum power, and conjugate-image solutions. The parameters ψ and χ are the main factors based on which the three solutions are proposed and, hence, they should be discussed thoroughly. The frequency of the electric fields and the distance between plates affect the conductance and the admittance of the underwater seawater couplers and, hence, affect the values of both ψ and χ.

4.1. The Parameters ψ and χ

The parameters ψ^2 and χ^2, which are expressed in Equation (14), are equivalent to the k-coefficient and Q-factor that are defined in [16], respectively. Specifically, the parameter $\psi^2 = k_1 k_2$ where $k_1 = g_{12}/g_1$ and $k_2 = g_{12}/g_2$ are the normalized conductance, while the parameter $\chi^2 = k_1 k_2 Q^2$ where Q is the quality factor. Although the paper used the parameters ψ and χ that are equivalent to the k and Q factors proposed in [16], the analysis in this paper provides three different solutions while the kQ-factor approach only focuses on the maximum available efficiency.

The analysis in this paper can become meaningless if negative resistances are present. For instance, if g_1, g_2 are negative the system operates as oscillator [18]. The negative terminal resistance is also possible if ψ is asymptotically approach unity, as shown in Figure 3. Specifically, $g_{12}^2 > g_1 g_2$ results in a negative θ_G and, hence, negative terminal resistance. Thus, the sign of the coefficient θ_G can be an indicator to whether or not the system is potentially an oscillator [18]. For a pure non-dissipative system with pure admittance coefficients in Equation (1), the coupling coefficient ($\kappa = Y_{12}/\sqrt{Y_1 Y_2} = C_{12}/\sqrt{C_1 C_2}$) is used to express the degree of coupling in the loosely coupled system. This parameter has a value between zero and unity. In such a system, the power output must equal the power input.

4.2. The Frequency Effect

Seawater has high conductivity caused by the dissolved salts presents as cations (Na^+, Mg^{2+}, Ca^{2+}, and K^+), and anions (Cl^- and SO_4^{2-}) [19]. A water molecule is a polar molecule directed along a symmetry axis with its negative endpoints at the oxygen atom and its positive endpoints at the hydrogen atoms [20]. When the external electric fields act on the water molecules, the permanent dipoles experience torques that reorient them along the direction of the electric field. Thus, the water becomes polarized, and the polarization is proportional to the applied field [21].

The plates attract the oppositely charged ions results in the adsorption of the anions and the cations to the oppositely charged electrodes. The adsorbed ions form a layer near the surface of the electrode, known as the "Helmholtz layer". The probability of formation of this layer in seawater is high due to the high concentration of the ions. At a low frequency, forming this layer reduces the conductance, which explains the reduction of the ψ shown in Figure 5b. However, with the increase in the frequency, the plates' polarity changes fast, causing the dissolved ions' fast mobility, increasing the seawater's mutual conductivity.

Water has higher relative permittivity than air, meaning submerging the coupling capacitor in water increases the capacitance. The polarization also causes accumulations of bound charges (electron charges) within the water and on the surfaces of the electrodes. These charges produce electric fields in opposition of the applied field, which causes the increase in the mutual- and self-capacitance and, hence, the admittance. Moreover, the effects of the fringing fields increase the capacitance. Nevertheless, the rate of the increase in mutual-susceptance (b_{12}) is less than the product of the conductance ($g_{11} \cdot g_{22}$) with the increasing of the frequency, which results in decreasing the χ parameter, as shown in Figure 5b.

The calculated results showed that the efficiency increases with the increase of both the parameters ψ and χ, as shown in Figure 3. Thus, the efficiency can be improved by decreeing the frequency, as depicted in Figure 6a. Likewise, the maximum available

power at the load increases with the parameters ψ and χ. As a result, more power can be transferred to the load at a low-frequency range if the maximum power transfer solution is followed. In contrast, if the maximum power transfer of the conjugate-image solutions is considered, then increasing the frequency improves the power transfer capability of the system, as shown in Figure 6b.

The previous studies suggested MHz frequency ranges for the CPT systems for underwater autonomous underwater vehicles [9–11] or underwater electric ship [12] charging applications. However, the three solutions showed that the increase in frequency could degrade the system efficiency and/or power transfer capabilities.

4.3. The Distance Effect

The distance between the plates at the same side (the transmitter or the receiver side) is fixed to 100 mm, as shown in Figure 4. Thus, the change conductance (g_{11} & g_{22}) is almost negligible. At the same time, the distance between the transmitter and the receiver plates (d) is changed over a range of 100 to 300 mm, resulting in decreasing the conductance (g_{12}). As a result, the parameter ψ decreases with the increase of the transfer distance, as shown in Figure 5a. In contrast, the change in the distance has a negligible effect on the mutual susceptance (b_{12}), as shown in Figure 5b. As the χ is the critical parameter in calculating the available power and the system efficiency, the difference between the results of the three solutions with the change of the distance is negligible, as shown in the overlapped lines in Figures 6 and 7.

5. Conclusions

This paper investigated a dissipative capacitive power transfer (CPT) system submerged in seawater using three solutions: maximum efficiency solution, maximum power solution, and conjugate-matching solution. The available load power and the efficiency were expressed as functions of capacitive coupling parameters. The experimental results showed that the available power decreased by the increasing of the frequency from 0.3 to 1 MHz and the separation distance change from 100 to 300 mm in the maximum available power solution. The maximum power solution gave the maximum normalized power of 0.994 at 300 kHz and a 100 mm distance. Likewise, the maximum efficiency was 83%, which was achieved using the maximum efficiency solution at the same frequency and distance. The efficiency was degraded when the frequency and the distance increased to 1 MHz. The CPT system can be a good solution for underwater wireless charging applications over a wide separation distance and low-frequency range.

Author Contributions: Conceptualization, H.M.; methodology, H.M.; validation, H.M., B.H. and T.Ø.; formal analysis, H.M.; investigation, H.M.; resources, H.M.; data curation, H.M.; writing—original draft preparation, H.M.; writing—review and editing, H.M. and B.H.; visualization, H.M.; supervision, B.H. and T.Ø.; project administration, B.H.; funding acquisition, B.H. All authors have read and agreed to the published version of the manuscript.

Funding: This research received no external funding.

Institutional Review Board Statement: Not applicable.

Informed Consent Statement: Not applicable.

Data Availability Statement: The data presented in this study are available on request from the corresponding author.

Conflicts of Interest: The authors declare no conflict of interest.

Abbreviations

The following abbreviations are used in this manuscript:

WPT	wireless power transfer
IPT	inductive power transfer
CPT	capacitive power transfer
EMI	electromagnetic interference

References

1. Ahmad, A.; Alam, M.S.; Chabaan, R. A Comprehensive Review of Wireless Charging Technologies for Electric Vehicles. *IEEE Trans. Transp. Electrif.* **2018**, *4*, 38–63. [CrossRef]
2. Covic, G.A.; Boys, J.T. Modern Trends in Inductive Power Transfer for Transportation Applications. *IEEE J. Emerg. Sel. Top. Power Electron.* **2013**, *1*, 28–41. [CrossRef]
3. Lu, F.; Zhang, H.; Mi, C. A Review on the Recent Development of Capacitive Wireless Power Transfer Technology. *Energies* **2017**, *10*, 1752. [CrossRef]
4. Mei, Y.; Wu, J.; He, X. Common Mode Noise Analysis for Inductive Power Transfer System Based on Distributed Stray Capacitance Model. *IEEE Trans. Power Electron.* **2022**, *37*, 1132–1145. [CrossRef]
5. Zhang, H.; Lu, F.; Hofmann, H.; Liu, W.; Mi, C.C. A Four-Plate Compact Capacitive Coupler Design and LCL-Compensated Topology for Capacitive Power Transfer in Electric Vehicle Charging Application. *IEEE Trans. Power Electron.* **2016**, *31*, 8541–8551. [CrossRef]
6. Lu, F.; Zhang, H.; Mi, C. A Two-Plate Capacitive Wireless Power Transfer System for Electric Vehicle Charging Applications. *IEEE Trans. Power Electron.* **2018**, *33*, 964–969. [CrossRef]
7. Lu, F.; Zhang, H.; Hofmann, H.; Mi, C.C. A Double-Sided LC-Compensation Circuit for Loosely Coupled Capacitive Power Transfer. *IEEE Trans. Power Electron.* **2018**, *33*, 1633–1643. [CrossRef]
8. Urano, M.; Ata, K.; Takahashi, A. Study on underwater wireless power transfer via electric coupling with a submerged electrode. In Proceedings of the IMFEDK 2017—2017 International Meeting for Future of Electron Devices, Kansai, Kyoto, Japan, 29–30 June 2017; pp. 36–37. [CrossRef]
9. Tamura, M.; Naka, Y.; Murai, K.; Nakata, T. Design of a Capacitive Wireless Power Transfer System for Operation in Fresh Water. *IEEE Trans. Microw. Theory Tech.* **2018**, *66*, 5873–5884. [CrossRef]
10. Tamura, M.; Naka, Y.; Murai, K. Design of capacitive coupler in underwater wireless power transfer focusing on kQ product. *IEICE Trans. Electron.* **2018**, *E101C*, 759–766. [CrossRef]
11. Tamura, M.; Murai, K.; Matsumoto, M. Design of Conductive Coupler for Underwater Wireless Power and Data Transfer. *IEEE Trans. Microw. Theory Tech.* **2021**, *69*, 1161–1175. [CrossRef]
12. Zhang, H.; Lu, F. Insulated Coupler Structure Design for the Long-Distance Freshwater Capacitive Power Transfer. *IEEE Trans. Ind. Inform.* **2020**, *16*, 5191–5201. [CrossRef]
13. Mahdi, H.; Hoff, B.; Ostrem, T. Evaluation of Capacitive Power Transfer for Small Vessels Charging Applications. *IEEE Int. Symp. Ind. Electron.* **2020**, *2020*, 1605–1610. [CrossRef]
14. Mahdi, H.; Hoff, B.; Østrem, T. Maximum Available Power of Undersea Capacitive Coupling in a Wireless Power Transfer System. In Proceedings of the 2021 IEEE Wireless Power Transfer Conference (WPTC), San Diego, CA, USA, 1–4 June 2021; pp. 1–4. [CrossRef]
15. Lecluyse, C.; Minnaert, B.; Kleemann, M. A Review of the Current State of Technology of Capacitive Wireless Power Transfer. *Energies* **2021**, *14*, 5862. [CrossRef]
16. Ohira, T. Extended k-Q product formulas for capacitive- and inductive-coupling wireless power transfer schemes. *IEICE Electron. Express* **2014**, *11*, 20140147. [CrossRef]
17. Dionigi, M.; Mongiardo, M.; Monti, G.; Perfetti, R. Modelling of wireless power transfer links based on capacitive coupling. *Int. J. Numer. Model. Electron. Netw. Devices Fields* **2017**, *30*, e2187. [CrossRef]
18. Roberts, S. Conjugate-Image Impedances. *Proc. IRE* **1946**, *34*, 198p–204p. [CrossRef]
19. Sverdrup, K.A.; Duxbury, A.B.; Duxbury, A. *An Introduction to the World's Oceans*; McGraw-Hill Higher Education: New York, NY, USA, 2005; pp. 149–150.
20. Griffiths, D. *Introduction to Electrodynamics*, 3rd ed.; Pearson: London, UK, 2008.
21. Jackson, J. *Classical Electrodynamics*, 3rd ed.; John Wiley & Sons: Hoboken, NJ, USA, 1999.

6

Under seawater Capacitive Power Transfer for Maritime Charging Applications

Hussein Mahdi, Reiji Hattori, Bjarte Hoff, and Trond Østrem

DOI: To be submitted

Paper's Contribution

Submerging the capacitive couplers under seawater results in high capacitive coupling due to the high permittivity of water. The conductive coupling because of the dissolved ions in the water is a challenge that faces the underwater CPT systems. The main contributions of the paper are: (1) It proposes and validates a mathematical model to calculate the maximum achievable efficiency of the underwater CPT system considering the dielectric losses of the medium and the compensation circuits, and (2) it examines the effect of changing separation distance and switching frequency on the transmitted power and the overall efficiency.

Under seawater Capacitive Power Transfer for Maritime Charging Applications

1st Hussein Mahdi
Department of Electrical Engineering
UiT - The Arctic University of Norway
Narvik, 8514, Norway
hussein.al-sallami@uit.no

2nd Reiji Hattori
Department of Applied Science
for Electronics and Materials (ASEM)
Kyushu University
Fukuoka, 816-8580 Japan
hattori@gic.kyushu-u.ac.jp

3rd Bjarte Hoff
Department of Electrical Engineering
UiT - The Arctic University of Norway
Narvik, 8514, Norway
bjarte.hoff@uit.no

4th Trond Østrem
Department of Electrical Engineering
UiT - The Arctic University of Norway
Narvik, Norway
trond.ostrem@uit.no

***Abstract*—Underwater capacitive power transfer (CPT) can provide an inexpensive and light charging solution with good misalignment tolerance for charging unmanned maritime vehicles. This paper investigates the effect of the changing of the frequency and the distance on the power transfer and overall efficiency of the underwater CPT system, considering the dielectric losses of the medium. It also proposed and validate a mathematical model for calculating the maximum available efficiency of the system. Using series compensations, the proposed CPT can transfer 48 W at 500 mm, 48 V input voltage, 516 kHz, and 54%.**

***Index Terms*—Underwater structures, marine vehicles, wireless charging, capacitive power transfer, maximum efficiency**

I. Introduction

Unmanned maritime vehicles (UMVs) have attracted considerable attention in recording oceanographic observations, studying climate change, and observing marine pollution. They can operate autonomously in challenging and hazardous shallow or deep water [1]. Both surface and underwater UMVs have been extensively used in marine exploitation investigation and emergency search rescue [2], [3]. Powered by lithium-ion batteries, these vehicles profile up hundreds to thousands of kilometers of the ocean vertically or horizontally under remote control over months [4].

Charging infrastructure can play a critical role in the development of battery-powered autonomous UMVs. Battery-swapping, wired charging, and wireless charging are three main charging approaches that can be adapted for charging maritime vehicles. Batteries swapping is time-consuming and requires human intervention, which losing their autonomy. Wired charging techniques are another approach that can be achieved manually or automatically. Automatically, various robotic docking and latching mechanism are proposed for both unmanned surface vehicles (USVs) [5] and autonomous underwater vehicles (AUVs) [6]. However, these techniques require high-precision connection mechanisms, which increase the design complexity and overall price of the system [7].

Wireless power transfer (WPT) technologies can provide autonomous charging without mechanical contact between the power source and maritime vehicles or ships. Inductive power transfer (IPT) uses inductive coupling to wirelessly charge AUVs [8]–[11]. However, the proposed IPT systems can transfer power over a distance range of tens of millimeters to reduce the underwater eddy current losses. Besides, the systems comprise heavy, expensive, and fragile parts. Capacitive power transfer (CPT) is another WPT technology that utilizes electric fields to transfer power. It is an inexpensive and light charging solution with good misalignment tolerance.

Tamura et al. [12], [13] proposed underwater CPT systems for charging USVs. In [12], they transferred $400\,\mathrm{W}$ power under freshwater over $20\,\mathrm{mm}$ distance at $10.77\,\mathrm{MHz}$ and ac-ac efficiency exceeding 90%. While in [13], they designed under seawater CPT system that can transfer data and $100\,\mathrm{W}$ power under freshwater over $20\,\mathrm{mm}$ distance at $6.78\,\mathrm{MHz}$ and ac-ac efficiency exceeding 90%. Operating at a high-frequency range increases the complexity of the design and increases the losses at wide separation distances. This paper will investigate the effect of the changing of the frequency and the distance on the power transfer and overall efficiency of the under seawater CPT system, considering the dielectric losses of the medium. It will examine the horizontal and vertical four-plate structure to reduce the cross-coupling effect and improve the system's transferability and efficiency.

The rest of the paper is organized as follows: Section III introduces simple optimization criteria using a two-port approach to achieve maximum power transfer efficiency. Compensation circuits are analyzed in section **??**. Section III presents the experimental results. Finally, Section IV concludes the work.

II. Modeling Approach

The two-port network is a general formulation for the CPT scheme in which the capacitive couplers can be modeled as

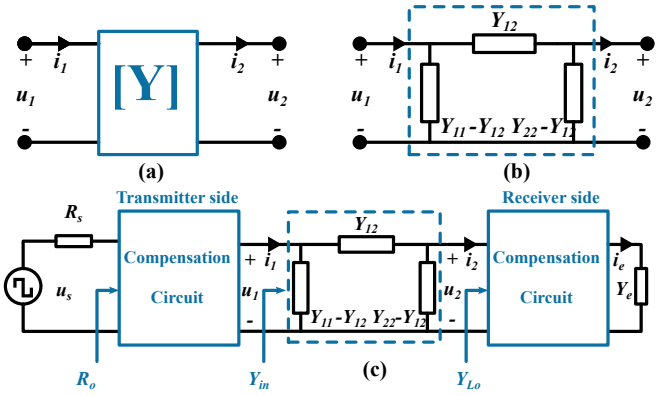

Fig. 1. The two-port network model of CPT system.

a black box from which only the voltages (u_1, u_2) and the currents (i_1, i_2) can be measured, as shown in Fig. 1(a). The two-port network comprises the capacitive coupling parameters, which can be modeled using the conventional CPT π-network model, as illustrated in Fig. 1(b). The relationship between the input current and voltage to the output current and voltage can be expressed as

$$\begin{bmatrix} u_1 \\ i_1 \end{bmatrix} = \begin{bmatrix} A & B \\ C & D \end{bmatrix} \begin{bmatrix} u_2 \\ i_2 \end{bmatrix} = \begin{bmatrix} \frac{Y_{22}}{Y_{12}} & \frac{1}{Y_{12}} \\ \frac{Y_{11}Y_{22}-Y_{12}^2}{Y_{12}} & \frac{Y_{11}}{Y_{12}} \end{bmatrix} \begin{bmatrix} u_2 \\ i_2 \end{bmatrix} \tag{1}$$

This mathematical representation is more convenient when the capacitive two-port network is cascaded with other networks, such as the compensation circuits, as shown in Fig. 1(c). The determinant of the matrix is unity. For a lossless CPT system (i.e., the dielectric medium between the couplers is lossless), A and D are purely real, while B and C are pure imaginary values. If the CPT system is symmetric (i.e., $Y_1 = Y_2$), then $A = D$.

In Fig. 1(c), the source resistor R_s represents the sum of the turn-on resistance of the switches in the inverter and the losses in the compensation circuit of the transmitter side. The resistor R_i represents the overall resistance of the CPT system seen by the source. The admittance Y_in represents the admittance at the transmitter side, while the admittance Y_out is the admittance at the receiver side. Finally, the admittance Y_e is the effective admittance of the load seen from the input of a rectifier. The input and output admittances can be expressed as

$$Y_\mathrm{in} = Y_{11} - \frac{Y_{12}^2}{Y_{22} + Y_\mathrm{Lo}} \tag{2}$$

$$Y_\mathrm{out} = Y_{22} - \frac{Y_{12}^2}{Y_{11} + Y_\mathrm{Lo}}, \tag{3}$$

where Y_Lo is the total admittance of the load and receiver compensation seen from the capacitive coupler.

The input power can be expressed as

$$P_\mathrm{in} = |u_1|^2 \,\mathrm{Re}(Y_\mathrm{in}) = \frac{|u_\mathrm{s}|^2 R_\mathrm{i}}{(R_\mathrm{i} + R_\mathrm{s})^2}, \tag{4}$$

where R_i represents the load, the dielectric losses in the seawater, and the losses in the compensation circuit of the receiver side seen by the transmitter side. Using (4), the normalized input voltage of the CPT two-port network can be written as

$$\left|\frac{u_1}{u_\mathrm{s}}\right|^2 = \frac{1}{\mathrm{Re}\,(Y_\mathrm{in})} \frac{R_\mathrm{i}}{(R_\mathrm{i} + R_\mathrm{s})^2} \tag{5}$$

The voltage gain across the network is

$$\left|\frac{u_2}{u_1}\right|^2 = \left|\frac{Y_{12}}{Y_{22} + Y_\mathrm{out}}\right|^2, \tag{6}$$

From (5) and (6), the normalized output voltage of the network can be expressed

$$\left|\frac{u_{22}}{u_\mathrm{s}}\right|^2 = \frac{1}{\mathrm{Re}\,(Y_\mathrm{in})} \frac{R_\mathrm{i}}{(R_\mathrm{i} + R_\mathrm{s})^2} \left|\frac{Y_{12}}{Y_{22} + Y_\mathrm{out}}\right|^2, \tag{7}$$

Using (7), the efficiency of the CPT considering the source losses can be express

$$\eta = \frac{R_\mathrm{i}}{R_\mathrm{i} + R_\mathrm{s}} \frac{\mathrm{Re}\,(Y_\mathrm{out})}{\mathrm{Re}\,(Y_\mathrm{in})} \left|\frac{Y_{12}}{Y_{22} + Y_\mathrm{out}}\right|^2, \tag{8}$$

Defining the following two parameters for the convenience of mathematical symbols:

$$\psi^2 = \frac{g_{12}^2}{g_{11}\, g_{22}} \tag{9a}$$

$$\chi^2 = \frac{b_{12}^2}{g_{11}\, g_{22}}, \tag{9b}$$

where g_{12} is the conductance, b is the susceptance, ψ represents the ratio between the coupling conductance and the self-conductance, and χ is equivalent to the multiplication of the quality factor and the coefficient of coupling (i.e., $\chi \approx k\,Q$).

The maximum efficiency is achieved when $\partial\eta/\partial g_\mathrm{out} = 0$ and $\partial\eta/\partial b_\mathrm{out} = 0$. First, $\partial\eta/\partial b_\mathrm{out} = 0$ is solved to optain

$$b_\mathrm{out} = g_2\,(\psi\,\chi) - b_2, \tag{10}$$

Substituting the value for (10) into $\partial\eta/\partial g_\mathrm{out} = 0$ gives

$$g_\mathrm{out} = g_2\,\sqrt{(\,1-\psi^2\,)\,(\,1+\chi^2\,)} \tag{11}$$

Then substituting both (10) and (10) into (8) gives

$$\eta_{max} = \frac{1}{1+a} \frac{\psi^2 + \chi^2}{\left(1 + \sqrt{(\,1-\psi^2\,)\,(\,1+\chi^2\,)}\right)^2 + (\psi\,\chi)^2}, \tag{12}$$

where $a = R_\mathrm{s}/R_\mathrm{i}$ normalized source resistance to the overall resistance of the CPT system seen by the source. The first term in (12) represents the efficiency of the source and the compensation circuit on the transmitter side. The second term represents the maximum available efficiency of the capacitive coupling network similar to the one reported in [14].

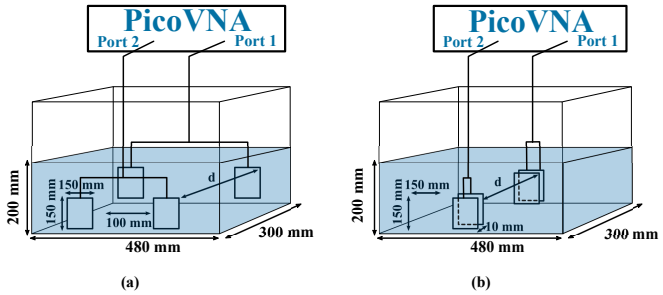

Fig. 2. The test setups: (a) Horizontal four plates configuration. (b) Vertical four plates configuration.

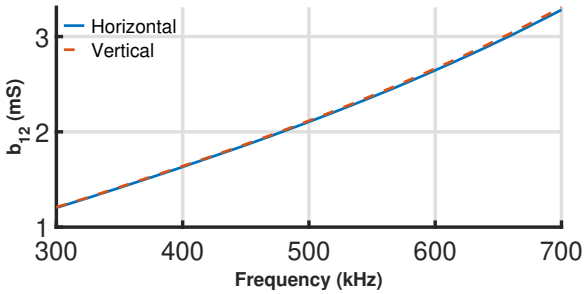

Fig. 3. The coupling susceptance under seawater for horizontal and vertical configurations.

If the parameter is unity (i.e., $R_s = R_i$), then maximum available power is achieved at 50% of maximum system efficiency similar to the solution in [14]. For a lossless medium, such as in an air-gapped CPT system, the (12) become

$$\eta^*_{max} = \frac{1}{1+a}\frac{\chi^2}{\left(1+\sqrt{(1+\chi^2)}\right)^2}, \tag{13}$$

Compared maximum efficiency of the lossless CPT system reported in [15], then χ represents the kQ product as mentioned previously in this section.

III. Experimental Results

Four 150 × 150 × 30 mm aluminum plates are used as capacitive couplers. The plates are insulated from water using a plastic lamination pouch and submerged in 480 × 300 × 200 mm seawater that is collected seawater from the local harbor. Using a Pico Vector Network Analyzer, the underwater admittance is measured at a distance (d) 300 mm for both horizontal and vertical configurations, as illustrated in Fig 2.

Fig. 3 shows the susceptance underwater as a function of frequency. The susceptances are linearly proportional to the frequency for horizontal and vertical configurations. The slopes of the lines are the coupling capacitance underwater. The coupling capacitance underwater is constant for both configurations over the frequency range.

Similarly, Fig. 4 presents the conductances underwater as a function of frequency. The conductances are ten times lower than the susceptances at the frequency ranges. The increase in the conductances with the increase of the frequency is attributed to the parasitic conductances of the wires that connect the plates to the VNA cables. Operating at low-frequency ranges reduces the conductive coupling under seawater, enhancing overall efficiency. The conductive coupling g_{12} of the vertical configuration has higher values than the horizontal one. The overall area of the horizontal configuration is higher than the vertical one, resulting in high conductive parameters.

The changing of the parameter ψ^2 with the frequency for horizontal and vertical configurations is shown in Fig. 5. The vertical configuration has higher values than the horizontal one as the conductive coupling g_{12} values of the vertical configuration are higher than the horizontal one. In contrast,

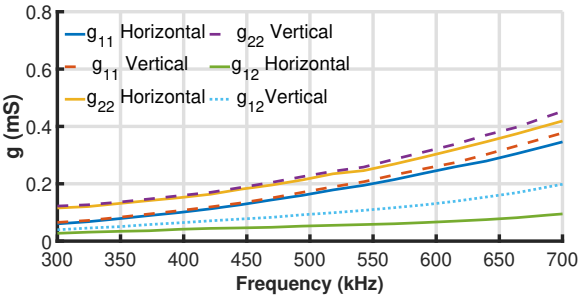

Fig. 4. The conductance of the under seawater coupling.

Fig. 6 shows that the parameter χ^2 increases with the decrease of the frequency for horizontal and vertical configurations. Although both the coupling susceptance and conductances decrease with the increase of the frequency, the rate of decrease in the conductive parameters in the denominator in (9b) is faster than the numerator making the parameter χ^2 linearly increase with the decrease of the frequency. As the χ asymptotically approaches infinity, the efficiency approaches 100% according to (12).

Using the relationship in (12), Fig. 7 shows the efficiency of the underwater capacitive coupling over a frequency range 300 kHz to 700 kHz. The underwater couplers have higher efficiency at lower frequency ranges. Although the vertical configuration has higher values of the parameter ψ^2 than the horizontal one, both vertical and horizontal configurations

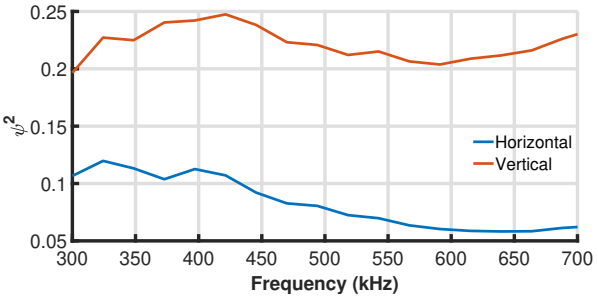

Fig. 5. The ψ of underwater capacitive coupling plates.

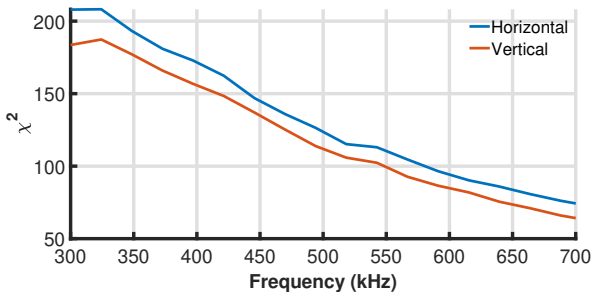

Fig. 6. The χ of underwater capacitive coupling plates.

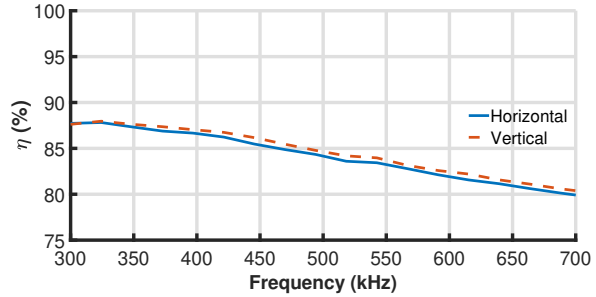

Fig. 7. The efficiency of underwater capacitive coupling plates.

have very close values of efficiency. This is attributed to the parameter χ^2, which is the key parameter to achieve highly efficient coupling at frequency range 300 kHz to 700 kHz, as the coupling conductivity is very low.

For experimental convenience, the vertical configuration will be further examined. Series compensation circuits are used. A GaN bridge inverter (Infineon EVAL1EDFG1HBGAN [16]) inverts the dc voltage into square-waveform, which is modeled as a square-wave voltage source in Fig. 1. Four Schottky diodes (C6D04065A [17]) are used to build a diode bridge that rectifies the ac transmitted power to dc. The overall CPT system configuration is illustrated in Fig. 8. PA2203A IntegraVision Power Analyzer is used to measure the output power and the dc-dc efficiency of the system.

The effect of the separation distance on the transmitted power and overall system efficiency is examined at 409 kHz and 48 Vdc input voltage. Fig. 9 shows the change in the output power and the overall efficiency of the system with the change in the separation distance. The output power and efficiency are not changing significantly with the changing of the separation distance between the transmitter and receiver couplers. When the separation distance increase from 50 mm to 500 mm, the efficiency increases from 43.5% to 44.7% while the output power decreases from about 30 W to 27 W. The enhancement in the efficiency is attributed to the decrease of the coupling conductance, and hence the parameter χ^2, with the increase of the separation distance as explained in [18].

Similarly, the effect of the operating frequency on the transmitted power and overall system efficiency is examined at the frequency ranges about 200 kHz to 700 kHz. Fig. 10

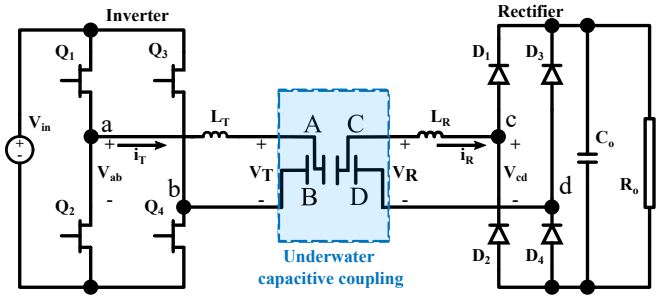

Fig. 8. The converter configuration of underwater CPT system.

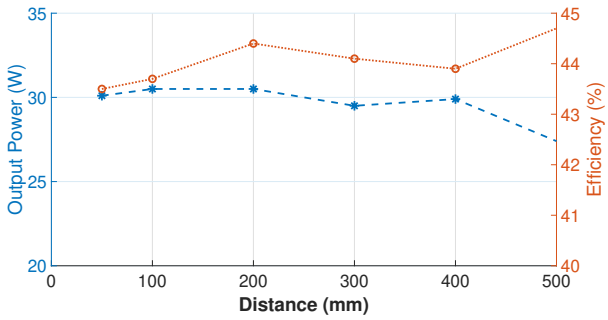

Fig. 9. The changing of the output power and overall system efficiency with changing the separation distance.

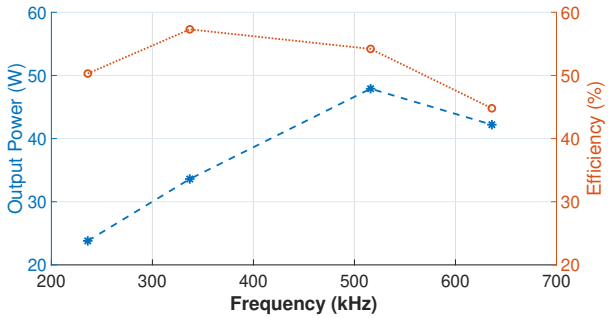

Fig. 10. The changing of the output power and overall system efficiency with changing of the operating frequency.

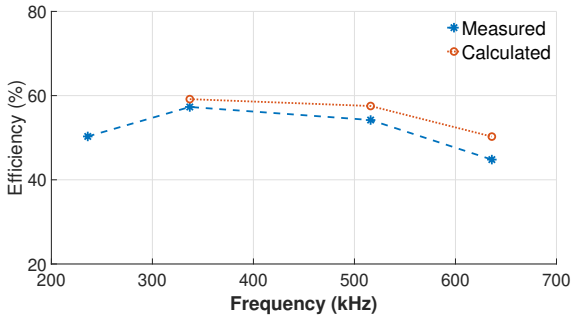

Fig. 11. The calculated and measured efficiencies with the change of the frequencies.

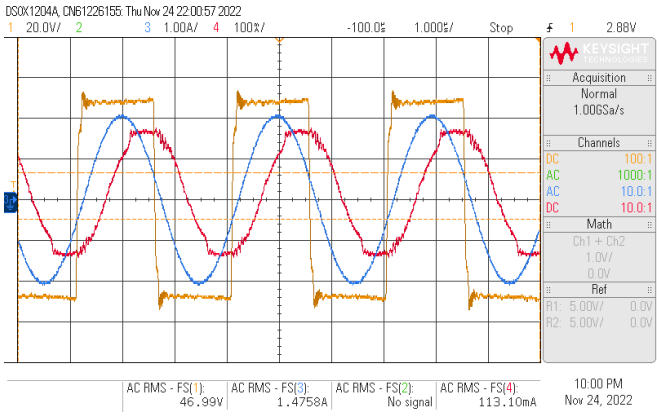

Fig. 12. The waveforms at maximum efficiency: the output voltage of the inverter V_{ab} (yellow), the transmitter current i_{T} (blue), and the receiver current i_{R} (red).

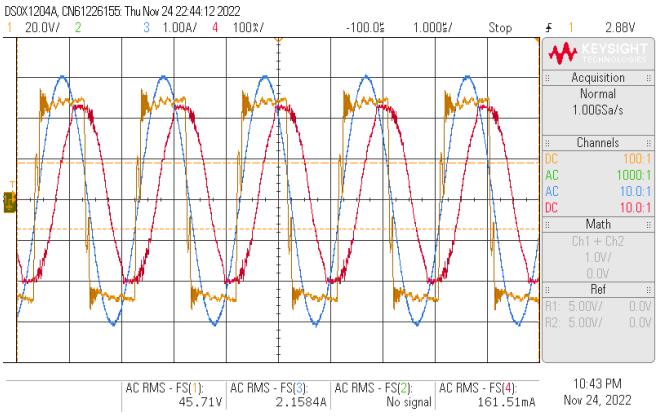

Fig. 13. The waveforms at maximum power: the output voltage of the inverter V_{ab} (yellow), the transmitter current i_{T} (blue), and the receiver current i_{R} (red).

shows the change in the output power and the overall efficiency of the system with the change in the operating frequency. The maximum efficiency is 57.3% is achieved at 337 kHz, while the maximum output power is about 48 W at 516 kHz operating frequency. Fig. 11 shows the calculated efficiencies from (12) and measured values under the change of the operating frequencies. The maximum ON-resistors of enhancement mode transistors and the losses in the transmitter inductor are considered as the source resistance R_{s}, as mentioned previously in section and shown in Fig.1. However, the internal resistance of the dc source is not considered in the calculated efficiencies, which might explain the difference between the calculated and measured values.

Fig. 12 and 13 shows the inverter output voltage and the transmitter and receiver current waveforms at maximum efficiency and maximum power, respectively. In both cases, the phase shift between the transmitter and receiver currents is about 90 degrees which result in zero transmitted reactive power [19]. Fig. 12 shows that the transmitter current is slightly lagging behind the output voltage of the inverter, which helps to achieve the zero voltage switching condition for the switches. In contrast, Fig. 13 shows that the transmitter current is in phase with the output voltage of the inverter, which means the zero phase angle condition is achieved, and hence a minimum VA rating of power supply is required. However, as the transmitter and receiver currents are high, there will be more losses in the system.

Table I summarizes a comparison of the performances of the designed system with the recently proposed underwater CPT systems. The papers [12], [13] investigate high-frequency operating CPT systems under fresh and seawater, respectively. They managed to transfer hundreds of watts over a separation distance of 20 mm, which is short enough to achieve high ac-ac efficiency of higher than 90%. However, operating at high-frequency to transfer high power might face practical challenges.

The researchers in [20] transmitted 100 W at 500 kHz operating frequency and separation distance of 400 mm. As the operation conditions are not far from this work, the efficiency that they achieved is 50%. However, the input voltage that they used is 100 V, increasing the input voltage results in increasing the resistance R_{i}. Thus, operating the system proposed in this paper at 100 V is expected to have better efficiency and higher power. Another approach to improve the efficiency further is using another compensation circuit to provide large voltage (i.e., large R_{i} hence better efficiency) and reactive compensation for underwater CPT transfer system.

Finally, paper [21] transferred 100 W at 625 kHz operating frequency and separation distance of 150 mm using more complex compensation circuits. However, the paper investigated the underwater effect by placing a seawater bag between air-gapped plates, which neglects the fringing effects and the cross-coupling effects between the plates. Neglecting the cross-coupling effects can explain the high efficiency that the paper achieved, as explained previously in [18]. Thus, the reported results will be different if the capacitive couplers are submerged in water.

IV. Conclusion

This paper investigated CPT submerged in seawater for maritime charging applications. It proposed and validated a mathematical model to calculate the maximum achievable efficiency of the CPT system considering the dielectric losses of the medium. Moreover, the effect of changing separation distance and switching frequency on the transmitted power and the overall efficiency is examined using SS compensation. While the distance has an almost negligible effect on the power transfer and efficiency, the operating frequency considerably affects the performance of the system. In this paper, SS compensation is used to transfer 48 W at 500 mm, 48 V input voltage, 516 kHz, and 54%. Operating the system at low frequencies can improve the overall efficiency while limiting the transferred power. Matching circuits are required to achieve a better solution to enhance efficiency and power transferability.

TABLE I
COMPARISON OF THE RECENTLY PROPOSED UNDERWATER CPT SYSTEMS.

Ref.	**Compensation**	**Frequency** (MHz)	**Distance** (mm)	**Power** (W)	**Efficiency** (%)
[13]	SS	6.78	20	1000	94.5[1]
[12]	SS	107.7	20	400	90[1]
[20]	SS	0.5	400	100	50
[21]	LCLC-LCLCL	0.625	150	100	80.2
This work	SS	0.516	500	48	54

[1]ac-ac efficiency

REFERENCES

[1] D. F. Campos, A. Matos, and A. M. Pinto, "Modular multi-domain aware autonomous surface vehicle for inspection," *IEEE Access*, vol. 10, pp. 113 355–113 375, 2022.

[2] G. Shao, Y. Ma, R. Malekian, X. Yan, and Z. Li, "A novel cooperative platform design for coupled usv–uav systems," *IEEE Transactions on Industrial Informatics*, vol. 15, no. 9, pp. 4913–4922, 2019.

[3] Y. Zhao, X. Qi, Y. Ma, Z. Li, R. Malekian, and M. A. Sotelo, "Path following optimization for an underactuated usv using smoothly-convergent deep reinforcement learning," *IEEE Transactions on Intelligent Transportation Systems*, vol. 22, no. 10, pp. 6208–6220, 2021.

[4] C. R. Teeneti, T. T. Truscott, D. N. Beal, and Z. Pantic, "Review of wireless charging systems for autonomous underwater vehicles," *IEEE Journal of Oceanic Engineering*, vol. 46, no. 1, pp. 68–87, 2021.

[5] K. Xue, C. Ren, X. Ji, and H. A. Qian, "Design, modeling and implementation of a projectile-based mechanism for usvs charging tasks," *IEEE Robotics and Automation Letters*, pp. 1–1, 2022.

[6] B. Allen, T. Austin, N. Forrester, R. Goldsborough, A. Kukulya, G. Packard, M. Purcell, and R. Stokey, "Autonomous docking demonstrations with enhanced remus technology," in *OCEANS 2006*, 2006, pp. 1–6.

[7] C. R. Teeneti, T. T. Truscott, D. N. Beal, and Z. Pantic, "Review of wireless charging systems for autonomous underwater vehicles," *IEEE Journal of Oceanic Engineering*, vol. 46, no. 1, pp. 68–87, 2021.

[8] J. Kim, K. Kim, H. Kim, D. Kim, J. Park, and S. Ahn, "An efficient modeling for underwater wireless power transfer using z-parameters," *IEEE Transactions on Electromagnetic Compatibility*, vol. 61, no. 6, pp. 2006–2014, 2019.

[9] C. Cai, Y. Zhang, S. Wu, J. Liu, Z. Zhang, and L. Jiang, "A circumferential coupled dipole-coil magnetic coupler for autonomous underwater vehicles wireless charging applications," *IEEE Access*, vol. 8, pp. 65 432–65 442, 2020.

[10] Z. Yan, K. Zhang, L. Qiao, Y. Hu, and B. Song, "A multiload wireless power transfer system with concentrated magnetic field for auv cluster system," *IEEE Transactions on Industry Applications*, vol. 58, no. 1, pp. 1307–1314, 2022.

[11] Y. Zeng, C. Lu, R. Liu, X. He, C. Rong, and M. Liu, "Wireless power and data transfer system using multidirectional magnetic coupler for swarm auvs," *IEEE Transactions on Power Electronics*, vol. 38, no. 2, pp. 1440–1444, 2023.

[12] M. Tamura, Y. Naka, K. Murai, and T. Nakata, "Design of a capacitive wireless power transfer system for operation in fresh water," *IEEE Transactions on Microwave Theory and Techniques*, vol. 66, no. 12, pp. 5873–5884, 2018.

[13] M. Tamura, K. Murai, and M. Matsumoto, "Design of conductive coupler for underwater wireless power and data transfer," *IEEE Transactions on Microwave Theory and Techniques*, vol. 69, no. 1, pp. 1161–1175, 2021.

[14] H. Mahdi, B. Hoff, and T. Østrem, "Optimal solutions for underwater capacitive power transfer," *Sensors*, vol. 21, no. 24, p. 8233, 2021.

[15] Y. Wang, H. Zhang, and F. Lu, "Review, analysis, and design of four basic cpt topologies and the application of high-order compensation networks," *IEEE Transactions on Power Electronics*, vol. 37, no. 5, pp. 6181–6193, 2022.

[16] CoolGaN, "High-frequency half-bridge evaluation board featuring EiceDRIVER™ GaN," May 2022, [Online; accessed 25. May. 2022]. [Online]. Available: https://www.infineon.com/cms/en/product/evaluation-boards/eval_1edf_g1b_hb_gan/

[17] Wolfspeed, "Silicon Carbide Schottky Diode," May 2022, [Online; accessed 25. May. 2022]. [Online]. Available: https://assets.wolfspeed.com/uploads/2020/12/C6D04065A.pdf

[18] H. Mahdi, B. Hoff, P. G. Ellingsen, and T. Østrem, "Conformal transformation analysis of capacitive wireless charging," *IEEE Access*, vol. 10, pp. 105 621–105 630, 2022.

[19] F. Lu, H. Zhang, and C. Mi, "A two-plate capacitive wireless power transfer system for electric vehicle charging applications," *IEEE Transactions on Power Electronics*, vol. 33, no. 2, pp. 964–969, 2018.

[20] L. Yang, Y. Zhang, X. Li, J. Jian, Z. Wang, J. Huang, L. Ma, and X. Tong, "Analysis and design of four-plate capacitive wireless power transfer system for undersea applications," *CES Transactions on Electrical Machines and Systems*, vol. 5, no. 3, pp. 202–211, 2021.

[21] L. Yang, M. Ju, and B. Zhang, "Bidirectional undersea capacitive wireless power transfer system," *IEEE Access*, vol. 7, pp. 121 046–121 054, 2019.

7

Discussion and Conclusions

This chapter summarizes the works in this research, discusses the relationship between the results of the research and the results of similar studies in the published literature, and indicates some of the research limitations. Finally, the chapter concludes this research and suggests future works.

7.1 Discussion

The maritime sector exerts considerable effort to phase out fossil fuels and mitigate their negative environmental effects. It implements policies to ensure sustainable operations in shipping, ports, and maritime fields. Maritime electrification can facilitate the integration of more renewable and environmentally friendly resources in this sector. Electric energy storage system technologies are needed because of the intermittency nature of most renewable energy resources. Lithium-ion batteries are a promising energy storage technology for the maritime industry, in general, and maritime vessels and vehicles, in specific. Charging infrastructure is essential for enhancing onboard battery systems and would encourage the development of more battery-powered ships and maritime vehicles.

Although the electrification of ships has more than a century of history, it has only started to receive more attention in the last decade. In the literature, different aspects related to the electrification of ships were studied, such as the

shipboard power system, onboard ESS, and shore-to-ship stability connections [93–95]. In contrast, paper J1 [96] investigates the converter topologies used in the electrification of ships found in the literature and on the market, trying to answer the research questions Q1 and Q2.

Power converters play an essential role in the electrification of ships, specifically battery-powered ones. However, they have received much less attention in the literature. Paper J1 [96] gives systematic instructions for designing, analyzing, and selecting a suitable ship converter. It aims to anticipate future trends and potential challenges. The main findings of the paper are: (1) The research focuses on large shipboard AC systems and has raised the dc power architectures as an alternative in the future, (2) wired connection is the conventional shore-to-ship connection where transformers and frequency converters are the main equipment, and (3) WPT technologies are promising options for maritime electric charging applications.

For large ships that require MW power, the conventional shore-to-ship connections are wired connections, or plug-ins known as "cold ironing". Cold ironing supplies ships with power through cables while they are at berth. For ships that require power up to 1 MW, some manufacturers have recently started to provide commercial inductive charging solutions. For small ships and unmanned maritime vehicles, wireless charging provides flexibility, mobility, convenience, and safety.

Inductive charging has attracted considerable attention in previous studies. In contrast, due to its power transfer and short-distance limitations, CPT receives less attention for maritime electrical charging applications. Paper C1 [90] proposes the CPT for small ships charging applications. The paper studies the operation principle and main design factors of a CPT system and evaluates the system using behavior circuit voltage type-based and circuit equivalent π-network models. The main finding is that enhancing the capacitive coupling can improve the efficiency and transferability of the system. The coupling capacitance can be increased by reducing the separation distance via integrating the couplers within a vacuum mooring system or submerging them underwater. The paper concludes that it is theoretically feasible to transfer hundreds of kWs using CPT.

Transferring hundreds of kWs in practice is difficult due to technical and safety limitations. It can even be challenging to transfer tens of kWs, as the system might suffer safety operation challenges, such as high voltage stress. Paper J2 discusses the theoretical and practical design considerations for CPT systems, answering the research question Q3. It also presents some design limitations and challenges of capacitive wireless charging. The aim is to be used a theoretical framework for the analysis and design of a CPT system.

Air-gapped CPT was well investigated in the published literature for on-road charging applications [46, 83, 97, 98]. Underwater CPT has also been investigated for maritime charging applications [88, 91, 92]. In [88], the coupling capacitance of underwater CPT was studied using FEM software. However, two seawater bags are placed between the couplers to enhance the coupling capacitance, but it does not emulate the practical application of CPT. In [91, 92], fresh and seawater CPT were investigated but at HF operating range and tens of millimeters separation distances. Operating in HF range limits the amount of power transferred due to safety and operational considerations.

Paper J3 [99] tries to fill the gap in the previous studies by examining the capacitive coupling when the mediums separating the couplers are air, freshwater, and seawater. The paper answers a part of the research question Q4 by examining the fringing effects in these mediums and proposing mathematical models that can be used to calculate the capacitive coupling. The main findings of the paper are: (1) It shows that submerging the couplers under seawater can enhance the coupling and changes in the gap distance and the operating frequency do not significantly affect the underwater coupling, (2) it demonstrates that at MF ranges the power can safely be transferred over a wider separation distance than air-gapped counterparts, and (3) it shows that the stay capacitances also increases resulting in a negative effect on the performance of the system.

Submerging the couplers in seawater increases the coupling capacitances to nF range, and hence the under seawater CPT systems can be operated in MF range. Because the permittivity of water is about eighty times higher than the permittivity of air, submerging the capacitive coupler results in an increase in the coupling. The power stored in a capacitor is proportional to the capacitance, the quadratic of the voltage across the capacitor, and the operating frequency. Thus, submerging the couplers underwater can increase the power transfer over a wider separation distance. Nevertheless, the high permittivity of the water increases the stray and parasitic capacitances. Besides, underwater capacitive charging suffers dielectric losses of the medium due to the dissolved ions.

Papers C2 [100] and C3 [101] answers the other part of the research question Q4 by investigating the effect of the conductivity of seawater. The papers use the conjugate-image approach to study the maximum available power and efficiency of a dissipative CPT system. However, the conjugate-image approach does not guarantee the optimal efficiency or maximum power transferability of the system.

paper J4 [102] expands the works in papers C2 and C3 to involve three possible solutions to achieve maximum efficiency, maximum power, or conjugate matching. Over a distance ranges from 100 mm to 300 mm and operating fre-

quency ranges from 300 kHz to 1 MHz, the main findings are as follows: (1) all the solutions are a function of the coupling admittances, thus measuring the admittances and choosing the compensation that is needed to achieve the required solution, (2) more power can be transferred, and better efficiency can be achieved at low operating frequencies than higher ones, and (3) the variation of efficiency and power transferability does not significantly change with the separation distance. The results only use the coupling parameters to calculate the ac-ac CPT system efficiency.

The limitation of papers C2, C3, and J4 is that they consider the ac power source lossless, which does not represent the practical case. A dc-ac inverter is required to achieve ac waveforms and generate alternating electric fields between the couplers. The inverter has two types of losses: switching losses that occur during the moment of switching and conducting losses that occur due to the conducting parasitic losses of the switches in the inverter.

Paper C4 considers the losses in the source to calculate the maximum efficiency of the system. The paper also examines the coupler structures, operating frequencies, and separation distances on the overall dc-dc efficiency and power transferability. In this paper, the proposed CPT system is suitable to charge a USV and UUV. Using series compensation, the system achieves 48 W with about 54% at 48 V input voltage, 500 mm separation distance, and 512 kHz operating frequency. The input resistance of the system seen watching from the source should be large enough to achieve high efficiency. Thus, an impedance matching or more complex compensation on the transmitter side should be adopted to achieve high efficiency.

An air-gapped CPT operating in MF range is also studied in paper J6 [103]. Although the shielded CPT system is proposed for a manufacturing system, it is suitable for maritime applications. The two platforms in the manufacturing system can emulate two maritime vehicles or ships charging each other. The system can transfer about 135 W using 300 × 450 mm coupling plates, and at a separation distance of 50 mm, a total efficiency of about 83.9%, and 1 MHz operating efficiency. However, the size of the plates can be large for USV or UUV. Increasing the operating frequency can improve the power density of the air-gapped system and the separation distance between the transmitter and receiver. Operating in a high-frequency range can be adapted to transfer from hundreds of watts to a few kW, but it adds extra design and operation challenges. Paper J2 examines a 13.56 MHz shielded CPT system to transfer 100 W over a 30 mm separation distance and an 87% ac-dc efficiency.

Submerging the plates in water can increase the capacitive coupling and the separation distance between the couplers. In Paper J3 [99], the proposed system transfers 129 W using 150 × 150 mm coupling plates, and at a separation

distance of 300 mm, a total efficiency of about 81.2%, and 1.1 MHz operating efficiency. Under the same operation conditions, the size of the coupling electrodes is reduced, and the separation distance between them is increased compared to the air-gapped CPT system in paper J6 [103]. The stray capacitance and conductivity are the main challenges facing CPT systems. Because of the presenting ions in seawater, the displacement current increases. This problem can be tackled by increasing the separation between the couplers or reducing the operating frequency. Regarding the stray capacitance, the coupling between adjacent plates, or the plates and the shielding, results in high stray and self-coupling coupling capacitance. The stray coupling problem can be solved by proposing a proper compensation.

Thus far, CPT systems can provide charging solutions for UUV, USV, and small ships that do not require high power. The CPT systems examined in this work can be scaled up to transfer a few kW. However, many challenges are facing CPT, such as the stray capacitance, the break-down voltage, and safety operation. The stray capacitance can result in leakage current circulating in the hull of ships or maritime vehicles, resulting in operational and safety issues. The stability of the grounding on the receiver side is another challenge that faces WPT in general and CPT in specific. Shielded CPT should be further investigated to solve this problem. The break-down voltage and compactness of the design are some challenges facing the shielded CPT system. Submerged coupler underwater requires accurate modeling and measurements to design a system with high efficiency. The stray capacitance should be examined, and the insulation of the electrodes requires correct modeling. The effect of the water circulation on the coupling parameters also should be considered for more practical aspects.

7.2 Conclusions

Charging infrastructure can play a critical role in concentrating the effort toward maritime electrification. Battery swapping provides fast energy refueling but suffers from the complexity of swapping structure, space requirement, high cost, and station congestion. Wired charging is the common charging approach for large ships, and it can take place manually or using robots. Wireless charging can provide an autonomous, flexible, and safe solution for small ships and maritime vehicles. Near-field WPT technology can offer autonomous and reliable charging over hundreds of millimeter distances. Inductive charging comprises heavy, expensive, and fragile parts and suffers from high eddy losses in near metals and sharp degradation in efficiency during misalignment conditions. Capacitive charging has recently been studied as an alternative to inductive charging in on-road applications, but it received low attention for maritime charging applications.

This work investigated CPT technology for charging small ships and unmanned maritime vehicles. Unlike on-road charging applications, air or water can be utilized as charging mediums to charge ships, USV, or UUV. Because of the low permittivity of the air, air-gapped CPT has capacitive coupling in pF range. Thus, a MHz operating frequency is required to transfer power over a few centimeters distances. The system transferability and efficiency degrade sharply with the increase in separation distances. The air-gapped CPT system can transfer about 135 W using 300 × 450 mm coupling plates, and at a separation distance of 50 mm, a total efficiency of about 83.9%, and 1 MHz operating efficiency. By increasing the operation frequency to 13.56 MHz, the air-gapped CPT system can transfer about 100 W using 150 × 250 mm coupling plates, and at a separation distance of 30 mm, and a total efficiency of about 87%.

Submerging the plates in water improves the capacitive coupling to hundreds of pF or few nF. The underwater CPT system transfers 129 W using 150 × 150 mm coupling plates, and at a separation distance of 300 mm, a total efficiency of about 81.2%, and 1.1 MHz operating efficiency. The underwater CPT system can also operate with MF range, which can transfer more power within hundreds of millimeters distances. But submerging the couplers in water also increases the cross-coupling, self-coupling, and stray capacitances, which has a negative effect on the system performance. Besides, the water conductivity can increase system losses and decrease overall efficiency. Both air-gapped and underwater CPT systems can provide charging solutions with up to transfer a few kW for small ships and unmanned maritime vehicles. However, these systems are still facing several challenges that need further investigation.

7.3 Future works

The shielded CPT system is more suitable for practical applications. Both air-gapped and underwater shielded-CPT require further study. An optimal design is required to achieve a trade-off between the size of the plates, the distances between them, the system efficiency, and the safe operation. The following points are investigated as an expansion to this work:

- The packaging of the shield capacitive couplers when the separation media is water should be modeled accurately. The coupling parameters are essential in designing a wireless capacitive charging system. Insulation material that encloses surrounds or supports the couplers, should be considered in the model. The insulation critically affects the stray capacitances, the breakdown voltages, and the safe operation.

- The stability of the ground voltage on the receiver side and the leakage current are important topics that require more investigation. The high-frequency oscillation on the ground voltage can result in EMI and safety problems.

- Changing of load can degrade the efficiency and transferability of the CPT system. Active or passive impedance matching networks require further studies. Besides, the dynamic motion in small ships and unmanned maritime vehicles can also change the coupling parameters. Control mechanisms are required and should be carefully examined under more practical scenarios.

- Any foreign objects between the couplers can highly affect the coupling parameters. The electric fields between the couplers can generate internal heat causing temperature rise in these objects or any nearby bodies. Transferring high power by means of electric fields can endanger the marine environment. The safety of the maritime charging system requires further investigation.

Bibliography

[1] The United Nations Conference on Trade and Development (UNCTAD). *Review of Maritime Transport 2018*. Tech. rep. 2018. DOI: 10.5822/978-1-61091-480-2_1. URL: https://unctad.org/webflyer/review-maritime-transport-2018%20(2022/11/29).

[2] International Maritime Organization. *Fourth IMO GHG Study 2020*. Tech. rep. London, 2021. URL: https://www.imo.org/en/OurWork/Environment/Pages/Fourth-IMO-Greenhouse-Gas-Study-2020.aspx%20(2020/07/24).

[3] Norbert Doerry, John Amy, and Cy Krolick. "History and the Status of Electric Ship Propulsion, Integrated Power Systems, and Future Trends in the U.S. Navy." In: *Proceedings of the IEEE* 103.12 (2015), pp. 2243–2251. DOI: 10.1109/JPROC.2015.2494159.

[4] Espen Skjong et al. "The Marine Vessel's Electrical Power System: From its Birth to Present Day." In: *Proceedings of the IEEE* 103.12 (2015), pp. 2410–2424. DOI: 10.1109/JPROC.2015.2496722.

[5] J. S. Thongam et al. "All-electric ships—A review of the present state of the art." In: *2013 Eighth International Conference and Exhibition on Ecological Vehicles and Renewable Energies (EVER)*. 2013, pp. 1–8. DOI: 10.1109/EVER.2013.6521626.

[6] Jan Fredrik Hansen and Frank Wendt. "History and State of the Art in Commercial Electric Ship Propulsion, Integrated Power Systems, and Future Trends." In: *Proceedings of the IEEE* 103.12 (2015), pp. 2229–2242. DOI: 10.1109/JPROC.2015.2458990.

[7] Sidun Fang et al. "Optimal Hierarchical Management of Shipboard Multibattery Energy Storage System Using a Data-Driven Degradation Model." In: *IEEE Transactions on Transportation Electrification* 5.4 (2019), pp. 1306–1318. DOI: 10.1109/TTE.2019.2956639.

[8] F. D. Kanellos. "Optimal Power Management With GHG Emissions Limitation in All-Electric Ship Power Systems Comprising Energy Storage Systems." In: *IEEE Transactions on Power Systems* 29.1 (2014), pp. 330–339. DOI: 10.1109/TPWRS.2013.2280064.

[9] J. Kumar, A. Memon, L. Kumpulainen, K. Kauhaniemi, O. Omid. "Design and analysis of new harbour grid models to facilitate multiple scenarios

of battery charging and onshore supply for modern vessels." In: *Energies* 12.12 (2019).

[10] DNV. *Alternative Fuels Insight (AFI) platform*. Available at https://www.dnv.com/services/alternative-fuels-insight-128171 (2023/04/05).

[11] Maria Maria Gallucci. *The First Battery-Powered Tanker is Coming to Tokyo*. Available at https://spectrum.ieee.org/first-battery-powered-tanker-coming-to-tokyo (2023/1/3).

[12] Roger Griffis and Jennifer Howard. "Oceans and Marine Resources in a Changing Climate: A Technical Input to the 2013 National Climate Assessment." In: Washington, DC: Island Press/Center for Resource Economics, 2013, pp. 1–6. DOI: 10.5822/978-1-61091-480-2_1.

[13] Ulf Johansen et al. "The Norwegian seafood industry â€" Importance for the national economy." In: *Marine Policy* 110 (2019), p. 103561. DOI: https://doi.org/10.1016/j.marpol.2019.103561.

[14] Hans V. Bjelland et al. "Exposed Aquaculture in Norway." In: *OCEANS 2015 - MTS/IEEE Washington*. 2015, pp. 1–10. DOI: 10.23919/OCEANS.2015.7404486.

[15] Blueye Robotics. *Underwater drones from Blueye*. Available at https://www.blueyerobotics.com/products/ (2022/12/31).

[16] kongsberg. *Eelume Articulated Underwater Robot*. Available at https://www.kongsberg.com/globalassets/maritime/km-products/product-documents/eelume----underwater-intervention-vehicle (2022/12/31).

[17] Probotic. *Probot*. Available at https://www.probotic.no/probot (2022/12/31).

[18] Maritime Robotics. *The Otter: Unmanned surface vehicle (USV) cost*. Available at https://www.maritimerobotics.com/otter (2022/12/14).

[19] Daniel Filipe Campos, Aníbal Matos, and Andry Maykol Pinto. "Modular Multi-Domain Aware Autonomous Surface Vehicle for Inspection." In: *IEEE Access* 10 (2022), pp. 113355–113375. DOI: 10.1109/ACCESS.2022.3217504.

[20] Guangming Shao et al. "A Novel Cooperative Platform Design for Coupled USV–UAV Systems." In: *IEEE Transactions on Industrial Informatics* 15.9 (2019), pp. 4913–4922. DOI: 10.1109/TII.2019.2912024.

[21] Yujiao Zhao et al. "Path Following Optimization for an Underactuated USV Using Smoothly-Convergent Deep Reinforcement Learning." In: *IEEE Transactions on Intelligent Transportation Systems* 22.10 (2021), pp. 6208–6220. DOI: 10.1109/TITS.2020.2989352.

[22] Chakridhar Reddy Teeneti et al. "Review of Wireless Charging Systems for Autonomous Underwater Vehicles." In: *IEEE Journal of Oceanic Engineering* 46.1 (2021), pp. 68–87. DOI: 10.1109/JOE.2019.2953015.

[23] Oystein Alnes, Sverre Eriksen, and Bjorn-Johan Vartdal. "Battery-Powered Ships: A Class Society Perspective." In: *IEEE Electrification Magazine* 5.3 (2017), pp. 10–21. DOI: 10.1109/MELE.2017.2718823.

[24] Cheng Siong Chin, Caizhi Zhang, and Zuchang Gao. "Deploying battery technology for marine vessel electrification." In: *IEEE Potentials* 40.6 (2021), pp. 24–33. DOI: 10.1109/MPOT.2020.2988292.

[25] Xiaoqi Tan et al. "Optimal Scheduling of Battery Charging Station Serving Electric Vehicles Based on Battery Swapping." In: *IEEE Transactions on Smart Grid* 10.2 (2019), pp. 1372–1384. DOI: 10.1109/TSG.2017.2764484.

[26] Bo Yang et al. "A 5.8-GHz Phased Array System Using Power-Variable Phase-Controlled Magnetrons for Wireless Power Transfer." In: *IEEE Transactions on Microwave Theory and Techniques* 68.11 (2020), pp. 4951–4959. DOI: 10.1109/TMTT.2020.3007187.

[27] Ahmed A. Shalaby et al. "A Dynamic Optimal Battery Swapping Mechanism for Electric Vehicles Using an LSTM-Based Rolling Horizon Approach." In: *IEEE Transactions on Intelligent Transportation Systems* 23.9 (2022), pp. 15218–15232. DOI: 10.1109/TITS.2021.3138892.

[28] Tianyu Wang. *EV battery-swapping finds new life in China*. Available at https://news.cgtn.com/news/2020-08-16/EV-battery-swapping-finds-new-life-in-China-SWZQhFZoEE/index.html (2021/12/07).

[29] Wärtsilä Corporation. *Wärtsilä swappable battery containers enabling inland waterway vessels to operate with zero emissions*. Available at https://www.wartsila.com/media/news/07-09-2021-wartsila-swappable-battery-containers-enabling-inland-waterway-vessels-to-operate-with-zero-emissions-2971607 (2022/12/14).

[30] SEAM. *Wärtsilä swappable battery containers enabling inland waterway vessels to operate with zero emissionsNorled partners up with SEAM for development of innovative battery system*. Available at https://seam.no/norled-partners-up-with-seam-for-development-of-innovative-battery-system/ (2022/12/14).

[31] Wenhao Jia et al. "Hybrid Swapped Battery Charging and Logistics Dispatch Model in Continuous Time Domain." In: *IEEE Transactions on Vehicular Technology* 71.3 (2022), pp. 2448–2458. DOI: 10.1109/TVT.2022.3143370.

[32] Zhaohao Ding et al. "Quality-of-Service Aware Battery Swapping Navigation and Pricing for Autonomous Mobility-on-Demand System." In: *IEEE Transactions on Industrial Informatics* 18.11 (2022), pp. 8247–8257. DOI: 10.1109/TII.2022.3172985.

[33] Iman Aghabali et al. "800-V Electric Vehicle Powertrains: Review and Analysis of Benefits, Challenges, and Future Trends." In: *IEEE Transactions on Transportation Electrification* 7.3 (2021), pp. 927–948. DOI: 10.1109/TTE.2020.3044938.

[34] Peter J. Ferrara, Mark A. Uva, and Jeff Nowlin. "Naval Ship-to-Shore High Temperature Superconducting Power Transmission Cable Feasibility." In: *IEEE Transactions on Applied Superconductivity* 21.3 (2011), pp. 984–987. DOI: 10.1109/TASC.2011.2112751.

[35] The International Electrotechnical Commission. *IEC 60092:2023 SER Standard | Electrical installations in ships ALL PARTS*. Available at https://www-standard-no.mime.uit.no/no/Nettbutikk/produktkatalogen/Produktpresentasjon/?ProductID=1000451 (2023/04/01).

[36] *Landstrømsforum Et forum for elektrifiseringen av skipsfarten (Norwegian)*. Available at https://www.nek.no/forum/landstromsforum/om-landstromsforum/#sirkulerte-dokumenter (2023/04/01).

[37] Siamak Karimi, Mehdi Zadeh, and Jon Are Suul. "Shore Charging for Plug-In Battery-Powered Ships: Power System Architecture, infrastructure, and Control." In: *IEEE Electrification Magazine* 8.3 (2020), pp. 47–61. DOI: 10.1109/MELE.2020.3005699.

[38] Kaiwen Xue et al. "Design, Modeling and Implementation of a Projectile-based Mechanism for USVs Charging Tasks." In: *IEEE Robotics and Automation Letters* (2022), pp. 1–1. DOI: 10.1109/LRA.2022.3154036.

[39] Ben Allen et al. "Autonomous Docking Demonstrations with Enhanced REMUS Technology." In: *OCEANS 2006*. 2006, pp. 1–6. DOI: 10.1109/OCEANS.2006.306952.

[40] ITU-R Recommendation ITU-R SM.2110. *Frequency ranges for operation of non-beam Wireless Power Transmission systems*. Available at https://www.itu.int/rec/R-REC-SM.2110-0-201709-S (2021/11/09).

[41] Triviño-Cabrera Alicia, González-González José M, and Aguado José A. *Wireless Power Transfer for Electric Vehicles: Foundations and Design Approach*. Springer International Publishing, 2020.

[42] Aqueel Ahmad, Mohammad Saad Alam, and Rakan Chabaan. "A Comprehensive Review of Wireless Charging Technologies for Electric Vehicles." In: *IEEE Transactions on Transportation Electrification* 4.1 (2018), pp. 38–63. DOI: 10.1109/TTE.2017.2771619.

[43] Su Y. Choi et al. "Advances in Wireless Power Transfer Systems for Roadway-Powered Electric Vehicles." In: *IEEE Journal of Emerging and Selected Topics in Power Electronics* 3.1 (2015), pp. 18–36. DOI: 10.1109/JESTPE.2014.2343674.

[44] Siqi Li et al. "Wireless Power Transfer by Electric Field Resonance and Its Application in Dynamic Charging." In: *IEEE Transactions on Industrial Electronics* 63.10 (2016), pp. 6602–6612. DOI: 10.1109/TIE.2016.2577625.

[45] Jiejian Dai and Daniel C. Ludois. "Single Active Switch Power Electronics for Kilowatt Scale Capacitive Power Transfer." In: *IEEE Journal of Emerging and Selected Topics in Power Electronics* 3.1 (2015), pp. 315–323. DOI: 10.1109/JESTPE.2014.2334621.

[46] Fei Lu, Hua Zhang, and Chris Mi. "A Review on the Recent Development of Capacitive Wireless Power Transfer Technology." In: *Energies* 10.11 (Nov. 2017), p. 1752. DOI: 10.3390/en10111752.

[47] Fei Lu et al. "A Double-Sided LCLC-Compensated Capacitive Power Transfer System for Electric Vehicle Charging." In: *IEEE Transactions on Power Electronics* 30.11 (2015), pp. 6011–6014. DOI: 10.1109/TPEL.2015.2446891.

[48] Wei Zhang and Chunting Chris Mi. "Compensation Topologies of High-Power Wireless Power Transfer Systems." In: *IEEE Transactions on Vehicular Technology* 65.6 (2016), pp. 4768–4778. DOI: 10.1109/TVT.2015.2454292.

[49] Hua Zhang et al. "A Four-Plate Compact Capacitive Coupler Design and LCL-Compensated Topology for Capacitive Power Transfer in Electric Vehicle Charging Application." In: *IEEE Transactions on Power Electronics* 31 (2016), pp. 8541–8551.

[50] Giuseppe Guidi and Jon Are Suul. "Minimizing Converter Requirements of Inductive Power Transfer Systems With Constant Voltage Load and Variable Coupling Conditions." In: *IEEE Transactions on Industrial Electronics* 63.11 (2016), pp. 6835–6844. DOI: 10.1109/TIE.2016.2582459.

[51] G. Guidi, J. A. Suul, F. Jenset and I. Sorfonn. "Wireless Charging for Ships: High-Power Inductive Charging for Battery Electric and Plug-In Hybrid Vessels." In: *IEEE Electrification Magazine* 5.3 (2017), pp. 22–32.

[52] Yiming Zhang et al. "Design of high-power static wireless power transfer via magnetic induction: An overview." In: *CPSS Transactions on Power Electronics and Applications* 6.4 (2021), pp. 281–297. DOI: 10.24295/CPSSTPEA.2021.00027.

[53] B. A. Kumar, M. Chandrasekar, T. R. Chelliah and U. Ramesh. "Coordinated Control of Electric Tugboats Considering Inductive Power Transfer for Better Fuel Efficiency." In: *2018 IEEE International Conference on Power Electronics, Drives and Energy Systems (PEDES), Chennai, India* (2018), pp. 1–6.

[54] H. Singh et al. "An intelligent dock for an autonomous ocean sampling network." In: *IEEE Oceanic Engineering Society. OCEANS'98. Conference Proceedings (Cat. No.98CH36259)*. Vol. 3. 1998, 1459–1462 vol.3. DOI: 10.1109/OCEANS.1998.726312.

[55] M.D. Feezor, F. Yates Sorrell, and P.R. Blankinship. "An interface system for autonomous undersea vehicles." In: *IEEE Journal of Oceanic Engineering* 26.4 (2001), pp. 522–525. DOI: 10.1109/48.972087.

[56] T. Kojiya et al. "Construction of non-contacting power feeding system to underwater vehicle utilizing electro magnetic induction." In: *Europe Oceans 2005*. Vol. 1. 2005, 709–712 Vol. 1. DOI: 10.1109/OCEANSE.2005.1511801.

[57] Ze-song Li et al. “Design considerations for electromagnetic couplers in contactless power transmission systems for deep-sea applications.” In: *Journal of Zhejiang University SCIENCE C* 11 (2010), pp. 824–834.

[58] Zhiyuan Cheng et al. “Design and Loss Analysis of Loosely Coupled Transformer for an Underwater High-Power Inductive Power Transfer System.” In: *IEEE Transactions on Magnetics* 51.7 (2015), pp. 1–10. DOI: 10.1109/TMAG.2014.2346737.

[59] Taofeek Orekan, Peng Zhang, and Cyuansi Shih. “Analysis, Design, and Maximum Power-Efficiency Tracking for Undersea Wireless Power Transfer.” In: *IEEE Journal of Emerging and Selected Topics in Power Electronics* 6.2 (2018), pp. 843–854. DOI: 10.1109/JESTPE.2017.2735964.

[60] Zhengchao Yan et al. “Frequency Optimization of a Loosely Coupled Underwater Wireless Power Transfer System Considering Eddy Current Loss.” In: *IEEE Transactions on Industrial Electronics* 66.5 (2019), pp. 3468–3476. DOI: 10.1109/TIE.2018.2851947.

[61] Plugless Power. *Plugless Power has been the industry leader in autonomous charging*. Available at https://www.pluglesspower.com/ (2020/09/09).

[62] WiTricity. *WiTricity is leading the charge in technology development and standardization.* Available at https://witricity.com/products/automotive/ (2020/07/27).

[63] Momentum Dynamics. *Wireless charging for electric vehicles.* Available at https://momentumdynamics.com/ (2020/09/09).

[64] Mojo Mobility. *Mojo Mobility partners with Original Equipment Manufactures (OEMs) to develop unique, differentiated solutions for wireless charging.* Available at https://www.mojomobility.com/solutions (2020/09/09).

[65] HEVO Inc. *Power Station Smart-EST Charging.* Available at https://hevo.com/rezonant-e8.html (2020/09/09).

[66] TGOOD. *Wireless EV Charging Achieves Breakthrough.* Available at http://tgood.com/int/en/news/wireless-ev-charging-achieves-breakthrough (2020/09/09).

[67] Toshiba. *7 kW Wireless Power Transmission Technology for EV Charging.* Available at https://www.global.toshiba/ww/technology/corporate/rdc/rd/fields/14-e01.html (2020/09/09).

[68] INTIS. *INTIS inductive energy transfer systems at a glance.* Available at https://www.intis.de/wireless-power-transfer.html (2020/09/09).

[69] Cheng Chen, Kama Huang, and Yang Yang. “Microwave Transmitting System Based on Four-Way Master–Slave Injection-Locked Magnetrons and Horn Arrays With Suppressed Sidelobes.” In: *IEEE Transactions on Microwave Theory and Techniques* 66.5 (2018), pp. 2416–2424. DOI: 10.1109/TMTT.2018.2790924.

[70] Alessandra Costanzo and Diego Masotti. "Energizing 5G: Near- and Far-Field Wireless Energy and Data Trantransfer as an Enabling Technology for the 5G IoT." In: *IEEE Microwave Magazine* 18.3 (2017), pp. 125–136. DOI: 10.1109/MMM.2017.2664001.

[71] Ke Jin and Weiyang Zhou. "Wireless Laser Power Transmission: A Review of Recent Progress." In: *IEEE Transactions on Power Electronics* 34.4 (2019), pp. 3842–3859. DOI: 10.1109/TPEL.2018.2853156.

[72] Kurs André et al. "Wireless Power Transfer via Strongly Coupled Magnetic Resonances." In: *Science* 317 (2007), pp. 83–86. DOI: 10.1126/science.1143254.

[73] Elisenda Bou-Balust, Aiguo Patrick Hu, and Eduard Alarcon. "Scalability Analysis of SIMO Non-Radiative Resonant Wireless Power Transfer Systems Based on Circuit Models." In: *IEEE Transactions on Circuits and Systems I: Regular Papers* 62.10 (2015), pp. 2574–2583. DOI: 10.1109/TCSI.2015.2469015.

[74] Xuezhe Wei, Zhenshi Wang, and Haifeng Dai. "A Critical Review of Wireless Power Transfer via Strongly Coupled Magnetic Resonances." In: *Energies* 7.7 (2014), pp. 4316–4341. DOI: 10.3390/en7074316.

[75] W.W. Mumford. "Directional Couplers." In: *Proceedings of the IRE* 35.2 (1947), pp. 160–165. DOI: 10.1109/JRPROC.1947.231592.

[76] Alicia Triviño-Cabrera and José A. Aguado Sánchez. "A Review on the Fundamentals and Practical Implementation Details of Strongly Coupled Magnetic Resonant Technology for Wireless Power Transfer." In: *Energies* 11.10 (2018), p. 2844. DOI: 10.3390/en11102844.

[77] Takehiro Imura. *Wireless Power Transfer: Using Magnetic and Electric Resonance Coupling Techniques*. Springer Singapore, 2020.

[78] Deepa Vincent et al. "Evolution of Hybrid Inductive and Capacitive AC Links for Wireless EV Charging—A Comparative Overview." In: *IEEE Transactions on Transportation Electrification* 5.4 (2019), pp. 1060–1077. DOI: 10.1109/TTE.2019.2923883.

[79] Jiejian Dai and Daniel C. Ludois. "A Survey of Wireless Power Transfer and a Critical Comparison of Inductive and Capacitive Coupling for Small Gap Applications." In: *IEEE Transactions on Power Electronics* 30.11 (2015), pp. 6017–6029. DOI: 10.1109/TPEL.2015.2415253.

[80] Chun T. Rim and Chris Mi. *Wireless Power Transfer for Electric Vehicles and Mobile Devices*. IEEE press, Wiley, 2017.

[81] Xiao Lu et al. "Wireless Charging Technologies: Fundamentals, Standards, and Network Applications." In: *IEEE Communications Surveys & Tutorials* 18.2 (2016), pp. 1413–1452. DOI: 10.1109/COMST.2015.2499783.

[82] Hoach The Nguyen et al. "Review Map of Comparative Designs for Wireless High-Power Transfer Systems in EV Applications: Maximum Efficiency, ZPA, and CC/CV Modes at Fixed Resonance Frequency Independent From Coupling Coefficient." In: *IEEE Transactions on Power*

Electronics 37.4 (2022), pp. 4857–4876. DOI: 10.1109/TPEL.2021.3124293.

[83] Yao Wang, Hua Zhang, and Fei Lu. "Review, Analysis, and Design of Four Basic CPT Topologies and the Application of High-Order Compensation Networks." In: *IEEE Transactions on Power Electronics* 37.5 (2022), pp. 6181–6193. DOI: 10.1109/TPEL.2021.3131625.

[84] Mehmet Zahid Erel et al. "A Comprehensive Review on Wireless Capacitive Power Transfer Technology: Fundamentals and Applications." In: *IEEE Access* 10 (2022), pp. 3116–3143. DOI: 10.1109/ACCESS.2021.3139761.

[85] IPT Technology. *IPT Charge Ship Inductive DC 100 kW*. Available at https://ipt-technology.com/product-ipt-charge-ship-100kw (2021/06/12).

[86] Wärtsilä. *Wireless Charging*. Available at https://www.wartsila.com/marine/build/power-systems/shore-connections/wireless-charging (2020/08/14).

[87] Jingang Li, Xuze Zhang, and Xiangqian Tong. "Research and Design of Misalignment-Tolerant LCC–LCC Compensated IPT System With Constant-Current and Constant-Voltage Output." In: *IEEE Transactions on Power Electronics* 38.1 (2023), pp. 1301–1313. DOI: 10.1109/TPEL.2022.3201124.

[88] Lei Yang, Minna Ju, and Ben Zhang. "Bidirectional Undersea Capacitive Wireless Power Transfer System." In: *IEEE Access* 7 (2019), pp. 121046–121054. DOI: 10.1109/ACCESS.2019.2937888.

[89] H. Zhang and F. Lu. "Feasibility Study of the High-Power Underwater Capacitive Wireless Power Transfer for the Electric Ship Charging Application." In: *2019 IEEE Electric Ship Technologies Symposium (ESTS), Washington, DC, USA* (2019), pp. 231–235.

[90] H. Mahdi, B. Hoff and T. Østrem. "Evaluation of Capacitive Power Transfer for Small Vessels Charging Applications." In: *2020 IEEE 29th International Symposium on Industrial Electronics (ISIE), Delft, Netherlands* (2020), pp. 1605–1610.

[91] Masaya Tamura et al. "Design of a Capacitive Wireless Power Transfer System for Operation in Fresh Water." In: *IEEE Transactions on Microwave Theory and Techniques* 66.12 (2018), pp. 5873–5884. DOI: 10.1109/TMTT.2018.2875960.

[92] Masaya Tamura, Kousuke Murai, and Marimo Matsumoto. "Design of Conductive Coupler for Underwater Wireless Power and Data Transfer." In: *IEEE Transactions on Microwave Theory and Techniques* 69.1 (2021), pp. 1161–1175. DOI: 10.1109/TMTT.2020.3041245.

[93] D. Kumar and F. Zare. "A Comprehensive Review of Maritime Microgrids: System Architectures, Energy Efficiency, Power Quality, and Regulations." In: *IEEE Access* 7 (2019), pp. 67249–67277.

[94] M. Mutarraf, Y. Terriche, K. Niazi, J. Vasquez, J. Guerrero. "Energy storage systems for shipboard microgrids—A review." In: *Energies* 11.12 (2018).

[95] Y. Khersonsky, M. Islam and K. Peterson. "Challenges of Connecting Shipboard Marine Systems to Medium Voltage Shoreside Electrical Power." In: *IEEE Transactions on Industry Applications* 43.3 (2007), pp. 838–844.

[96] Hussein Mahdi, Bjarte Hoff, and Trond Østrem. "A Review of Power Converters for Ships Electrification." In: *IEEE Transactions on Power Electronics* (2022), pp. 1–18. DOI: 10.1109/TPEL.2022.3227398.

[97] Fei Lu et al. "A CLLC-compensated high power and large air-gap capacitive power transfer system for electric vehicle charging applications." In: *2016 IEEE Applied Power Electronics Conference and Exposition (APEC)*. 2016, pp. 1721–1725. DOI: 10.1109/APEC.2016.7468099.

[98] Hua Zhang et al. "Six-Plate Capacitive Coupler to Reduce Electric Field Emission in Large Air-Gap Capacitive Power Transfer." In: *IEEE Transactions on Power Electronics* 33 (2018), pp. 665–675.

[99] Hussein Mahdi et al. "Conformal Transformation Analysis of Capacitive Wireless Charging." In: *IEEE Access* 10 (2022), pp. 105621–105630. DOI: 10.1109/ACCESS.2022.3210960.

[100] Hussein Mahdi et al. "A Class-E-Based Resonant AC-DC Converter With Inherent PFC Capability." In: *IEEE Access* 9 (2021), pp. 46664–46673. DOI: 10.1109/ACCESS.2021.3067800.

[101] Hussein Mahdi, Bjarte Hoff, and Trond Østrem. "Maximum Available Efficiency of Undersea Capacitive Coupling in a Wireless Power Transfer System." In: *2021 IEEE 30th International Symposium on Industrial Electronics (ISIE)*. 2021, pp. 1–5. DOI: 10.1109/ISIE45552.2021.9576386.

[102] Hussein Mahdi, Bjarte Hoff, and Trond Østrem. "Optimal Solutions for Underwater Capacitive Power Transfer." In: *Sensors* 21.24 (2021), p. 8233. DOI: https://doi.org/10.3390/s21248233.

[103] Hussein Mahdi et al. "Investigation of Wireless Electrification for a Reconfigurable Manufacturing Cel." In: *Journal of Manufacturing Systems* (2023). DOI: 10.1016/j.jmsy..

A

Additional Published Papers

Investigation of wireless electrification for a reconfigurable manufacturing cell

H. Mahdi, H. Arnarson, B. Solvang, and B. A. Bremdal

DOI: 10.1016/j.jmsy.2023.01.002

Paper's Contribution

This paper investigates wireless electrification for manufacturing applications and proposes an autonomous battery platform based on CPT for the electrification of a Reconfigurable Manufacturing System (RMS). Moreover, it builds and demonstrates how an RMS can be energized using WPT to increase flexibility and automation. Finally, the paper tests and demonstrates the CPT system with the battery platform to prove the concept.

Journal of Manufacturing Systems 67 (2023) 379–388

Contents lists available at ScienceDirect

Journal of Manufacturing Systems

journal homepage: www.elsevier.com/locate/jmansys

Technical paper

Investigation of wireless electrification for a reconfigurable manufacturing cell

Hussein Mahdi [b], Halldor Arnarson [a,*], Bjørn Solvang [a], Bernt Arild Bremdal [c]

[a] Department of Industrial Engineering, UiT The Arctic University of Norway, Lodve Langesgate 2, Narvik, 8514, Nordland, Norway
[b] Department of Electrical Engineering, UiT The Arctic University of Norway, Lodve Langesgate 2, Narvik, 8514, Nordland, Norway
[c] Department of Computer Science and Computational Engineering, UiT The Arctic University of Norway, Lodve Langesgate 2, Narvik, 8514, Nordland, Norway

ARTICLE INFO

Keywords:
Wireless power transfer (WPT)
Battery platform
Capacitive power transfer (CPT)
Reconfigurable manufacturing system (RMS)
Industry 4.0

ABSTRACT

Reconfigurable manufacturing systems (RMS) with a rearrangeable structure can quickly adjust their productivity to meet the dynamic market changes and the demand for high-variety products. Industry 4.0 technologies have enhanced the RMS flexibility and made the automation of the reconfiguration of the manufacturing system possible. As an Industry 4.0 technology, wireless power transfer (WPT) can further increase the flexibility of RMS by providing safe, reliable, and maintenance-free autonomous charging. This paper examines the wireless electrification of RMS by investigating different WPT configurations that increase flexibility and autonomy, creating a highly flexible RMS. It also proposes a battery charging platform for further enhancement of the flexibility of RMS. As a low-cost WPT solution, the paper tests capacitive charging systems. The proposed charging system has about 135 W power transfer capability at a 5 cm distance and about 84% efficiency.

1. Introduction

Automated manufacturing systems have experienced noticeable changes passing through three main paradigms. The first paradigm is Dedicated Manufacturing System (DMS), which focuses on mass production for cost-effectiveness but with a low variation. The second paradigm is Flexible Manufacturing System (FMS) that address the production variety with low production volume. Finally, Reconfigurable Manufacturing System (RMS) is the third paradigm with high volume and high variation production combining the characteristics of the previous two paradigms. The RMS has a rearrangeable structure that can quickly adjust its productivity, variety, and flexibility based on the demand [1].

The dynamic market changes and the increasing competition between manufacturers to produce high-quality products with innovative technologies make the RMS an attractive paradigm. Bi et al. [2] proposed a systematic design methodology for RMS, including architecture, configuration, and control design. In practice, however, there is still a lack of research on how to solve design issues because a limited number of case studies are available [3]. Although the researchers have exerted considerable effort in developing RMS for several decades, there are still significant challenges, and barriers to the actual development of RMS in industry [4]. Rösiö et al. [5] explored the theoretical and practical challenges to achieving RMS design and summarized them in three main challenges: to use a structured design methodology and gain knowledge in reconfigurability and its characteristics, and to include the reconfigurability knowledge in a structured design methodology.

For research and educational purposes, the Engineering Research Center for Reconfigurable Manufacturing Systems at the University of Michigan developed a distributed reconfigurable factory testbed [6]. Kovalenko et al. [7] proposed real and virtual environment interaction (digital twin) framework to evaluate the performance of different machines and system configurations in a mixed virtual–real environment. Zuehlke D. [8] proposed adopting the basic principle of the Internet-of-Thing (IoT) in a testbed to proof-the-concept that moving toward intelligent manufacturing is a reality. Although the researcher tried to emulate RMS using a testbed, however, these systems require human intervention to rearrange the system, which is a time-consuming process and may suffer from limited positioning.

In general, the RMS suffers from several challenges, such as it is not the complete solution to meet all of the manufacturing requirements [2]. Besides, there is still no perfect or the most realistic model and method for RMS implementation. The rearrangement of the RMS structure is also time-consuming [6]. The RMS still depends on labor to rearrange the system structure and energize the platforms, which might affect the production time and limit the flexibility of the systems. And recently, the COVID-19 pandemic has added more challenges to

* Corresponding author.
E-mail address: halldor.arnarson@uit.no (H. Arnarson).

https://doi.org/10.1016/j.jmsy.2023.01.002
Received 4 July 2022; Received in revised form 20 December 2022; Accepted 4 January 2023
Available online 24 February 2023

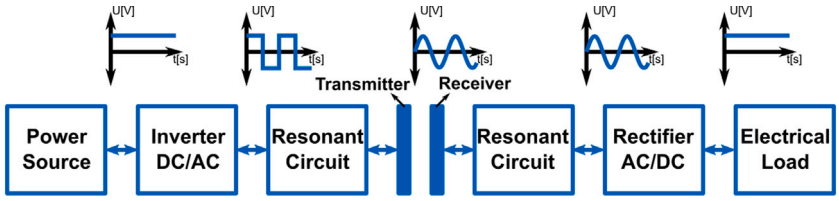

Fig. 1. An illustration of wireless electrification system.

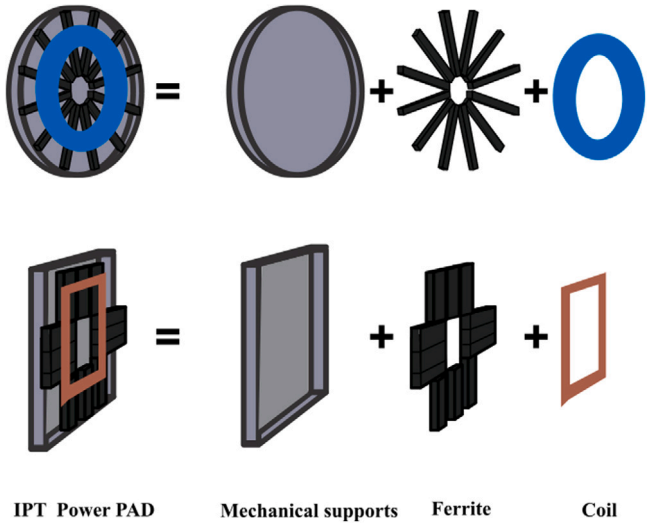

Fig. 2. An exploded view of IPT's different shape power pads.

the manufacturing systems, including lockdown and maintaining social distance [9], which can increase the rearrangement time of RMS and reduce its flexibility.

To tackle the challenges above, Arnarson et al. [10] introduced the autonomous RMS by using a mobile robot to rearrange robot arm platforms automatically to achieve flexibility and mobility. As an expansion, Arnarson et al. [11] presented a highly flexible RMS by retrofitting a number of manufacturing machines to automate the reconfiguration of the system, decrease the setup and programming time, and enhance the system's flexibility. Randanovi et al. [12] tried to solve one of the common problems of the conventional wired electrification of RMS by standardizing the connectors and plugs. In contrast, Arnarson et al. [11] considered Wireless Power Transfer (WPT) as an emerging industry 4.0 technology for electrifying RMS that tried to remove the plugs, connectors, and cables to increase the flexibility and reliability of the electrification of RMS.

The previous research on RMS investigated testbed manufacturing cells which are aimed for educational and research purposes [6–8]. Recently, researchers tried to develop a practical RMS using industry 4.0 technologies [11]. However, the proposed system still requires labor to connect the machines to electricity or charging batteries. As an industry 4.0 technology, wireless electrification can provide the required energy to these platforms without mechanical contact, similar to how IoT communication brings wireless communication. Previous research investigated wireless electrification for various applications in general and industrial robots in specific. There are also various products for robot charging applications on the market. However, the focus is more on one type of WPT, which utilizes magnetic fields.

This paper investigates the state-of-the-art WPT for robotics in manufacturing applications in the literature and on the markets. Based on the investigation, the paper proposes a novel approach to the electrification of manufacturing applications based on Capacitive Power Transfer (CPT), which creates a new foundation for RMS that significantly increases the system's flexibility and reconfigurability. Thus, we propose and test a battery platform using CPT that utilizes electric fields to wirelessly electrify other manufacturing machines in an RMS. We can summarize the main contribution of the paper as follows:

- Investigating wireless electrification for manufacturing applications.
- Proposing an autonomous battery platform based on CPT for electrification of RMS.
- Build an RMS and demonstrate how it can be energized using wireless power transfer to increase flexibility and automation.
- Simulating, testing, and demonstrating the CPT system with the battery platform to prove the concept.

We organize the rest of this paper as follows: Section 2 presents the general concept of wireless electrification of RMS. Section 3 investigates the state-of-the-art WPT for robotics and manufacturing applications. Section 4 expands the RMS by building a battery platform that can power the system in static, dynamic, or quasi-dynamic mode. Section 5 presents the experimental and testing results of the CPT system. Section 6 gives a comprehensive discussion of WPT systems in general and CPT systems in specific. Section 7 concludes this work and presents our future works.

Table 1
A comparison between the main three groups of WPT.

	Near-field	Mid-range	Far-field
Wave	Electric/Magnetic	Magnetic	Electromagnetic
Rang	Very short (cm)	short (m)	Medium long (km)
Frequency	low high	high	Very high extreme high
Power	low moderate	Moderate	Very low
Architecture	Simple/Moderate	Complex	Complex

2. Wireless electrification

Wireless electrification, or WPT, is to transfer electric power without mechanical contact. International Telecommunication Union [13] defines WPT as "*the transmission of power from a power source to an electrical load using the electromagnetic field.*" The three main groups of these technologies are near-field, mid-range, and far-field [14]. The classification depends on the size of the transmitter and the receiver, and the transfer distance. Table 1 summarizes a comparison between the three main groups in terms of the type of wave, distance range, operating frequency range, power level, and system architecture.

Near-field WPT utilizes medium- to high-frequency range electromagnetic fields for high-power charging applications. Thus, the separation distance between the transmitter and the receiver is in the cm range. WPT can provide static, quasi-dynamic, and dynamic electrification [15,16]. It can also energize the system autonomously and potentially address the challenges in the conventional conductive charging approach, including long charging time, wear and tear of the contractors and plugs, and the hazard of the electric shock. Using WPT in RMS provides autonomous electrification and removes the time consumption of plugging the cables.

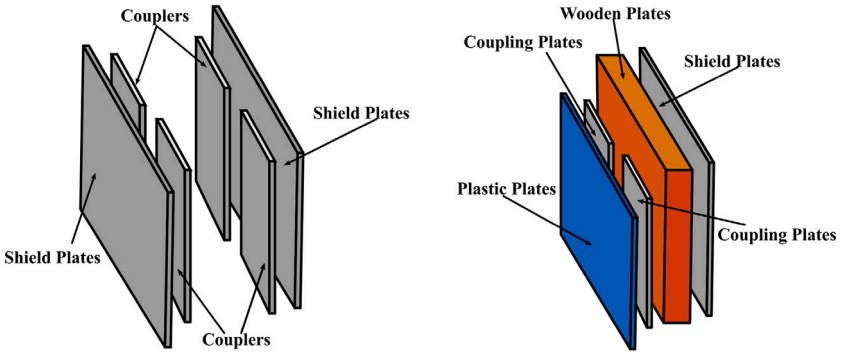

Fig. 3. Capacitive coupler: six plates CPT system (left) and an exploded view of capacitive couplers (right).

Fig. 1 illustrates the functional blocks in the WPT system. The inverter converts the DC source voltage into a square wave which depends on the operation frequency of the inverter. The resonant circuit improves the system's overall efficiency by minimizing the reactive power, achieving soft-switching, and high misalignment tolerance. The resonant circuits also act as low-pass filters that filter out the high harmonics in the current of the inverter and reduce electromagnetic interference. Finally, the rectifier stage converts the ac resonant current into a DC. The wireless electrification system might need other DC/DC converters, for instance, between the power source and the inverter or between the rectifier and the load, which depends on the design specifications. The near-field WPT embraces three sub-group, namely, Inductive Power Transfer (IPT) and Capacitive Power Transfer (CPT).

2.1. Inductive power transfer

Inductive electrification, or IPT, operates on loosely coupled magnetic fields between transmitter and receiver coils. It includes inductive and inductive resonance. The only difference between inductive and inductive resonance is the resonance compensation circuits. The transmitter and receiver of the IPT system are also called "power pads," composed of coils to produce alternating magnetic fields, Ferrite to align and shield the fields, and mechanical supports, as shown in Fig. 2. The Litz wire provides a solution for increasing the conductivity of the coil at high operation frequency while screening the magnetic fields. Nevertheless, both the Litz wire and the Ferrite make the pads expensive, heavy, and fragile [17]. Depending on the dimension of the power pads, the coupling and hence the efficiency of IPT systems can significantly change with the separation distance, and misalignment changes [18]. Increasing the power pads is one way to achieve better misalignment performance [19]. However, it will increase the overall system's weight, cost, and design complexity.

2.2. Capacitive power transfer

Capacitive electrification, or CPT, utilizes alternating electrical fields that are confined between transmitter and receiver plates, also called "capacitive couplers," to transfer power. We can build CPT systems using two-, four-, or six-plates configurations. Fig. 3 illustrates a six-plate configuration of the CPT system's transmitter–receiver, which includes four plates forming the capacitive couplers and two plates screening the electric fields. The six plates configuration can reduce the safety clearance range from 1 m to 10 cm [20]. The transmitter and the receiver consist of aluminum capacitive couplers, plastic plates, wooden plates, and shielding plates. The plastic plates offer insulation protection, while the outer plates work as a shield to screen the leakage electric fields and offer extra protection. The wooden plates insulate the screening plates from the couplers. Based on the structure, the capacitive coupler is lighter and costs less than the IPT power pad. The CPT system is still sensitive to misalignment [20], yet it has a much better misalignment performance than the IPT system [17].

Table 2
A Comparison between IPT and CPT.

	IPT	CPT
Power Range	tens of kW	hundreds of W
Eddy Current Losses	high	low
Misalignment Performance	bad	good
Cost	high	low
Pads'/Couplers' Weight	heavy	light
Efficiency	high	medium
Fields Shielding	complex	simple

To sum up, IPT systems contain Litz wires and magnetic screenings, which are expensive, fragile, and heavy. Besides, the magnetic fields can interact with the metal parts of the platforms resulting in high eddy losses, which can increase the temperature of the platforms. As an alternative, CPT is more suitable for the platform as it tackles the challenges that face IPT systems. Table 2 lists a comparison between IPT and CPT systems in terms of power density, losses, misalignment performance, cost, weight, and efficiency.

3. The state-of-the-art WPT for robotics in manufacturing applications

Wireless power transfer has several distinctive advantages, including reliability, flexibility, and autonomy, making it an attractive solution in many applications. More than 30 years ago, Esser and Skudelny [21] investigated wireless inductive electrification using rotatable transformers fixed on the joint of a robot. They managed to transfer 20 kW over 100 µm. About ten years later, Hirai et al. [22] proposed IPT for an autonomous decentralized manufacturing system for electrification and data transfer purposes. The proposed system transferred a consecutive 1250 GB data transmission under the continuous 2 kW power transmission over 100 µm to 500 µm to a servomotor. Since then, the research has focused more on IPT industrial robot applications. In this section, however, we focus on the most recent studies on high-power WPT for robotics in manufacturing applications and investigate the available WPT solutions on the market. Low power and data transfer are out of the scope of this paper.

3.1. Robotic arms

Wireless power transfer offers robotic arms distinct merits such as no risk of electrocution, high convenience and robustness, and water- and dust-proof [23]. Thus, wireless electrification (WPT) applications for robot arms have gained more attention. Inductive electrification (IPT) is the common approach used in robotic arms by applying magnetic connections at the joint. Han et al. [23] energized two permanent magnet dc motors in a robot arm using IPT. And they reported output power of 142.9 W at 88.7% transmission efficiency. Besides, Kikuchi et al. [24] proposed IPT to power a robot manipulator used

Table 3
Summary of WPT applications in the literature.

Ref.	Application	Power [W]	Eff. [%]	Freq. [kHz]	Dist. [mm]
[23]	Robotic Arm	142.9	88.7	85	100
[24]	Robotic Arm	311.6	92	246	5
[25]	Robotic Arm	39.9	78	6780	250
[26]	Robotic Arm	85.9	84	150	100
[28]	Logistic Robot	150	90	300	200
[30]	Transport Robot	30	74.2	100	8

in warehouse automation systems. They built a prototype with a maximum power of 311.6 W and total efficiency of 94%. Moreover, Tokano et al. [25] experimented with a 39.9 W and 78.0% power-delivery efficiency for conventional robot arms. Finally, Wu et al. [26] proposed and tested a 85.9 W multidegree freedom and bidirectional transmission capability WPT system for robot arm's joints (see Table 3).

3.2. Transport and mobile robots

For flexible manufacturing, IPT systems have found their application with clean factory automation through the dynamic powering of vehicles on monorails which have spread to floor-mounted automatic guided vehicles and other industrial vehicles [27]. Zhang et al. [28] proposed an IPT system for a logistic robot within a confined three-dimensional space around the charging station. In addition, Lee et al. [29] proposed an IPT system for continuous wireless powering of multiple transport robots in an electrified monorail system. Table 3 lists the available wireless solution in the literature.

3.3. WPT on the market

Many manufacturers are working to develop WPT technologies for robot joints of robotic arms applications. TDK [31] offers a 200 W IPT system for mobile robots that has a power distance 100 mm to 300 mm, 88% efficiency, and a 50 W IPT system for robot arms. Moreover, Waypoint Robotics [32] offers a 300 W non-contact charging and energy delivery system that ensures maximum availability of their mobile robot fleet. Delta [33] provides a 1 kW IPT system for mobile with a maximum efficiency of 93%. In addition, Wibotic [34] provides a 300 W IPT charging solution for mobile robots. Table 3 lists the WPT systems on the market for manufacturing.

Thus far, the previous research has focused more on IPT industrial robot applications and less focus on manufacturing cells. The examples in the literature and on the market only use IPT. The IPT systems comprise expensive, fragile, and heavy components, and they have high eddy losses. In contrast, CPT is more suitable for the platform as it tackles the challenges that face IPT systems. To the authors' knowledge, there has not been any investigation on CPT to power a manufacturing cell. In the next section, we propose a CPT system for the electrification of a RMS manufacturing cell.

4. RMS with battery platform

4.1. The structure of the proposed RMS

Previously, Arnarson et al. [11] proposed an RMS consisting of five platforms; two industrial robots (Scara and Nachi), a conveyor platform, a conveyor lift platform, and a 3D printing platform. The RMS can move and rearrange automatically with the help of a mobile robot in a manufacturing environment that is flexible and scalable, and it has the potential to be fully autonomous. A demonstration video [35] shows the mobile robot picking up the platforms and assembling two manufacturing layouts. In this paper, we expand the system by proposing a battery platform to increase the flexibility of the RMS (see Fig. 4).

Table 4
Power usages of the modules.

Module	Power [W]
IRB1 (Scara)	141
IRB2 (Nachi)	242
Conveyor	38
Conveyor lift	54
3D printer	350

4.2. Battery platform

In this paper, we suggest adding two extra platforms to the system, containing only batteries. While one platform is charging, the other is powering the system, as shown in Fig. 5. When the platform powering the system is running out of power, a fully-charged battery platform can replace it. The capacity of the batteries on the battery platform decides how long the platform can power the system. The mobile robot drives to pick up a full battery platform at the charging station and places it within the RMS. Then, the mobile robot picks up the empty battery platform and transports it to the charging station. Afterward, the mobile robot can do other logistics tasks. A video https://youtu.be/o3jhAhYdPUc demonstrates a simulation of how the battery platforms change.

The battery platform can also power other platforms in the system in the static, dynamic, or quasi-dynamic modes, as shown in Fig. 6. Thus, the mobility of the battery platform gives the system more flexibility, reconfigurability, and reliability. In addition, the battery platform can also charge the mobile robot. When the mobile robot is moving the battery platform, the battery platform can charge the mobile robot. This allows a flexible method to charge the mobile robot without the need to turn to a charging point, but it depends on the capacity of the batteries.

5. Experimental validation and testing

5.1. The power requirement

All the platforms have small computers and microcontrollers to collect data from the sensors and operate independently. For each platform, we measured the power consumption under normal operation. This means measuring the total power consumption of the computers and robots/conveyors while they are moving. Table 4 lists the power usage of all platforms under test operation conditions. The platforms require low power consumption to run the system, which ranges 43 W to 350 W. As the required power is not high, using WPT can be a flexible solution to power the system.

It should be noted that the conveyor uses only 38 W in this system since the motor uses a gearbox with a 75:1 ratio. The idea of this demonstration is to show that a manufacturing system that has low power consumption can be wirelessly powered. Each platform is equipped with batteries that can be used to supply the manufacturing platforms with power peaks as long as the power draw is not higher than from the WPT system. Large machines, such as CNC and 3D printers, consume large power, which will be a challenge to electrification wirelessly. These large machines are not reconfigurable, as they require re-calibration; hence the reconfigurable platforms are rearranged around them. Thus, we will not consider wireless electrification for these large machines.

5.2. Capacitive wireless electrification for RMS

As an inexpensive and simple solution for electrifying the RMS, we will continue investigating the CPT system. We use the same configuration shown in Fig. 3 to build the capacitive couplers. The size of the couplers is 25 × 25 cm, the wooden plate is 30 × 70 cm, and the shield plate is 25 × 70 cm. The distance between the plates on

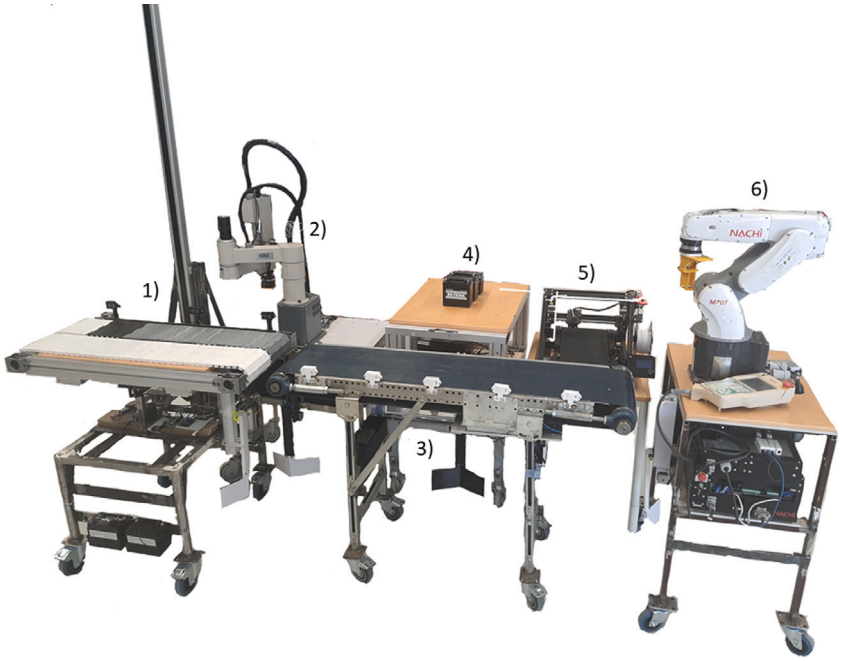

Fig. 4. The expansion of RMS with battery platform. (1) conveyor with lifting (2) Scara platform, (3) conveyor, (4) battery platform, (5) 3D printer, and (6) Nachi platform.

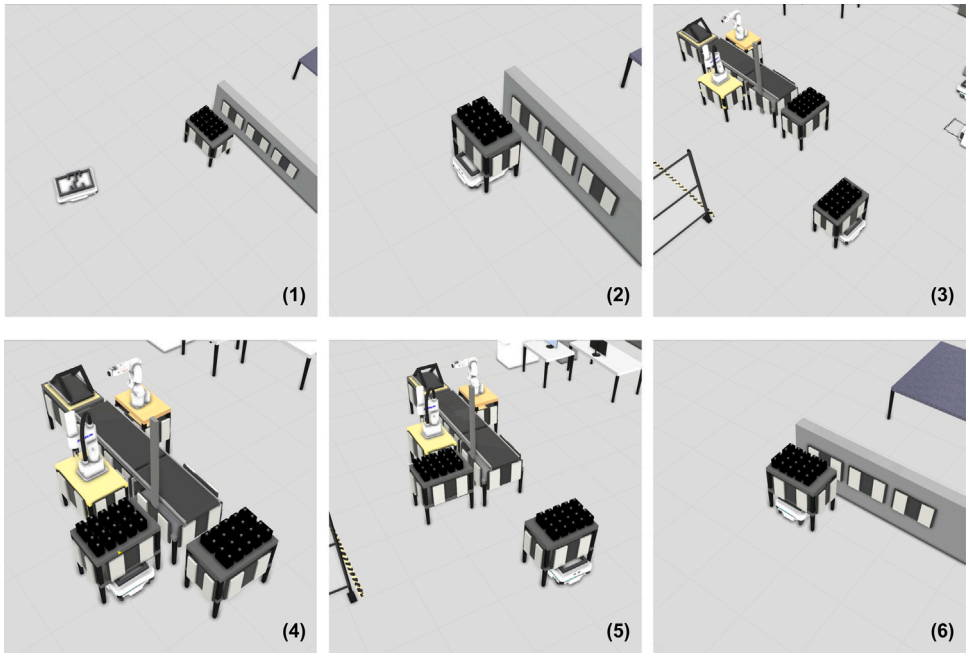

Fig. 5. The operation principle of the battery platform: The mobile robot drives to pick up a full battery platform (steps 1 to 4), picks up the empty battery platform, and transports it to the charging station (steps 5 to 6).

the same sides is 10 cm. We utilize a GaN bridge inverter (Infineon EVAL1EDFG1HBGAN [36]) and four Schottky diodes (C6D04065 A [37]) to build the rectifier bridge. We also used air-cored inductors in the series resonant circuit to compensate both transmitter and the receiver sides with the inductance of 235.1 μH for L_T and 268.3 μH for L_R.

Fig. 7 presents testing results in the laboratory. The CPT output power is about 109 W with an efficiency of about 73% at 150 V input voltage and 1.3 MHz. The maximum voltage is more than 600 V across the couplers, and the maximum current through the receiver side inductor is about 1 A. Due to the harmonics, the current is not a pure sine waveform. This video https://youtu.be/-mubROmWRcI shows the testing of the CPT system.

We can further increase the output power by increasing the input voltage. To further improve the efficiency and increase the transmitting distance, we also increased the size of the coupling plates to 30 × 45 cm, and the distance between the couplers was 18 cm. The CPT output power is about 134.6 W with a total efficiency of about 84% at 1 MHz and about 5 cm distance between the transmitter and the receiver.

Fig. 8 shows the separation distance's effect on the CPT system's efficiency. The efficiency decreases with the increase of the distance, which we can attribute to the sensitivity of the compensation circuits (i.e., the resonant frequency) to the distance change. One way to

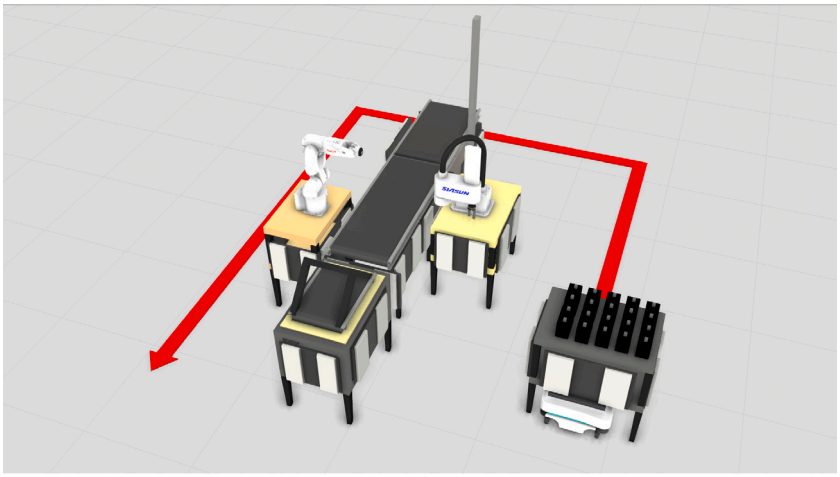

a)

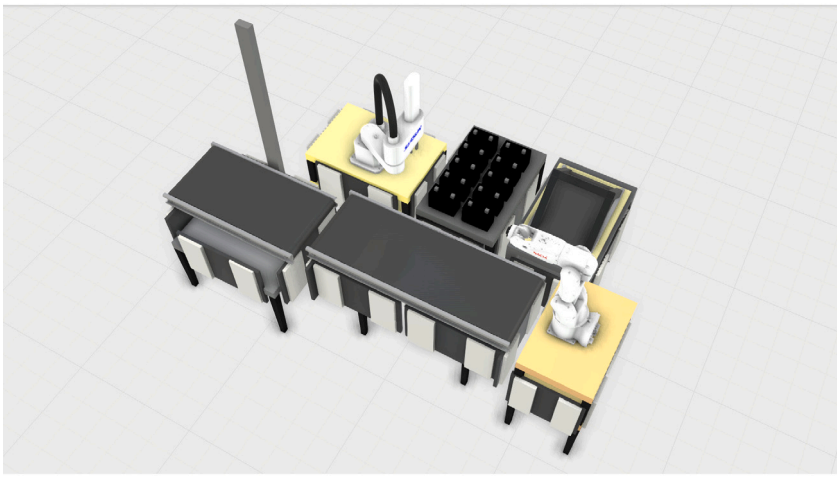

b)

Fig. 6. The two operation modes of battery platform: (a) The dynamic mode. (b) the static mode.

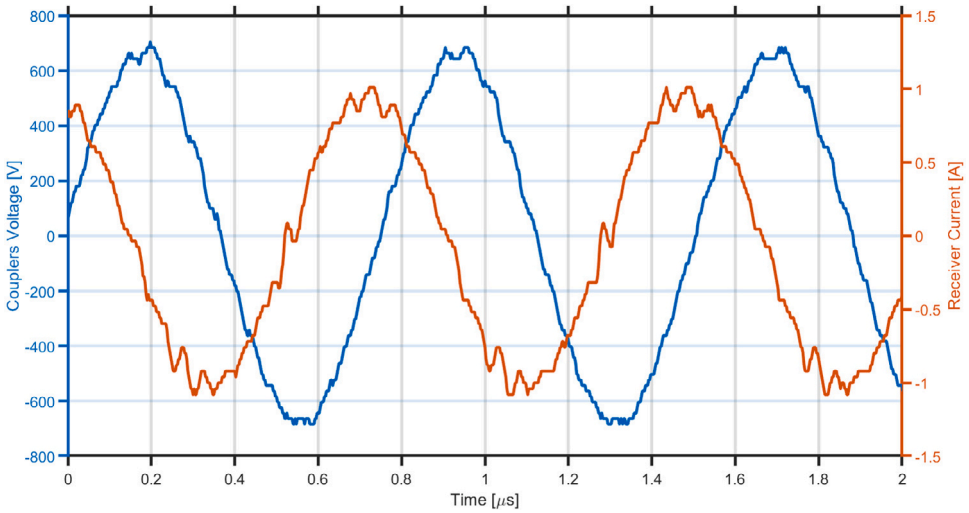

Fig. 7. The voltage across the couplers and the current on the receiver side.

enhance the efficiency is by proposing control techniques to operate the inverter at a frequency that can adapt to the change in the distance.

When the maximum output voltage of the inverter is 300 V, the voltage across the couplers can reach about 1.9 kV, which is high voltage stress, as shown in Fig. 9. Fig. 10 shows the currents through the transmitter's and the receiver's indicators. The transmitter's current is about 2.2 times the amplitude higher than the receiver's current.

To prove the concept, we designed a battery platform with three batteries connected in parallel as a power source and the CPT system transmitter plates, shown in Fig. Fig. 4. We also equipped it with

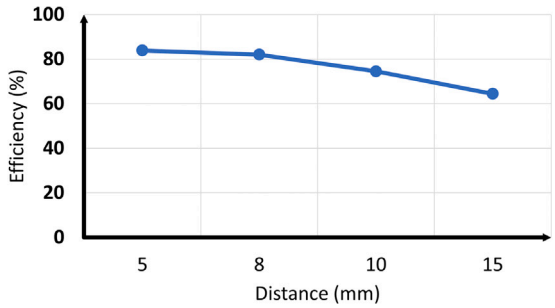

Fig. 8. The efficiency of the CPT system versus the change in the separation distance between the platforms.

a converter that steps up the 12 V input voltage to 300 V voltage to achieve the required electric field strength. Moreover, we retrofitted the conveyor platform with the receiver couplers, and the step-down converter stage converted the output voltage from 300 V to 12 V. The functional blocks of the proposed CPT system show the parts of the systems and the components that are used in each part, as shown in Fig. 11.

Fig. 12 shows the demonstration of a CPT system between two platforms. In the demonstration, the mobile robot picks up the battery platform and brings it to the other platforms. Then, the battery platform starts energizing the conveyor platform, which is not equipped with batteries. Fig. 12 and the video https://youtu.be/KRwIdJ8fu5A show the experiment described above.

6. Discussion

Arnarson et al. [11] tried to tackle the challenges that RMS encounters by retrofitting manufacturing machines with industry 4.0 technologies. Their system can automatically arrange five platforms using a mobile robot for manufacturing a specific product. The system is flexible and scalable and can be autonomous, but all platforms are energized with batteries, which require human intervention to charge them. Thus, there is a need for an autonomous method for charging or electrifying the platforms to make the proposed system fully autonomous.

Dealing with the charging problem, Randanovi et al. [12] tried to solve one of the common problems of the conventional wired electrification of RMS by standardizing the connectors and plugs. Another solution is to use the same principle of charging a mobile robot through electro-mechanical parts, but this solution limits the platforms' positioning and increases the need for maintenance due to the wear and tear of these contacts.

From the opposing point of view, Arnarson et al. [11] proposed WPT, which tried to remove the plugs, connectors, and cables to increase the flexibility and reliability of the electrification of RMS. They also proposed WPT as industry 4.0 technology to increase the flexibility of the manufacturing system. One of the industry 4.0 technologies is the IoT, where we can communicate wireless between machines and sensors. Similarly, we can wirelessly electrify machines and other robots, removing restrictions and making them more flexible. It was, therefore, suitable to include WPT as an industry 4.0 technology and be implemented in the following paradigms of RMS.

Using WPT, we can utilize static or dynamic WPT to electrify the system to improve its flexibility and reduce the time to reconfigure the system [11]. The dynamic WPT can electrify the platforms and the mobile robot, increasing the system's extent and cost. In contrast, static WPT offers a good option to electrify the platforms from each other or a main fixed machine. The system will get better efficiency by correcting the misalignment between the platforms.

The researchers previously investigated WPT for industrial robot electrification with power ranges from tens to hundreds of watts. On the market, there are already commercial solutions with power ranges 50 W to 300 W. However, IPT is commonly used in the literature and industrial robot applications markets. We can utilize static IPT for high power requirements of the platforms or vast distances between them. However, IPT systems contain heavy, fragile, and expensive power pads and are sensitive to misalignment and eddy losses, decreasing the overall system efficiency.

One limitation of the WPT system which proposed to RMS in [11] is that when the platforms are not connected to a wireless charging point, they need to be moved back when their battery is running low. As a novel approach to the electrification of manufacturing applications, we proposed a battery platform that can electrify other platforms of mobile robots in static, dynamic, or quasi-dynamic charging modes to increase the flexibility and reliability of the WPT charging system.

Building this platform, we increased the distance between the couplers to 5 cm and the input voltage to 300 V to achieve 134.6 W and about 84% system efficiency at 1 MHz. The proposed system demonstrated that static CPT is a low-cost alternative. However, the system's efficiency can be degraded with the increase in the distance as the system operates in an open loop. To solve this problem, we will prove a control technique that changes the operating frequency with the change in the separation distance to track the maximum efficiency of the system.

The results also showed that increasing the input voltage increases the voltage across the couplers to about 2 kV, which increases the electric fields between the plates. However, the shielding plates screen the electric fields from interacting with the platform's parts or endangering the workers near the plates. The results also show that the current on the transmitter and receiver sides have harmonics, which can have electromagnetic interference with the system. We can tackle this problem by investigating better compensation circuits to filter out the harmonics and enhance the electromagnetic compatibility of the CPT system in RMS.

Implementing the battery platform allows us to reconfigure the system in any place. Depending on the capacity of the batteries, the battery platform can charge other platforms or mobile robots in static or motion, which can further increase the flexibility and reliability of the system. For instance, the battery platform can electrify the 3D printer platform, which has the maximum power usage of 350 W, for 8 h if we connect ten batteries in parallel. The capacity of the batteries is an essential factor that decides the charging period, but increasing the capacity by adding more batteries will increase the weight of the platform resulting in a docking problem for the mobile robot, as Arnarson et al. [11] discussed.

7. Conclusion and future works

This paper investigated WPT solutions for robotics in manufacturing applications. Focuses are more on IPT industrial robot applications manufacturing cells in the literature and on the market. However, the paper presented the general concept of wireless electrification using near-field WPT technologies, namely, IPT or CPT for RMS. It also proposed and tested a static CPT system as an inexpensive and light alternative for manufacturing cells, as the proposed system comprises no expensive, fragile, or heavy parts. Utilizing a six-plates configuration, the safety clearance of the CPT system can be reduced to a few centimeters. As a novel approach to the electrification of manufacturing applications, a battery platform is designed based on the CPT system, which is a part of an RMS consisting of five other platforms: two industrial robots (Scara and Nachi), a conveyor platform, a conveyor lift platform, and a 3D printing platform. The battery platform can charge the batteries of other platforms. Hence it gives the system more flexibility, reconfigurability, and reliability. The proposed CPT system gives an output power of 135 W with 84% efficiency at 5 cm separation

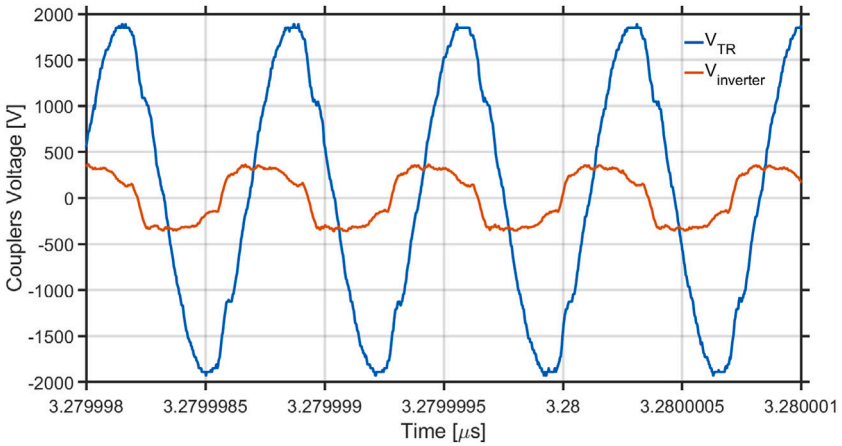

Fig. 9. The output voltage of the inverter (V_{inverter}) and the voltage across the couplers (V_{TR}).

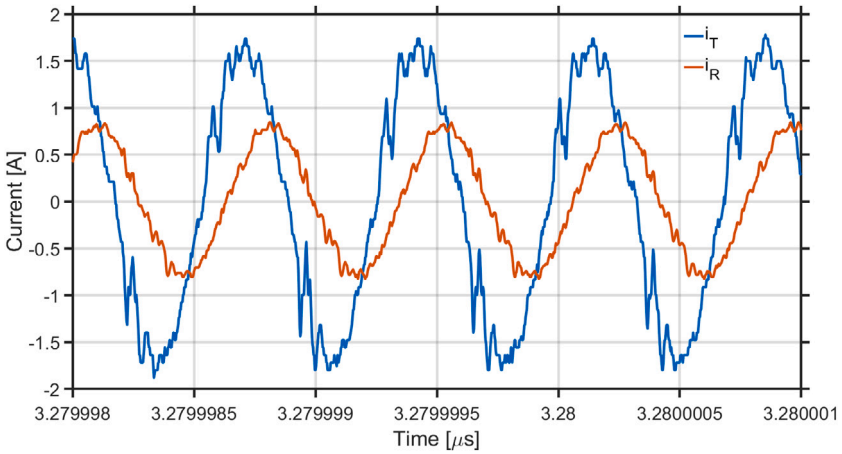

Fig. 10. The current on the transmitter side (i_{T}) and the receiver side (i_{R}).

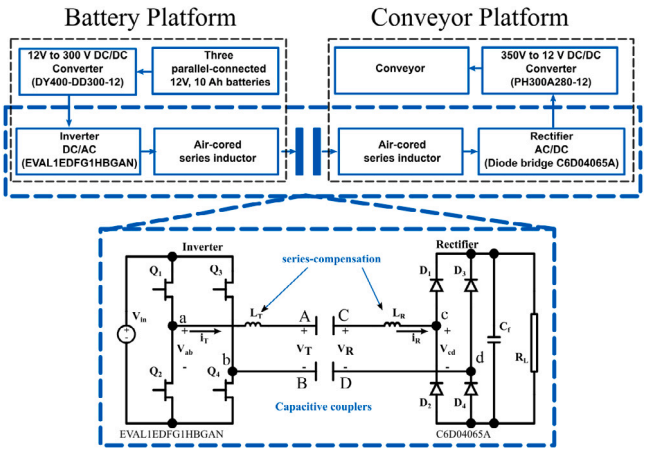

Fig. 11. The experimental setup.

distance. The efficiency decreases with the increase of the distance, which can be attributed to the sensitivity of the compensation circuits to the distance change. One way to enhance the efficiency of the system is by proposing control techniques to operate the inverter at a frequency that can adapt to the change in the distance. As further work, we will further improve the system efficiency and increase the transfer distance by proposing different resonant circuits. We will also investigate a control technique to achieve high efficiency with the variation of the separation distance.

Declaration of competing interest

The authors declare that they have no known competing financial interests or personal relationships that could have appeared to influence the work reported in this paper.

Acknowledgment

This project has received funding from the European Union's Horizon 2020 Research and Innovation Programme under grant agreement No. 825196. All authors approved the version of the manuscript to be published.

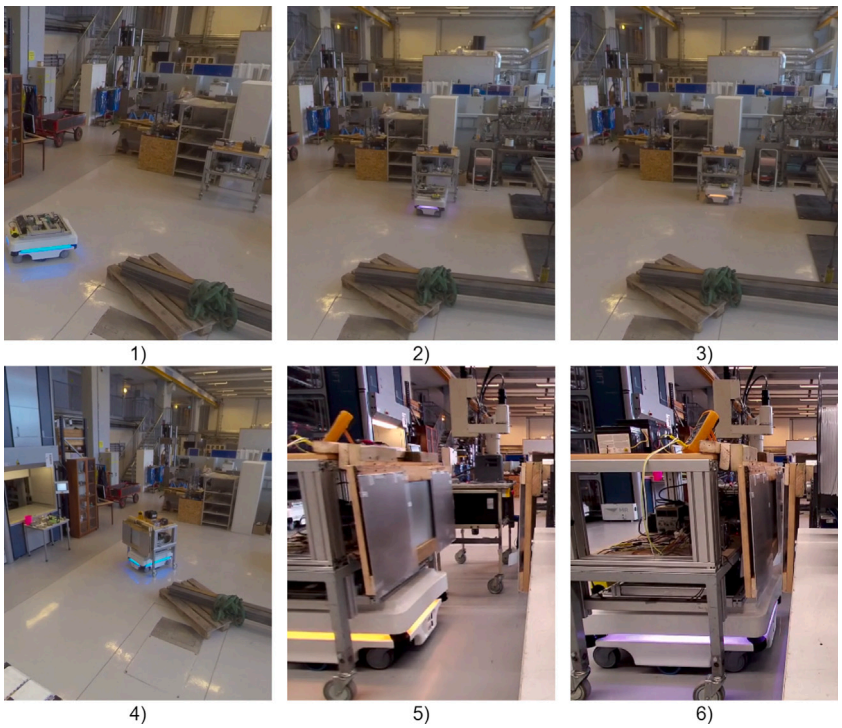

Fig. 12. Demonstration of how the CPT is implemented into the RMS: The mobile robot drives to pick up a full battery platform (step 1 to 4) and transports it to the charging RMS (step 5 to 6).

References

[1] Koren Y, Heisel U, Jovane F, Moriwaki T, Pritschow G, Ulsoy G, et al. Reconfigurable manufacturing systems. CIRP Ann 1999;48(2):527–40. http://dx.doi.org/10.1016/S0007-8506(07)63232-6.

[2] Bi ZM, Lang SYT, Shen W, Wang L. Reconfigurable manufacturing systems: the state of the art. Int J Prod Res 2008;46(4):967–92. http://dx.doi.org/10.1080/00207540600905646.

[3] Andersen A-L, Brunoe TD, Nielsen K, Rösiö C. Towards a generic design method for reconfigurable manufacturing systems: Analysis and synthesis of current design methods and evaluation of supportive tools. J Manuf Syst 2017;42:179–95. http://dx.doi.org/10.1016/j.jmsy.2016.11.006.

[4] Andersen A-L, Nielsen K, Brunoe TD. Prerequisites and barriers for the development of reconfigurable manufacturing systems for high speed ramp-up. Procedia CIRP 2016;51:7–12. http://dx.doi.org/10.1016/j.procir.2016.05.043.

[5] Rösiö C, Säfsten K. Reconfigurable production system design – theoretical and practical challenges. J. Manuf Technol Manag 2013;24:998–1018. http://dx.doi.org/10.1108/JMTM-02-2012-0021.

[6] Kim D-Y, Park J-W, Baek S, Park KB, Kim H-R, Park J-I, et al. A modular factory testbed for the rapid reconfiguration of manufacturing systems. J Intell Manuf 2020;31:661–80. http://dx.doi.org/10.1007/s10845-019-01471-2.

[7] Kovalenko I, Saez M, Barton K, Tilbury DM. SMART: A system-level manufacturing and automation research testbed. Smart Sustain Manuf Syst 2017;1:232–61. http://dx.doi.org/10.1520/SSMS20170006.

[8] Zühlke D. SmartFactory - towards a factory-of-things. Annu Rev Control 2010;34:129–38. http://dx.doi.org/10.1016/j.arcontrol.2010.02.008.

[9] Malik AA, Masood T, Kousar R. Reconfiguring and ramping-up ventilator production in the face of COVID-19: Can robots help? J Manuf Syst 2021;60:864–75.

[10] Arnarson H, Solvang B. Reconfigurable autonomous industrial mobile manipulator system. In: 2022 IEEE/SICE international symposium on system integration. 2022, p. 772–7. http://dx.doi.org/10.1109/SII52469.2022.9708887.

[11] Arnarson H, Mahdi H, Solvang B, Bremdal BA. Towards automatic configuration and programming of a manufacturing cell. J Manuf Syst 2022;64:225–35. http://dx.doi.org/10.1016/j.jmsy.2022.06.005.

[12] Radanovič P, Jereb J, Kovač I, Ude A. Design of a modular robotic workcell platform enabled by plug & produce connectors. In: 2021 20th international conference on advanced robotics. ICAR, 2021, p. 304–9. http://dx.doi.org/10.1109/ICAR53236.2021.9659345.

[13] ITU-R Recommendation ITU-R SM2110. Frequency ranges for operation of non-beam wireless power transmission systems. 2017, Available at https://www.itu.int/rec/R-REC-SM.2110-0-201709-S (2021/11/09).

[14] Alicia T-C, José M G-G, José A A. Wireless power transfer for electric vehicles: Foundations and design approach. 1st ed. Springer International Publishing: Imprint: Springer; 2020.

[15] Ahmad A, Alam MS, Chabaan R. A comprehensive review of wireless charging technologies for electric vehicles. IEEE Trans Transp Electr 2018;4(1):38–63. http://dx.doi.org/10.1109/TTE.2017.2771619.

[16] Liu W, Chau KT, Lee CHT, Han W, Tian X, Lam WH. Full-range soft-switching pulse frequency modulated wireless power transfer. IEEE Trans Power Electron 2020;35(6):6533–47. http://dx.doi.org/10.1109/TPEL.2019.2952573.

[17] Lu F, Zhang H, Mi C. A review on the recent development of capacitive wireless power transfer technology. Energies 2017;10(11). http://dx.doi.org/10.3390/en10111752, URL https://www.mdpi.com/1996-1073/10/11/1752.

[18] Zheng C, Ma H, Lai J-S, Zhang L. Design considerations to reduce gap variation and misalignment effects for the inductive power transfer system. IEEE Trans Power Electron 2015;30(11):6108–19. http://dx.doi.org/10.1109/TPEL.2015.2424893.

[19] Hossain A, Darvish P, Mekhilef S, Tey KS, Tong CW. A new coil structure of dual transmitters and dual receivers with integrated decoupling coils for increasing power transfer and misalignment tolerance of wireless EV charging system. IEEE Trans Ind Electron 2022;69(8):7869–78. http://dx.doi.org/10.1109/TIE.2021.3108697.

[20] Zhang H, Lu F, Hofmann H, Liu W, Mi CC. Six-plate capacitive coupler to reduce electric field emission in large air-gap capacitive power transfer. IEEE Trans Power Electron 2018;33(1):665–75. http://dx.doi.org/10.1109/TPEL.2017.2662583.

[21] Esser A, Skudelny H-C. A new approach to power supplies for robots. IEEE Trans Ind Appl 1991;27(5):872–5. http://dx.doi.org/10.1109/28.90341.

[22] Hirai J, Kim T-W, Kawamura A. Practical study on wireless transmission of power and information for autonomous decentralized manufacturing system. IEEE Trans Ind Electron 1999;46(2):349–59. http://dx.doi.org/10.1109/41.753774.

[23] Han W, Chau KT, Hua Z, Pang H. Compact wireless motor drive using orthogonal bipolar coils for coordinated operation of robotic arms. IEEE Trans Magn 2022;58(2):1–8. http://dx.doi.org/10.1109/TMAG.2021.3082018.

[24] Kikuchi S, Sakata T, Takahashi E, Kanno H. Development of wireless power transfer system for robot arm with rotary and linear movement. In: 2016 IEEE international conference on advanced intelligent mechatronics. 2016, p. 1616–21. http://dx.doi.org/10.1109/AIM.2016.7577001.

[25] Tokano K, Zhu W, Osato T, Nguyen K, Sekiya H. Optimal design of 6.78 MHz wireless power transfer system for robot arm. In: 2021 IEEE international symposium on circuits and systems. 2021, p. 1–5. http://dx.doi.org/10.1109/ISCAS51556.2021.9401073.

[26] Wu J, Dai X, Gao R, Jiang J. A coupling mechanism with multidegree freedom for bidirectional multistage WPT system. IEEE Trans Power Electron 2021;36(2):1376–87. http://dx.doi.org/10.1109/TPEL.2020.3010955.

[27] Covic GA, Boys JT. Inductive power transfer. Proc IEEE 2013;101(6):1276–89. http://dx.doi.org/10.1109/JPROC.2013.2244536.

[28] Zhang Z, Zhang B. Omnidirectional and efficient wireless power transfer system for logistic robots. IEEE Access 2020;8:13683–93. http://dx.doi.org/10.1109/ACCESS.2020.2966225.

[29] Lee ES, Kim MY, Kang SM, Han SH. Segmented IPT coil design for continuous multiple charging of an electrified monorail system. IEEE Trans Power Electron 2022;37(3):3636–49. http://dx.doi.org/10.1109/TPEL.2021.3115511.

[30] Zhang Y, Yang J, Jiang D, Li D, Qu R. Design, manufacture, and test of a rotary transformer for contactless power transfer system. IEEE Trans Magn 2022;58(2):1–6. http://dx.doi.org/10.1109/TMAG.2021.3094135.

[31] TDKCo. Magnetic resonance method of wireless power transfer technology for industrial equipment. 2022, URL https://product.tdk.com/en/techlibrary/developing/wireless/index.html. [Online; Accessed 25 May 2022].

[32] Waypoint Robotics. EnZone™ — Wireless charging and energy on demand. 2022, URL https://waypointrobotics.com/enzone-wireless-power-system/. [Online; Accessed 25 May 2022].

[33] Delta Co. MOOVair 1 kW wireless charging system. 2022, URL https://www.deltaww.com/en-US/products/Industrial-Battery-Charging/5776. [Online; Accessed 25 May 2022].

[34] GaN system. WiBotic autonomous charging. 2022, URL https://gansystems.com/gan-applications/wibotic-300-w-wireless-power-system/. [Online; Accessed 25 May 2022].

[35] Arnarson H. Super flexible reconfigurable manufacturing system (5x speed). 2022, URL https://youtu.be/UXUlaawd8Ps. [Online; Accessed 21 Feb 2022].

[36] CoolGaN. High-frequency half-bridge evaluation board featuring EiceDRIVER™ GaN. 2022, URL https://www.infineon.com/cms/en/product/evaluation-boards/eval_1edf_g1b_hb_gan/. [Online; Accessed 25 May 2022].

[37] Wolfspeed. Silicon Carbide Schottky Diode. 2022, URL https://assets.wolfspeed.com/uploads/2020/12/C6D04065A.pdf. [Online; Accessed 25 May 2022].

Towards automatic configuration and programming of a manufacturing cell.

H. Mahdi, H. Arnarson, B. Solvang, and B. A. Bremdal

DOI: 10.1109/ISIE45063.2020.9152514

Paper's Contribution

This paper proposes a new Reconfigurable Manufacturing System (RMS) where a mobile robot can reconfigure the system. The proposed system is constructed by retrofitting old manufacturing machines with Industry 4.0 technology. It can be rearranged and monitored using a digital twin solution. Moreover, it is simulated and verified using laboratory experiments and video demonstrations. The paper also proposes static and dynamic WPT as industry 4.0 technology for RMS.

Journal of Manufacturing Systems 64 (2022) 225–235

Contents lists available at ScienceDirect

Journal of Manufacturing Systems

journal homepage: www.elsevier.com/locate/jmansys

Towards automatic configuration and programming of a manufacturing cell

Halldor Arnarson [a,*], Hussein Mahdi [b], Bjørn Solvang [a], Bernt Arild Bremdal [c]

[a] Department of Industrial Engineering, UiT The Arctic University of Norway, Lodve Langesgate 2, Narvik 8514, Nordland, Norway
[b] Department of Electrical Engineering, UiT The Arctic University of Norway, Lodve Langesgate 2, Narvik 8514, Nordland, Norway
[c] Department of Computer Science and Computational Engineering, UiT The Arctic University of Norway, Lodve Langesgate 2, Narvik 8514, Nordland, Norway

ARTICLE INFO

Keywords:
Reconfigurable manufacturing system (RMS)
Industry 4.0
Digital twin
Wireless Power Transfer (WPT)
Mobile Robot

ABSTRACT

Manufacturing industries are moving from mass production towards customized production, aiming for high-quality products with innovative technologies, low prices, and high reliability. A reconfigurable manufacturing system (RMS) is an attractive approach to facilitate the movement toward such flexible manufacturing systems. However, reconfiguration and programming of RMS are time-consuming and labor-intensive. Industry 4.0 technologies (such as robotics, digital twin technology, and IoT solutions) decrease human interaction in the preparation phase of a new production series. One challenge that industry 4.0 does not address is a flexible electrification of the system. The lack of electrical outlets limits the available space on the shop floor, and extensive cabling constrains the motion of humans and machines in the same area. This paper solves these challenges by proposing a highly flexible RMS system with advanced robotics, a digital twin programming interface, and a wireless power transfer (WPT) solution. Experimental results, through simulations and verification by laboratory experiments, show great potential in the reduction of human interaction and time to set up a new manufacturing line.

1. Introduction

Globalization has put intense competition between manufacturing companies to produce high-quality products with innovative technologies, low prices, and high reliability. The increasing competition between manufacturers motivates them to move away from mass production towards mass customization and personalized production [1]. Competitors need to adapt and change depending on the market changes, product changes, system failures [2], or global health crises [3].

We can categorize manufacturing systems into three main categories; dedicated manufacturing system (DMS), flexible manufacturing system (FMS), and reconfigurable manufacturing system (RMS). The DMS focuses on high volume and low variety production, while the FMS focuses on low volume and wide variety. In contrast, RMS combines the advantages of both systems to produce with high volume and wide variety. Koren et al. [4] defined RMS as a manufacturing system that can adjust its resources. Thus, RMS is an attractive approach to solve the previously mentioned challenges.

Reconfiguration of RMS can be time consuming. Kim et al. [5] found that in their RMS, the most time-consuming part is the physical rearrangement of the modules and reconfiguring of the system. The system also needs physical labor to rearrange or change the modules in the manufacturing system. As the RMS is scalable, increasing the size of the system results in scaling up the RMS challenges. In other words, with the increasing number of modules of the RMS, the reconfigurable time increases, and the required labor to reconfigure the system will also increase. Moreover, increasing the system scalability adds more demand on the computation, communication, and system complexity [6].

Industry 4.0 is the next technological revolution that focuses on increasing connectivity, automation, and intelligence in manufacturing [7]. The technologies in industry 4.0 are advanced robotics, the internet of things (IoT), cyber-physical systems (CPS), cloud computing, augmented reality, additive manufacturing, and big data are essential for the success of RMS in the future [8]. Industry 4.0 technologies can improve and automate the rearrangement of RMS. However, Bortolini et al. [9], revealed that there is still a lack of research on industry 4.0 integration in RMS. Maganha et al. [10] mentioned that using industry 4.0 technologies must be considered when designing the layout of the system and that the technologies can allow for smart layout design of the RMS.

Morgan et al. [11] suggested that there is a need to retrofit current

* Corresponding author.
E-mail address: halldor.arnarson@uit.no (H. Arnarson).

https://doi.org/10.1016/j.jmsy.2022.06.005
Received 7 April 2022; Received in revised form 23 May 2022; Accepted 13 June 2022
Available online 4 July 2022

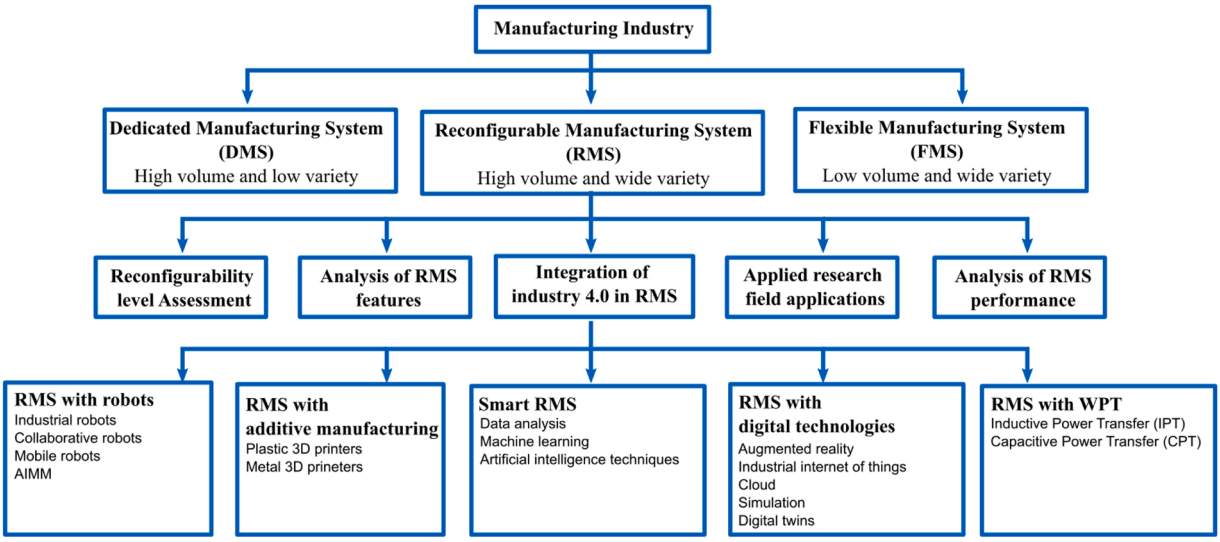

Fig. 1. The research direction for RMS based on Bortolini schematic [9], with a focus on industry 4.0 integration to RMS.

manufacturing equipment with the new technologies. Thus, we can retrofit old robots with new controllers, IoT functionality, and adaptable control systems. Using advanced robotics, IoT, and digital twins, we can control and automate the reconfiguration of RMS. The robots can rearrange the modules in such a system, while the IoT offers wireless control and communication.

Although industry 4.0 tackles most RMS problems, there is still a challenge with electrification. Systems need labor to connect all parts to power, and it is time-consuming. Besides, the conventional electrification uses cables that require large areas, which limits the flexibility of the systems. Therefore, there is a need for more flexible methods to power RMS without human intervention. Wireless power transfer (WPT) can energize the system autonomously and has the potential to address the challenges in the conventional conductive charging approach, including long charging time, wear and tear of the contractors and plugs, and hazard of the electric shock.

To the authors' knowledge, there is no publications which use mobile robot to rearrange the machines in the manufacturing cells. Arnarson et al. [12] used one mobile robot to move multiple robot arms. We can expand this conceptual idea by moving different manufacturing machines using a mobile robot. In addition, there is no investigation of WPT for manufacturing systems or consideration of WPT as an industry 4.0 technology. Industry 4.0 is a dynamic concept where various technologies are in industry 4.0 can and will change over time [7]. For instance, one of the main technologies in industry 4.0 is IoT which can connect devices wirelessly. WPT provides wireless electrification of systems, we can argue that WPT is a new and emerging industry 4.0 technology that can allow manufacturing systems to become more flexible, modular, and automated.

Expanding Bortolini framework [9], we can categorize the research directions of industry 4.0 in RMS, as shown in Fig. 1. The first industry 4.0 technology is RMS with robots, including industrial robots, collaborative robots, mobile robots, and autonomous industrial mobile manipulators (AIMM) in RMS. RMS with additive manufacturing looks at implementing 3D printers into the system. RMS with digital technologies which embrace augmented reality, industrial internet of things (IIoT), cloud, simulation, and digital twins. Smart RMS encompass data analysis, machine learning, and other artificial intelligence techniques. Finally, RMS with WPT looks at flexible and autonomous electrification for manufacturing systems.

In this paper, we propose an autonomous RMS by integrating a mobile robot into RMS, to increase the reconfigurability of the system, decrease the setup and programming time, and enhance the system's flexibility. Besides, we investigate different WPT configurations that increase flexibility and autonomy, creating a highly flexible RMS. We can summarize the main contribution of the paper as follows: .

- Proposing a new RMS in which a mobile robot can reconfigure the system.
- Rearranging, and monitoring the proposed system using a digital twin solution.
- Proposing static and dynamic WPT as industry 4.0 technology for RMS.
- Retrofitting old manufacturing machines with industry 4.0 technology.
- Simulating and verifying through laboratory experiments and video presentations.

We organize the remainder of this paper as follows: Section 2 presents previous studies on RMS. Section 3 proposes the concept of a highly flexible mobile RMS with WPT. Section 4 describes a mobile RMS with a digital twin, a physical demonstration of the system. Then, we discuss the results in Section 5. Finally, we conclude and present our future works in Section 6.

2. Previous studies

Sanderson et al. [13] developed the Smart Manufacturing and Reconfigurable Technologies (SMART), which is an assembly system that can be set up with different configurations. The system is based on the HAS-200 system [14] and applies adaptive multi-agent control. There are other similar examples on smart RMS [15–18]. They used standardized platforms from the CP Factory. CP Factory is a universal modular manufacturing systems for research, training, and teaching, produced by FESTO [19]. The systems use platforms that can be rearranged based on the system's capacity and functionality.

In another study, Kim et al. [5] introduced a modular factory testbed. The system consists of 10 main workstations producing portable battery chargers, electric endodontic handpieces, and electric toothbrushes. The system uses a infrared communication system that automatically recognizes how the system is configured. However, all the previous systems (i.e., CP factory, HAS-200, and testbed) are only used for training, educational, and research purposes.

Adamietz et al. [20] presented a miniaturized RMS. The system uses a standardized container, in which it is possible to change the manufacturing modules inside the container. This system can have a

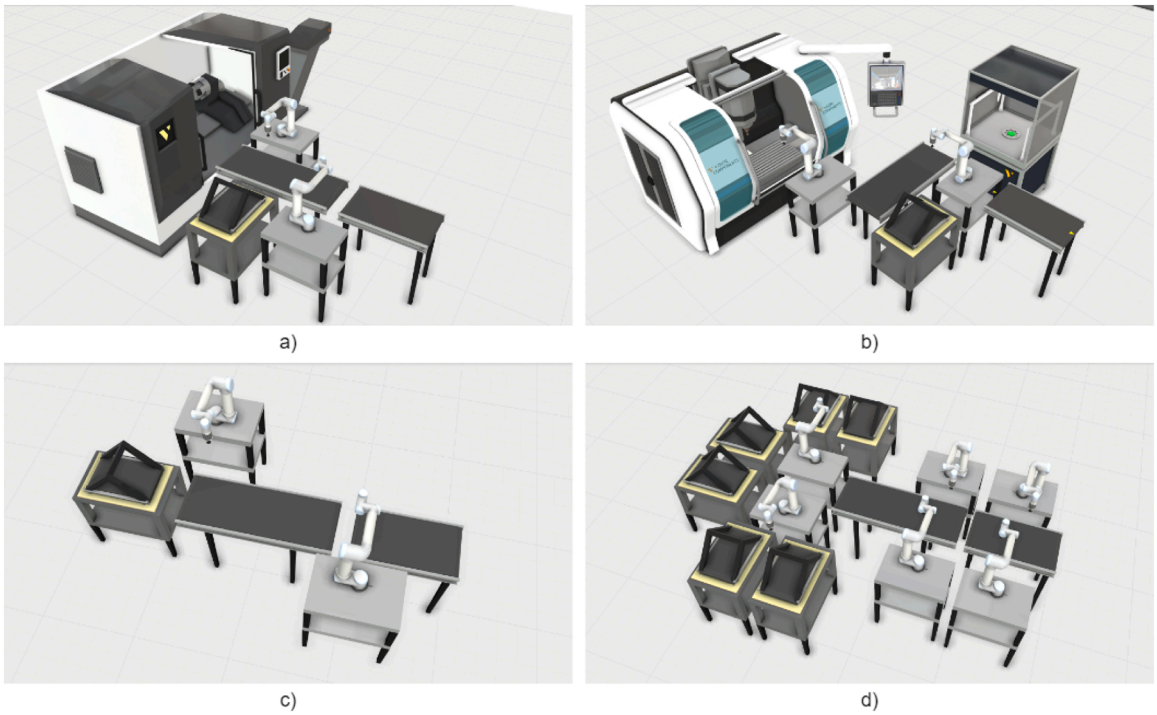

Fig. 2. Different examples of how the system can be configured (a, b) and scaled up and down (c, d): (a) The platforms are arranged around the turning center, (b) the platforms are arranged around a large 3D printer, (c) a small manufacturing system using the platforms, and (d) the previous manufacturing system is expanded with more platforms to increase production.

maximum of six small modules, three large modules, or a combination of big and smaller modules. The system reconfiguration takes less than 8 h using a forklift, where a human needs to move the parts between the machines.

Seok et al. [21] built a modular manufacturing system using the additive manufacturing concept. Their system consists of, 3D printers, post-processing, inspection, and packing modules. It uses a 3D printer as the main manufacturing process, and it is possible to achieve personalized production or mass customization. We can categorize the system as an RMS with digital technologies.

One approach that can save time and automate the RMS is the AIMM principle. Hongtai et al. [22] explained the concept of AIMM as a mobile robot combined with an industrial manipulator. The robots are easy to integrate and can carry out tasks at different workstations. The AIMM increases manufacturing flexibility and we can implement it into existing manufacturing systems [23]. Recently, Inoue et al. [24] proposed AIMM to be a key component of RMS. Andersen et al. [25] examined how to integrate an AIMM into a modular CP Factory.

Regardless of these previous studies, there is little attention to building and designing RMS for manufacturing industries. For instance, Singh et al. [26] revealed that there is inadequate research on the development of principles for reconfigurable machines. Moreover, Khanna et al. [27] found that the implementation of RMS into manufacturing systems is still a significant problem. In addition, there is a lack of studies that explain RMS in practices and how RMS can be adapted and used by companies [28].

The previous studies showed that the physical reconfiguration of the platforms is the most time-consuming, and they require labor to change and modify the layout. Morgan et al. [11] proposed smart reconfigurable machines that can change autonomously. In another study, Singh et al. [26] found that there is immense potential for further research on wireless sensor networks for automatic configuration, interoperability, and scalability.

WPT plays a crucial role in charging applications without human intervention, making it attractive for developing flexible and reliable RMS systems. It reduces the hazards of electrical shocks by plugin cables. It can also minimize the systems' maintenance by removing the plugs, cables, and contractors. WPT provides an attractive solution in different applications: IoT devices [29,30], lightning [31–33], heating [34], wind turbines and oil drilling tools [35], energy encryption [36], unmanned aerial and underwater vehicles [37–40,41], and transportation applications [42–44].

To summarize, we found there is less focus on industry 4.0 integration. Moreover, all the previously proposed systems suffer from setup, layout, and programming restrictions. In addition, systems are still highly dependent on humans for reconfiguration and powering the system. If we use advanced robotics, IoT, and digital twin to rearrange the system, this can improve the flexibility and reconfigurability of the system. At the same time, implementing WPT will make manufacturing systems more flexible, modular and automated and support the other industry 4.0 technologies.

3. Concept of a highly flexible system

3.1. RMS with robots

To integrate industry 4.0 in RMS, we can use the concept of AIMM to utilize robots in a flexible manner. Arnarson et al. [12] proposed an AIMM for RMS, where the AIMM is divided into two separate parts, one for the mobile robot and a second for a robot arm. The mobile robot and robot arm can work together or separately. With such a system, one mobile robot can move multiple platforms and increase the utilization of both the robot arm and the mobile robot. In this example, they created two robot platforms. Using the same principle, we can expand the idea by adding conveyors, 3D printers, or other manufacturing machines to the platforms instead of a robot arm.

A mobile robot can move and rearrange all system parts to manufacture a specific product. The mobile robot can also rearrange around large manufacturing machines (CNC, turning, and 3D printer) that are fixed and hard to move. This solution is scalable since adding new

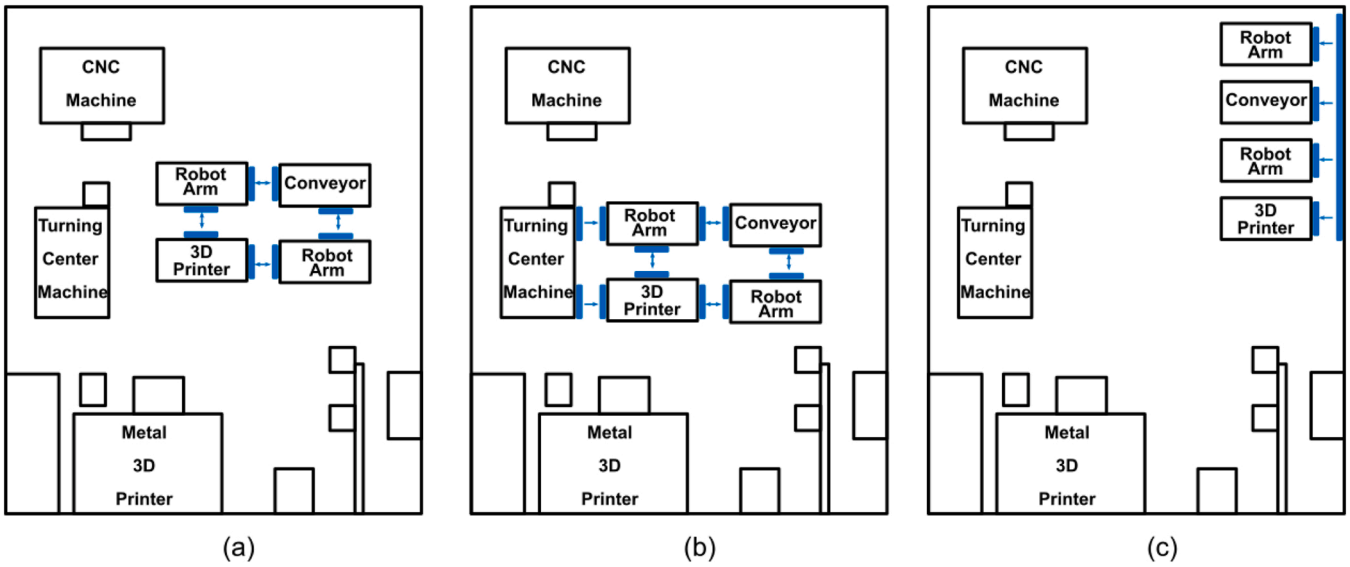

Fig. 3. A top-view of three different scenarios for static WPT: (a) the platforms charge each other through a mesh configuration. (b) the platforms charge each other through a mesh configuration while a big machine energizes the whole system. (c) the platforms charge from the main source while they are parking.

platforms to the system can increase the output and production capacity. Therefore, it is easy to downscale and upscale production based on demand. Fig. 2 shows how to configure the system with different scalable layouts. At the same time, we can also use collaborative robots in open environments where humans are working or industrial robots for tasks that require higher precision and accuracy.

3.2. 3D printing

Another emerging industry 4.0 technology is additive manufacturing, in which we can get an even more flexible and automated RMS. For instance, in the conventional manufacturing approach to produce a plastic box, we need to build a mold and other related manufacturing machines that are not flexible. In comparison, plastic 3D printer can produce a plastic box or any other plastic part. In other words, additive manufacturing can increase the mass customization capability of the RMS. In this video https://youtu.be/Z6WQe1bf648 and in [45], we demonstrate how a flexible additive manufacturing in RMS in which a plastic 3D printer can print different parts automatically and a mobile robot pick up the 3D printer and move it to different places. In addition, we can use the manufacturing material more efficiently and produce less waste.

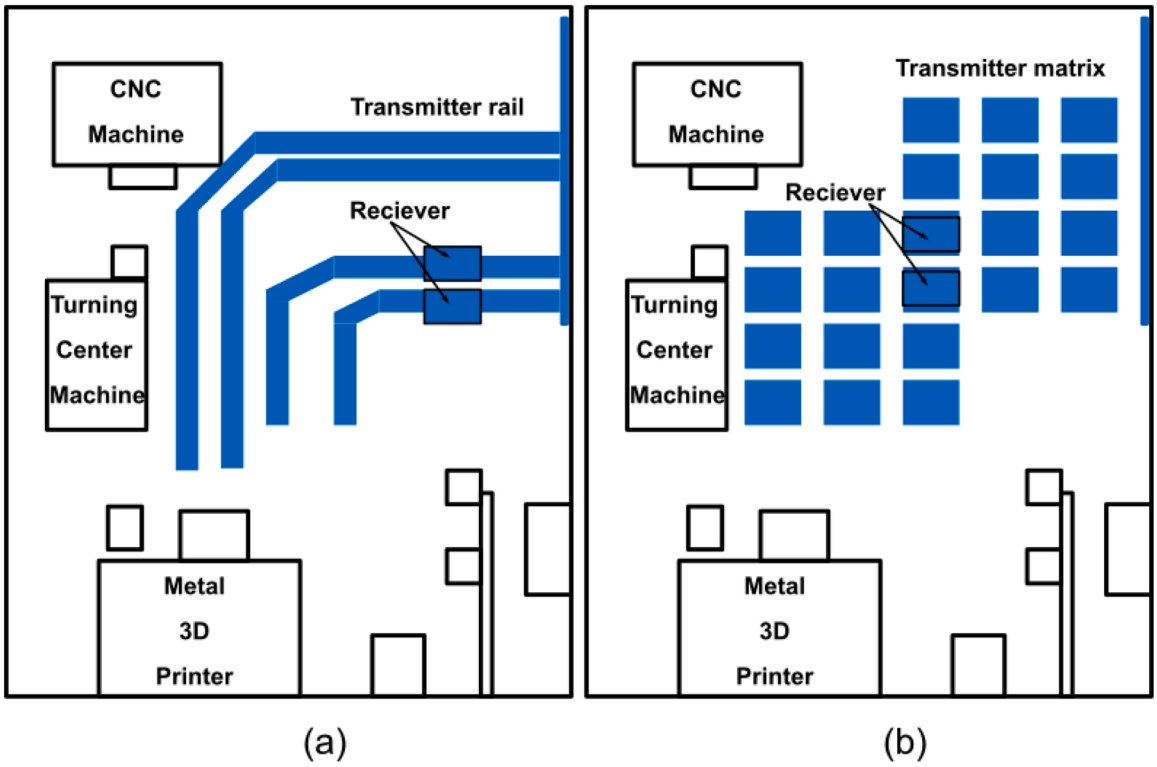

Fig. 4. A top-view of two approaches of dynamic WPT: (a) railway transmitters. (b) matrix transmitters.

3.3. Digital technologies

IIoT facilitates communication, allowing remote monitoring and control of the manufacturing system. Thus, we can retrofit the conventional manufacturing systems with IIoT to create communication between machines in the system. Besides, we can simulate the system to see how the reconfiguration and layout of the system will look in reality. The disadvantage of having only offline simulation is that we cannot test the RMS in real-time. It cannot be used for control or monitoring the RMS. In addition, the current solution for manufacturing systems is basic human-machine interfaces, where the labor communicates with the machines through a screen. This type of interface makes it difficult to program a reconfiguration of the manufacturing system.

However, if we use the digital twin of the system to test and see how the configuration looks and works. The digital twin is a real-time digital replica of the manufacturing system where we can transfer the data bidirectional between the physical and digital systems. Based on a digital twin we can simulate [46], control [47], monitor [48], predict failures of the system. In this paper, we simulate and monitor the system at the same time using a digital twin principle.

3.4. Smart RMS

Arnarson et al. [49] introduced industrial big data in RMS, for a smarter RMS system. In this work, they used the principles of industrial big data analysis moving towards automated RMS. Industrial big data analysis combined with artificial intelligence moves us toward a fully automated manufacturing system in which the system can manufacture any products without human intervention.

3.5. RMS with WPT

It is hard to achieve fully automated manufacturing systems with a conventional wired electrification approach. If we use WPT, we can gain autonomous electrification of the system and hence a fully automated system. Besides, WPT provides more flexibility and reliability to the RMS. In this section, we introduce the main concept of WPT to industry 4.0 technologies and give examples of static and dynamic implementation of WPT in RMS, while we provide more detailed descriptions and experimental results in further work.

The International Telecommunication Union defines WPT as the transmission of power from a power source to an electrical load wirelessly using a electromagnetic field [50]. WPT incorporates three main groups: near-field, mid-range, and far-field. The differences between these groups are in terms of the type of the electromagnetic wave, distance range, operating frequency level, power level, and the complexity of the system's architecture.

We can utilize either static or dynamic near-field WPT for RMS. The static approach offers electrification when the platforms are not moving. Fig. 3 illustrates three different scenarios. The arrows show the direction of the power flow. In scenario (a), we can fix the WPT transmitter-receiver on the platforms while electrifying each other through a mesh configuration. In contrast, in scenario (b), the platforms energize from a stationary machine, such as a turning center, while charging. The last scenario (c) is when the platform is not in use and charges from the main power source.

On the other hand, dynamic WPT can offer a power source for the platforms and mobile robots. We can implement the dynamic WPT through two approaches, namely, the railway approach and matrix one, as shown in Fig. 4. The railway transmitters provide continuous power to the platforms in the railway approach. However, the allocation of the platform should be predetermined, which limits the flexibility of the RMS. In contrast, the matrix approach offers a flexible charging solution. Nevertheless, it provides discrete charging, and hence we should optimize the distance between the transmitters, increasing the complexity and cost of the WPT system.

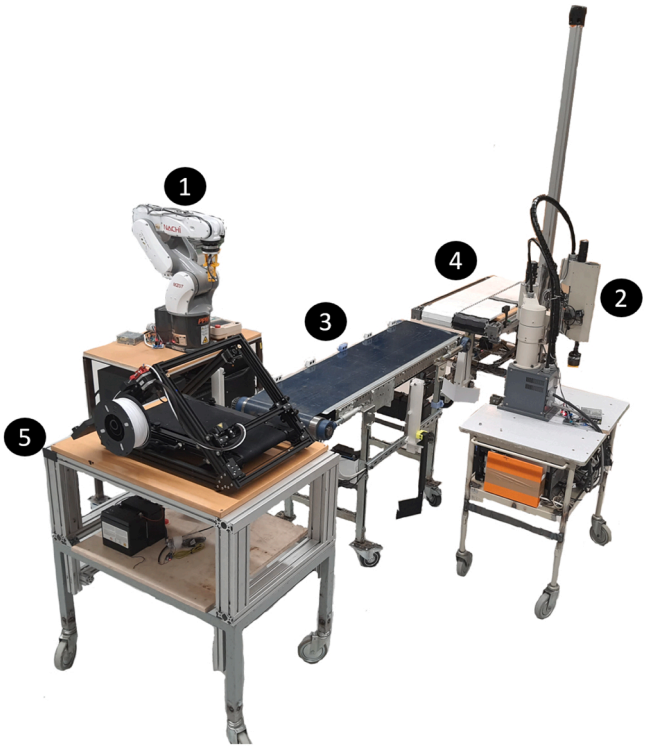

Fig. 5. The proposed RMS: (1) IRB1 platform, (2) IRB2 platform, (3) conveyor, (4) conveyor with lifting, and (5) 3D printer.

4. Reconfigurable manufacturing system

In this section, we describe the RMS and give a demonstration both by simulation and testing.

4.1. RMS description

Our system consists of five platforms:

- **IRB1 platform:** Has a four degree of freedom robot arm (SCARA-type). In this system it is used for simple assembly, pick and place and sorting operations.

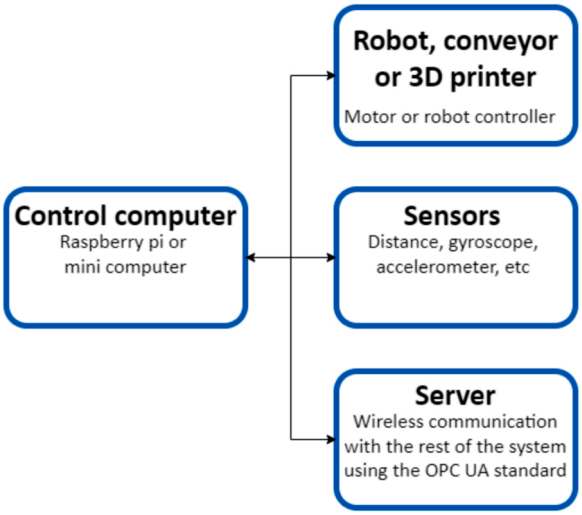

Fig. 6. The main components on each platform.

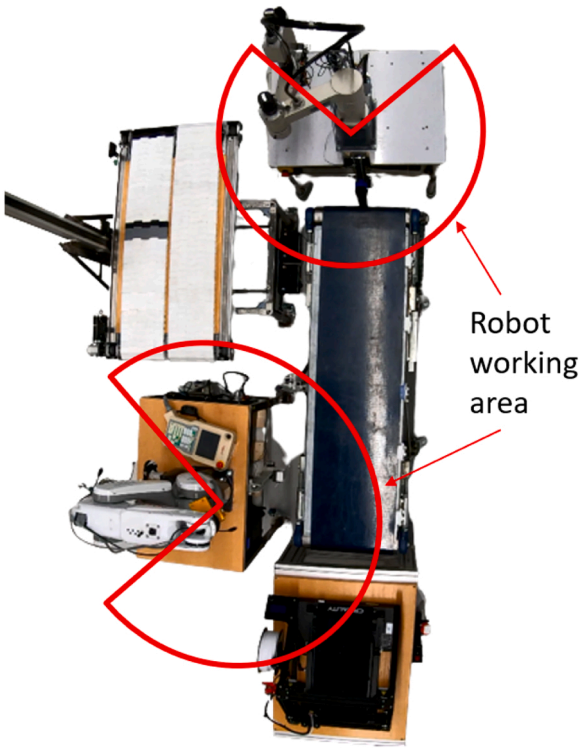

Fig. 7. An illustration of the placement requirements of the system.

- **IRB2 platform:** Is a six degree of freedom robot arm. The robot arm can be used for the same operations as the IRB1 robot, but can also do more complex tasks such as machine tending, polishing, etc.
- **Conveyor platform:** The conveyor platform is used to transport the parts between the robot arms.
- **Conveyor with lifting platform:** Is used to transport parts out of the manufacturing system. Since it has a lift module it is more adaptable then the conveyor platform.
- **3D printer platform:** The 3D print platform contains a Creality CR-30, which is a 3D printer that prints on a conveyor. It can automatically remove the parts as they are being printed.

Fig. 5 shows a specific setup of the RMS.

We have developed the platforms by retrofitting them with small single-board computers and sensors. We have used different sensors to measure distance, angular velocity, and acceleration. As the robot arms require a more powerful computer, we have used (i5–10210 U CPU) to run the inverse kinematics calculator in ROS MoveIT and image recognition models in parallel. While the conveyor, conveyor lift and 3D printer platform use a Raspberry pi for control. All the computers are equipped with WIFI for wireless communication and we have also utilized extra microcontrollers on some of the platforms to collect data and control motors. Fig. 6 depicts the setup of each platform.

A MiR100 mobile robot transports the platforms to the selected location. It has a carrying capacity of 100 kg and can pull up to 300 kg [51]. The accuracy of the mobile robot is ± 50 mm, which limits the flexibility of the system [12]. The low accuracy of the mobile robot can deteriorate the docking reliability of the platform. Nevertheless, a marker solution is used and enhance the docking accuracy of the mobile robot within ± 5 mm [51].

We can describe the docking sequence as follows: First, once the mobile robot reaches in front of the platform it adjust itself to the marker. Second, the marker moves up, so the mobile robot can drive under the platform. Third, the mobile robot drives forward with a fixed distance. Fourth, the hooking system is activated and fasten the mobile robot with the platform. A demonstration video to show the docking and uncoupling sequence can be fund at https://www.youtube.com/watch?v=RtOX0HGiqRs. When the mobile robot uncouples from a platform, the mobile robot software saves the platform's position. Besides, the mobile robot calculates and saves 1.5 m from the platform as the docking point for the mobile robot.

For communications the platforms are connected to the Open Platform Communications Unified Architecture (OPC UA). The OPC UA is a IEC 62541 standard and is used for communication in industrial applications [52]. It allows all platforms to connect to the same server and communicate seamlessly which facilitates the control of the robots, conveyors and other motors in the system. This communication protocol will also help to bring about machine-to-machine communication, and hence all platforms can operate without human intervention.

4.2. Platform placement

As mentioned in Section 2, reconfiguring of the RMS can be time consuming and often needs human labor. The idea behind this system is

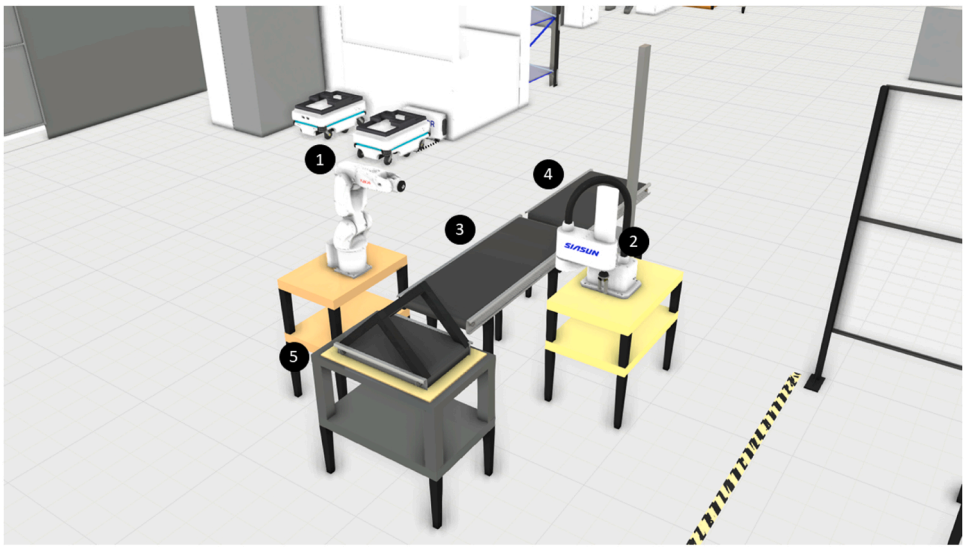

Fig. 8. A screenshot from Visual Components showing the digital twin of the platforms. (1) IRB1 platform, (2) IRB2 platform, (3) conveyor, (4) conveyor with lifting, and (5) 3D printer.

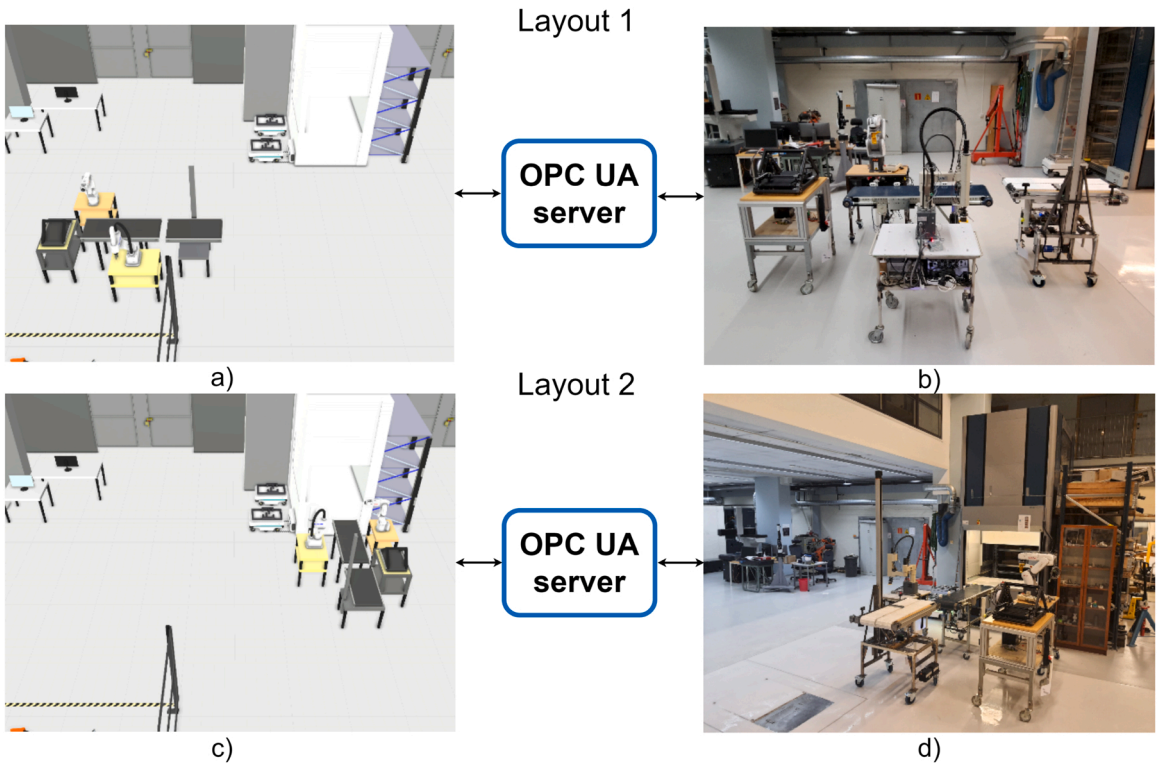

Fig. 9. Two layout configurations in the Visual Components (On the left side), and the resulting configuration assembled with the mobile robot (on the right side): a) The first digital layout. b) The first physical layout. c) The second digital layout. d) The second physical layout.

to reconfigure and change the system's layout automatically with a mobile robot. Also, we can change the layout of the system based on demands. However, the system still faces some challenges. For instance, the IRB1 robot has a movement radius of 0.6 m, while the IRB2 robot has a maximum reach of 0.9 m. For this system to work, the robot arms need to reach the platforms they are working with, as shown in Fig. 7, which add a constraint on system's arrangement. One way to tackle the challenges of choosing the layout of our system is by using a digital twin solution.

Van Der Horn et al. [53] have described the digital twin as a virtual representation of a physical system, where the virtual and physical systems share the data. The virtual model of the manufacturing system can be used to test and visually various configurations of the layout. We can also use it to send information about the placement of the platforms. In addition, we can combine a digital twin with a modular system to create fast reconfiguration, integration, and safety validation of the system [3].

Previously, Arnarson et al. [54] have developed a two-way digital twin model in the Visual Components Premium simulation software [55] and conducted laboratory testing of the system. As Visual Components Premium supports the OPC UA standard, we can use the digital twin model as a visual tool to plan the system's layout and simulate assembly and production flow for different system layouts. Fig. 8 shows the digital twin model of the five platforms. The model in the software has the same scales and positions of the components as the physical system. The simulation takes the positions of the digital platforms and sends them to the OPC UA server. The mobile robot can automatically get the new coordinates of the platforms and start moving them. Eventually, the simulation software decides how the mobile robot picks the platform.

4.3. Demonstrations of the RMS system

Two demonstrations show the functionality of our system.

Table 1
The time the mobile robot used to reconfigure both layouts measured in minutes.

	Layout 1	Layout 2
IRB1 Platform	2.2	2.2
IRB2 platform	2.2	2.3
Conveyor platform	2.1	2.9
Conveyor Lift	2.0	1.9
3D print platform	2.3	2.6
Total time [min]	10.8	11.8

4.3.1. Demonstration of simulation design

The first demonstration shows the automatic reconfiguration. Two layouts are created in the Visual Components model, and when the simulation is executed the positions of the platforms are sent to the server. Afterwards, the mobile robot reads the positions of the platforms from the OPC UA server and pick up and place the platform in the same position given by the model in Visual Components. The resulting configuration of the mobile robot can be seen in Fig. 9.

A video demonstration shows the functionality of the system and can be found at https://youtu.be/UXUlaawd8Ps with 5x speed and another video https://youtu.be/s8r-Q5eMy2M with normal speed. The purpose of the video is to showcase how the mobile robot can automatically change a manufacturing system's layout. The video starts with all platforms in different locations in the laboratory. Then mobile robot picks the platforms and places them into the configuration in Fig. 9. Second, the mobile robot takes apart the system and reconfigures a new manufacturing system with the vertical storage machine (Compact lift). The time it takes to move and place each platform and the total time of the configuration can be found in Table 1.

4.3.2. Demonstration of production simulation

In the second demonstration, we showcase the flexibility and reconfigurability of the system in the simulation model. For this experiment, we use the process modeling component of Visual

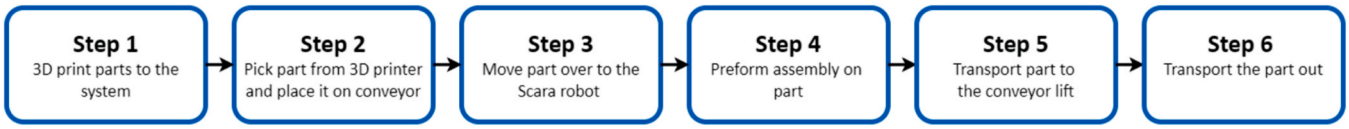

Fig. 10. The production sequence used to produce and assemble a box in the simulation.

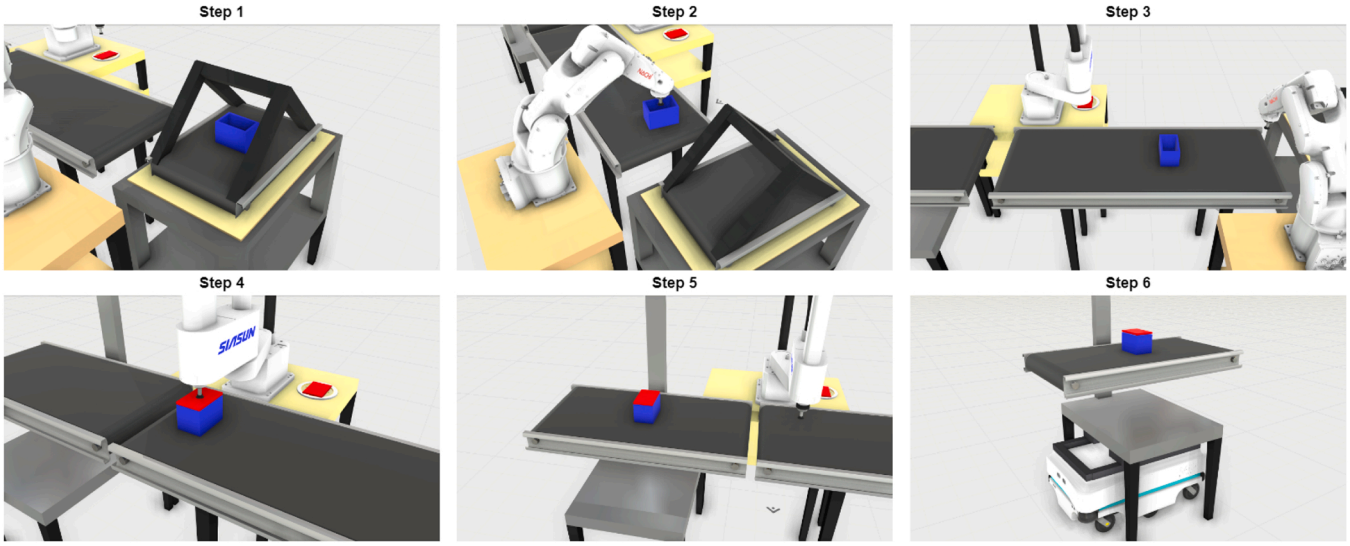

Fig. 11. An illustration of each step in the simulation.

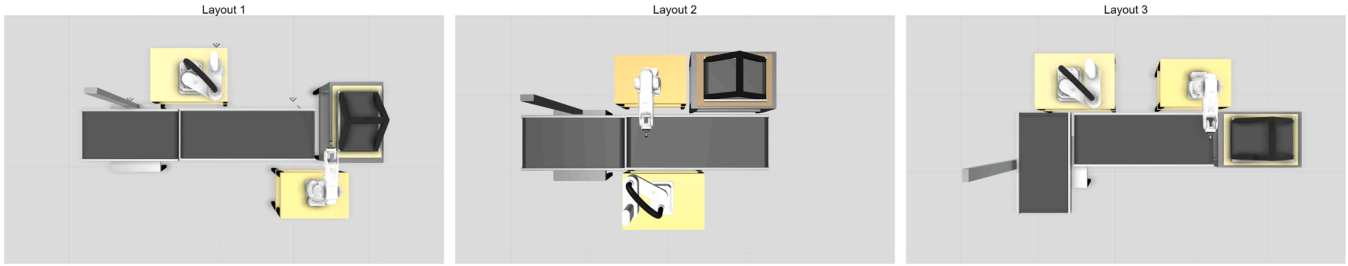

Fig. 12. Three different layout configuration to produce the box.

Table 2
The time it takes to complete each step in the simulation, without considering the 3D printing time measured in seconds.

Manufacturing setup	1	2	3
Step 1	4.6	4.6	4.6
Step 2	3.0	2.8	2.6
Step 3	11.3	2.4	9.8
Step 4	3.1	3.6	3.3
Step 5	10.1	9.5	2.9
Step 6	17.6	17.5	25.0
Total time [sec]	49.7	40.4	48.2

Components to program the system's movements. The simulation shows the production and assembling of a box in six steps, as shown in Fig. 10. The production process are: a box without a lid is 3D printed with the 3D printer platform. When the box reaches the end of the 3D printer, the IRB2 robot picks up the box and places it on the large conveyor. The conveyor transports the box to the IRB1 robot, which takes the lid and places it on top of the box. At last, the box is transported over to the conveyor lift, and the mobile robot transports the conveyor lift out. Fig. 11, illustrates all steps.

We can execute the same production plan of the box with different configurations and placement of the platforms. To test this, we create three different configurations, as can be seen in Fig. 12. A video demonstration https://youtu.be/6ir7RUN_uk0 of the three simulations shows a different production time for each layout. Table 2 lists the production times for each step in all three layouts. We can use the simulation to estimate the production time and test if there are any collisions in the simulation.

4.4. Demonstration of manufacturing application

To demonstrate a manufacturing application of the system, we simulate and implement an assembly of a manufacturing system around a CNC machine. In the simulation, the first step is to drag the platforms and rearrange them around the CNC machine. The second step is to check if the robot arms can reach the positions. The last step, using the digital twin we can transfer the positions of all the platforms to the mobile robot where it reconfigures the platforms automatically. Fig. 13 shows the demonstration of the proposed RMS for manufacturing application. The video https://youtu.be/vxsg4zgJzTU demonstrates the aforementioned three steps. The results shows the system needs around 12.75 min for rearranging around the CNC machine. In this demonstration, we can use one mobile robot to fill raw material to the CNC

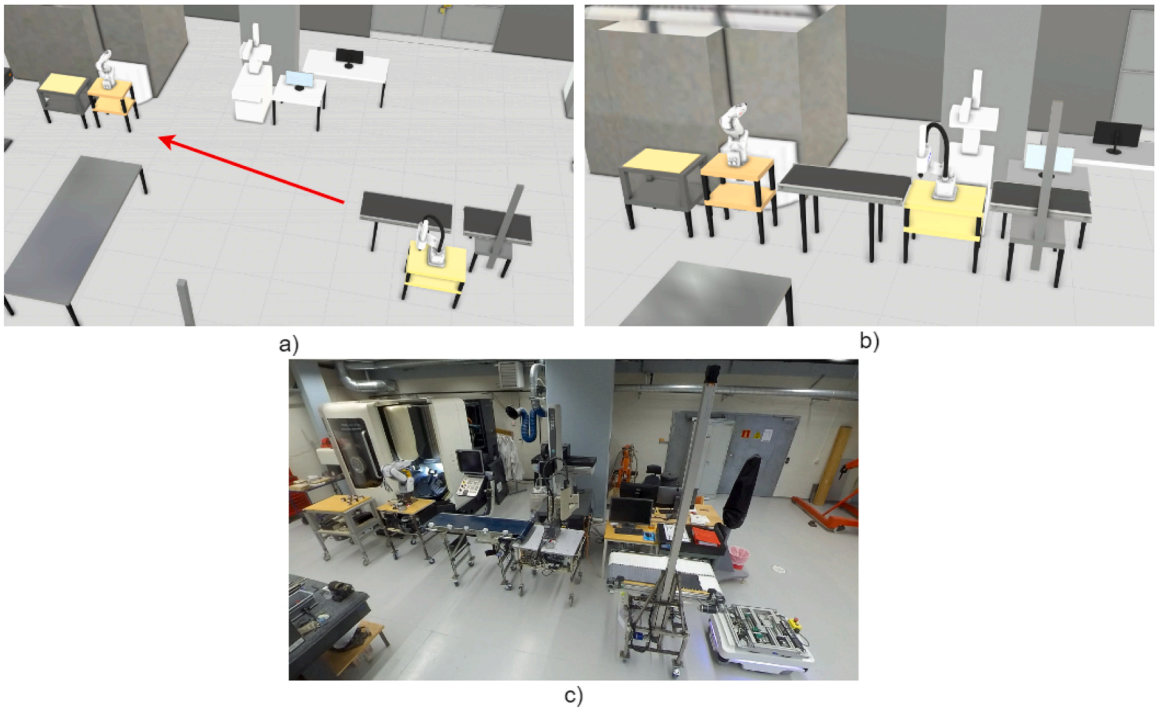

Fig. 13. Demostration of industrial application: a) Configuring the platforms around the CNC machine. b) Simulating to check that the robot arm can reach their position. c) The physical configuration of the platforms around the CNC machine.

machine, rearrange the system, and take out the manufactured products.

5. Discussion

Traditionally, RMS need human interaction to reconfigure the system. In this paper, we have proposed a new RMS solution that decreases the need for humans in the setup of a new manufacturing line. A mobile robot can reconfigure the platforms without any human intervention. A total reconfiguration of the system requires 10:8 min to (numerical range) 11:8 min depending on the layout.

We utilized additive manufacturing as an industry 4.0 technology to produce various products. We simulated three different layouts to manufacture a box using a 3D printer. According to the simulation, the production time took 49.7 s, 40.4 s, and, 48.2 s, respectively, without considering the 3D printing time. However, this was a simple example of producing one type of product, but the 3D printer can print any part as long as it fits within the dimensions of the 3D printer. Besides, using a 3D printer for production can easily automate the production process. Thus we create a platform with a 3D printer that can be controlled, operated, and monitored remotely.

Using industry 4.0 digital technologies, we retrofitted old machines with sensors and controllers, and by applying the IIoT, we got communication between all parts of the system. We used a two-way digital twin with simulation to program the system and choose the layout of the platforms. It gives the operator a simple drag and drop interface to position the platforms. We can also simulate the manufacturing process to test and see if the robot arm reaches its desired position. It creates a simple and intuitive interface for fast and simple programming of the layout.

The IIoT and digital twin can automate the system and put the building blocks for smart RMS. We can collect and store data from all platforms in real-time, which we can use to train machine learning algorithms to classify and predict the RMS. We can implement reinforcement learning and image recognition to create self adaptable control system for the robots. At the same time, we can apply image recognition models to detect when prints are failing or any other failure in the RMS.

Industry 4.0 technologies have enhanced the flexibility and reconfigurability of manufacturing systems by integrating robots, additive manufacturing, digital technologies, and smart RMS. However, we have several challenges that the proposed RMS is still facing.

The first challenge is to arrange the layout of the system in such a way that considering the limited working area of the robot arms. Currently, we address this challenge by simulation through a digital twin. However, we need to find a better solution to solve this problem autonomously. The second challenge is that the mobile robot needs extra force to move the trolleys and often ends up spinning while moving the platforms. In addition, if one of the ten wheels gets stuck, it will dramatically reduce the accuracy and cause collisions with other platforms. As a better solution, we can remove all wheels of the platforms and use a mobile robot with high lifting capacity. Then the mobile robot would be able to lift the platform and place them in different positions. Regardless of these challenges, the system has a unique characteristic that can not only be reconfigured in different layouts but can also be rearranged in other locations irrespective of the manufacturing space.

We also proposed WPT systems to electrify the platforms and increase the flexibility of the manufacturing system. In addition, we can utilize static or dynamic WPT to electrify the system. The dynamic WPT can electrify both the platforms and the mobile robot, increasing the system's extent and cost. In contrast, static WPT offers a good option to electrify the platforms from each other or a main fixed machine. The system will get better efficiency by correcting the misalignment between the platforms.

6. Conclusion

We have proposed a number of industry 4.0 technologies to build an highly flexible RMS. We also expand the industry 4.0 technologies principle by adding WPT. The WPT system increases the flexibility and reliability of the proposed RMS. Our system includes five platforms containing robot arms, a conveyor belt, a conveyor lift, and a 3D printer. We have retrofitted the platforms and used a mobile robot to reconfigure

the platforms automatically. Then, we created a simulation model that controls and arranges the platforms using the digital twin to configure the system. The simulation model has the same scale and coordinates as the mobile robot. Using the OPC UA server, we send the coordinates of the platforms from the simulation model to the physical model. In addition, we present two demonstrations: the first simulation showing the system's flexibility with the production and assembly of a box, and the second simulation showing how the mobile robot can reconfigure the platforms based on the simulation model.

7. Future works

The proposed system can be further expanded and automated.

7.1. Automatic layout design

As can be seen from the simulation results, there are multiple solutions for positioning the platforms. Therefore, optimizing the layout with the shortest path or smallest area can reduce manufacturing time and costs. We seek to develop a mathematical model that can find a sub-optimal layout for a system with multiple platforms as further work. With the mathematical model, the system will rearrange the layout automatically depending on what we need to manufacture.

7.2. Automatic programming/control

Another challenge facing the system is to control and program the platforms automatically. Due to the mobile robot inaccuracy, the platforms aren't positioned with high accuracy. Therefore, using pre-programmed programs on the robot arms will not be feasible. Besides, the literature has previously shown that manually controlling, programming, and setting up the system is time-consuming, requiring expertise in control systems [5]. We will investigate and create a system that can be programmed automatically depending on what will be manufactured.

7.3. Wireless electrification of RMS

Finally, we will study in detail different approaches of WPT and examine capacitive power transfer (CPT) as a low-cost solution for powering the RMS. In addition, we expand the system with a mobile battery platform that can power other platforms using CPT.

Declaration of Competing Interest

The authors declare that they have no known competing financial interests or personal relationships that could have appeared to influence the work reported in this paper.

Acknowledgment

This project has received funding from the European Union's Horizon 2020 research and innovation programme under grant agreement No 825196.

References

[1] Fathi M, Ghobakhloo M. Enabling mass customization and manufacturing sustainability in industry 4.0 context: a novel heuristic algorithm for in-plant material supply optimization. Sustainability 2020;12(16).
[2] Koren Y, Shpitalni M. Design of reconfigurable manufacturing systems. J Manuf Syst 2010;29(4):130–41. https://doi.org/10.1016/j.jmsy.2011.01.001.
[3] Malik AA, Masood T, Kousar R. Reconfiguring and ramping-up ventilator production in the face of covid-19: Can robots help? J Manuf Syst 2021;60:864–75.
[4] Koren Y, Heisel U, Jovane F, Moriwaki T, Pritschow G, Ulsoy G, et al. Reconfigurable manufacturing systems. CIRP Ann 1999;48(2):527–40. https://doi.org/10.1016/S0007-8506(07)63232-6.
[5] Kim DY, Park JW, Baek S, Park KB, Kim HR, Park JI, et al. A modular factory testbed for the rapid reconfiguration of manufacturing systems. J Intell Manuf 2020;31(3):661–80. https://doi.org/10.1007/s10845-019-01471-2.
[6] Putnik G, Sluga A, ElMaraghy H, Teti R, Koren Y, Tolio T, et al. Scalability in manufacturing systems design and operation: state-of-the-art and future developments roadmap. CIRP Ann 2013;62(2):751–74. https://doi.org/10.1016/j.cirp.2013.05.002. ⟨https://www.sciencedirect.com/science/article/pii/S0007850613001923⟩.
[7] Klingenberg CO, Borges MAV, Antunes Jr JAV. Industry 4.0 as a data-driven paradigm: a systematic literature review on technologies. J Manuf Technol Manag 2021;32(3, SI):570–92. https://doi.org/10.1108/JMTM-09-2018-0325.
[8] Singh A, Gupta P, Asjad M. Reconfigurable manufacturing system (rms): Accelerate towards industries 4.0. Proc Int Conf Sustain Comput Sci, Technol Manag (SUSCOM) 2019;01. https://doi.org/10.2139/ssrn.3354485.
[9] Bortolini M, Galizia FG, Mora C. Reconfigurable manufacturing systems: Literature review and research trend. J Manuf Syst 2018;49:93–106. https://doi.org/10.1016/j.jmsy.2018.09.005. ⟨https://www.sciencedirect.com/science/article/pii/S0278612518303650⟩.
[10] Maganha I, Silva C, Ferreira LMDF. The layout design in reconfigurable manufacturing systems: a literature review. Int J Adv Manuf Technol 2019;105(1–4):683–700. https://doi.org/10.1007/s00170-019-04190-3.
[11] Morgan J, Halton M, Qiao Y, Breslin JG. Industry 4.0 smart reconfigurable manufacturing machines. J Manuf Syst 2021;59:481–506. https://doi.org/10.1016/j.jmsy.2021.03.001.
[12] H. Arnarson, B. Solvang, 2022. Reconfigurable autonomous industrial mobile manipulator system, in: 2022 IEEE/SICE International Symposium on System Integration (SII), 2022, 772–777.10.1109/SII52469.2022.9708887.
[13] D. Sanderson, J. C. Chaplin, L. De Silva, P. Holmes, S. Ratchev, 2016. Smart manufacturing and reconfigurable technologies: Towards an integrated environment for evolvable assembly systems, in: 2016 IEEE 1st International Workshops on Foundations and Applications of Self* Systems (FAS*W), 2016, 263–264.10.1109/FAS-W.2016.61.
[14] SMC, SMC International Training – The didactic division of SMC Corporation, [Online; accessed 3. Feb. 2022] (Feb 2022). ⟨https://www.smctraining.com⟩.
[15] Madsen O, Møller C. The aau smart production laboratory for teaching and research in emerging digital manufacturing technologies. Procedia Manuf 2017;9:106–12. https://doi.org/10.1016/j.promfg.2017.04.036. 7th Conference on Learning Factories, CLF 2017.
[16] daCunha C, Cardin O, Gallot G, Viaud J. Designing the digital twins of reconfigurable manufacturing systems: application on a smart factory. IFAC-Pap 2021;54(1):874–9. https://doi.org/10.1016/j.ifacol.2021.08.103. 17th IFAC Symposium on Information Control Problems in Manufacturing INCOM 2021.
[17] U. of Wisconsin, IMS Centre Laboratories | Intelligent Manufacturing Systems (IMS) Centre, [Online; Accessed 2. Feb. 2022] (Feb 2022). ⟨https://www.uwindsor.ca/intelligent-manufacturing-systems/299/ims-centre-laboratories⟩.
[18] N. Jäpel, Industrie 4.0 Modellfabrik, [Online; accessed 2. Feb. 2022] (Feb 2022). https://www.htw-dresden.de/hochschule/fakultaeten/info-math/forschung/smart-production-systems/industrie-40-modellfabrik.
[19] Festo, CP Factory - The Cyber-Physical Factory, [Online; accessed 5. Feb. 2022] (Feb 2022). ⟨https://www.festo-didactic.com/int-en/learning-systems/learning-factories,cim-fms-systems/cp-factory/cp-factory-the-cyber-physical-factory.htm?fbid=aW50LmVuLjU1Ny4xNy4xOC4xMjkzLjc2NDM⟩.
[20] Adamietz R, Giesen T, Mayer P, Johnson A, Bibb R, Seifarth C. Reconfigurable and transportable container-integrated production system. Robot Comput-Integr Manuf 2018;53:1–20. https://doi.org/10.1016/j.rcim.2018.02.008. ⟨https://www.sciencedirect.com/science/article/pii/S0736584517301515⟩.
[21] Kang HS, Noh SD, Son JY, Kim H, Park JH, Lee JY. The FaaS system using additive manufacturing for personalized production. RAPID Prototyp J 2018;24(9):1486–99. https://doi.org/10.1108/RPJ-11-2016-0195.
[22] H. Cheng, H. Chen, Y. Liu, Object handling using autonomous industrial mobile manipulator, in: 2013 IEEE International Conference on Cyber Technology in Automation, Control and Intelligent Systems, 2013, 36–41.10.1109/CYBER.2013.6705416.
[23] Hvilshoj M, Bogh S, Nielsen OS, Madsen O. Autonomous industrial mobile manipulation (AIMM): past, present and future. Ind ROBOT- Int J Robot Res APPLICATION 2012;39(2):120–35. https://doi.org/10.1108/01439911211201582.
[24] Inoue S, Urata A, Kodama T, Huwer T, Maruyama Y, Fujita S, et al. High-precision mobile robotic manipulator for reconfigurable manufacturing systems. Int J Autom Technol 2021;15(5):651–60. https://doi.org/10.20965/ijat.2021.p0651.
[25] Andersen RE, Hansen EB, Cerny D, Madsen S, Pulendralingam B, Bøgh S, et al. Integration of a skill-based collaborative mobile robot in a smart cyber-physical environment. Procedia Manuf 2017;11:114–23. https://doi.org/10.1016/j.promfg.2017.07.209. 27th International Conference on Flexible Automation and Intelligent Manufacturing, FAIM2017, 27-30 June 2017, Modena, Italy.
[26] Singh A, Gupta S, Asjad M, Gupta P. Reconfigurable manufacturing systems: journey and the road ahead. Int J Syst Assur Eng Manag 2017;8(2, 2):1849–57. https://doi.org/10.1007/s13198-017-0610-z.
[27] Khanna K, Kumar R. Reconfigurable manufacturing system: a state-of-the-art review, BENCHMARKING-AN. Int J 2019;26(8):2608–35. https://doi.org/10.1108/BIJ-05-2018-0140.
[28] R. Pansare, G. Yadav, M.R. Nagare, Reconfigurable manufacturing system: a systematic review, meta-analysis and future research directions, JOURNAL OF ENGINEERING DESIGN AND TECHNOLOGY 10.1108/JEDT-05–2021-0231.
[29] Song C, Ding Y, Eid A, Hester JGD, He X, Bahr R, et al. Advances in wirelessly powered backscatter communications: From antenna/rf circuitry design to printed

flexible electronics. Proc IEEE 2022;110(1):171–92. https://doi.org/10.1109/JPROC.2021.3125285.
[30] Psomas C, You M, Liang K, Zheng G, Krikidis I. Design and analysis of swipt with safety constraints. Proc IEEE 2022;110(1):107–26. https://doi.org/10.1109/JPROC.2021.3130084.
[31] Qu X, Zhang W, Wong S-C, Tse CK. Design of a current-source-output inductive power transfer led lighting system. IEEE J Emerg Sel Top Power Electron 2015;3(1):306–14. https://doi.org/10.1109/JESTPE.2014.2318045.
[32] Jiang C, Chau KT, Leung YY, Liu C, Lee CHT, Han W. Design and analysis of wireless ballastless fluorescent lighting. IEEE Trans Ind Electron 2019;66(5):4065–74. https://doi.org/10.1109/TIE.2017.2784345.
[33] Han W, Chau KT, Jiang C, Liu W, Lam WH. High-order compensated wireless power transfer for dimmable metal halide lamps. IEEE Trans Power Electron 2020;35(6):6269–79. https://doi.org/10.1109/TPEL.2019.2950206.
[34] Han W, Chau KT, Zhang Z. Flexible induction heating using magnetic resonant coupling. IEEE Trans Ind Electron 2017;64(3):1982–92. https://doi.org/10.1109/TIE.2016.2620099.
[35] Zhang Y, Yang J, Jiang D, Li D, Qu R. Design, manufacture, and test of a rotary transformer for contactless power transfer system. IEEE Trans Magn 2022;58(2):1–6. https://doi.org/10.1109/TMAG.2021.3094135.
[36] Zhang Z, Chau KT, Qiu C, Liu C. Energy encryption for wireless power transfer. IEEE Trans Power Electron 2015;30(9):5237–46. https://doi.org/10.1109/TPEL.2014.2363686.
[37] Zeng Y, Rong C, Lu C, Tao X, Liu X, Liu R, et al. Misalignment insensitive wireless power transfer system using a hybrid transmitter for autonomous underwater vehicles. IEEE Trans Ind Appl 2022;58(1):1298–306. https://doi.org/10.1109/TIA.2021.3110496.
[38] Wang D, Cui S, Zhang J, Bie Z, Song K, Zhu C. A novel arc-shaped lightweight magnetic coupler for auv wireless power transfer. IEEE Trans Ind Appl 2022;58(1):1315–29. https://doi.org/10.1109/TIA.2021.3109839.
[39] Wu P, Xiao F, Huang H, Sha C, Yu S. Adaptive and extensible energy supply mechanism for uavs-aided wireless-powered internet of things. IEEE Internet Things J 2020;7(9):9201–13. https://doi.org/10.1109/JIOT.2020.3005133.
[40] Wei Z, Yu X, Ng DWK, Schober R. Resource allocation for simultaneous wireless information and power transfer systems: a tutorial overview. Proc IEEE 2022;110(1):127–49. https://doi.org/10.1109/JPROC.2021.3120888.
[41] Liu W, Chau KT, Lee CHT, Cao L, Han W. Wireless power and drive transfer for piping network. IEEE Trans Ind Electron 2022;69(3):2345–56. https://doi.org/10.1109/TIE.2021.3068675.
[42] Covic GA, Boys JT. Modern trends in inductive power transfer for transportation applications. IEEE J Emerg Sel Top Power Electron 2013;1(1):28–41. https://doi.org/10.1109/JESTPE.2013.2264473.
[43] Guidi G, Suul JA, Jenset F, Sorfonn I. Wireless charging for ships: High-power inductive charging for battery electric and plug-in hybrid vessels. IEEE Electrif Mag 2017;5(3):22–32. https://doi.org/10.1109/MELE.2017.2718829.
[44] Ahmad A, Alam MS, Chabaan R. A comprehensive review of wireless charging technologies for electric vehicles. IEEE Trans Transp Electrif 2018;4(1):38–63. https://doi.org/10.1109/TTE.2017.2771619.
[45] H. Arnarson, B. Solvang, 2022. Reconfigurable 3d printing platform for warehouses, in: 2022 6th International Conference on Green Technology and Sustainable Development (GTSD 2022), (Accepted), 2022, 772–777.
[46] H. Arnarson, 2022. Demonstration of production simulation, [Online; accessed 7. Feb. 2022] (Feb 2022). https://youtu.be/6ir7RUN_uk0.
[47] H. Arnarson, 2022. Super flexible reconfigurable manufacturing system (5x speed), [Online; accessed 21. Feb. 2022] (FEB 2022). https://youtu.be/UXUlaawd8Ps.
[48] H. Arnarson, 2022. Digital twin labratory using open access middleware for real-time communication and cooperation, [Online; Accessed 24. Mar. 2022] (MAR 2022). https://www.youtube.com/watch?v=HXskVx1IVyg.
[49] H. Arnarson, B. A. Bremdal, B. Solvang, 2022. Reconfigurable manufacturing: Towards an industrial big data approach, in: 2022 IEEE/ASME International Conference on Advanced Intelligent Mechatronics (AIM), (Accepted), 2022.
[50] ITU-R Recommendation ITU-R SM.2110, Frequency ranges for operation of non-beam wireless power transmission systems, Available at ⟨https://www.itu.int/rec/R-REC-SM.2110–0-201709-S⟩ (2021/ 11/09).
[51] M. I. Robots, 2022. Mobile robot from mobile industrial robots - mir100, [Online; accessed 27. Jan. 2022] (Jan 2022). https://www.mobile-industrial-robots.com/solutions/robots/mir100.
[52] O. Foundation, Unified architecture, [Online; accessed 04. Feb. 2022].⟨https://opcfoundation.org/about/opc-technologies/opc-ua/⟩.
[53] VanDerHorn E, Mahadevan S. Digital twin: Generalization, characterization and implementation. Decis Support Syst 2021;145:113524. https://doi.org/10.1016/j.dss.2021.113524.
[54] H. Arnarson, B. Solvang, B. Shu, 2020. The application of open access middleware for cooperation among heterogeneous manufacturing systems, in: 2020 3rd International Symposium on Small-scale Intelligent Manufacturing Systems (SIMS), 2020, 1–6.10.1109/SIMS49386.2020.9121537.
[55] Visual Components, Visual Components Premium - Visual Components, [Online; accessed 27. Jan. 2022] (Jan 2022). ⟨https://www.visualcomponents.com/products/premium⟩.

A Class-E-Based Resonant AC-DC Converter With Inherent PFC Capability,.

H. Mahdi, A. M. Ammar, Y. Nour, and M. A. E. Andersen

DOI: 10.1109/ACCESS.2021.3067800.

Paper's Contribution

This paper proposes a converter incorporating a diode bridge, a class-E inverter, and a class-D rectifier is presented for the PFC stage in single-phase offline converters. It presents a prototype to validate the analysis and the suggested design method. The prototype operates with zero-voltage switching (ZVS) across the load range. It achieves up to 211 W of output power at an efficiency of 88%, with an inherent power factor of 0.99 and a total harmonic distortion (THD) of 8.8 %. The converter can operate at output power down to 25 W, with a power factor of 0.95, THD of 28 %, and an efficiency of 88 %.

IEEE Access
Multidisciplinary | Rapid Review | Open Access Journal

Received February 12, 2021, accepted March 15, 2021, date of publication March 22, 2021, date of current version March 30, 2021.

Digital Object Identifier 10.1109/ACCESS.2021.3067800

A Class-E-Based Resonant AC-DC Converter With Inherent PFC Capability

HUSSEIN MAHDI[1], (Graduate Student Member, IEEE), AHMED M. AMMAR[2], (Member, IEEE), YASSER NOUR[2], (Senior Member, IEEE), AND MICHAEL A. E. ANDERSEN[2], (Member, IEEE)

[1]Department of Electrical Engineering, UiT Norges Arktiske Universitet, 8514 Narvik, Norway
[2]Department of Electrical Engineering, Technical University of Denmark, 2800 Kongens Lyngby, Denmark

Corresponding author: Ahmed M. Ammar (ammma@elektro.dtu.dk)

This work was supported by the European Union's Horizon 2020 Research and Innovation Programme under Grant 731466.

ABSTRACT This paper investigates the use of the class-E inverter for power factor correction (PFC) applications. Analytical and state-space models are derived showing the class-E inverter's capability of achieving inherent PFC operation with a constant duty cycle. The inherent PFC operation limits the controller responsibility to the regulation of the output voltage, which is key for resonant converters with challenging control. A converter incorporating a diode bridge, a class-E inverter, and a class-D rectifier is presented for the PFC stage in single-phase offline converters. A prototype is designed to validate the analysis and presented design method. The prototype operates with zero-voltage switching (ZVS) across the load range and achieves up to 211 W of output power at an efficiency of 88 %, with an inherent power factor of 0.99 and a total harmonic distortion (THD) of 8.8 %. Frequency modulation is used to achieve lower output power down to 25 W, with a power factor of 0.95, THD of 28 %, and an efficiency of 88 %.

INDEX TERMS AC-DC power conversion, class-E inverter, power factor correction, resonant power conversion, zero-voltage switching.

I. INTRODUCTION

Large-scale deployment of switch-mode power supplies to the utility introduces line current harmonics. The injected current harmonics result in voltage distortion and reduce the reliability of the grid [1], [2]. As a result, several international standards expressly limit the magnitudes of input current harmonics and set a limit for the minimum power factor. Thus, a power factor correction (PFC) converter needs to be employed in offline converters for different applications to comply with these standards.

The typical solution for offline converters is a two-stage structure that is illustrated in Fig. 1. A front-end stage ac-dc PFC converter rectifies the ac line voltage to a relatively smooth dc voltage while regulating the input current to follow the ac line voltage. A following dc-link capacitor filters the double-the-line frequency component. Finally, a dc-dc converter provides the current and voltage levels that apply to the load. This work's focus is on the PFC front-end stage of the offline converter.

The associate editor coordinating the review of this manuscript and approving it for publication was Tariq Masood.

Conventionally, pulse width modulation (PWM) converters are employed for the PFC stage, including boost [3]–[6], buck [7]–[9], buck-boost [10]–[12], SEPIC [13], [14], Cuk [15], and flyback [16] topologies. They offer high power quality and efficiency [17]. However, their hard-switching nature results in high switching losses, which sets an upper limit for the switching frequency and, in turn, the power density. In addition, their sharp switching current and voltage waveforms have high-frequency harmonic components, complicating electromagnetic interference (EMI) filters design.

Resonant converters operation is based on soft switching, which results in substantially lower switching losses and EMI noise at higher switching frequencies [18], [19]. The soft-switching nature has been previously studied in class-E inverter [20] and class-D inverter [21]. As a result, resonant converters have been investigated for use in many applications, one of which is offline converters, where prior art reported their use in the ac-dc stage [22]–[25], dc-dc stage [26]–[29], or both stages [30]–[32].

This paper investigates the feasibility of employing the class-E inverter for the PFC stage in single-phase offline

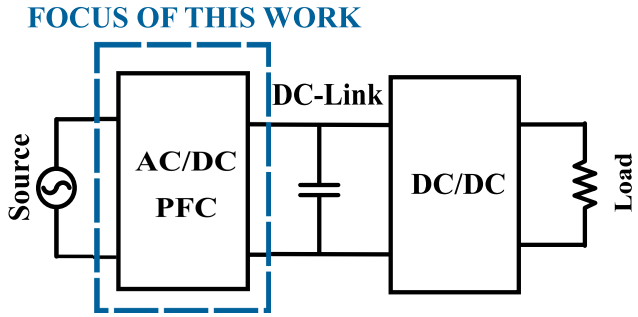

FIGURE 1. Offline converter structure.

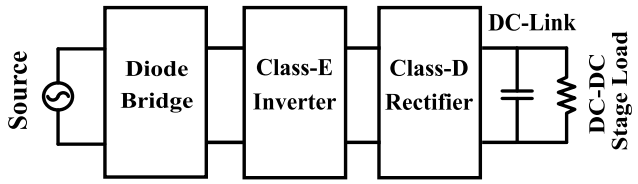

FIGURE 2. The architecture of the proposed converter.

converters [33]. Mathematical models are derived for the circuit showing inherent PFC capability with a constant duty-cycle operation. A converter comprising an input bridge, a class-E inverter, and a class-D rectifier is presented. Fig. 2 shows the proposed converter block diagram. The converter operation is based on zero-voltage switching (ZVS) and achieves PFC inherently. The inherent PFC operation limits the controller responsibility to the regulation of the output voltage, which is key for resonant converters with challenging control. At the same time, the soft-switching operation enables the design of PFC converters with high switching frequencies and power densities.

This paper is organized as follows: Section II describes the principle of operation of the presented converter. Mathematical models based on analytical and state-space approaches are covered in Section III. Section IV presents the design procedure. Prototype implementation and experimental verification results are illustrated in Section V. Finally, conclusion is provided in Section VI.

II. PRINCIPLE OF OPERATION

The schematic of the presented converter is shown in Fig. 3, which comprises a front-end diode bridge rectifier $D_1 - D_4$, a class-E inverter, and a class-D current-driven rectifier. The diode bridge rectifies the ac input voltage. A capacitor C_{in} is connected in parallel with the bridge to suppress the EMI and absorb the reverse current from the inverter. A class-E ZVS inverter drives the resonant tank with a current $i_r(t)$, where the shape of the waveform depends on the loaded quality factor of the tank Q_L and the duty-cycle D. A class-D rectifier converts the high-frequency current into a dc output voltage V_o, where the voltage stress across the rectifier diodes equals the output voltage.

Considering that the switching frequency f_s is much higher than the line frequency f_l, the input voltage to the inverter $v_{rec}(t)$ is assumed constant across the switching

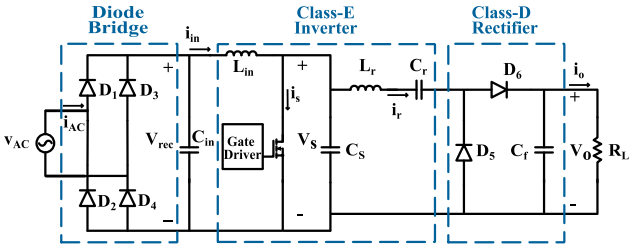

FIGURE 3. Class-E converter for PFC applications.

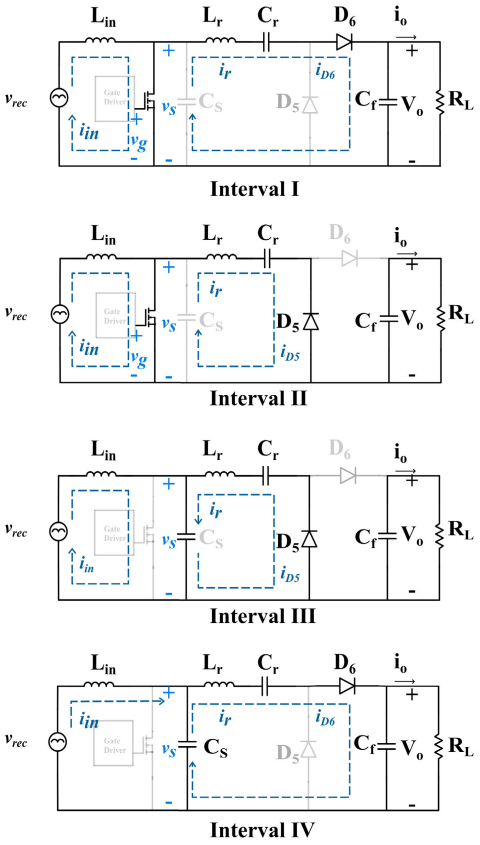

FIGURE 4. Simplified circuit diagram for a half-line cycle operation.

cycle. With a high-enough quality factor for the resonant tank, the first-harmonic approximation (FHA) approach for modeling resonant converters is valid, and the resonant current is a sinewave with the form

$$i_r(\theta_s) = I_r \sin(\theta_s + \phi) \tag{1}$$

where I_r is the current amplitude, $\theta_s = \omega_s t$ is the current angle across the switching cycle, and ϕ is the phase shift with the switching node voltage.

The switching cycle is divided into four intervals, as shown in Fig. 4, with the corresponding voltage and current waveforms illustrated in Fig. 5, including the voltage across the switch gate $v_g(t)$, the drain-source voltage of the switch, i.e. switching node voltage $v_s(t)$, the inverter input current $i_{in}(t)$, the resonant current $i_r(t)$, and the diodes currents $i_{D5}(t)$ and $i_{D6}(t)$.

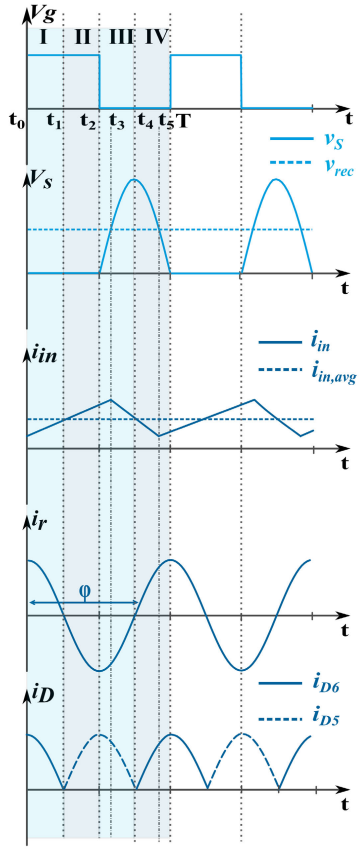

FIGURE 5. Voltage and current waveforms across two switching cycles.

In interval I ($t_0 - t_1$), the switch is on and the rectified voltage $v_{rec}(t)$ is higher than $v_s(t)$, thus the input current $i_{in}(t)$ increases linearly, charging the input inductor L_{in}. The resonant current is positive and flows in D_6, while D_5 is in reverse bias. Accordingly, the current flowing through the switch is the difference between $i_{in}(t)$ and $i_r(t)$.

In interval II ($t_1 - t_2$), the switch is still on, and the input current $i_{in}(t)$ keeps charging the input inductor L_{in}, while the resonant current reverses its direction and flows in D_5 with D_6 in reverse bias.

In interval III ($t_2 - t_4$), the switch is turned off and the capacitor C_s starts charging with the input current. Thus, $v_s(t)$ begins to increase, yet it is still less than the $v_{rec}(t)$. As a result, $i_{in}(t)$ keeps increasing until it reaches its maximum at t_3 when $v_{rec}(t)$ equals $v_s(t)$. Afterwards, the input inductor L_{in} starts discharging in the capacitor C_s, resulting in increasing of the voltage stress across the switch to its maximum value by the end of this interval.

In interval IV ($t_4 - T$), the switch is still turned off, the resonant current reverses its direction, turning D_5 off and D_6 on. The capacitor C_s starts discharging, and the switch voltage reduces until $v_{rec}(t)$ equals $v_s(t)$ at t_5, with the inductor L_{in} discharging as $v_{rec}(t) < v_s(t)$. From t_5 to the end of the interval, the inductor L_{in} is charging, and the capacitor C_s continues discharging until full depletion. By the end of this interval, the switch is turned on by the gate driver, and a new cycle begins.

If the switching frequency is higher than the resonant frequency f_o of the series-resonant tank ($L_r - C_r$), the tank and rectifier represent an inductive load and ZVS can be achieved. That is shown in Fig. 5 where the switch turns on at zero voltage, with a negative current in the resonant tank. By modulating the switching frequency f_s with respect to the resonant frequency f_o, the converter gain changes and accordingly the output power is modulated. The choice of the duty cycle affects ZVS operation as well as the stress on the switch. Theoretically, the switch voltage stress in a class-E inverter reaches about 3.6 times the input voltage with 50 % duty cycle [34]. However, in practice, this stress could reach more than four times the input voltage due to the nonlinearity of the switch node capacitance C_s [35], [36]. Accordingly, this topology is more suited for low-input-voltage applications.

III. MATHEMATICAL MODELLING

In this section, the mathematical models for the class-E inverter are investigated with respect to the input impedance. The conventional analytical and state-space approaches are considered. In the former approach, the design procedure derives the equations from the waveforms, while the latter is based on the basic circuit equations from Ohm's and Kirchhoff's laws. The principle of operation of the class-E rectifier as an input current shaping stage explained in [31], [32] is adopted in this work.

A. ANALYTICAL APPROACH

The analysis of the proposed topology is carried out across the switching cycle and using the approach given in [34], which assumes an ideal semiconductor switch and a high-enough input inductance such that the dc component of the input current I_{in} is only considered. From the principle of operation given in Section II and the V_s waveform in Fig. 5, the capacitor C_s current can be written as follows

$$i_{C_s}(\theta_s) = \begin{cases} 0, & 0<\theta_s \leqslant 2\pi\ D \\ I_{in} - I_r \sin(\theta_s + \phi), & 2\pi\ D<\theta_s \leqslant 2\pi \end{cases} \tag{2}$$

The voltage across the switch is then calculated

$$\begin{aligned} &v_s(\theta_s) \\ &= \frac{1}{\omega_s C_s} \int_0^{\theta_s} i_{C_s}(\theta)\, d\theta \\ &= \begin{cases} 0, & 0<\theta_s \leqslant 2\pi D \\ \dfrac{1}{\omega_s C_s}\{I_{in}(\theta_s - 2\pi D) & \\ +I_r[\cos(\theta_s + \phi) - \cos(2\pi D + \phi)]\}, & 2\pi D<\theta_s \leqslant 2\pi \end{cases} \end{aligned} \tag{3}$$

where θ is the variable of integration. Under optimal operation conditions, where ZVS is achieved, the voltage across the switch equals zero by the end of the switching period. Substituting $\theta_s = 2\pi$ in (3) and equating to zero, the following

expression for the resonant current amplitude is derived.

$$I_r = I_{in}\frac{2\pi(1-D)}{\cos(2\pi D+\phi)-\cos(\phi)} \tag{4}$$

Considering zero-derivative voltage switching (ZdVS, $dv_s(2\pi)/d\phi = 0$) is also achieved, taking the derivative for (3) with $\theta_s = 2\pi$ and equating to zero, the following expressions for the phase shift ϕ is derived.

$$\tan(\phi) = \frac{\cos(2\pi D)-1}{2\pi(1-D)+\sin(2\pi D)} \tag{5}$$

It can be seen that ϕ is a function of the duty cycle D. Following, the rectified voltage can be written as follows

$$V_{rec} = \frac{1}{2\pi}\left[\int_0^{2\pi} v_{L_{in}}(\theta)\,d\theta + \int_0^{2\pi} v_s(\theta)\,d\theta\right] \tag{6}$$

As the average voltage across the input inductor is zero, eliminating the first term and substituting (3) in (6) then evaluating the integration gives

$$V_{rec} = \frac{I_{in}}{\omega_s C_s}\left\{\frac{(1-D)[\pi(1-D)\cos(\pi D)+\sin(\pi D)]}{\tan(\pi D+\phi)\sin(\pi D)}\right\} \tag{7}$$

Dividing (7) by I_{in} gives the following expression for the input resistance.

$$R_{in} = \frac{1}{\omega_s C_s}\left\{\frac{(1-D)[\pi(1-D)\cos(\pi D)+\sin(\pi D)]}{\tan(\pi D+\phi)\sin(\pi D)}\right\} \tag{8}$$

Since (8) is a function of the duty cycle D and phase shift ϕ, which is itself a function of duty cycle as shown by (5), then operating with a constant duty cycle results in a constant input resistance that is independent of line changes. As a result, the converter is seen as a resistor from the input across the line cycle and power factor correction is achieved.

B. STATE-SPACE APPROACH

While the analytical approach assumes an ideal switching device and a sinusoidal resonant current to ensure the validity of the FHA approach, in the state-space approach, the design parameters are computed numerically. The state-space approach is used in prior art [37]–[39] to design class-E dc-dc converters with any loaded quality factor of the resonant tank and any size for the input inductor. Accordingly, it is considered in this section for flexibility across different designs.

By adding the switch on-resistance to the model, the switch is replaced with a resistor as follows

$$r_s = \begin{cases} r_{on}, & 0<\theta_s \leqslant 2\pi D \\ r_{off}, & 2\pi D<\theta_s \leqslant 2\pi \end{cases} \tag{9}$$

where r_{on} and r_{off} are the equivalent resistances of the switch in on- and off-states, respectively. The circuit has four energy storage components (L_{in}, L_r, C_s and C_r), which define the dimension of the state vector. The following expressions are obtained by applying Kirchhoff voltage and current laws.

$$\begin{cases} \omega_s L_{in}\dfrac{di_{in}(\theta_s)}{d\theta_s} = v_{rec}(\theta_s) - v_s(\theta_s) \\ \omega_s C_r\dfrac{dv_{C_r}(\theta_s)}{d\theta_s} = i_r(\theta_s) \\ \omega_s L_r\dfrac{di_r(\theta_s)}{d\theta_s} = v_s(\theta_s) - v_{C_r}(\theta_s) - i_r(\theta_s)R_{eff} \\ \omega_s C_s\dfrac{dv_s(\theta_s)}{d\theta_s} = i_{in}(\theta_s) - \dfrac{v_s(\theta_s)}{r_s} - i_r(\theta_s) \end{cases} \tag{10}$$

where $v_{C_r}(\theta_s)$ is the voltage across the resonant tank capacitor C_r and R_{eff} is the class-D rectifier effective resistance. By normalizing the impedance in (10) with the effective resistances, it can be rearranged and rewritten in the following matrix form

$$\dot{x} = A\cdot x + B\cdot u \tag{11a}$$

$$A = \begin{bmatrix} \dfrac{1}{\omega_s C_s r_s} & 0 & \dfrac{1}{\omega_s R_{eff} C_s} & \dfrac{-1}{\omega_s R_{eff} C_s} \\ 0 & 0 & 0 & \dfrac{1}{\omega_s R_{eff} C_r} \\ \dfrac{-R_{eff}}{\omega_s L_{in}} & 0 & 0 & 0 \\ \dfrac{1}{Q_L} & 0 & \dfrac{-1}{Q_L} & \dfrac{-1}{Q_L} \end{bmatrix} \tag{11b}$$

$$B = \begin{bmatrix} 0 \\ 0 \\ \dfrac{R_{eff}}{\omega_s L_{in}} \\ 0 \end{bmatrix} \tag{11c}$$

$$x = \begin{bmatrix} v_s(\theta_s) \\ v_{c_r}(\theta_s) \\ i_{in}(\theta_s) \\ i_r(\theta_s) \end{bmatrix} \tag{11d}$$

$$Q_L = \frac{\omega_s\cdot L_r}{R_{eff}} \tag{11e}$$

where x is the state vector, A is the system matrix, B is the control matrix, and u is the input vector. From (11), the number of parameters is nine, i.e. ω_s, D, Q_L, L_{in}, L_r, C_r, C_s, R_{eff}, $r_s \in \mathbb{R}^9$, and the solution of the equation is

$$x(\theta_s) = x_n(\theta_s) + x_f(\theta_s) \tag{12}$$

where $x_n(\theta_s)$ is the natural response of the system and $x_f(\theta_s)$ is the forced response. These two terms can be calculated as follows [40].

$$x_n(\theta_s) = e^{A\theta_s}\cdot x(0^-) \tag{13a}$$

$$x_f(\theta_s) = A^{-1}\cdot(e^{A\theta_s} - I)\cdot B\cdot u \tag{13b}$$

where $e^{A\theta_s}$ is the exponential matrix, $x(0^-)$ is the initial condition vector, and I is the identity matrix, while the currents are normalized with the input current and the voltages are normalized with the input voltage. Since the waveforms are continuous and periodic, the initial conditions can be found by applying the continuity condition of the waveforms such that

$$x_{on}(0^-) = x_{off}(\theta)|_{\theta=2\pi(1-D)} \tag{14a}$$

TABLE 1. Design specifications.

Parameters	Specifications
RMS Input Voltage (V)	120
Line Frequency (Hz)	60
Output Power (W)	300
Output Voltage (V)	200
Switching Frequency (kHz)	90

$$x_{off}(0^-) = x_{on}(\theta)|_{\theta=2\pi D} \tag{14b}$$

Substituting (12)–(14) in (11) gives

$$\begin{bmatrix} x_{on}(2\pi) \\ x_{off}(2\pi) \end{bmatrix} = \begin{bmatrix} -e^{2\pi D A_{on}} & I \\ I & -e^{2\pi(1-D)A_{off}} \end{bmatrix}^{-1} \cdot \begin{bmatrix} A_{on}^{-1}(e^{2\pi D A_{on}} - I) \\ A_{off}^{-1}(e^{2\pi(1-D)A_{off}} - I) \end{bmatrix} \cdot B \tag{15}$$

where A_{on} and A_{off} are the system matrices in (11) when r_s is equal to r_{on} and r_{off}, respectively. Under optimal operation conditions, where ZVS and ZdVS are achieved, (15) can be re-evaluated and solved numerically using the Matlab *fsolve* solver. However, there are nine parameters and two optimum operation conditions. Therefore, ω_s, D, Q_L, L_{in}, L_r, R_{eff}, $r_s \in \mathbb{R}^7$ are chosen as the design parameters, while C_r and C_s are solved as unknown parameters.

Since (11) is in the form of a first-order differential equation, the solution with oscillating input can also be written as

$$x(\theta_l) = M\cos(\theta_l) + N\sin(\theta_l) = G\sin(\theta_l - \alpha) \tag{16a}$$

$$G = \sqrt{M^2 + N^2} = \frac{B}{\sqrt{2}} \tag{16b}$$

$$\alpha = \tan^{-1}\left(\frac{N}{M}\right) = \frac{\omega_l}{A} \tag{16c}$$

where M and N are solution parameters that are found from the initial conditions, $\theta_l = \omega_l t$ is the input current angle across the line cycle, G is the gain vector, and α is the phase shift matrix. Equation (16a) mathematically shows that the response of the system, $i_{in}(\theta_l)$ which is the main interest, to the oscillating input voltage has the same frequency of the input and phase-shifted by α. From (16c), it can be proven that the input current is in phase with the input voltage (i.e. $\alpha \approx 0$), and hence the converter emulates a resistor.

IV. CONVERTER DESIGN

This section describes the design procedure of the presented converter. Table 1 summarizes the converter design specifications. The converter is designed to operate from US mains input voltage for a rated output power of 300 W and an output voltage of 200 V. A 90-kHz switching frequency is chosen for this design which is intended to prove the analysis and inherent PFC capability. Fig. 6 shows the normalized switches voltage and current stresses with respect to the input voltage and current. A duty cycle of 40 % is chosen for minimal stress on the switch.

In the analytical approach, the design procedure based on the FHA approach and given in [34] is followed in this paper.

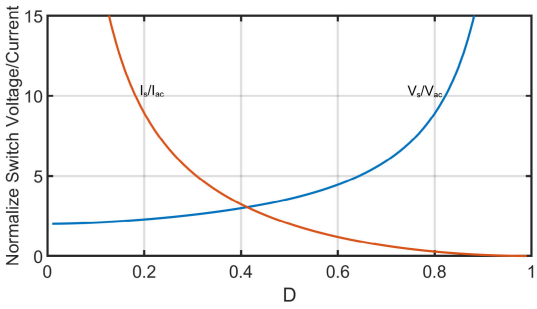

FIGURE 6. Normalized switch stresses vs. duty cycle.

To ensure the validity of the FHA approach, a high-quality factor of seven is chosen for this design. The procedure begins with the calculation of the class-D rectifier effective input resistance.

$$R_{eff} = \frac{2R_L}{\pi^2} = \frac{V_o^2}{\pi^2 \cdot P_o} \tag{17}$$

where R_L is the load resistance, V_o is the output voltage, and P_o is the output power. The phase angle of the resonant current can be written as

$$\phi = \pi + \arctan\left(\frac{\cos(2\pi D) - 1}{2\pi(1-D) + \sin(2\pi D)}\right) \tag{18}$$

The capacitor C_s is calculated from (19), as shown at the bottom of the next page. The switching frequency is chosen to be higher than the resonant frequency such that the net impedance of the tank is inductive. The inductor L_r can be divided into two series inductances, such that L_{r1} resonates with the capacitor C_r at the switching frequency, while L_{r2} is responsible for the phase lagging shown in (18) and can be calculated from (20), as shown at the bottom of the next page. Then, the resonant capacitor can be found as follows

$$C_r = \frac{1}{\omega_s^2 L_{r1}} = \frac{1}{\omega_s^2(L_r - L_{r2})} = \frac{1}{\omega_s(Q_L \cdot R_{eff} - \omega_s L_{r2})} \tag{21}$$

The input inductance *Lin* should be large enough to ensure a small ripple current through the choke (10 % of dc current), and calculated as follows.

$$L_{in} \geq \frac{7R_{eff}}{f_s} \tag{22}$$

Regarding the output capacitor C_f, it needs to be large enough to filter the double-the-line frequency in single-phase PFC applications, and is calculated from the following expression, with η being the efficiency, and ω_l being the angular line frequency [32].

$$C_f \geq \frac{\eta P_o}{0.04 V_o^2 \omega_l} \tag{23}$$

The state-space approach is carried out numerically in MATLAB. Table 2 lists the calculated values of the components from both models. It can be observed that the values obtained from both models are highly correlated.

TABLE 2. Calculated component values.

Component	Analytical Model	State-Space Model	Difference (%)
L_{in} (μH)	205.84	205.84	0
L_r (μH)	350.59	350.59	0
C_s (nF)	15.19	14.74	3.01
C_r (nF)	11.74	12.50	6.27

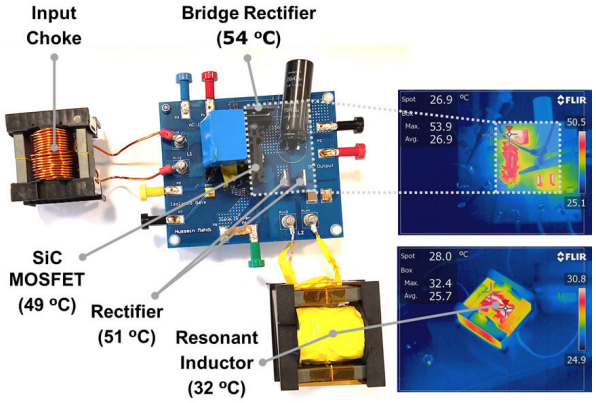

FIGURE 7. Prototype picture and thermal performance at full load.

TABLE 3. Bill of materials.

Component	Value	Type
$D_1 - D_4$	GBU10A	Bridge Rectifier
C_{in} (μF)	1	SMD Film Capacitor
L_{in} (mH)	1.3	3C97 ETD49/25/16
Q_1	C3M0075120D	1200-V SiC MOSFET
C_s (nF)	15	SMD Ceramic Capacitor
L_r (μH)	342.9	3C97 ETD59/31/22
C_r (nF)	2×5.6	SMD Ceramic Capacitor
$D_5 - D_6$	C3D10065A	SiC Schottky Diode
C_f (μF)	470	250-V Electrolytic Capacitor

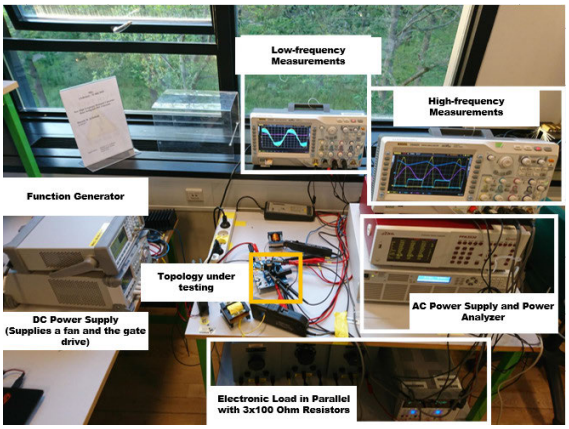

FIGURE 8. Prototype under testing.

V. PROTOTYPE IMPLEMENTATION AND EXPERIMENTAL VERIFICATION

This section covers the implementation of a prototype built based on the analysis and design procedure. Experimental results are then presented and discussed.

A. IMPLEMENTATION

The prototype of the proposed topology is assembled on a two-layer PCB. Fig. 7 shows a picture of the prototype, and Table 3 lists the bill of materials based on the parameters obtained from the design procedure given in Section IV. Compared with silicon devices, wide-bandgap devices have reduced reverse-recovery charge and better figures of merit [41]–[43]. Considering the high voltage stress across the switch, a silicon carbide (SiC) device is more suited for this application than a gallium nitride (GaN) device, as the breakdown voltage limit for commercially available GaN devices is 650 V. Cascode GaN device structures offer higher breakdown voltages up to 900 V, yet that comes with higher on-resistance than otherwise offered by SiC devices, which is a key parameter for soft-switching topologies. The C3M0075120D device by Cree/Wolfspeed is chosen and is driven using a single-channel isolated gate driver (UCC5350SBD by Texas Instruments). From (22), a minimum value for the input choke of 205 µH is needed to guarantee a small ripple on the input current and ensure the validity of the analytical approach equations, where a larger value of 1.3 mH is chosen to help reduce EMI and core loss, and it does not affect the converter operation.

B. EXPERIMENTAL RESULTS

Fig. 8 shows the testing lab setup. The converter is tested from US-mains input voltage, delivering up to 211 W of power at 89.5 kHz and 55 % duty cycle, where thermal considerations limited the delivery for the specified output power.

Fig. 9 shows the line-frequency waveforms at 211 W load. The input and output voltages are measured using high-voltage differential probes (LeCroy ADP305 and Testec SI 9001), and the current is displayed using a clamp-on current probe (Siemens 7KA1412-8AA). The figure shows the input current to be proportional to the input voltage, with a minor phase difference, achieving a power factor of 0.99 inherently. The dashed waveform is the input current filtered by the moving-average function in MATLAB and shown for clarity.

$$C_s = \frac{cos(\pi D + \phi)[(1-D)\pi\cos(\pi D) + sin(\pi D)] \cdot 2\sin(\pi D)\sin(\pi D + \phi)}{\pi^2(1-D)\omega_s R_{eff}} \tag{19}$$

$$L_{r2} = \frac{R_{eff}}{\omega_s} \cdot \frac{2(1-D)^2\pi^2 - 1 + 2\cos(\phi)\cos(2\pi D + \phi) - \cos\big(2(\pi D + \phi)\big)[\cos(2\pi D) - \pi(1-D)\sin(2\pi D)]}{4\sin(\pi D)\sin(\pi D + \phi)\cos(\pi D + \phi)[(1-D)\pi\cos(\pi D) + \sin(\pi D)]} \tag{20}$$

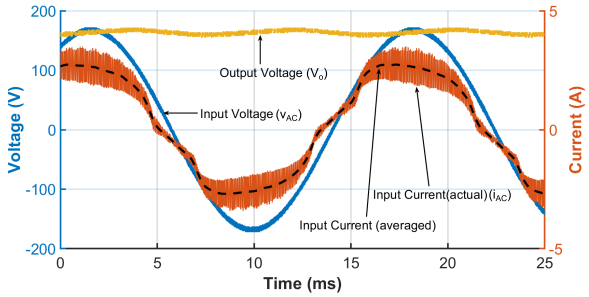

FIGURE 9. Experimental line-frequency waveforms of the proposed converter at 211 W.

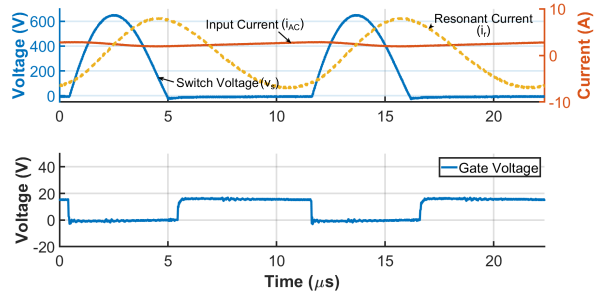

FIGURE 10. Experimental switching-frequency waveforms of the proposed converter at 211 W.

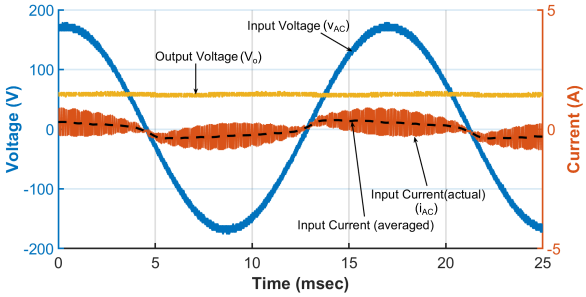

FIGURE 11. Experimental line-frequency waveforms of the proposed converter at 25 W.

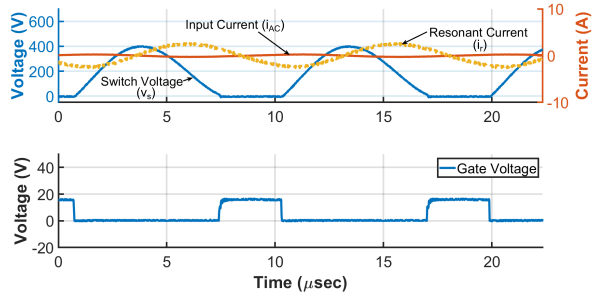

FIGURE 12. Experimental switching-frequency waveforms of the proposed converter at 25 W.

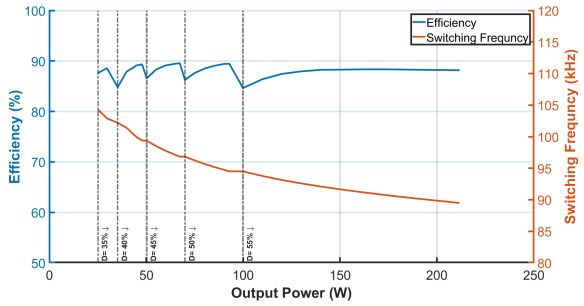

FIGURE 13. The efficiency and switching frequency of the proposed converter at different output power levels.

Fig. 10 shows the switching-frequency waveforms at 211 W. The resonant current has a sinusoidal waveform, which goes in accordance with the analysis and design procedure based on the FHA approach, and it is about 15 A peak-to-peak. While the input current in the inductor L_{in} is mainly a dc component with 0.4 A peak-to-peak ripple. The figure illustrates the inductive mode of operation, where the resonant current lags the switch node voltage and the switch voltage returns to zero before the switch is turned on, achieving ZVS.

A short interval of reverse conduction of the FET is observed, where the switch-node capacitance is fully depleted before the switch turns on. However, with the reduced reverse recovery charge in SiC devices, the contribution of reverse conduction to the overall power loss is insignificant and can be eliminated with the precise adjustment of the switch driving signal duty cycle.

Fig. 11 and 12 show the line-frequency and switching-frequency waveforms at 25 W. The figures show that a high-power factor is still achieved at the light load, where the ZVS operation is maintained through the adjustment of the switch duty cycle.

Fig. 13 shows the obtained efficiency and employed switching frequency across the load range. The results show that the output power can be regulated from 211 W down to 25 W with switching frequency modulation between 89.5 kHz to 104.3 kHz, respectively. The peak obtained efficiency is 88.3 % at 90 W with 96 kHz and a duty cycle of 0.5. The small dips in the efficiency curve are attributed to the partial loss of ZVS, which is corrected by adjusting the duty cycle. For lower output power down to 0 W (e.g. dimming functionality in LED driver applications), the overall converter can be switched on/off with a low-frequency PWM signal in a burst-mode control fashion. That helps limit the maximum switching frequency of the converter and achieve high efficiency at light loads.

The power quality results are shown in Fig. 14, where a power factor of 0.99 and a total harmonic distortion (THD) of 8.8 % are achieved at full load, while the minimum power factor is 0.95 at 25 W with a THD of 28 %. The harmonic spectra of the input current at the 211 W and 25 W are illustrated in Fig. 15.

Fig. 16 shows the power loss breakdown at full load operation. The currents of the different components are obtained from experimental and simulation results, and the loss is calculated based on parameters from the devices datasheets. It can be seen that 26 % of the overall loss is incurred as conduction losses in the switch, whereas 22 % of loss is dissipated in the resonant inductor, while 30 % is lost in the rectifier diodes and 16 % in the bridge, which goes in

TABLE 4. Comparison with reported literature.

Reference	[3]	[7]	[10]	[13]	[15]	[22]	[23]	[25]	[30]	[31]	This Work
Year	2019	2015	2018	2016	2017	2020	2020	2014	2013	2009	2021
Type	PWM	PWM	PWM	PWM	PWM	Resonant	Resonant	Resonant	Resonant	Resonant	Resonant
Topology	Boost	Buck	Buck-Boost	SEPIC	Cuk	Class-D Converter	Class-D Inverter	Class-D Rectifier	Class-DE Rectifier	Class-E Rectifier	Class-E Inverter
Aux. circuit	None	Filter	None	None	Filter	None	Charge Pump	Matching Network	Matching Network	Matching Network	None
V_{in} (V_{rms})	Universal	Universal	220	120	Universal	230	230	220	220	220	120
Power (W)	1000	300	245	200	300	105	50	36.4	36	36	211
V_{out} (V)	400	80	400	400	300	450	300	342	327	343	165
PF	0.99	0.94	0.99	0.97	0.99	0.99	0.99	0.98	0.99	0.99	0.99
THD (%)	-	25.7	< 10	27.2	< 6	5.2	8.6	20	1.4	5.6	8.8
Efficiency (%)	96	97	97	96	-	94	88	94	90	86	88
Switching Frequency (kHz)	550	65	4000	50	500	2000	1000	50	84	61	90
PFC Functionality	Inherent	Controlled	Controlled	Controlled	Controlled	Controlled	Inherent	Inherent	Inherent	Inherent	Inherent
Components Count[1]	6	11	8	14	12	10	11	11	13	12	10
Switches	1	2	2	2	1	2	2	2	2	2	1
Diodes	1	2	2	5	5	2	3	2	2	1	2
Magnetic Components	1	3	1	3	3	1	1	2	2	2	2

1. Including the bridge as a single component and excluding the input filter.

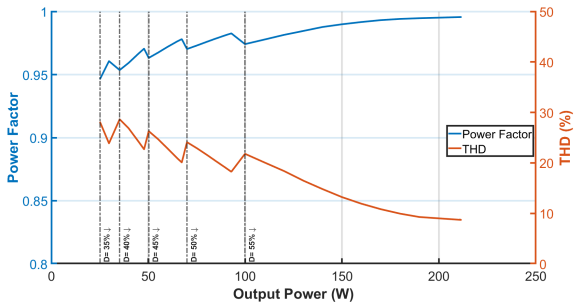

FIGURE 14. The obtained power factor and THD across load range.

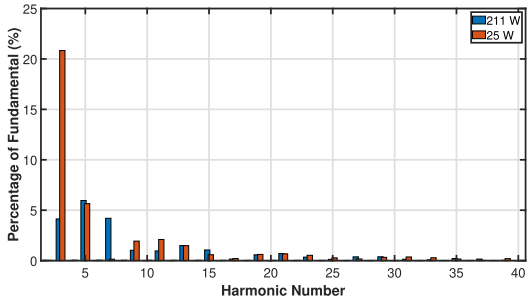

FIGURE 15. Input current harmonic spectra at 211 W and 25 W loads.

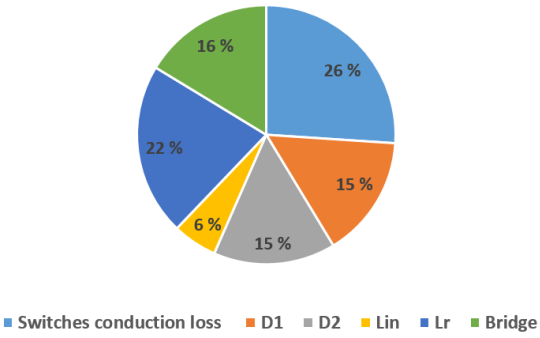

FIGURE 16. Power loss breakdown at full load.

accordance with the thermal pictures in Fig. 7. By improving the resonant inductor implementation and the choice of rectifier diodes and bridge, higher efficiency can be achieved.

Table 4 compares the proposed work with a number of reported solutions for PFC applications for the low-mid power range. It can be observed that the obtained power factor and THD figures fall within the ranges reported by prior art. In addition, the proposed converter achieves PFC inherently across a wide load range. That provides freedom from the limited bandwidths of commercial PFC controllers and simplifies control requirements. In terms of cost, the proposed solution offers a relatively low number of components, with a single switch, two diodes (in addition to the input bridge) and two magnetic devices. The switch is referenced to ground, with a simple driving circuitry. In comparison with the work in [13], which is also designed to operate from 120 V_{rms} and delivers about the same output power, the proposed converter has a lower efficiency, yet offers a higher power factor and lower THD, with reduced component count and lower cost.

Compared with the reported resonant PFC converters, the proposed solution does not require any additional circuit or matching network, which reduces the overall system bill of materials. In addition, as the topology features an input inductor, it requires a simpler input filter and diode bridge implementations, where the input current is not pulsating as in the case of [23].

It is noted that the proposed converter's efficiency is lower than that reported by PWM converters, yet it is on par with several reported resonant converter solutions. Similar to most of the reported solutions, the proposed topology is compatible with universal input mains, as the analysis and modeling results are valid for any input voltage in the range of 85-265 V_{rms}, and inherent PFC functionality is achieved. With respect to the prototype, the switch circuit needs to be designed for the worst-case conditions, which comes with the higher input voltage. In addition, in order to ensure the validity of the FHA equations by operation near-resonance, the output voltage will change across the range of the input rms voltage. That will require the subsequent dc-dc stage to have a wide-input line regulation capability.

As the target of the presented prototype is to demonstrate the inherent PFC capability, there is a space for improvement with an optimized high-frequency design that takes benefit of the ZVS capabilities of the proposed work towards high-power-density implementations with higher efficiencies.

VI. CONCLUSION

This paper investigates the use of the class-E inverter for PFC applications. The circuit analytical model proves that the converter emulates a resistance to the input when operating with a constant duty cycle. That is asserted from the obtained state-space model, where the phase shift between the input current and voltage is shown to equal almost zero. A resonant converter incorporating a class-E inverter with a class-D rectifier is designed for the front-end ac-dc stage in a two-stage offline converter. The inherent PFC operation limits the controller responsibility to the regulation of the output voltage, which is key for resonant converters with challenging control. A prototype is built and tested to prove the concept. The prototype achieves zero-voltage switching and inherent PFC along the load range between 25 W and 211 W, with a peak efficiency of 88 %, a peak power factor of 0.99 and a minimum THD of 8.8 % at full load.

REFERENCES

[1] B. Singh, B. N. Singh, A. Chandra, K. Al-Haddad, A. Pandey, and D. P. Kothari, "A review of single-phase improved power quality AC-DC converters," *IEEE Trans. Ind. Electron.*, vol. 50, no. 5, pp. 962–981, Oct. 2003, doi: 10.1109/TIE.2003.817609.

[2] J. P. M. Figueiredo, F. L. Tofoli, and B. L. A. Silva, "A review of single-phase PFC topologies based on the boost converter," in *Proc. 9th IEEE/IAS Int. Conf. Ind. Appl. (INDUSCON)*, Sao Paulo, Brazil, Nov. 2010, pp. 1–6, doi: 10.1109/INDUSCON.2010.5740015.

[3] R. T. Ryan, D. N. Hogan, R. J. Morrison, and J. G. Hayes, "Digital closed-loop control strategy to maintain the phase shift of a multi-channel BCM boost converter for PFC applications," *IEEE Trans. Power Electron.*, vol. 34, no. 7, pp. 7001–7012, Jul. 2019, doi: 10.1109/TPEL.2018.2875273.

[4] A. Jha and B. Singh, "A bridgeless boost PFC converter fed LED driver for high power factor and low THD," in *Proc. IEEMA Eng. Infinite Conf. (eTechNxT)*, New Delhi, India, Mar. 2018, pp. 1–6, doi: 10.1109/ETECHNXT.2018.8385333.

[5] C. Xue, Y. Zhou, and W. Xu, "Modeling and stability analysis of parallel-connected PFC boost converter," in *Proc. Chin. Control Decis. Conf. (CCDC)*, Nanchang, China, Jun. 2019, pp. 1775–1779, doi: 10.1109/CCDC.2019.8832540.

[6] H. Xu, D. Chen, F. Xue, and X. Li, "Optimal design method of interleaved boost PFC for improving efficiency from switching frequency, boost inductor, and output voltage," *IEEE Trans. Power Electron.*, vol. 34, no. 7, pp. 6088–6107, Jul. 2019, doi: 10.1109/TPEL.2018.2872427.

[7] C.-Y. Yang, Y.-C. Liu, P.-J. Tseng, T.-F. Pan, H.-J. Chiu, and Y.-K. Lo, "DSP-based interleaved buck power factor corrector with adaptive slope compensation," *IEEE Trans. Ind. Electron.*, vol. 62, no. 8, pp. 4665–4677, Aug. 2015, doi: 10.1109/TIE.2015.2400421.

[8] Y.-C. Liu, F.-C. Syu, H.-C. Hsieh, K. A. Kim, and H.-J. Chiu, "Hybrid switched-inductor buck PFC converter for high-efficiency LED drivers," *IEEE Trans. Circuits Syst. II, Exp. Briefs*, vol. 65, no. 8, pp. 1069–1073, Aug. 2018, doi: 10.1109/TCSII.2017.2787554.

[9] C. Lin, Y. Liu, H. Chiu, Y. Lo, C. Lin, P. Tseng, and S. Cheng, "Study on an interleaved buck power factor corrector with gallium nitride field effect transistor and integrated inductor," *IET Power Electron.*, vol. 7, no. 10, pp. 2506–2516, Oct. 2014, doi: 10.1049/iet-pel.2013.0642.

[10] A. J. Hanson and D. J. Perreault, "A high frequency power factor correction converter with soft switching," in *Proc. IEEE Appl. Power Electron. Conf. Expo. (APEC)*, San Antonio, TX, USA, Mar. 2018, pp. 2027–2034, doi: 10.1109/APEC.2018.8341296.

[11] B. Zhao, A. Abramovitz, and K. Smedley, "Family of bridgeless buck-boost PFC rectifiers," *IEEE Trans. Power Electron.*, vol. 30, no. 12, pp. 6524–6527, Dec. 2015, doi: 10.1109/TPEL.2015.2445779.

[12] M. O. Badawy, Y. Sozer, and J. A. De Abreu-Garcia, "A novel control for a cascaded buck–boost PFC converter operating in discontinuous capacitor voltage mode," *IEEE Trans. Ind. Electron.*, vol. 63, no. 7, pp. 4198–4210, Jul. 2016, doi: 10.1109/TIE.2016.2539247.

[13] A. M. Al Gabri, A. A. Fardoun, and E. H. Ismail, "Bridgeless PFC-modified SEPIC rectifier with extended gain for universal input voltage applications," *IEEE Trans. Power Electron.*, vol. 30, no. 8, pp. 4272–4282, Aug. 2015, doi: 10.1109/TPEL.2014.2351806.

[14] A. J. Sabzali, E. H. Ismail, M. A. Al-Saffar, and A. A. Fardoun, "New bridgeless DCM Sepic and Cuk PFC rectifiers with low conduction and switching losses," *IEEE Trans. Ind. Appl.*, vol. 47, no. 2, pp. 873–881, Mar. 2011, doi: 10.1109/TIA.2010.2102996.

[15] A. Jha and B. Singh, "Cuk PFC converter for high brightness LED driver with brightness control," in *Proc. IEEE 7th Power India Int. Conf. (PIICON)*, Bikaner, India, Nov. 2016, pp. 1–6, doi: 10.1109/POWERI.2016.8077311.

[16] C. Zhao, J. Zhang, and X. Wu, "An improved variable on-time control strategy for a CRM flyback PFC converter," *IEEE Trans. Power Electron.*, vol. 32, no. 2, pp. 915–919, Feb. 2017, doi: 10.1109/TPEL.2016.2594201.

[17] R. W. Erickson and D. Maksimovic, *Fundamentals of Power Electronics*. Boston, MA, USA: Springer, 2007.

[18] L. S. Mendonca, T. C. Naidon, G. G. de Freitas, M. L. D. S. Martins, and F. E. Bisogno, "Energy-based normalization for resonant power converters," *IEEE Trans. Power Electron.*, vol. 33, no. 8, pp. 6526–6536, Aug. 2018, doi: 10.1109/TPEL.2017.2784570.

[19] M. Salem, A. Jusoh, N. R. N. Idris, H. S. Das, and I. Alhamrouni, "Resonant power converters with respect to passive storage (LC) elements and control techniques—An overview," *Renew. Sustain. Energy Rev.*, vol. 91, pp. 504–520, Aug. 2018, doi: 10.1016/j.rser.2018.04.020.

[20] T. Nagashima, X. Wei, T. Suetsugu, M. K. Kazimierczuk, and H. Sekiya, "Waveform equations, output power, and power conversion efficiency for class-E inverter outside nominal operation," *IEEE Trans. Ind. Electron.*, vol. 61, no. 4, pp. 1799–1810, Apr. 2014, doi: 10.1109/TIE.2013.2267693.

[21] N. J. Dahl, A. M. Ammar, and M. A. E. Andersen, "Identification of ZVS points and bounded low-loss operating regions in a class-D resonant converter," *IEEE Trans. Power Electron.*, early access, Jan. 15, 2021, doi: 10.1109/TPEL.2021.3052176.

[22] F. M. Spliid, A. M. Ammar, and A. Knott, "Analysis and design of a resonant power converter with a wide input voltage range for AC/DC applications," *IEEE J. Emerg. Sel. Topics Power Electron.*, vol. 8, no. 3, pp. 2056–2066, Sep. 2020, doi: 10.1109/JESTPE.2019.2963266.

[23] A. M. Ammar, F. M. Spliid, Y. Nour, and A. Knott, "Analysis and design of a charge-pump-based resonant AC-DC converter with inherent PFC capability," *IEEE J. Emerg. Sel. Topics Power Electron.*, vol. 8, no. 3, pp. 2067–2081, Sep. 2020, doi: 10.1109/JESTPE.2020.2966143.

[24] A. M. Ammar, F. M. Spliid, Y. Nour, and A. Knott, "A series-resonant charge-pump-based rectifier with inherent PFC capability," in *Proc. 20th Workshop Control Modeling Power Electron. (COMPEL)*, Toronto, ON, Canada, Jun. 2019, pp. 1–5, doi: 10.1109/COMPEL.2019.8769705.

[25] C. Ekkaravarodome, V. Chunkag, K. Jirasereeamornkul, and M. K. Kazimierczuk, "Class-D zero-current-switching rectifier as power-factor corrector for lighting applications," *IEEE Trans. Power Electron.*, vol. 29, no. 9, pp. 4938–4948, Sep. 2014, doi: 10.1109/TPEL.2013.2284872.

[26] A. M. Ammar, Y. Nour, and A. Knott, "A high-efficiency 1 MHz 65 W GaN-based LLC resonant DC-DC converter," in *Proc. IEEE Conf. Power Electron. Renew. Energy (CPERE)*, Aswan City, Egypt, Oct. 2019, pp. 448–452, doi: 10.1109/CPERE45374.2019.8980041.

[27] Y. Wang, F. Li, Y. Qiu, S. Gao, Y. Guan, and D. Xu, "A single-stage LED driver based on flyback and modified class-E resonant converters with low-voltage stress," *IEEE Trans. Ind. Electron.*, vol. 66, no. 11, pp. 8463–8473, Nov. 2019, doi: 10.1109/TIE.2018.2890502.

[28] A. M. Ammar, K. Ali, and D. J. Rogers, "A bidirectional GaN-based CLLC converter for plug-in electric vehicles on-board chargers," in *Proc. 46th Annu. Conf. IEEE Ind. Electron. Soc. (IECON)*, Singapore, Oct. 2020, pp. 1129–1135, doi: 10.1109/IECON43393.2020.9254560.

[29] N. J. Dahl, A. M. Ammar, A. Knott, and M. A. E. Andersen, "An improved linear model for high-frequency class-DE resonant converter using the generalized averaging modeling technique," *IEEE J. Emerg. Sel. Topics Power Electron.*, vol. 8, no. 3, pp. 2156–2166, Sep. 2020, doi: 10.1109/JESTPE.2019.2945182.

[30] C. Ekkaravarodome, K. Jirasereeamornkul, and M. K. Kazimierczuk, "Implementation of a DC-side class-DE low-dv/dt rectifier as a PFC for electronic ballast application," *IEEE Trans. Power Electron.*, vol. 29, no. 10, pp. 5486–5497, Oct. 2014, doi: 10.1109/TPEL.2013.2290105.

[31] J. Sasiluk and J. Kamon, "The electronic ballast using class-E rectifier with tapped inductor for power factor correction," in *Proc. Int. Symp. Intell. Signal Process. Commun. Syst.*, Bangkok, Thailand, Feb. 2009, pp. 1–4, doi: 10.1109/ISPACS.2009.4806768.

[32] K. Jirasereeamornkul, M. K. Kazimierczuk, I. Boonyaroonate, and K. Chamnongthai, "Single-stage electronic ballast with class-E rectifier as power-factor corrector," *IEEE Trans. Circuits Syst. I, Reg. Papers*, vol. 53, no. 1, pp. 139–148, Jan. 2006, doi: 10.1109/TCSI.2005.855039.

[33] A. M. Ammar, "Advances in resonant power conversion for offline converter applications," Ph.D. dissertation, Tech. Univ. Denmark, Lyngby, Denmark, 2020.

[34] M. Kazimierczuk and D. Czarkowski, *Resonant Power Converters*. 2nd ed. Hoboken, NJ, USA: Wiley, 2012.

[35] M. J. Chudobiak, "The use of parasitic nonlinear capacitors in class E amplifiers," *IEEE Trans. Circuits Syst. I, Fundam. Theory Appl.*, vol. 41, no. 12, pp. 941–944, Dec. 1994, doi: 10.1109/81.340867.

[36] T. M. Andersen, S. K. Christensen, A. Knott, and M. A. E. Andersen, "A VHF class E DC-DC converter with self-oscillating gate driver," in *Proc. 26th Annu. IEEE Appl. Power Electron. Conf. Expo. (APEC)*, Fort Worth, TX, USA, Mar. 2011, pp. 885–891, doi: 10.1109/APEC.2011.5744699.

[37] H. Sekiya, I. Sasase, and S. Mori, "Computation of design values for class E amplifiers without using waveform equations," *IEEE Trans. Circuits Syst. I, Fundam. Theory Appl.*, vol. 49, no. 7, pp. 966–978, Jul. 2002, doi: 10.1109/TCSI.2002.800474.

[38] H. Sekiya, J. Lu, and T. Yahagi, "Design of generalized class E2 DC/DC converter," *Int. J. Circuit Theory Appl.*, vol. 31, no. 3, pp. 229–248, May 2003, doi: 10.1002/cta.229.

[39] P. C. Luk, S. Aldhaher, W. Fei, and J. F. Whidborne, "State-space modeling of a class E^2 converter for inductive links," *IEEE Trans. Power Electron.*, vol. 30, no. 6, pp. 3242–3251, Jun. 2015, doi: 10.1109/TPEL.2014.2332451.

[40] G. Strang, *Differential Equations and Linear Algebra*. Cambridge, MA, USA: Wellesley-Cambridge, 2015, p. 510.

[41] F. Wang and Z. Zhang, "Overview of silicon carbide technology: Device, converter, system, and application," *CPSS Trans. Power Electron. Appl.*, vol. 1, no. 1, pp. 13–32, Dec. 2016, doi: 10.24295/CPSSTPEA.2016.00003.

[42] J. Millán, "A review of WBG power semiconductor devices," in *Proc. Int. Semiconductor Conf. (CAS)*, Sinaia, Romania, Oct. 2012, pp. 57–66, doi: 10.1109/SMICND.2012.6400696.

[43] J. Tsao *et al.*, "Ultrawide-bandgap semiconductors: Research opportunities and challenges," *Adv. Electron. Mater.*, vol. 4, Jan. 2018, Art. no. 1600501, doi: 10.1002/aelm.201600501.

HUSSEIN MAHDI (Graduate Student Member, IEEE) received the B.Sc. degree in electrical power engineering from Yarmouk University, in 2011, the M.Sc. degree in environmental and renewable energy engineering from German Jordanian University (GJU), in 2015, and the second M.Sc. degree in electrical engineering from The Arctic University of Norway (UiT), in 2019, where he is currently pursuing the Ph.D. degree.

He is also working as a Graduate Research and a Teaching Assistant with The Arctic University of Norway (UiT). His research interests include resonant converters, soft switching topologies, control of power converters, and wireless power transfer.

AHMED M. AMMAR (Member, IEEE) received the B.Sc. degree in electronics and communications engineering from Mansoura University, Mansoura, Egypt, in 2011, the M.Sc. degree in microelectronics system design from Nile University, Giza, Egypt, in 2014, and the Ph.D. degree in electrical engineering from the Technical University of Denmark, Kongens Lyngby, Denmark, in 2020.

He was a Visiting Researcher with the University of Minnesota, Minneapolis, USA, and the University of Oxford, Oxford, U.K. He is currently a Postdoctoral Researcher with the Department of Electrical Engineering, Technical University of Denmark. He is also a Mentor with Siemens Business. His experience includes positions at different industries, including Intel Corporation, Hillsboro, OR, USA; Imec, Leuven, Belgium; and Mentor Graphics, Cairo, Egypt. His current research interests include power electronics, resonant power conversion, integrated power converters, power management, and delivery circuits and systems.

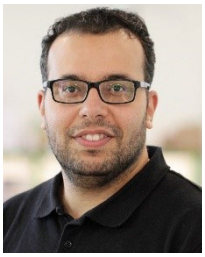

YASSER NOUR (Senior Member, IEEE) received the B.Sc. and M.Sc. degrees in electrical engineering from South Valley University, Aswan, Egypt, in 2007 and 2011, respectively. He received the Ph.D. degree in electrical engineering from the Technical University of Denmark, Kongens Lyngby, Denmark.

He was a Research Engineer with Enpirion Inc., a Staff Engineer with the Altera's Egypt Technology Center, and a Staff Engineer with Symmid Corporation Sdn Bhd, Malaysia. His research interests include analog integrated circuits design, integrated power converters, high-voltage low-power converters, integrated magnetics, and passive components.

MICHAEL A. E. ANDERSEN (Member, IEEE) received the M.Sc.E.E and Ph.D. degrees in power electronics from the Technical University of Denmark, Kongens Lyngby, Denmark, in 1987 and 1990, respectively.

Since 2009, he has been the Deputy Head of the Department of Electrical Engineering, Technical University of Denmark, where he is currently a Professor of power electronics. He has authored or coauthored more than 300 publications. His research interests include switch mode power supplies, piezoelectric transformers, power factor correction, and switch-mode audio power amplifiers.

Evaluation of Capacitive Power Transfer for Small Vessels Charging Applications

Hussein Mahdi, Bjarte Hoff, Trond Østrem

DOI: 10.1109/ISIE45063.2020.9152514

Paper's Contribution

This paper evaluates Capacitive Power Transfer (CPT) for charging small ships and theoretically calculates the charging requirement for the fully electric ship GMV Zero (Astrid Helene). The analysis is based on the maximum efficiency and maximum power models available in the literature. The paper also proposes reducing the air gap distance between the plates or submerging the plates in water to increase the power transfer capability.

Maximum Available Power of Undersea Capacitive Coupling in a Wireless Power Transfer System

Hussein Mahdi, Bjarte Hoff, Trond Østrem

DOI: 10.1109/WPTC51349.2021.9458006

Paper's Contribution

This paper studies the maximum available power of a dissipative capacitive power transfer (CPT) system submerged in seawater. The paper uses the conjugate-image approach to drive the maximum available power of an underwater CPT and its corresponding efficiency as functions of capacitive coupling parameters.

Maximum Available Power of Undersea Capacitive Coupling in a Wireless Power Transfer System

Hussein Mahdi[1], Bjarte Hoff[2], and Trond Østrem[3]
Department of Electrical Engineering, UiT - The Arctic University of Norway, Narvik, Norway
[1] hussein.al-sallami@uit.no, [2] bjarte.hoff@uit.no, and [3] trond.ostrem@uit.no

***Abstract*— This paper studies the maximum available power of a dissipative capacitive power transfer (CPT) system submerged in seawater. The CPT system's maximum power capability is driven using the network theory, precisely the conjugate-image approach. The equations of the maximum available load power and the system's corresponding efficiency are expressed as a function of the capacitive coupling parameters. The experimental results demonstrate that the maximum available power and the corresponding efficiency decreases by a maximum of 10%, which occurs at 1.4 MHz, when the plates' separation distance change from 100 mm to 300 mm. Besides, the system has higher power transfer capability and higher efficiency at a low-frequency range than a high one. The maximum available load power decreases by about 22.5% when increasing the frequency from 300 kHz to 1.4 MHz. Thus, the CPT system can provide a good solution to charge electric ships and underwater vehicles over a wide separation distance and low-frequency range.**

***Index Terms*—Wireless power transmission, Couplings, Impedance matching, and Network theory.**

I. Introduction

A capacitive power transfer (CPT) system transfers power across coupling plates based on the alternating electric field principle. The CPT system is an attractive wireless power transfer option because it has a simple structure, low cost and weight, low electromagnetic interference (EMI), low ability to penetrate through metals, and good misalignment performance [1], [2]. Due to these intrinsic features, CPT has been proposed for electric vehicles [3], [4], underwater vehicles [5]–[7], and ships charging applications [8], [9].

One way to model the capacitive coupling plates (couplers) is an equivalent π model [4], [10]. Based on this model, the maximum available efficiency of a CPT system is investigated using the coupling coefficient (k), the quality factor (Q), and their extended product (kQ) [11]. The investigation is later extended to include three possible solutions, namely, (1) the one that maximizes the efficiency, (2) one that maximizes the transferred power, and (3) one that realizes power matching [12], [13].

The previous solutions are analyzed for a nondissipative CPT system, in which a direct coupling with a lossless dielectric is considered. However, if a CPT system is submerged in seawater to enhance the coupling capacitance of the plates, then the seawater's dielectric losses cannot be neglected. The high percentage of the dissolved ions increase the electric conductivity and the losses of the water. Thus, the analysis for a dissipative system is needed.

The maximum available CPT system's efficiency has been previously considered for a dissipative system in [14]. The study uses the conjugate-impedance approach to drive the maximum efficiency for the CPT system submerged in seawater. Similarly, this paper addresses the conjugate-impedance analysis to achieve the maximum available power solution for a dissipative CPT system.

The maximum available load power and overall system efficiency are expressed using the coupling parameters. The paper experimentally utilised the derived equations over a 100 to 300 mm separation distance, and in $300\,\mathrm{kHz}$ to $1.5\,\mathrm{MHz}$ operating frequency. The rest of the paper is organized as follows: Section II provides the theoretical analysis. Section III presents the experimental results and discussion. The conclusion is drawn in section IV.

II. Theoretical Analysis

A CPT system can be modelled using both the π model and its equivalent linear two-port network, as shown in Fig. 1. The two-port network representation is considered to make a general formulation for the CPT scheme. In this representation, the couplers are considered as a black box from which only the voltages (u_1, u_2) and the currents (i_1, i_2) can be measured. The voltage-to-current relation can be expressed through an admittance matrix:

$$\begin{bmatrix} i_1 \\ i_2 \end{bmatrix} = \begin{bmatrix} Y_{\mathrm{I}} & -Y_{\mathrm{M}} \\ -Y_{\mathrm{M}} & Y_{\mathrm{II}} \end{bmatrix} \begin{bmatrix} u_1 \\ u_2 \end{bmatrix}, \tag{1}$$

where Y_{I} and Y_{II} are the self-admittance coefficients, and Y_{M} is the mutual admittance coefficient, which can be expressed as:

$$\begin{cases} Y_{\mathrm{I}} &= \overbrace{(G_1 + G_{\mathrm{M}})}^{G_{\mathrm{I}}} + \mathrm{j}\overbrace{(B_1 + B_{\mathrm{M}})}^{B_{\mathrm{I}}} \\ Y_{\mathrm{M}} &= G_{\mathrm{M}} + \mathrm{j}B_{\mathrm{M}} \\ Y_{\mathrm{II}} &= \underbrace{(G_2 + G_{\mathrm{M}})}_{G_{\mathrm{II}}} + \mathrm{j}\underbrace{(B_2 + B_{\mathrm{M}})}_{B_{\mathrm{II}}} \end{cases}, \tag{2}$$

where (G) is the conductance, $(B = \omega C)$ is the susceptance parts of the admittance, and ω is the angular frequency. The admittance matrix Y can be calculated from the scattering matrix S:

$$\begin{aligned} Z &= Z_o(I - S)^{-1}(I + S) \\ Y &= Z^{-1} \end{aligned}, \tag{3}$$

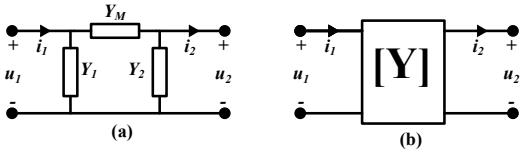

Fig. 1. Network representation of CPT: (a) A π model. (b) A linear two-port network.

where $Y = \begin{bmatrix} Y_{\rm I} & -Y_{\rm M} \\ -Y_{\rm M} & Y_{\rm II} \end{bmatrix}$, $S = \begin{bmatrix} S_{11} & S_{12} \\ S_{21} & S_{22} \end{bmatrix}$, and Z_o is the reference admittance which has a real positive value and is practically chosen to be $50\,\Omega$.

Fig. 2(a) shows the connection of the two-port network to transmitter and receiver external circuits. The input admittance $Y_{\rm in}$, as seen by the transmitter side, is expressed as:

$$Y_{\rm in} = Y_{\rm I} - \frac{Y_{\rm M}^2}{Y_{\rm II} + Y_{\rm L}} \tag{4}$$

where $Y_{\rm L} = G_L + {\rm j}B_L$ is the load admittance. The source circuit ($i_{\rm s}$ and $Y_{\rm S} = G_S + {\rm j}B_S$) is replaced by its Norton equivalent at the receiver side, as illustrated in Fig. 2(b). The Norton equivalent can be expressed as:

$$Y_{\rm N} = Y_{out} = Y_{\rm II} - \frac{Y_{\rm M}^2}{Y_{\rm I} + Y_{\rm S}}, \tag{5}$$

$$i_{\rm N} = \frac{-Y_{\rm M}}{Y_{\rm I} + Y_{\rm S}} i_{\rm s}. \tag{6}$$

The input admittance can be considered as the conjugate of the source admittance ($Y_{\rm in} = Y_{\rm S}^*$) and the output admittance is the conjugate of the load admittance ($Y_{out} = Y_{\rm L}^*$), based on the conjugate-image theorem [15]. If the network is nondissipative, then (4) and (5) are identical. However, for a dissipative network, (4) and (5) can be solved for $Y_{\rm S}$ and $Y_{\rm L}$. The following two expressions can be introduced to clearing the fraction term in both (4) and (5):

$$\theta_{\rm G} = \frac{G_{\rm s}}{G_{\rm I}} = \frac{G_{\rm L}}{G_{\rm II}} \tag{7a}$$

$$\theta_{\rm B} = \frac{B_{\rm s} + B_{\rm I}}{G_{\rm I}} = \frac{B_{\rm L} + B_{\rm II}}{G_{\rm II}} \tag{7b}$$

The expressions $\theta_{\rm G}$ and $\theta_{\rm B}$ are defined in [15] as intermediate variables, but their physical meanings are not given. The source and load admittance can be rewritten as:

$$Y_{\rm S} = G_{\rm I}\,(\theta_{\rm G} + {\rm j}\theta_{\rm B}) - {\rm j}B_{\rm I} \tag{8a}$$

$$Y_{\rm L} = G_{\rm II}\,(\theta_{\rm G} + {\rm j}\theta_{\rm B}) - {\rm j}B_{\rm II} \tag{8b}$$

While the mutual admittance term can be expressed as:

$$Y_{\rm M}^2 = G_{\rm I}\,G_{\rm II}\,(1 - \theta_{\rm G} + {\rm j}\theta_{\rm B}\,)\,(1 + \theta_{\rm G} + {\rm j}\theta_{\rm B}\,) \tag{9}$$

From (9), the two expressions ($\theta_{\rm G}$ and $\theta_{\rm B}$) can be redefined.

$$\theta_{\rm G} = \sqrt{\left(1 - \frac{G_{\rm M}^2}{G_{\rm I}\,G_{\rm II}}\right)\left(1 + \frac{B_{\rm M}^2}{G_{\rm I}\,G_{\rm II}}\right)} \tag{10a}$$

$$\theta_{\rm B} = \frac{G_{\rm M}\,B_{\rm M}}{G_{\rm I}\,G_{\rm II}} \tag{10b}$$

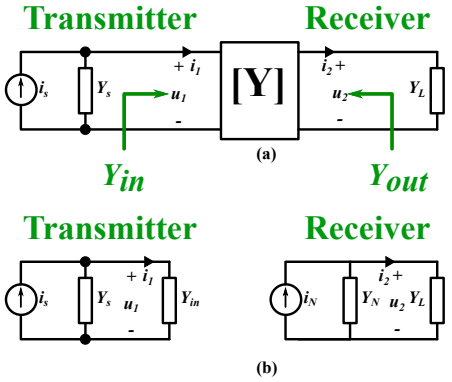

Fig. 2. A general representation of CPT system: (a) Two-port network connected to source and load. (b) The transmitter and receiver equivalent circuits.

The input ($P_{\rm in}$) and output power ($P_{\rm L}$) can be expressed as:

$$\begin{aligned} P_{\rm in} &= \frac{1}{2}{\rm Re}(Y_{\rm in} + Y_{\rm S})|u_1|^2 = \frac{1}{2}\frac{{\rm Re}(Y_{\rm in} + Y_{\rm S})|i_{\rm s}|^2}{|Y_{\rm S} + Y_{\rm in}|^2} \\ &= \frac{1}{2}\frac{{\rm Re}(Y_{\rm in} + Y_{\rm S})|Y_{\rm II} + Y_{\rm L}|^2|i_{\rm s}|^2}{|\,(Y_{\rm II} + Y_{\rm L})\,(Y_{\rm S} + Y_{\rm in})\,|^2} \end{aligned} \tag{11}$$

$$\begin{aligned} P_{\rm L} &= \frac{1}{2}{\rm Re}(Y_L)|u_2|^2 = \frac{1}{2}\frac{{\rm Re}(Y_{\rm L})|i_{\rm N}|^2}{|Y_{\rm N} + Y_{\rm L}|^2} \\ &= \frac{1}{2}\frac{{\rm Re}(Y_{\rm L})|Y_{\rm M}|^2|i_{\rm s}|^2}{|\,(Y_{\rm N} + Y_{\rm L})\,(Y_{\rm I} + Y_{\rm S})\,|^2} \end{aligned} \tag{12}$$

where ${\rm Re}(\,)$ is the real part of the complex expression. The maximum available power by the source is achieved when $Y_{\rm in} = Y_{\rm S}^*$, and it can be calculated as:

$$P_{\rm s,max} = \frac{1}{2}\frac{G_{\rm s}|i_{\rm s}|^2}{|\,(Y_{\rm in} + Y_{\rm S})\,|^2} = \frac{1}{8}\frac{|i_{\rm s}|^2}{G_{\rm in}} \tag{13}$$

Defining the following two parameters for the convenience of mathematical symbols:

$$\psi^2 = \frac{G_{\rm M}^2}{G_{\rm I}\,G_{\rm II}} \tag{14a}$$

$$\chi^2 = \frac{B_{\rm M}^2}{G_{\rm I}\,G_{\rm II}} \tag{14b}$$

ψ represents the ratio between the coupling and the self-conductance. χ is an equivalent to the quality factor. Similarly, the maximum available power derived to the load by Norton-equivalent circuit is achieved when $Y_{\rm N} = Y_{\rm L}^*$. The maximum available load power can be calculated from (12) and (14) as follows.

$$P_{\rm L,max} = P_{\rm s,max}\frac{\psi^2 + \chi^2}{(1 + \theta_{\rm G})^2 + \theta_{\rm B}^2} \tag{15}$$

For a nondissipative network and lossless source, that is $\psi = 0$ and $G_s = 0$ respectively, the maximum available power becomes:

$$P_{\rm L,max} = P_{\rm s,max}\frac{\chi^2}{(1 + \chi^2\,)} \tag{16}$$

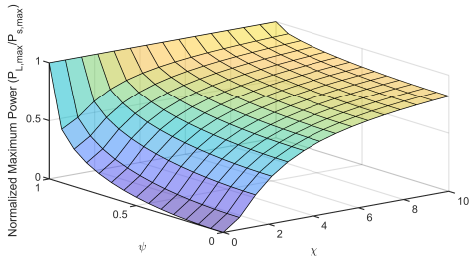

Fig. 3. The theoretical maximum available power calculated from (15).

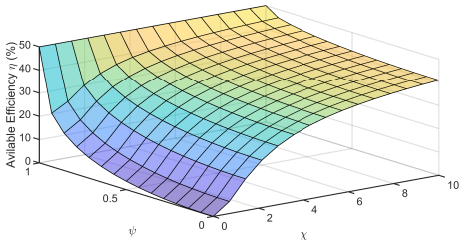

Fig. 4. The theoretical available efficiency at maximum power transfer calculated from (17).

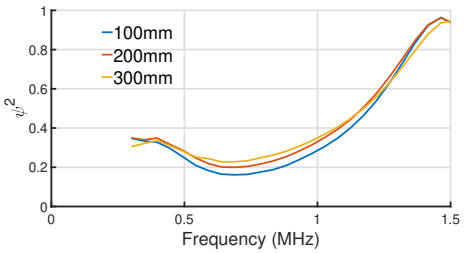

Fig. 6. The measured ψ^2 versus frequency

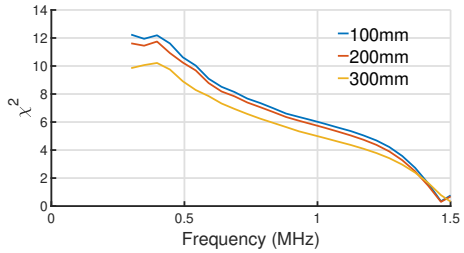

Fig. 7. The measured χ^2 versus frequency

which is the same equation that reported in [12]. From (11) (12), the available efficiency at maximum power transfer of CPT system is given as:

$$\eta = \frac{P_{\mathrm{L}}}{P_{\mathrm{in}}} = \frac{1}{2}\frac{\psi^2+\chi^2}{(1+\theta_{\mathrm{G}})^2+\theta_{\mathrm{B}}^2} \tag{17}$$

For a nondissipative network and lossless source, the efficiency becomes:

$$\eta = \frac{1}{2}\frac{\chi^2}{(1+\chi^2)} \tag{18}$$

From (15) and as illustrated in Fig. 3, when χ and ψ increases, the maximum available load power increases to reach the $P_{\mathrm{s,max}}$. Likewise, from (17) when χ and ψ increases, the maximum efficiency of the CPT system reaches 50%, as shown in Fig 4. For a nondissipative CPT system and from (16) and (18), as asymptotically $\chi \to \infty$ provides $P_{L,max} \to P_{s,max}$ and $\eta \to 50\%$, respectively.

III. Experimental Results and Discussion

Two pairs of square-shaped electrodes of 6082 aluminium sheets covered with a plastic lamination pouch for isolation were used to realize the couplers. A PicoVNA Vector Network Analyzers is used in the measurements, as illustrated in Fig. 5. The measurement is carried out over a distance (d) from $100\,\mathrm{mm}$ to $300\,\mathrm{mm}$ and a frequency range from $300\,\mathrm{kHz}$ to $1.5\,\mathrm{MHz}$ in seawater that is collected from the local harbour.

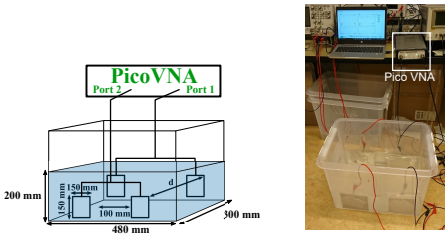

Fig. 5. The measurement setups

The two coefficients ψ^2 and χ^2 are measured using (14). Fig. 6 shows that the ψ^2 cannot be neglected over the frequency range. Thus, if the nondissipative analysis is used, then imprecise results are achieved. The increase of ψ^2 the increase of the ions' mobility in the seawater. When the frequency of the electric fields increases, the coupling conductivity and hence ψ^2 also increases.

Fig. 7 shows that χ^2 monotonically decreases with the increase of frequency. This coefficient is asymptotically approaching zero around $1.5\,\mathrm{MHz}$, which is the self-resonant frequency of the couplers (at which $C_M \to 0$ and $\chi^2 \to 0$). The maximum rates of change of ψ^2 and χ^2 are 42% at $736.5\,\mathrm{kHz}$ and 24% at $736.5\,\mathrm{kHz}$, respectively, when the separation distance is increased from $100\,\mathrm{mm}$ to $300\,\mathrm{mm}$.

According to (15) and (17), the CPT system is expected to give higher power transfer capability and better efficiency at lower frequency ranges than at higher ones. Fig. 8 depicts the maximum load power, which is plotted using the measured values of ψ^2 and χ^2 and into (15) and (16). The results show that at low frequencies, more power can be transferred than at higher ones. For example, the maximum power that can be transferred to the load at $100\,\mathrm{mm}$ separation distance decreases from about 86% of the maximum source power at $300\,\mathrm{kHz}$ to about 57% at $1.5\,\mathrm{MHz}$.

The results also demonstrate that the change of the separation distance has almost a negligible effect on the maximum power transfer capability. The maximum available power decreases by a maximum of 10% at 1.4 MHz when the

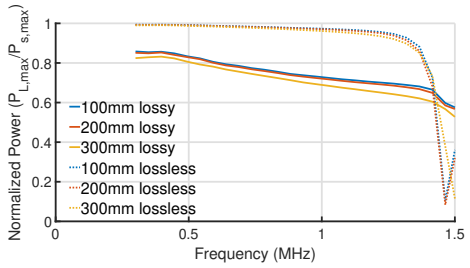

Fig. 8. The normalized power for lossy (15) and lossless (16) CPT system versus frequency.

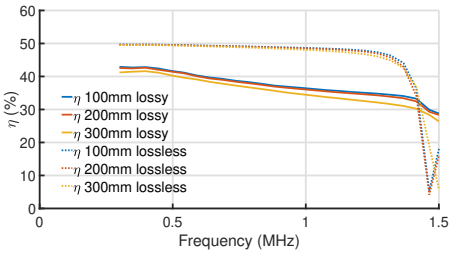

Fig. 9. The efficiency for lossy (17) and lossless (18) CPT system versus frequency at maximum power transfer.

plates' separation distance change from 100 mm to 300 mm. Moreover, the analysis for a nondissipative system gives overestimated results compared to the analysis for the dissipative one, except when approaching 1.5 MHz. The maximum available load power decreases by about 22.5% when increasing the frequency from 300 kHz to 1.4 MHz.

The available efficiency of the CPT system, from (17) and (18), is also investigated over the frequency and distance ranges at maximum power transfer. Fig 9 illustrates that the nondissipative analysis gives overestimated values compared to the dissipated analysis. Similar to maximum available power, the separation distance has a negligible effect on the efficiency. Besides, the system has higher efficiencies at a low-frequency range than at a higher one. At 100 mm distance, for instance, the CPT system's efficiency decreases from about 43% at 300 kHz to about 28% at 1.5 MHz.

IV. Conclusion

This paper investigates a dissipative capacitive power transfer (CPT) system submerged in seawater using the conjugate-image approach to drive the maximum available power. The maximum available load power and the corresponding efficiency have been expressed as functions of capacitive coupling parameters. The experimental results show that the maximum available power and the corresponding efficiency of the system decrease maximum by 10% when the plates' separation distance change from 100 mm to 300 mm.

The system has higher power transfer capability and efficiency at low frequencies than at higher ones.When increasing the frequency from 300 kHz to 1.4 MHz, the maximum available power decreases by about 22.5%. Unlike in the case of air-gapped CPT systems, which require high frequency to increase their power transfer capabilities, seawater CPT systems can operate at low frequencies to transfer high power with low EMI problem. Higher efficiency can also be achieved if the maximum power transfer is not considered as in [14]. Based on the analysis, the CPT system can provide an attractive wireless charging solution to electric ships and underwater vehicles with a wide separation distance and low-frequency range.

References

[1] F. Lu, H. Zhang, and C. Mi, "A Review on the Recent Development of Capacitive Wireless Power Transfer Technology," *Energies*, vol. 10, no. 11, p. 1752, nov 2017.

[2] L. Huang, A. P. Hu, A. Swain, S. Kim, and Y. Ren, "An overview of capacitively coupled power transfer - A new contactless power transfer solution," *Proceedings of the 2013 IEEE 8th Conference on Industrial Electronics and Applications, ICIEA 2013*, pp. 461–465, 2013.

[3] F. Lu, H. Zhang, and C. Mi, "A Two-Plate Capacitive Wireless Power Transfer System for Electric Vehicle Charging Applications," *IEEE Transactions on Power Electronics*, vol. 33, no. 2, pp. 964–969, 2018.

[4] H. Zhang, F. Lu, H. Hofmann, W. Liu, and C. C. Mi, "A Four-Plate Compact Capacitive Coupler Design and LCL-Compensated Topology for Capacitive Power Transfer in Electric Vehicle Charging Application," *IEEE Transactions on Power Electronics*, vol. 31, no. 12, pp. 8541–8551, 2016.

[5] M. Tamura, Y. Naka, K. Murai, and T. Nakata, "Design of a Capacitive Wireless Power Transfer System for Operation in Fresh Water," *IEEE Transactions on Microwave Theory and Techniques*, vol. 66, no. 12, pp. 5873–5884, 2018.

[6] M. Tamura, Y. Naka, and K. Murai, "Design of capacitive coupler in underwater wireless power transfer focusing on kQ product," *IEICE Transactions on Electronics*, vol. E101C, no. 10, pp. 759–766, 2018.

[7] M. Urano, K. Ata, and A. Takahashi, "Study on underwater wireless power transfer via electric coupling with a submerged electrode," *IMFEDK 2017 - 2017 International Meeting for Future of Electron Devices, Kansai*, pp. 36–37, 2017.

[8] H. Zhang and F. Lu, "Feasibility Study of the High-Power Underwater Capacitive Wireless Power Transfer for the Electric Ship Charging Application," *2019 IEEE Electric Ship Technologies Symposium, ESTS 2019*, pp. 231–235, 2019.

[9] H. Mahdi, B. Hoff, and T. Ostrem, "Evaluation of Capacitive Power Transfer for Small Vessels Charging Applications," *IEEE International Symposium on Industrial Electronics*, vol. 2020-June, pp. 1605–1610, 2020.

[10] L. Huang and A. P. Hu, "Defining the mutual coupling of capacitive power transfer for wireless power transfer," *Electronics Letters*, vol. 51, no. 22, pp. 1806–1807, 2015.

[11] T. Ohira, "Extended k-Q product formulas for capacitive- and inductive-coupling wireless power transfer schemes," *IEICE Electronics Express*, vol. 11, no. 9, pp. 1–7, 2014.

[12] M. Dionigi, M. Mongiardo, G. Monti, and R. Perfetti, "Modelling of wireless power transfer links based on capacitive coupling," *International Journal of Numerical Modelling: Electronic Networks, Devices and Fields*, vol. 30, no. 3-4, 2017.

[13] J. Kracek and M. Svanda, "Power balance of capacitive wireless power transfer," *Proceedings of European Microwave Conference in Central Europe, EuMCE 2019*, vol. 7, pp. 521–524, 2019.

[14] H. Mahdi, B. Hoff, and T. Ostrem, "Maximum Available Efficiency of Undersea Capacitive Coupling in a Wireless Power Transfer System," *IEEE International Symposium on Industrial Electronics*, 2021 (accepted).

[15] S. Roberts, "Conjugate-Image Impedances," *Proceedings of the IRE*, vol. 34, no. 4, pp. 198p–204p, 1946.

Maximum Available Efficiency of Undersea Capacitive Coupling in a Wireless Power Transfer System

Hussein Mahdi, Bjarte Hoff, Trond Østrem

DOI: 10.1109/ISIE45552.2021.9576386

Paper's Contribution

This paper studies the maximum efficiency of a dissipative capacitive power transfer (CPT) system submerged in seawater. The paper uses the conjugate-image approach to calculate maximum efficiency and its corresponding power as functions of capacitive coupling of underwater CPT systems.

Maximum Available Efficiency of Undersea Capacitive Coupling in a Wireless Power Transfer System

1st Hussein Mahdi
Department of Electrical Engineering
UiT - The Arctic University of Norway
Narvik, Norway
hussein.al-sallami@uit.no

2nd Bjarte Hoff
Department of Electrical Engineering
UiT - The Arctic University of Norway
Narvik, Norway
bjarte.hoff@uit.no

3rd Trond Østrem
Department of Electrical Engineering
UiT - The Arctic University of Norway
Narvik, Norway
trond.ostrem@uit.no

***Abstract*— This paper studies the maximum available efficiency of a capacitive power transfer (CPT) system submerged in seawater. The maximum efficiency for a dissipative CPT system is derived using the network theory, namely the conjugate-image method. Submerging CPT system in seawater gives a coupling capacitance in the nF range, which is higher than that in an air-gapped CPT system with similar dimensions. The experimental results demonstrate that the capacitive coupling decrease by 6.3% when the distance increase from 100 mm to 300 mm. The results also show that the efficiency decreases by about 17.5% when the frequency increases from 300 kHz to 1 MHz. These results imply that submerging the CPT system in seawater does not need to operate at a high-frequency range, as in air-gapped CPT counterparts. Thus, a loosely coupled underwater CPT system is a promising solution for wireless charging applications.**

***Index Terms*—Wireless power transmission, Couplings, Energy efficiency, Impedance matching, and Network theory.**

I. Introduction

A capacitive power transfer (CPT) system utilizes alternating electric fields confined between coupling plate electrodes (capacitive coupler) to transfer electric power. The CPT system has low cost and weight and shows good misalignment performance [1]. Thus, it is proposed for electric vehicles [2], [3], underwater vehicles [4]–[6], and ships charging applications [7], [8].

The air-gapped capacitive coupling is in the pF range, which requires high-frequency or high voltage across couplers for high power transfer [9]. Submerging the coupling plates in water improves the capacitance range because of the high relative permittivity and conductivity of seawater compared to air. The increased coupling could enhance transferred power over a wide transfer distance range.

The air-gapped capacitive coupling is previously studied, and an equivalent π model is proposed in [10] and [3]. Based on this model, the maximum available efficiency of the CPT system is investigated using the coupling coefficient (k), the quality factor (Q), and their product (kQ) parameters [11]. The investigation is extended to include three possible solutions:

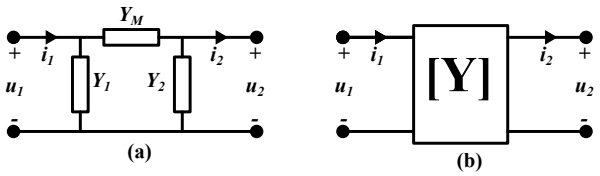

Fig. 1. Network representation of CPT: (a) A π model. (b) A linear two-port Network.

the one that maximizes the efficiency, one that maximizes the transferred power, and one that realizes power matching [12].

The efficiency of CPT systems submerged in water is examined using the same parameters, k, Q, and kQ in [4], [5], [13]. The maximum available efficiency of a submerged CPT system in freshwater is about 81% [5] and 91% [4] at transfer distance of $20\,\mathrm{mm}$ and MHz frequency range. Under the same separation distance and frequency range, an efficiency of over 90% is achieved in sweater [13].

The previous studies have only considered the direct coupling with a lossless dielectric. In addition, the submerged CPT system is investigated over narrow separation distance and high-frequency ranges. In contrast, this paper addresses the indirect coupling analysis for the maximum available efficiency solution, in which the dielectric losses of water are considered in the analysis.

The paper proposes the equations of maximum available efficiency, its corresponding maximum power, and voltage and current gain using the coupling parameters. Moreover, the coupling capacitance, the maximum available efficiency, and its corresponding available power are tested over a wide separation distance of 100 to 300 mm and low-frequency range of $300\,\mathrm{kHz}$ to $1.5\,\mathrm{MHz}$ operating frequency.

The rest of the paper is organized as follows: Section II provides the theoretical analysis. Section III presents the experimental results and discussion. The conclusion is drawn in section IV.

II. Theoretical Analysis

A CPT system can be modelled using the π model, as well as a linear two-port network, as shown in Fig. 1. The two-port representation of the CPT network is considered to make a general formulation for the CPT scheme. The two-port network assumes a black box model from which only the voltages (u_1, u_2) and the currents (i_1, i_2) can be measured. The voltage-to-current relation can be expressed through an admittance matrix:

$$\begin{bmatrix} i_1 \\ i_2 \end{bmatrix} = \begin{bmatrix} Y_\mathrm{I} & -Y_\mathrm{M} \\ -Y_\mathrm{M} & Y_\mathrm{II} \end{bmatrix} \begin{bmatrix} u_1 \\ u_2 \end{bmatrix}, \tag{1}$$

where Y_I and Y_II are the self-admittance coefficient, and Y_M is the mutual admittance coefficient. These coefficients can be found from the π model as:

$$\begin{cases} i_1 &= Y_\mathrm{I} u_1|_{u_2=0} \Rightarrow Y_\mathrm{I} = Y_\mathrm{M} + Y_1 \\ i_2 &= Y_\mathrm{II} u_2|_{u_1=0} \Rightarrow Y_\mathrm{II} = Y_\mathrm{M} + Y_2 \end{cases} \tag{2}$$

The admittance matrix Y can be calculated from the scattering matrix S:

$$\begin{aligned} Z &= Z_o (I - S)^{-1} (I + S) \\ Y &= Z^{-1} \end{aligned}, \tag{3}$$

where $Y = \left[\begin{smallmatrix} Y_\mathrm{I} & -Y_\mathrm{M} \\ -Y_\mathrm{M} & Y_\mathrm{II} \end{smallmatrix}\right]$, $S = \left[\begin{smallmatrix} S_{11} & S_{12} \\ S_{21} & S_{22} \end{smallmatrix}\right]$, and Z_o is the reference admittance which has a real positive value and is practically chosen to be $50\,\Omega$.

Fig. 2(a) illustrates when the two-port network is connected to a source and a load. The source is replaced by its Norton equivalent (I_s and Y_s). The input admittance Y_in, as seen by the transmitter side, is expressed as:

$$Y_\mathrm{in} = Y_\mathrm{I} - \frac{Y_\mathrm{M}^2}{Y_\mathrm{II} + Y_\mathrm{L}} \tag{4}$$

The corresponding Norton equivalent at the receiver side, as illustrated in Fig. 2(b), can be expressed as:

$$Y_\mathrm{N} = Y_{out} = Y_\mathrm{II} - \frac{Y_\mathrm{M}^2}{Y_\mathrm{I} + Y_\mathrm{s}} \tag{5}$$

$$i_\mathrm{N} = \frac{-Y_\mathrm{M}}{Y_\mathrm{I} + Y_\mathrm{s}} i_\mathrm{s} \tag{6}$$

Based on the conjugate-image theorem of a network analysis [14], the input admittance is the conjugate of the source admittance ($Y_\mathrm{in} = Y_\mathrm{s}^*$) and the output admittance is the conjugate of the load admittance ($Y_{out} = Y_\mathrm{L}^*$). If the network is nondissipative then (4) and (5) are identical. However, for a dissipative network, (4) and (5) can be solved for Y_s and Y_L.

The following two expressions can be introduced to clearing the fraction term in both (4) and (5):

$$\theta_\mathrm{G} = \frac{G_\mathrm{s}}{G_\mathrm{I}} = \frac{G_\mathrm{L}}{G_\mathrm{II}} \tag{7a}$$

$$\theta_\mathrm{B} = \frac{B_\mathrm{s} + B_\mathrm{I}}{G_\mathrm{I}} = \frac{B_\mathrm{L} + B_\mathrm{II}}{G_\mathrm{II}} \tag{7b}$$

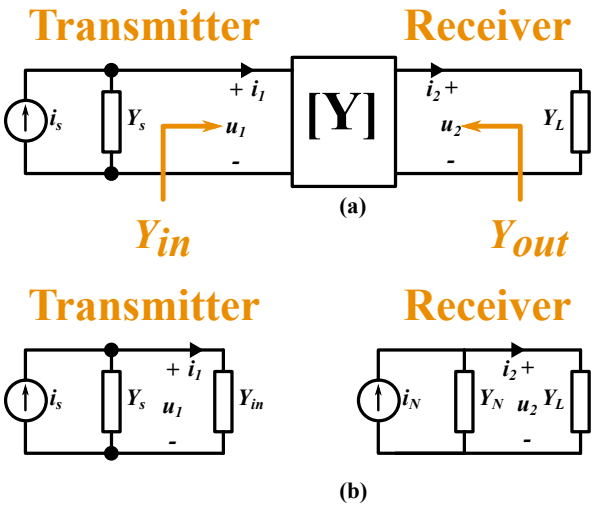

Fig. 2. A general representation of CPT system: (a) Two-port network connected to source and load. (b) The transmitter and receiver equivalent circuits.

The letters G and B represent the conductance and the susceptance parts of the admittance, respectively. Then, the source and load admittance can be rewritten as:

$$Y_\mathrm{s} = G_\mathrm{I}\,(\theta_\mathrm{G} + \mathrm{j}\theta_\mathrm{B}) - \mathrm{j}B_\mathrm{I} \tag{8a}$$

$$Y_\mathrm{L} = G_\mathrm{II}\,(\theta_\mathrm{G} + \mathrm{j}\theta_\mathrm{B}) - \mathrm{j}B_\mathrm{II} \tag{8b}$$

The mutual admittance term can be expressed as:

$$Y_\mathrm{M}^2 = G_\mathrm{I}\,G_\mathrm{II}\,(1 - \theta_\mathrm{G} + \mathrm{j}\theta_\mathrm{B}\,)\,(1 + \theta_\mathrm{G} + \mathrm{j}\theta_\mathrm{B}\,) \tag{9}$$

From (9), the two expressions can be redefined as:

$$\theta_\mathrm{G} = \sqrt{\left(1 - \frac{G_\mathrm{M}^2}{G_\mathrm{I}\,G_\mathrm{II}}\right)\left(1 + \frac{B_\mathrm{M}^2}{G_\mathrm{I}\,G_\mathrm{II}}\right)} \tag{10a}$$

$$\theta_\mathrm{B} = \frac{G_\mathrm{M}\,B_\mathrm{M}}{G_\mathrm{I}\,G_\mathrm{II}}, \tag{10b}$$

where $Y_\mathrm{M} = G_\mathrm{M} + B_\mathrm{M}$. Substitute $(i_2 = -Y_\mathrm{L}\,u_2\,)$ in (1) gives the voltage ratio.

$$\begin{aligned} G_u = \frac{u_2}{u_1} &= \frac{Y_\mathrm{M}}{Y_\mathrm{II} + Y_\mathrm{L}} \\ &= \sqrt{\frac{G_\mathrm{I}\,(1 - \theta_\mathrm{G} + \mathrm{j}\theta_\mathrm{B}\,)}{G_\mathrm{II}\,(1 + \theta_\mathrm{G} + \mathrm{j}\theta_\mathrm{B}\,)}} \end{aligned} \tag{11}$$

Similarly from (11), the current ratio is expressed as:

$$\begin{aligned} G_i = \frac{i_2}{i_1} &= \frac{-Y_\mathrm{in}}{Y_\mathrm{L}} \cdot \frac{Y_\mathrm{M}}{Y_\mathrm{II} + Y_\mathrm{L}} \\ &= \frac{-\left(G_\mathrm{I}\,(\theta_\mathrm{G} - \mathrm{j}\theta_\mathrm{B}) + \mathrm{j}B_\mathrm{I}\right)}{G_\mathrm{II}\,(\theta_\mathrm{G} + \mathrm{j}\theta_\mathrm{B}) - \mathrm{j}B_\mathrm{II}} \sqrt{\frac{G_\mathrm{I}\,(1 - \theta_\mathrm{G} + \mathrm{j}\theta_\mathrm{B}\,)}{G_\mathrm{II}\,(1 + \theta_\mathrm{G} + \mathrm{j}\theta_\mathrm{B}\,)}} \end{aligned} \tag{12}$$

Equations (11) and (12) show that voltage and current gains are function of the load. The input (P_in) and output power (P_L) can be expressed:

$$P_\mathrm{in} = \frac{1}{2}\mathrm{Re}(Y_\mathrm{in})\,|u_1|^2 \tag{13}$$

$$P_{\mathrm{L}} = \frac{1}{2}\mathrm{Re}(Y_L)\,|u_2|^2 \tag{14}$$

Where Re(Y) is the real part of the admittance. From (8), (11), (13) (14), the efficiency of CPT system is given as:

$$\eta = \frac{P_{\mathrm{L}}}{P_{\mathrm{in}}} = \frac{Y_{\mathrm{M}}\,Y_{\mathrm{M}}^*}{G_{\mathrm{I}}\,G_{\mathrm{II}}}\,\frac{1}{(1+\theta_{\mathrm{G}})^2+\theta_{\mathrm{B}}^2} \tag{15}$$

Defining the following two parameters:

$$\chi^2 = \frac{B_{\mathrm{M}}^2}{G_{\mathrm{I}}\,G_{\mathrm{II}}} \tag{16a}$$

$$\psi^2 = \frac{G_{\mathrm{M}}^2}{G_{\mathrm{I}}\,G_{\mathrm{II}}} \tag{16b}$$

The parameter ψ represents the ratio between the coupling and the self-conductance. The parameter χ is an equivalent to the quality factor. The (15) is rewritten as:

$$\eta = \frac{\psi^2+\chi^2}{(1+\theta_{\mathrm{G}})^2+\theta_{\mathrm{B}}^2} \tag{17}$$

In a nondissipative network, that is $\psi = 0$, the efficiency becomes:

$$\eta = \frac{\chi^2}{\left(1+\sqrt{(1+\chi^2)}\right)^2} \tag{18}$$

which is the same formula that reported in [12].

Rewriting (13) in terms of the source current (i_{s}) and applying the conjugate-image principle, the maximum available source power can be calculated as follows.

$$\begin{aligned} P_{\mathrm{s,max}} &= \frac{1}{2}\,\frac{G_{\mathrm{s}} i_{\mathrm{s}}\,i_{\mathrm{s}}^*}{(Y_{\mathrm{in}}+Y_{\mathrm{s}})\,(Y_{\mathrm{in}}^*+Y_{\mathrm{s}}^*)} \\ &= \frac{1}{8}\,\frac{i_{\mathrm{s}}\,i_{\mathrm{s}}^*}{G_{\mathrm{in}}} \end{aligned} \tag{19}$$

The maximum power driven to the load can be written as a function of (19).

$$\begin{aligned} P_{\mathrm{L}} &= \frac{1}{2}\,\frac{G_{\mathrm{L}} i_{\mathrm{s}}\,i_{\mathrm{s}}^*}{(Y_{\mathrm{in}}+Y_{\mathrm{s}})\,(Y_{\mathrm{in}}^*+Y_{\mathrm{s}}^*)}\,\frac{Y_{\mathrm{M}}\,Y_{\mathrm{M}}^*}{(Y_{\mathrm{II}}+Y_{\mathrm{L}})\,(Y_{\mathrm{II}}^*+Y_{\mathrm{L}}^*)} \\ &= 4\,P_{\mathrm{s,max}}\,\frac{\psi^2+\chi^2}{\theta_{\mathrm{G}}\left[(1+\theta_{\mathrm{G}})^2+\theta_{\mathrm{B}}^2\right]} \end{aligned} \tag{20}$$

The formula is reduced to (21) for a nondissipative netwrok ($\psi = 0$ and $\theta_{\mathrm{B}} = 0$) similar to the one reported in [12].

$$P_{\mathrm{L}} = 4\,P_{\mathrm{s,max}}\,\frac{\chi^2}{\sqrt{(1+\chi^2)}\left(1+\sqrt{(1+\chi^2)}\right)^2} \tag{21}$$

III. Experimental Results and Discussion

The capacitive couplers are made of two square-shaped electrodes of 6082 aluminum sheets covered with a plastic lamination pouch for isolation. PicoVNA Vector Network Analyzers (VNA) is used in the measurements, as illustrates in Fig. 3. The measurement is carried out over a distance (d) from 100 mm to 300 mm and frequency range from 300 kHz to 1.5 MHz. Seawater is collected from the local harbor.

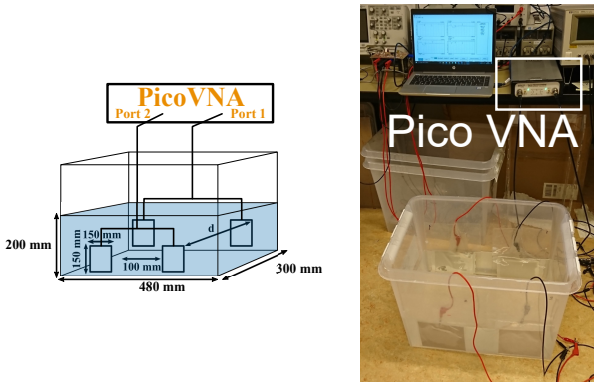

Fig. 3. The measurement setups

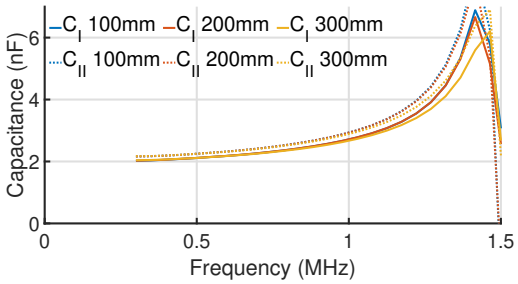

Fig. 4. The self-capacitance C_{I} and C_{II} versus frequency

Fig. 4 illustrates the ranges of self-capacitance C_{I} and C_{II} with changes of the frequency. The C_{I} almost equals C_{II} where the maximum difference between the values is about 0.8 nF. The capacitance increases by about 34% with the increase of the frequency until the self-resonation at 1.7 MHz. When the separation distance increases from 100 mm to 300 mm the capacitance decreases by only 1%, the overlapped lines in the figure depict that the effects of the separation distance are negligible.

Similarly, the mutual capacitance is illustrated in Fig. 5. The value of the capacitance does not vary significantly with changes in the frequency and separation distance. Both the mutual and the self-capacitance of the seawater system are in nF range. The capacitance is much higher than whose in air-

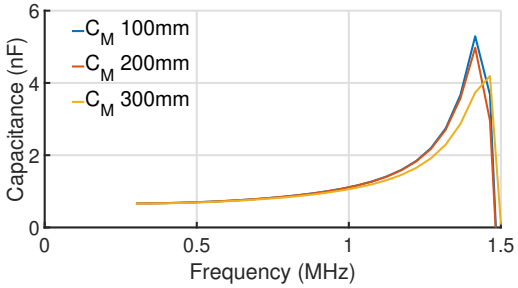

Fig. 5. The mutual capacitance C_{M} versus frequency

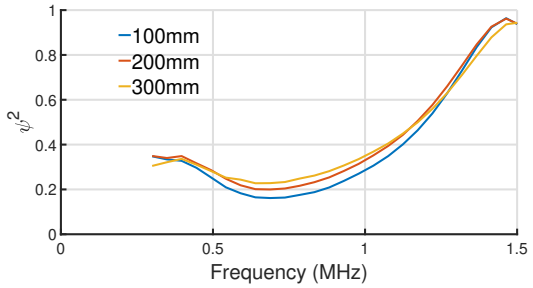

Fig. 6. ψ^2 versus frequency

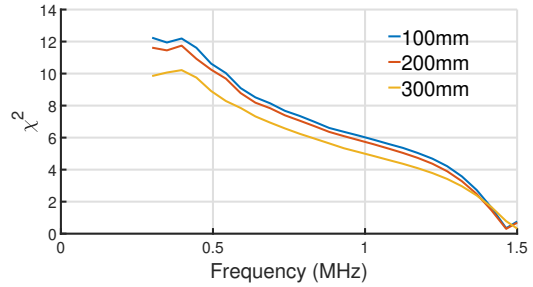

Fig. 7. χ^2 versus frequency

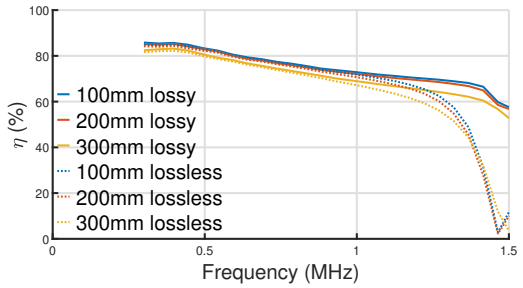

Fig. 8. Maximum efficiency versus frequency

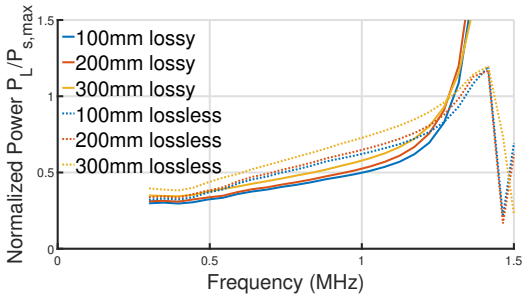

Fig. 9. Available normalized load power at maximum efficiency versus frequency

gapped CPT reported in [3]. This behavior is attributed to the electrical properties of seawater and the fringing effect of the electric fields near the edges of the conducting plates.

The two parameters ψ^2 and χ^2 are calculated over the frequency range using (16) and shown in Fig. 6 and Fig. 7, respectively. Fig. 6 shows that the ψ is not zero over the frequency range. Thus, the nondissipative (lossless) analysis could give imprecise results.

According to (18), if $\chi \to \infty$ provides an efficiency of $\eta \to 100\%$. The results show that it monotonically decreases with the increase of frequency. Thus, the CPT system is expected to give higher efficiency at lower frequency ranges. As depicted in Fig. 8, the efficiency is plotted using (17) and (18) over the frequency range.

The results show that the efficiency decreased by about 16% when the frequency increases from 300 kHz to 1 MHz which attributes to the reduction of the χ^2 parameter with the increase of the frequency. The maximum efficiency is about 86% which is achieved at a separation distance of 100 mm and frequency of 300 kHz. The 14% losses are due to the conductivity behavior of seawater.

Since the separation distance has a negligible effect on ψ^2 and χ^2, then the effect of the separation distance on efficiency is almost negligible, as shown in Fig. 8. In addition, the lossy and lossless analysis give the same efficiency at low frequency range. This shows that the χ^2 parameter is a crucial parameter in measuring the maximum efficiency and its corresponding maximum available transmitted power.

The available normalized power derived, from (20) and (21), is also investigated over the frequency and distance ranges. The results demonstrate that the lossless analysis gives over-estimated values compared to the dissipative (lossy) analysis, as shown in Fig 9. Besides, the maximum available power to the load is deficient at the system's maximum efficiency. Moreover, the normalized power does not significantly change with distance or frequency. The results also demonstrate that both lossy and lossless analysis fails near the self-resonant frequency.

IV. Conclusion

The paper investigates a capacitive power transfer system (CPT) submerged in seawater. The investigation is carried out using the conjugate-image method to drive the maximum efficiency for a dissipative CPT system. The experiment results show that both the seawater's mutual and self-capacitances is in nF range, which is much higher than whose in air-gapped CPT. The results also show that the maximum change in the available efficiency is about 6.3% when the transfer distance increases from 100 mm to 300 mm. Besides, the efficiency decreases by about 17.5% when the frequency increases from 300 kHz to 1 MHz. The maximum efficiency is about 86% which is achieved at a separation distance of 100 mm and frequency of 300 kHz. Thus, the CPT system can be used for wide-distance charging applications, but the analysis should be extended to include the solution that maximises the transferred power.

REFERENCES

[1] F. Lu, H. Zhang, and C. Mi, "A Review on the Recent Development of Capacitive Wireless Power Transfer Technology," *Energies*, vol. 10, no. 11, p. 1752, nov 2017.

[2] ——, "A Two-Plate Capacitive Wireless Power Transfer System for Electric Vehicle Charging Applications," *IEEE Transactions on Power Electronics*, vol. 33, no. 2, pp. 964–969, 2018.

[3] H. Zhang, F. Lu, H. Hofmann, W. Liu, and C. C. Mi, "A Four-Plate Compact Capacitive Coupler Design and LCL-Compensated Topology for Capacitive Power Transfer in Electric Vehicle Charging Application," *IEEE Transactions on Power Electronics*, vol. 31, no. 12, pp. 8541–8551, 2016.

[4] M. Tamura, Y. Naka, K. Murai, and T. Nakata, "Design of a Capacitive Wireless Power Transfer System for Operation in Fresh Water," *IEEE Transactions on Microwave Theory and Techniques*, vol. 66, no. 12, pp. 5873–5884, 2018.

[5] M. Tamura, Y. Naka, and K. Murai, "Design of capacitive coupler in underwater wireless power transfer focusing on kQ product," *IEICE Transactions on Electronics*, vol. E101C, no. 10, pp. 759–766, 2018.

[6] M. Urano, K. Ata, and A. Takahashi, "Study on underwater wireless power transfer via electric coupling with a submerged electrode," *IMFEDK 2017 - 2017 International Meeting for Future of Electron Devices, Kansai*, pp. 36–37, 2017.

[7] H. Zhang and F. Lu, "Feasibility Study of the High-Power Underwater Capacitive Wireless Power Transfer for the Electric Ship Charging Application," *2019 IEEE Electric Ship Technologies Symposium, ESTS 2019*, pp. 231–235, 2019.

[8] H. Mahdi, B. Hoff, and T. Ostrem, "Evaluation of Capacitive Power Transfer for Small Vessels Charging Applications," *IEEE International Symposium on Industrial Electronics*, vol. 2020-June, pp. 1605–1610, 2020.

[9] F. Lu, H. Zhang, H. Hofmann, and C. C. Mi, "A Double-Sided LC-Compensation Circuit for Loosely Coupled Capacitive Power Transfer," *IEEE Transactions on Power Electronics*, vol. 33, no. 2, pp. 1633–1643, 2018.

[10] L. Huang and A. P. Hu, "Defining the mutual coupling of capacitive power transfer for wireless power transfer," *Electronics Letters*, vol. 51, no. 22, pp. 1806–1807, 2015.

[11] T. Ohira, "Extended k-Q product formulas for capacitive- and inductive-coupling wireless power transfer schemes," *IEICE Electronics Express*, vol. 11, no. 9, pp. 1–7, 2014.

[12] M. Dionigi, M. Mongiardo, G. Monti, and R. Perfetti, "Modelling of wireless power transfer links based on capacitive coupling," *International Journal of Numerical Modelling: Electronic Networks, Devices and Fields*, vol. 30, no. 3-4, 2017.

[13] M. Tamura, K. Murai, and M. Matsumoto, "Design of Conductive Coupler for Underwater Wireless Power and Data Transfer," *IEEE Transactions on Microwave Theory and Techniques*, vol. 69, no. 1, pp. 1161–1175, 2021.

[14] S. Roberts, "Conjugate-Image Impedances," *Proceedings of the IRE*, vol. 34, no. 4, pp. 198p–204p, apr 1946.